ABSTRACT

Title of Dissertation: IMPROVING OUR UNDERSTANDING OF TROPICAL CYCLONE UNUSUAL MOTION AND RAPID INTENSIFICATION

William James Schouler Miller, Doctor of Philosophy, 2019

Dissertation directed by: Professor Da-Lin Zhang, Department of Atmospheric and Oceanic Science

Despite steady improvement in their tropical cyclone (TC) track and intensity forecasts over recent decades, operational numerical weather prediction (NWP) models still struggle at times in predicting two TC phenomena: climatologically unusual motion and rapid intensification (RI). Atlantic TCs typically move clockwise along curved tracks skirting the southern, western, and northwestern periphery of the Western Atlantic Ridge. Hurricane Joaquin (2015) followed a particularly unusual hairpin loop-shaped track that was poorly predicted by most operational NWP models, including the National Centers for Environmental Prediction (NCEP) Global Forecast System (GFS). Over recent years,

considerable interest has also developed in understanding the cause-and-effect relationship between RI, defined here as a maximum surface wind (V_{MAX}) intensification rate exceeding 15 m s^{-1} (24 h^{-1}), and outbreaks of inner core deep convection, known as convective bursts (CBs), that have been observed to precede or coincide with RI in some TCs. A deeper physical understanding of the atmospheric processes governing TC unusual motion and RI, together with retrospective case study analyses of model forecast errors, will help us to identify NWP model components – data assimilation and physical parameterizations, for example – that may need further improvement.

This research project seeks to (i) identify the atmospheric features that steered Hurricane Joaquin (2015) along the southwestward leg of its looping track and (ii) investigate the thermodynamic and three-dimensional characteristics of CBs as a first step toward developing a more comprehensive understanding of how CBs may facilitate RI. To accomplish (i), we generate a high-resolution Weather Research and Forecasting (WRF) model Control (CTL) simulation of Hurricane Joaquin (2015) that reproduces its looping track and intensification trends. Comparing CTL forecast fields against sensitivity WRF simulations initialized from perturbed analyses and against two representative GFS forecasts, we find that a sufficiently strong mid-to-upper level ridge northwest of Joaquin and a vortex sufficiently deep to interact with northeasterly geostrophic flows surrounding the ridge are both necessary for steering Joaquin southwestward. These results suggest that more accurate track forecasts for TCs developing in vertically sheared environments may be at least partly contingent on improved vortex initialization; for these cases, assimilation of more inner-core observations such as cloudy radiances and airborne radar-derived winds could be particularly beneficial.

We address (ii) by comparing parcel traces, thermodynamic variables, and vertical accelerations along trajectories run through CB updraft cores with trajectories representative of the background eyewall ascent in a Hurricane Wilma (2005) WRF simulation. We compute three-dimensional trajectories from WRF-output winds using a model developed for this study that implements an experimental advection correction algorithm designed to reduce time interpolation errors, with the latter confirmed by tests on analytical and numerically-simulated flows. Results show that Wilma's CBs are characterized by significant thermal buoyancy, particularly in the upper troposphere; this is consistent with their lower environmental air entrainment rates and reduced midlevel hydrometeor loading relative to the background ascent, and with their updrafts being rooted in portions of the boundary layer where ocean surface heat and moisture fluxes are locally higher.

IMPROVING OUR UNDERSTANDING OF TROPICAL CYCLONE UNUSUAL MOTION AND RAPID INTENSIFICATION

by

William James Schouler Miller

Dissertation submitted to the Faculty of the Graduate School of the
University of Maryland, College Park, in partial fulfillment
of the requirements for the degree of
Doctor of Philosophy
2019

Advisory Committee:
Professor Da-Lin Zhang, Chair/Advisor
Professor Eugenia Kalnay
Professor Ross Salawitch
Professor James Carton
Assistant Professor Jonathan Poterjoy
Professor Xiangdong Ji, Dean's Representative

Dedication

My dissertation is dedicated to my parents, James and Maria Miller, and my sister, Lydia Miller, for being such a loving and supportive family and for always believing in me through all the ups and downs of my graduate school journey.

Acknowledgements

I owe special thanks to my advisor, Prof. Da-Lin Zhang, for his outstanding academic mentorship, career advice, and encouragement during my years of Masters and Ph.D. study here at the University of Maryland. His ideas and revision suggestions have formed an indispensable part of this research. Dr. Zhang took me on as a first-year graduate student when I had no prior research background in dynamic meteorology and no experience in computer programming, and he was patient with me during the early months while I developed the scientific background knowledge and computing skills needed for performing this research. I am also grateful to Prof. Zhang for giving me considerable freedom in choosing the direction of my research later in my Ph.D. study period; this enabled me to further grow as a scientist.

Several other AOSC faculty members have taken special interest in my work and provided me with some valuable guidance. Dr. Kayo Ide's suggestions were especially helpful for me when designing analytical tests for the trajectory model described in Chapter 4. I thank Dr. Daryl Kleist for his advice while I was learning how to use data assimilation as a research tool, and I also thank Dr. Eugenia Kalnay for her helpful ideas on how to interpret my Hurricane Joaquin (2015) WRF simulation results. Dr. Jonathan Poterjoy has more recently joined my thesis committee and I value his feedback on my research as well as his career advice.

I am greatly indebted to Dr. Jeff Anderson, Dr. Glen Romine, Nancy Collins, Tim Hoar, and the rest of the UCAR DART project team for their help while I was learning to use the WRF-DART system for my research. Dr. Thomas Payerle of the University of

Maryland Division of Information Technology provided me with invaluable assistance while I was building WRF-DART on the University of Maryland Deepthought2 high-performance computer, and with other high-performance computing challenges that I have faced throughout my Ph.D. research.

Table of Contents

List of Tables

List of Figures

List of Commonly Used Symbols

CB-E1	CB element #1 (chapter 5)
D_{AVG}	mean updraft diameter
d_{EDGE}	minimum parcel distance to updraft edge in any Cardinal direction
E1	updraft element #1 (chapter 5)
f	Coriolis Parameter
g	Gravitational Constant
ω	total angular speed
ω'	perturbation angular speed
Ω	advective component of angular speed
p	pressure
q_V	water vapor mixing ratio
q_{LIQ}	liquid hydrometeor mixing ratio
q_{FRZ}	frozen hydrometeor mixing ratio
q_{HYD}	total hydrometeor mixing ratio ($= q_{LIQ} + q_{FRZ}$)
q_{TOT}	total water mixing ratio ($= q_{HYD} + q_V$)
RH	Relative Humidity
RH_{ENV}	environmental Relative Humidity
r_m	optimal steering radius for forecast storm
r_o	optimal steering radius for observed storm
T	Temperature
θ	potential temperature
θ_e	equivalent potential temperature
$\theta_{e,ENV}$	environmental equivalent potential temperature
θ_v	virtual potential temperature
u_r	total radial speed
u_r'	perturbation radial speed
U_r	advective component of radial speed
$\boldsymbol{V}_{opt,m}$	optimal steering flow vector for forecast storm
$\boldsymbol{V}_{opt,o}$	optimal steering flow vector for observed storm
V_R	radial wind speed
V_T	tangential wind speed
w	vertical velocity
w_{MAX}	maximum w along a trajectory
w_{MAX}-8	subsample of MBL-Origin trajectories with $w_{MAX} < 8$ m s^{-1}
w_{MAX}-12	subsample of MBL-Origin trajectories with 8 m s^{-1} $< w_{MAX} \leq 12$ m s^{-1}
w_{MAX}-16	subsample of MBL-Origin trajectories with 12 m s^{-1} $< w_{MAX} \leq 16$ m s^{-1}
w_{MAX}-20	subsample of MBL-Origin trajectories with 16 m s^{-1} $< w_{MAX} \leq 20$ m s^{-1}
w_{MAX}-CB	subsample of MBL-Origin trajectories with 20 m s^{-1} $< w_{MAX}$

List of Commonly Used Abbreviations

2D	Two-dimensional
3D	Three-dimensional
3DVAR	Three-dimensional Variational Data Analysis
AAM	Absolute Angular Momentum
AC	Advection Correction
AMSU-A	Advanced Microwave Sounding Unit-A
AMV	Atmospheric Motion Vector
ARW	Advanced Research core of the WRF model
BA	Buoyant Acceleration
BEC	Background Error Covariance
CB	Convective Burst
CTL	Hurricane Joaquin (2015) Control WRF simulation
DART	Data Assimilation Research Testbed
ECMWF	European Center for Medium-Range Weather Forecasting
EAKF	Ensemble Adjustment Kalman Filter
EnKF	Ensemble Kalman Filter
0.25˚-FNL	NCEP Final Analysis at 0.25˚ horizontal grid resolution
1˚-FNL	NCEP Final Analysis at 1˚ horizontal grid resolution
GFS	Global Forecast System
IDE_{HORIZ}	horizontal Individual Displacement Error
IDE_{VERT}	vertical Individual Displacement Error
ΔIDE_{HORIZ}	differenced horizontal Individual Displacement Error
ΔIDE_{VERT}	differenced vertical Individual Displacement Error
LHR	Latent Heat Release
LI	Linear Interpolation
MBL	Maritime Boundary Layer
MBL-Origin	group of all backward trajectories originating in the MBL (section 5.2.2)
NOAA	National Oceanic and Atmospheric Administration
NONUDGE	CTL simulation re-run without analysis nudging
NCEP	National Centers for Environmental Prediction
NHC	National Hurricane Center
NWP	Numerical Weather Prediction
PBL	Planetary Boundary Layer
PGA	vertical perturbation Pressure Gradient Acceleration
P_{MIN}	minimum central SLP
RI	Rapid Intensification
RK2	Runge-Kutta 2 numerical time integration scheme
RMSE	Root Mean Square Error
RMW	Radius of Maximum Wind
SCAPE	Slantwise Convective Available Potential Energy
SLP	Sea Level Pressure

SST	Sea Surface Temperature
TC	Tropical Cyclone
UTC	Coordinated Universal Time
V_{MAX}	maximum 10-m wind speed
VWS	Vertical Wind Shear
WISHE	Wind-Induced Surface Heat Exchange
WRF	Weather Research and Forecasting model
WRFDA	WRF Data Assimilation system

Chapter 1. Introduction

1.1 Background and motivation

Tropical cyclones (TCs)[1] are one of the most destructive natural hazards on Earth, and protection of life and property is critically dependent on accurate forecasts of their track and intensity. When TCs threaten coastlines with damaging winds, storm surge, and/or flooding rains, emergency managers need several days' lead time prior to storm arrival to make decisions on issuing evacuation orders. The National Hurricane Center (NHC) in Miami FL, which is responsible for public TC forecasts in the Atlantic and Eastern Pacific basins, relies heavily on numerical weather prediction (NWP) model guidance. The suite of available NWP model output includes lower resolution global models such as the U.S. National Centers for Environmental Prediction (NCEP) Global Forecast System (GFS), as well as convection-resolving regional models optimized for TCs - such as the Hurricane Weather Research and Forecast model (HWRF). Regional models use boundary conditions provided from the global models.

On average, NHC forecast accuracy has improved substantially over recent decades, particularly for TC tracks (Rappaport et al. 2009). More accurate NWP model output is arguably the greatest contributing factor to this success. Unfortunately, NWP models still struggle in predicting two TC phenomena that are less well understood: *climatologically unusual motion* and *rapid intensification (RI)*. RI in Atlantic TCs is

[1] The National Hurricane Center defines a TC as a "rotating, organized system of clouds and thunderstorms that originates over tropical or subtropical waters and has a closed low-level circulation" (https://www.nhc.noaa.gov/climo/). Mature TCs are also referred to as hurricanes in the Atlantic and eastern Pacific basins, typhoons in the northwestern Pacific basin, and cyclones in the Indian basin.

defined as a maximum surface wind (V_{MAX}) intensification rate exceeding 15 m s^{-1} (24 h^{-1}) (Kaplan and DeMaria 2003). The focus of the work described herein is to investigate the scientific processes controlling TC unusual motion and RI, using two selected case studies. If our ultimate objective is reducing NWP model forecast errors, improved scientific understanding of these phenomena is an important first step towards this end, for the following reasons. First, it will help us better assess the *predictability* of unusual motion and RI. In other words, to what extent do the occasionally large errors in model forecasts result from unusually rapid error growth during model integration? Second, a better understanding of how well our current suite of NWP models can resolve the underlying physical processes should help us identify model components in need of further improvement - such as, for example, data assimilation, model physics, and/or resolution. The following two subsections introduce the forecast challenges posed by TC unusual motion and RI and raise some preliminary scientific questions. The final section of this chapter outlines major objectives of this research project.

1.1.1 Climatologically unusual TC motion

Mean NHC 24-48 h forecast TC position errors have dropped by 70% since 1990 (Cangialosi and Franklin 2016) – one of the greatest achievements in all of NWP. Increased grid resolution, improved model physics parameterizations, and more accurate initialization fields (i.e., analyses) have all improved operational forecast models' representation of large-scale wind and temperature fields (Rappaport et al. 2009; Galarneau and Davis 2013). Advanced data assimilation algorithms (Hamill et al. 2011) and the assimilation of new observations over traditionally data-sparse oceans, which include clear-sky satellite radiances and National Oceanic and Atmospheric Administration

(NOAA) Gulfstream-IV (G-IV) synoptic surveillance aircraft dropsondes (Aberson 2010), have both helped to improve the accuracy of large-scale flow fields in operational GFS analyses. Traditionally, TC motion has been understood as the advection of an isolated vorticity anomaly by a surrounding "mean wind" vertically averaged over a "steering layer" (Chan and Gray 1982); the mean wind includes any near-storm flow asymmetries generated by the vortex through the "beta effect" (Holland 1983, 1984). Provided that the mean wind field surrounding a TC vortex is not substantially sheared, either in the horizontal or the vertical dimensions, accurate model prediction of TC motion is generally less sensitive to the model resolution of inner core structures compared to that of larger-scale flows (Galarneau and Davis 2013). This condition often holds for the climatologically typical anticyclonic TC motion that follows geostrophic steering currents surrounding the Western Atlantic Ridge; for these typical tracks, westward to northwestward motion in the tropics/subtropics is followed by midlatitude recurvature to the northeast.

Notably however, Landsea and Cangialosi (2018) have recently reported a "leveling off" in NHC TC track forecast improvement trends over the five-year period ending in 2016, especially for the longer 120-h lead times – see their Fig. 1, reproduced below as Figure 1.1. Their study focused on trends in mean seasonal TC track forecast errors. On one hand, these authors found no NHC track forecast improvement over the same five-year period relative to a simple climatology and persistence model, which implies that the mean track error statistics over this period are *not completely* skewed by a few outlier cases with unusually low predictability. They discussed one possible explanation for this result: that longer-lead TC track forecasts may be approaching the

Lorenz (1969) predictability limit that results from errors cascading upwards from smaller scales to the synoptic scale.

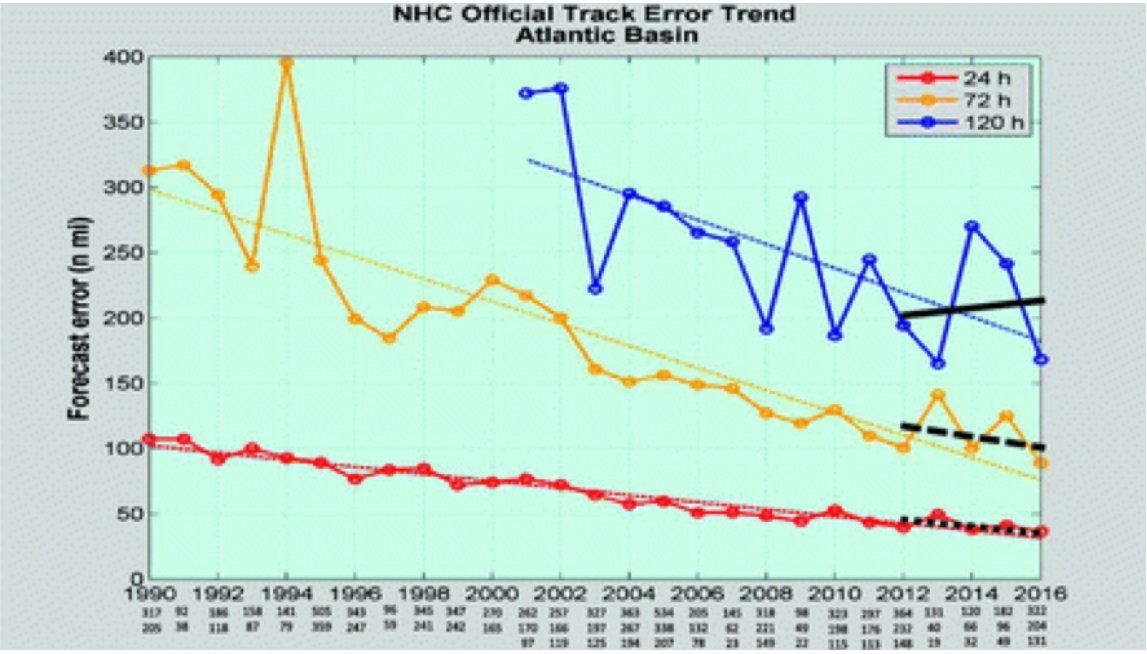

Figure 1.1 Track forecast errors (in n mi) from the NHC for the Atlantic basin for the 24- (red), 72- (yellow), and 120-h (blue) predictions. The best fit linear trend is indicated for each time frame in the colored dotted lines. The 2012–16 best fit linear trend is appended for each time series in black. Samples sizes for the 24-, 72-, and 120-h forecasts are indicated (from top to bottom) along the *x* axis. Adapted from Landsea and Cangialosi (2018) Fig. 1.

Landsea and Cangialosi (2018) also pointed out how the 2012-2016 period included a few notable Atlantic TCs with large NHC forecast track errors, such as Tropical Storm Debby (2012), Hurricane Sandy (2012), and Hurricane Joaquin (2015). Common to all three cases was a bifurcation in NWP model forecast tracks at lead times longer than 72 h, with two distinct "camps" of ensemble member and deterministic model solutions. The latter two storms, both of which caused extensive destruction and loss of life, also followed climatologically unusual tracks. For Sandy (2012), the deterministic European Center for Medium-range Weather Forecasting (ECMWF) model correctly predicted the storm to

"hook leftward" at an unusually high latitude and strike the northeast U.S. many cycles earlier than the GFS; the latter continued to forecast a northeastward recurvature into the open Atlantic during this period. Steering currents caused by an anomalous upper-level blocking pattern, featuring a large high over the northern Atlantic south of Greenland and a deep trough over the southeastern U.S., helped to draw Sandy northwestward onto the U.S. coast (Blake et al. 2013). Torn et al. (2015) further showed how the bifurcated early cycle GFS ensemble track spread – with the two member groups roughly in line with the deterministic ECMWF and GFS solutions, respectively - resulted in part from subtle differences in the model representation of rainband latent heating that in turn impacted the ridge intensity north of Sandy. Unusual TC motion is not confined to the Atlantic basin. Zhang et al. (2018) analyzed 1320 western Pacific typhoons from a 65-year period ending in 2013 and found that 564 storms followed unusual tracks at some point in their lifetimes, which they categorized into the following sub-types: sharp westward turning, sharp eastward turning, sharp northward turning, sharp southward turning, looping, rotating, or zigzagging.

Hurricane Joaquin (2015) followed a particularly unusual looping track (Fig. 1.2; adapted from Torn et al. 2018 Fig. 4a). Beginning as an extratropical upper-level low south of Bermuda (Berg 2016), Joaquin underwent "tropical transition" (Davis and Bosart 2004; Bentley et al. 2017), also climatologically rare for Atlantic major hurricanes. During tropical transition, Joaquin's precursor disturbance drifted southwestward toward the Bahamas while deep convection developed nearby (Berg 2016). Around 0600 UTC 29 Sep, Joaquin began a 60-h RI episode, with its V_{MAX} increasing from 18 to 61 m s^{-1}. Joaquin continued moving southwestward during RI; satellite-derived wind imagery revealed a

complex near-storm steering environment (to be described more fully in section 2.2) with substantial vertical wind shear (VWS), particularly northwest of the storm. Here, an elongated northeast-southwest oriented mid-to-upper level ridge overlay a relative weakness in low-to-mid level ridging. Joaquin's motion slowed for the next 24 hours as it began a slow clockwise turn through the Bahamas under a weak steering flow regime that developed as a digging mid-to-upper level trough over the eastern U.S. eroded the aforementioned mid-to-upper level ridge. After 1800 UTC 02 Oct Joaquin began accelerating northeastward, completing its loop; although the storm initially re-intensified, it eventually weakened as it moved into a less favorable environment near Bermuda (Berg 2016).

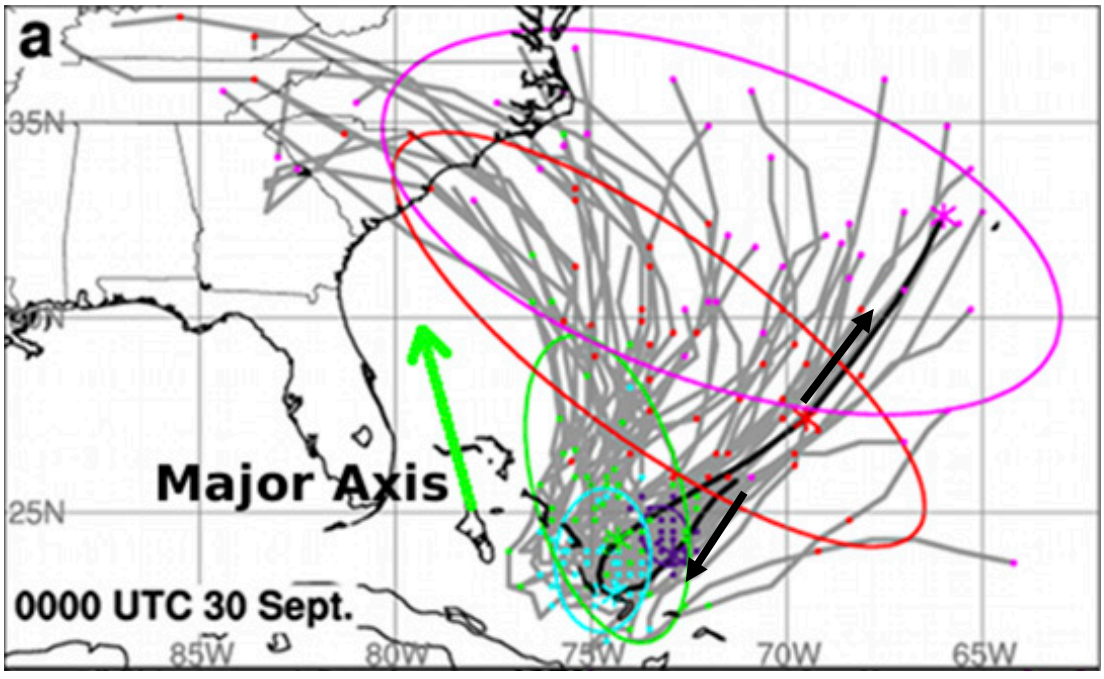

Figure 1.2 Operational ECMWF ensemble forecasts of Hurricane Joaquin (2015) initialized at 0000 UTC 30 Sep (gray lines). Dots indicate the location of each ensemble member at 24-h intervals, while the colored ellipses show a bivariate normal fit to the positions at each 24 h. Purple, cyan, green, red, and magenta denote 24-h, 48-h, 72-h, 96-h, and 120-h locations, respectively. The direction of the 72-h major axis is denoted by the

green vector. The thick black line connects NHC best-track storm positions from the 0000 UTC 30 Sep – 0000 UTC 05 Oct period, and black arrows point in the direction of storm motion. Adapted from Torn et al. (2018) Fig. 4a.

Joaquin's track was poorly forecast by most operational models, particularly early in its southwest movement period (Berg 2016). Figure 1.2 shows the bifurcated ECMWF ensemble track guidance initialized at 0000 UTC 30 Sep. Members are concentrated into two camps: one similar to the correct looping track solution and the other forecasting a northwestward turn leading to a Carolina landfall. The deterministic ECMWF caught on to the former track solution beginning with the 0000 UTC 29 Sep forecast cycle. However, the GFS and other typically reliable global deterministic models held on to the northwest-turn idea through the 1800 UTC 30 Sep forecast initialization. By this time, the GFS and HWRF forecasts of a U.S. major hurricane landfall at less than 5 days' lead time caused considerable alarm among potentially affected residents. The widely diverging track solutions between the deterministic ECMWF and other global models on 29-30 Sep also presented NHC forecasters with a significant challenge.

The unusually large spread in Joaquin's track forecast among operational deterministic models and ensemble members implies inherent low predictability, whereby large storm motion differences can develop out of small atmospheric state variations that are (i) present in the model initial conditions, and/or (ii) develop early in the model integration. Nystrom et al. (2018, hereafter N18) and Torn et al. (2018) used ensemble forecasts from the Weather Research and Forecasting (WRF) model and operational ECMWF respectively to show how members that eventually recurved Joaquin away from the U.S. tracked further south during the initial 24 hours. While the ECMWF ensemble member position uncertainty was concentrated in the meridional direction over the first 72

hours, it became zonally aligned later on (see the time evolution of the colored ellipse orientation in Fig. 1.2). Torn et al. (2018) showed how Joaquin's initialized vortex at 0000 UTC 30 Sep was located near a large-scale deformation flow axis of contraction, such that small north-south displacements could expose the storm to different flow regimes. N18 also discussed the significance of the early-period north-south ensemble member position spread in the context of the large-scale flow evolution. As the eastern U.S. trough developed into a closed low over the Florida Panhandle late in the forecast period, southern (northern) members experienced stronger westerly (easterly) cyclonic flows surrounding the Florida low; this was consistent with their northeastward out-to-sea (northwestward U.S. landfalling) motion.

It is worthwhile to further investigate why the operational GFS model struggled with Joaquin's track prediction during early forecast cycles. As a starting point, we ask: *what atmospheric features were most important in steering Joaquin southwestward during its early development period?* Berg (2016) noted that the early-cycle GFS forecasts terminated Joaquin's southwestward motion more quickly compared to the more accurate ECMWF track forecast, consistent with the N18 and Torn et al. (2018) ensemble sensitivity analyses. Notably, the northeast-southwest orientation of the mid-to-upper level high positioned northwest of Joaquin aligned well with the storm's southwestward motion vector (to be shown in section 2.2); this suggests that northeasterly geostrophic flows surrounding the high may have been important to steering the storm. If so, then *how sensitive was the storm's southwest motion to the vortex having sufficient depth to interact with these flows?* Previous studies have shown that TC motion in vertically sheared steering environments can be sensitive to the vortex depth, with upper-tropospheric steering winds

having a greater influence on stronger storms, which are generally characterized by taller and more vigorous inner-core convection (Dong and Neumann 1986; Galarneau and Davis 2013). Finally, *did the GFS track forecast errors result from inadequate representation of the vortex, surrounding environment, or some combination of both?*

1.1.2 Convective bursts and RI

Hurricanes Charley (2004), Harvey (2017) and Michael (2018) are recent examples of TCs that underwent RI within 24 hours of making landfall on the U.S. coastline (Franklin et al. 2006; Blake and Zelinsky 2018; Beven et al. 2019). NWP forecast models struggled to capture the Charley (2004) and Michael (2018) intensification rates, and NHC forecasters were placed in the unfortunate position of having to upwardly revise intensity forecasts for these two storms throughout the final day prior to landfall. Coastal residents who had chosen not to evacuate based on earlier lower-intensity forecasts were left unprepared for these storms' ferocity. One of the more enigmatic aspects of TC RI is the fact that the environmental conditions favorable to it, such as high sea surface temperature (SST), low VWS, and high ambient low-to-middle tropospheric relative humidity (Kaplan and DeMaria 2003) are not otherwise distinguished from those favoring normal TC intensification rates (Hendricks et al. 2010). RI in TCs is likely controlled by complex multi-scale interactions between the environment and inner-core processes that are still not well understood (Rogers et al. 2010; McFarquhar et al. 2012; Rogers et al. 2013; Qin et al. 2018b).

Observations have shown that RI can be preceded or accompanied by outbreaks of inner-core deep convection, known as "hot towers" or "convective bursts" (Gentry et al. 1970; Rodgers et al. 1998; Heymsfield et al. 2001; Molinari et al. 2006; Houze 2009;

Guimond et al. 2010). Over recent years, considerable interest has developed around gaining a better understanding of the possible role that CBs play in facilitating RI. According to one hypothesis, perhaps first articulated in Heymsfield et al. (2001), compensating subsidence flanking the inner edges of CB updrafts enhances warming in the middle or upper levels of a TC eye; see their schematic, reproduced here as Fig. 1.3, for a conceptual overview of this process. Eye warming – in other words, a positive local potential temperature tendency – can proceed via this mechanism provided that (i) adiabatic warming locally exceeds evaporative/sublimative cooling in the subsidence currents[2] and (ii) the swirling wind circulation is sufficiently robust to "trap" the heating inside the eye (Hack and Schubert 1986). In understanding (ii), note that higher inertial stability, defined in cylindrical coordinates as

$$F^2 = \left(f + \frac{2V_T}{r}\right)\left[f + \frac{1}{r}\frac{\partial (rV_T)}{\partial r}\right], \qquad (1.1)$$

where f is the Coriolis Parameter, V_T is the tangential wind component, and r is the local radius (Chen and Zhang 2013) indicates greater vortex resistance to radial flows.[3] Warming

[2] Here, we consider potential temperature (θ) in an axisymmetric cylindrical (r, λ, z) coordinate system, where $u_r = Dr/Dt$, in terms of the forcing terms on the local θ tendency: $\partial\theta/\partial t = D\theta/Dt - u_r\frac{\partial\theta}{\partial r} - w\frac{\partial\theta}{\partial z}$. They are, from left to right, the material derivative absorbing all Lagrangian θ sources and sinks, horizontal advection, and vertical advection. Provided static stability $\frac{\partial\theta}{\partial z}$ is positive, eye subsidence (i.e. negative w) is a positive forcing on $\partial\theta/\partial t$ via the vertical advection term $-w\frac{\partial\theta}{\partial z}$.

[3] Eliassen (1952) first derived an equation describing a transverse circulation in the r-z plane of a symmetric vortex in hydrostatic and gradient wind balance that slowly evolves in response to heat and momentum sources. This equation has been widely used in theoretical TC studies to describe the "in-up-out" secondary circulation consisting of a low-level inflow, eyewall updraft core, and upper tropospheric outflow (Charney and Eliassen 1964; Shapiro and Willoughby 1982; Hack and Schubert 1986) – an excellent review of this topic can be found in Montgomery and Smith (2014) sections 2.1- 2.5. Inertial stability F^2, which is proportional to the Coriolis parameter, V_T/r, and the vertical

in the eye vertical column hydrostatically induces a lower surface pressure. It is well known that for intensifying TCs, minimum central sea level pressure (P_{MIN}) falls accompany increasing V_{MAX}, and several alternative empirical and analytical "pressure-wind relationships" have been developed relating P_{MIN} to V_{MAX} (Kieu et al. 2010). For a vortex under gradient wind balance, V_T intensifies in response to falling central pressures via geostrophic adjustment, provided that pressure field changes occur on a horizontal scale larger than the vortex Rossby radius of deformation (Fang and Zhang 2010). However, gradient wind balance is not satisfied in a TC boundary layer (Montgomery and Smith 2014). Whether P_{MIN} intensification ultimately drives V_{MAX} intensification or vice versa remains a difficult, still unresolved question in the TC research community, and we shall revisit this question briefly again in Chapter 6. Besides the Heymsfield et al. (2001) subsidence warming mechanism, CBs have also been shown to facilitate TC intensification through their aggregation and vertical stretching of low-level cyclonic vorticity (Montgomery and Smith 2014; Nguyen and Molinari 2015) and by their moistening of the midlevel inner core (Nolan 2007; Montgomery et al. 2006).

component of relative vorticity, appears in Eliassen's (1952) equation as a stabilizing term acting to resist the transverse circulation in the radial direction.

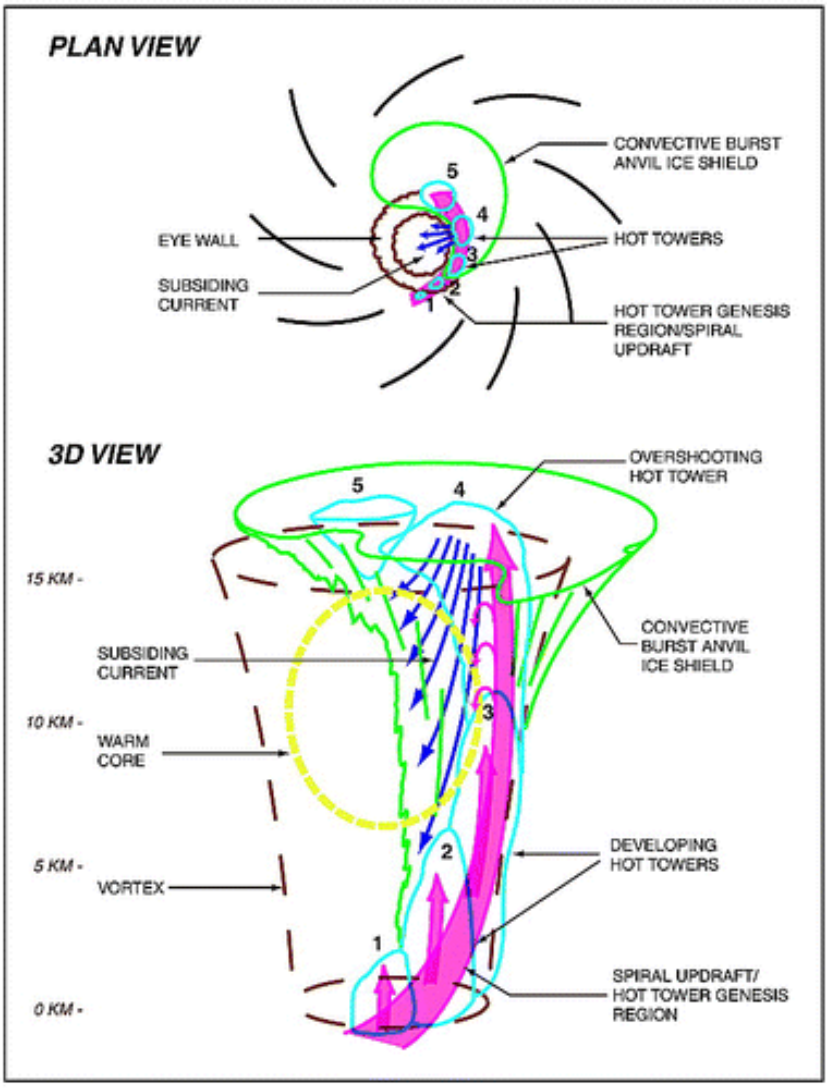

Figure 1.3 Conceptual summary of the proposed mechanism through which CB updraft compensating subsidence contributes to TC eye warming. Adapted from Heymsfield et al. (2001) Fig. 12.

Figure 1.4 shows a vertical cross-section of an intense CB in the rapidly intensifying Hurricane Dennis (2005) as observed by airborne Doppler radar. We find peak vertical velocity exceeding 15 m s^{-1} in the upper troposphere and a ~ 5 m s^{-1} subsidence current on the inward edge of the cloudy region near the developing eye. Chen and Zhang (2013) described how RI onset in their WRF-simulated Hurricane Wilma (2005) was accompanied by an outbreak of eyewall CBs with roughly 30-min lifetimes. Their Fig. 5,

reproduced below as Fig. 1.5, shows subsidence currents (dashed blue lines) that initially surround CB updraft cores becoming trapped inside of the radius of maximum wind (black circles) coincident with the development of a cloud-free eye. Using a heat budget, Miller et al. (2015) found that adiabatic subsidence-induced vertical θ advection (i.e. $-w\frac{\partial \theta}{\partial z}$) accounted for the largest portion of Wilma's upper-level eye warming. This was shown in their Fig. 10, reproduced here as Fig. 1.6.

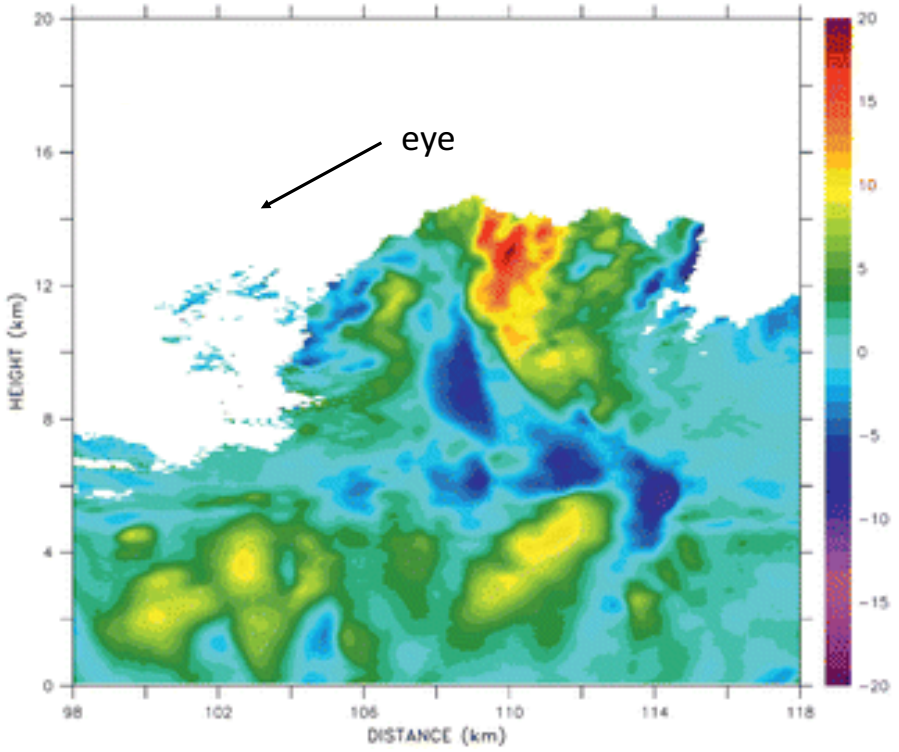

Figure 1.4 Zoomed-in view of an eyewall CB in rapidly intensifying Hurricane Dennis (2005). Vertical velocity (shaded; m s^{-1}) is retrieved from airborne Doppler radar. Adapted from Guimond et al. (2010) Fig. 9b.

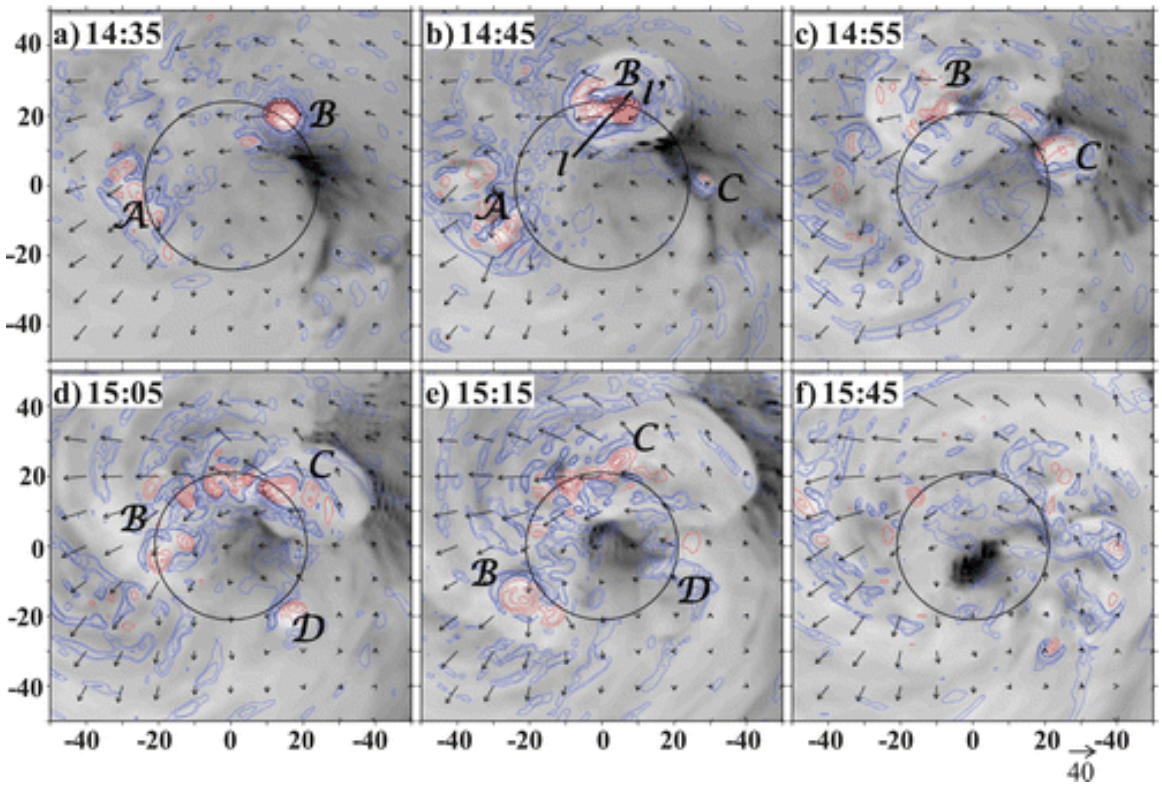

Figure 1.5 Horizontal maps of the predicted outgoing longwave radiation superimposed with storm-relative flow vectors [see the scale below (f)] and vertical motion (upward/red contours at interval of 5 m s^{-1}, downward/blue contours at –0.5, –1, –2, –4, –6, –8, and –10 m s^{-1}) at z = 15 km over the subdomains of 100 km × 100 km, centered at P_{MIN}, that are taken at an interval of 10 min, except for (f) and (g) between which a 30-min interval is used, during the period from (a) 14:00 to (g) 15:45 (i.e., at the onset of RI). The mean radius of maximum wind at z = 1 km is also plotted. Letters A–D are used to trace the evolution of four different convective bursts. Line l–l′ in (b) denotes the location of a vertical cross section shown in Chen and Zhang (2013) Fig. 6. Adapted from Chen and Zhang (2013) Fig. 5.

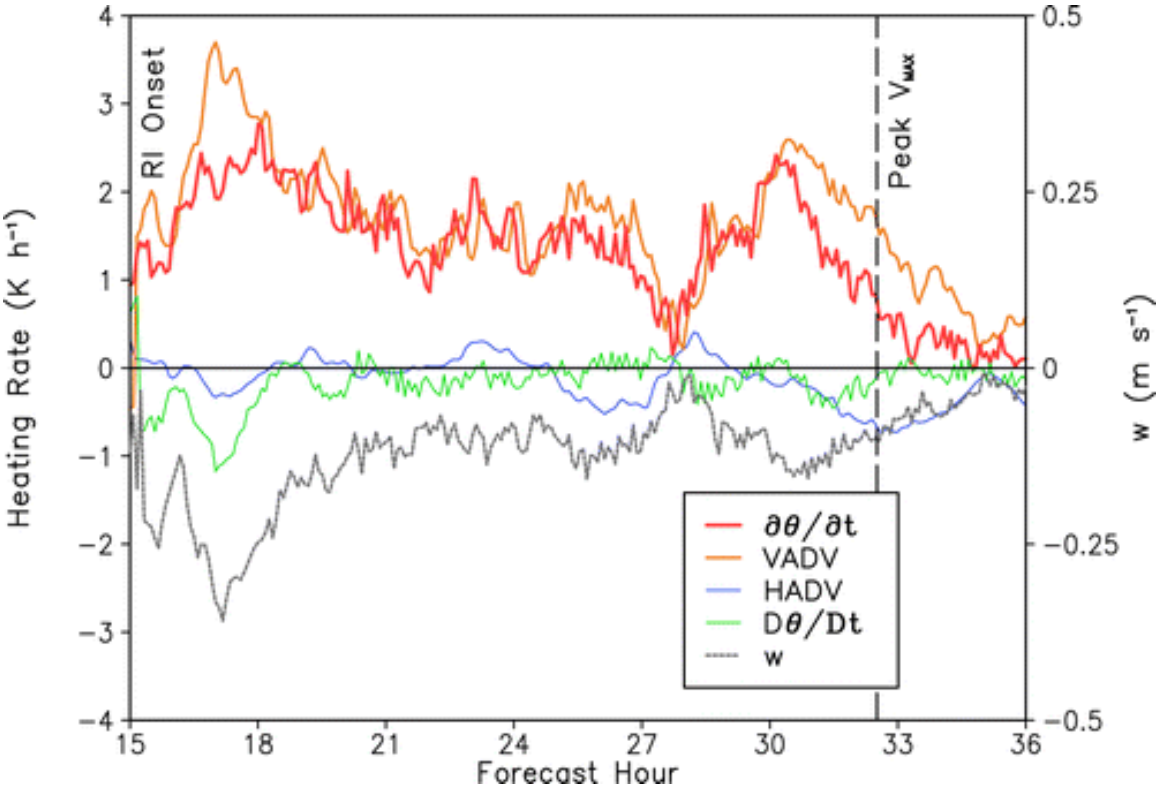

Figure 1.6 Time series of forcing terms on the potential temperature local tendency [$\partial\theta/\partial t = D\theta/Dt - u\frac{\partial\theta}{\partial x} - v\frac{\partial\theta}{\partial y} - w\frac{\partial\theta}{\partial z}$], in the Chen et al. (2011) Hurricane Wilma (2005) WRF simulation, averaged over a 10 km × 10 km; z = 12–16 km control volume centered at the P_{MIN} centroid. HADV and VADV respectively denote horizontal and vertical advections. Curves show data that have been smoothed into a 1-h running mean, with equal weighting applied to the 30-min periods prior to and after the indicated time. Adapted from Miller et al. (2015) Fig. 10.

Given the now widely acknowledged important, potentially even fundamental, role of buoyant deep convection in the RI of TCs, we ask: *how can a mature TC eyewall environment support CB development?* While wind-induced heat and moisture fluxes above warm SSTs provide an ample source of high-equivalent potential temperature (θ_e) air to a TC boundary layer (Emanuel 1986; Zhang et al. 2002), (i) excessive hydrometeor loading from the moist tropical environment (Zhang et al. 2000), (ii) warming from latent heating (Emanuel 1986), (iii) increased static stability associated with warm core

development (Vigh and Schubert 2009), and (iv) the entrainment of surrounding dry air (Cram et al. 2007) could all potentially render the eyewall a less favorable environment for maintaining buoyant updrafts. Also, *given the rapidly rotating TC eyewall flows, to what extent can CB updraft roots be traced to portions of the boundary layer where ocean surface heat fluxes are locally higher?* For instance, Chen and Zhang (2013) showed that the number of CBs generated in their Hurricane Wilma (2005) simulation was strongly sensitive to SST. *How do CB updrafts interact with the locally sheared (both horizontally and vertically) swirling winds? How do local pressure perturbations from hydrostatic balance affect CB updraft accelerations?* Most previous modeling studies (Chen and Zhang 2013; Chen and Gopalakrishnan 2015; Nguyen and Molinari 2015) and observations of CBs in TCs (Heymsfield et al. 2001; Molinari et al. 2006; Houze 2009; Guimond et al. 2010) have used a Eulerian reference frame. A Lagrangian analysis of CB structure and thermodynamics could potentially offer some new insights in addressing the above questions. Ultimately, a better understanding of the conditions favorable to CB development in TCs could be beneficial both to forecasters evaluating the potential for storms to undergo RI and to NWP model developers seeking to improve their models' ability to resolve and predict CBs.

1.2 Objectives

Major objectives of the research described herein are listed below in numbered format, with bulleted points outlining the methods used in addressing them.

i) Investigate the atmospheric features responsible for the unusual looping track of Hurricane Joaquin (2015). Was Joaquin's motion primarily controlled by larger-scale features, or was it also sensitive to the vortex depth?

- Use the WRF model to generate a high-resolution Control (CTL) simulation of Hurricane Joaquin (2015) that reproduces the looping track.
- To investigate hypotheses regarding important steering features, perturb the CTL analysis by assimilating synthetic observations into the WRF Data Assimilation system (WRFDA) and run sensitivity WRF simulations from the perturbed analyses.

ii) Examine the source of the large Hurricane Joaquin (2015) track forecast errors in several operational GFS forecasts. More specifically, what features important to steering Joaquin were not well resolved in these GFS forecasts?

- Use a steering flow error diagnostic equation developed by Galarneau and Davis (2013) to quantify Joaquin's motion error in the GFS forecasts in terms of vector differences from the NHC best-track motion. This equation enables us to isolate model error in representing the large-scale steering environment from model error in representing the vortex size, depth, and interaction with its steering environment.
- To identify specific features poorly resolved by the GFS, compare its gridded analysis and forecast fields to the NCEP Final Analysis, the latter being used as a proxy for the "true" atmospheric state.

iii) Develop a new algorithm for computing three-dimensional trajectories from WRF model output. Implement advection correction (AC) into the time

interpolation algorithm used for mapping WRF output data at relatively coarse temporal resolution to the high resolution computational timestep needed to satisfy computational stability constraints in the trajectory calculations. The purpose of AC – an experimental technique not used in any publically available trajectory models – is to reduce wind estimation errors at the parcel position by interpolating data in a reference frame that translates with the swirling TC wind circulation.

- Adapt a Cartesian coordinates-based AC algorithm originally developed by Gal-Chen (1982) for radar data processing and later extended by Shapiro et al. (2015) for trajectory calculations to cylindrical coordinates, which are more appropriate for analyzing TC flows.
- Evaluate the impact of the new cylindrical coordinates-based AC algorithm on trajectories run from the Hurricane Joaquin (2015) CTL simulation output at 5-minute temporal resolution by comparing them to "truth" trajectories generated from 1-min CTL output using traditional linear time interpolation.

iv) Use the algorithm developed for objective (iii) to run trajectories through CBs generated in the Chen et al. (2011) Hurricane Wilma (2005) WRF prediction and compare their three-dimensional structures and thermodynamic properties to the background eyewall ascent.

- Examine the three-dimensional structure, θ_e conservation, and parcel vertical accelerations for a selected CB trajectory to try to better understand how it becomes differentiated from Wilma's background eyewall ascent.

- Use a statistical analysis of a large trajectory sample to establish systematic differences between Wilma's CBs and the background eyewall ascent in terms of parcel thermodynamics, environmental air entrainment, and vertical accelerations.

The remainder of this dissertation is organized as follows. Chapter 2 (published as Miller and Zhang 2019a) investigates the atmospheric features steering Hurricane Joaquin (2015) along its unusual looping track and identifies which steering features were not well resolved by the operational GFS. Chapter 3 describes the data assimilation methods used in generating WRF analyses for CTL and its sensitivity tests; this chapter expands on material published in Miller and Zhang (2019a) Appendix I. Chapter 4 (published as Miller and Zhang 2019b) introduces the three-dimensional trajectory computation algorithm developed for this research project and validates it using tests on analytical and numerically-simulated flow fields. In Chapter 5 (submitted for publication as Miller and Zhang 2019c), this trajectory algorithm is used to trace the roots of CBs in the Chen et al. (2011) Hurricane Wilma (2005) WRF prediction and study their thermodynamic properties. Chapter 6 provides a dissertation summary, concluding remarks, and ideas for future work.

Chapter 2. Understanding the Unusual Looping Track of Hurricane Joaquin (2015) and its Forecast Errors

Material presented in this chapter has been published in Monthly Weather Review as Miller and Zhang (2019a)

2.1 Introduction

Since 1990, NHC mean TC 24-72 h forecast position errors have been reduced by 70% (Cangialosi and Franklin 2016), giving residents and emergency managers valuable additional time to prepare for hurricanes threatening the U.S. coast. TC intensity forecasting has shown less improvement, particularly for RI cases (Kaplan et al. 2010), characterized by P_{MIN} deepening rates exceeding 42 hPa $(24\ h)^{-1}$ (Holliday and Thompson 1979) or by V_{MAX} intensification exceeding 15 m s^{-1} $(24\ h)^{-1}$ (Kaplan and DeMaria 2003). This discrepancy has often been explained by the fact that TCs are steered by their large-scale flow environments (George and Gray 1976; Chan and Gray 1982; Wu and Emanuel 1995), whereas TC intensification depends upon complex multiscale interactions between favorable environmental conditions, such as high SSTs, and inner-core processes (Chen et al. 2011; Qin and Zhang 2018b), some of which remain poorly understood.

Increased grid resolution, improved physics parameterizations, and more accurate initialization fields have improved the representation of environmental conditions and inner-core convective organization in operational forecast models. New observations over traditionally data-sparse oceans, which include satellite radiances and dropsondes released from NOAA G-IV synoptic surveillance aircraft (Aberson 2010), are now being routinely assimilated into operational models. Hybrid data assimilation, which blends climatological background forecast errors with "errors of the day" extracted from multivariate forecast

ensemble covariances, has been shown to improve TC track forecasts for the operational NCEP GFS model (Hamill et al. 2011) and for regional models (Wang 2011).

Despite these improvements, the GFS has struggled with the track prediction of a few recent high-profile TC cases with unusual movements. Brennan and Majumdar (2011) investigated why several GFS runs failed to predict the northward turn of Hurricane Ike (2008) in the western Gulf of Mexico and instead forecast a due-west track into the lower Rio Grande valley at 3-4 days' lead time. They traced the track errors to the model initial conditions, which over-intensified the subtropical ridge north of the storm. Another notable case was Hurricane Sandy (2012), which the GFS forecast to recurve into the Atlantic for many cycles after the ECMWF model correctly predicted a northeast U.S. landfall. Unlike Brennan and Majumdar (2011) and other previous studies (Wu and Emanuel 1995; Wu et al. 2004), which found that distant synoptic-scale features primarily controlled TC steering, Bassill (2014) and Torn et al. (2015) both traced the GFS Sandy track forecast errors to the model representation of the near-storm environment, and specifically to the impact of latent heating from rainband convection on the intensity of a ridge north of the storm.

Hurricane Joaquin (2015) was a particularly unusual case, and its track was not well forecast by most operational models (Berg 2016, see his Fig. 9). Following genesis, the storm began a climatologically rare southwestward drift toward the Bahamas. The GFS was consistent in predicting the storm to quickly curve westward and then northward, through the 1800 UTC 30 September forecast cycle, with numerous runs showing a hurricane landfall on the mid-Atlantic coast on 04 October. Notably, the ECMWF model broke ranks from the other guidance beginning with the 0000 UTC 29 September cycle,

maintaining the southwestward motion longer before sharply recurving to the storm the northeast and missing the U.S. coast - the correct solution.

Nystrom et al. (2018, hereafter N18) simulated Joaquin using an ensemble of Weather Research and Forecasting (WRF) model forecasts initialized at 1200 UTC 29 Sep, and they found that the recurving members had tracked further south during the first 24 h, compared to the U.S. landfalling members. N18 showed how the south-tracking members were steered by stronger westerly winds later in the forecast period. This was consistent with their having moved further south relative to a mid-to-upper-level low pressure system over the southeast United States, into an environment where the cyclonic winds surrounding the low had a stronger westerly component. Key findings from this study were that (i) Joaquin's track forecast uncertainty was most sensitive to 700-hPa winds in the near-storm environment (the 600 – 900 km radial band); and (ii) inner-core features did not significantly affect the steering of Joaquin. To show the latter, they re-ran the forecast ensemble after applying the same initial conditions within 300 km to every member and found that 80% of the original ensemble track spread was retained. In their analysis of the operational ECMWF ensemble initialized at 0000 UTC 30 Sep, Torn et al. (2018) showed that Joaquin's forecast position uncertainty, which was concentrated in the north-south direction over the first 72-h forecast, was most sensitive to ensemble member differences in the near-storm (within 500 km) steering winds that developed over the first 24 h. This was consistent with the initialized ensemble members being located near the axis of contraction for a large-scale deformation flow, such that relatively small displacements in their meridional positions could expose them to different steering-flow regimes.

TC motion has been traditionally understood in terms of the advection of an isolated vorticity anomaly by the surrounding mean wind. Research over the past few decades has grappled with the more challenging question of how best to define the environmental flow around a TC. Chan and Gray (1982) composited rawinsonde observations surrounding a large sample of western Pacific and Atlantic TCs stratified by latitude, forward speed, size, and intensity; they found that TC motion is best correlated to winds averaged over a 5°-7° radial band in the 700-500 hPa layer. This and earlier studies (e.g., George and Gray 1976; Gray 1977), though comprehensive, were limited by a relatively sparse global observational network. More recent case studies using airborne radar data (Marks et al. 1992) and model simulations (Liu et al. 1999) reported TC motion to be consistent with flows averaged over a much smaller region, within a 100-km radius. Nevertheless, the size of the radial disk or band around a TC where the circulation interacts with the steering flow may depend on both vortex size and flow asymmetries in the near-storm environment (Holland 1983, 1984; Galarneau and Davis 2013, hereafter GD13). Other studies have emphasized the sensitivity of TC motion to the "steering layer" used for vertically averaging the environmental winds. Dong and Neumann (1986) compiled statistics from operational global analyses and showed that steering layer depth was directly proportional to TC intensity, which is consistent with stronger TCs tending to have deeper vortices. Through analysis of omega dropwindsondes released around Hurricane Josephine (1984) during a field campaign, Franklin (1990) showed that for a vertically sheared environment, a TC can be steered by a relatively narrow tropospheric layer and that these flows may not be well estimated by a deep-layered average. Together, this body of work suggests that

even if the large-scale environment is well defined, TC motion may be sensitive to the vortex intensity, structure and size, particularly for complex flow environments.

The objectives of this study are (i) to obtain a successful 114-h control simulation (CTL) of Hurricane Joaquin (2015) in terms of its track, intensity and inner-core structures, as validated against various observations; (ii) to use this simulation, along with sensitivity tests, to further explore the causes of Joaquin's unusual southwest motion; and (iii) to better understand why the operational GFS forecast struggled in predicting this motion. These objectives will be accomplished by identifying atmospheric features that were resolved differently by two representative GFS forecasts, as compared to CTL and the NCEP Final Analysis (FNL). Using these differences as a guide, we perturb the CTL initial conditions by assimilating synthetic observations and run sensitivity forecasts from these analyses. Accomplishing the above objectives will help address the following questions. First, given that the environment surrounding Joaquin was characterized by moderate vertical wind shear (VWS), with northeasterly winds more prominent in the mid-to-upper troposphere (to be shown in the next section), to what extent was Joaquin's southwest motion dependent (if at all) on the vortex having sufficient vertical depth? Second, what features in Joaquin's surrounding environment influenced the steering flows? Third, did the GFS track forecast errors result from inadequate representation of the vortex, surrounding environment, or some combination of both?

The next section provides a case overview. Section 2.3 describes the WRF model settings, initial condition perturbation strategy, and steering flow diagnostics methods. Section 2.4 validates CTL against observations, followed by steering flow analysis given in section 2.5. Major findings and conclusions are summarized in the final section.

2.2 Case overview

Unlike most Atlantic major hurricanes, Joaquin underwent tropical transition (Davis and Bosart 2004; Bentley et al. 2017) from an extratropical precursor disturbance (Berg 2016). Late on 26 Sep, a mid-to-upper level low that had been drifting westward across the subtropical Atlantic acquired a surface reflection about 650 km northeast of the central Bahamas. Although the surface center was initially displaced northwest of disorganized convection, it was designated as a tropical depression on 0000 UTC 28 Sep when convection developed nearby. Joaquin reached tropical storm intensity 24 h later, and it began a 60-h RI period 6 h thereafter, with its V_{MAX} increasing from 18 to 61 m s^{-1}. Although VWS of 7-12 m s^{-1} affected the storm during RI, high SSTs exceeding 29ºC may have facilitated the intensification.

Figure 2.1 shows how the large-scale environment surrounding Joaquin evolved as the storm moved southwestward. At 0000 UTC 30 Sep, when Joaquin is roughly halfway between its genesis position and its southwestern loop apex, a deep mid-to-upper-level trough extends from the Great Lakes southward into the Gulf of Mexico (Figs. 2.1a,b). Joaquin is sandwiched between a southwest-northeast oriented upper-level ridge on its northwest side and an upper-level trough over the southeastern Caribbean (Fig. 2.1a). Another upper-level low can be found well northeast of Joaquin, near 35ºN, 55ºW. The lower-to-middle level environment is dominated by an expansive ridge centered over the northern Atlantic southeast of Nova Scotia and by another ridge over western Cuba and the Yucatán Peninsula (Fig. 2.1b). The cloudy region well east of Joaquin near 35ºN, 55ºW (Fig. 2.1b) is associated with a west-northwestward moving frontal trough that had

absorbed the remnants of Tropical Storm Ida (Cangialosi 2015) several days prior. Forty-eight hours later, as Joaquin nears the southwestern loop apex, the eastern U. S. trough has dug further south and east (Fig. 2.1c). Downstream of this trough, the upper-level ridge northwest of Joaquin has eroded. Meanwhile, the upper-level low northeast of Joaquin has drifted southwestward to a position near 30ºN, 60ºW (Fig. 2.1c), and the expansive cloudy region associated with the old frontal boundary has expanded westward toward Joaquin (Fig. 2.1d).

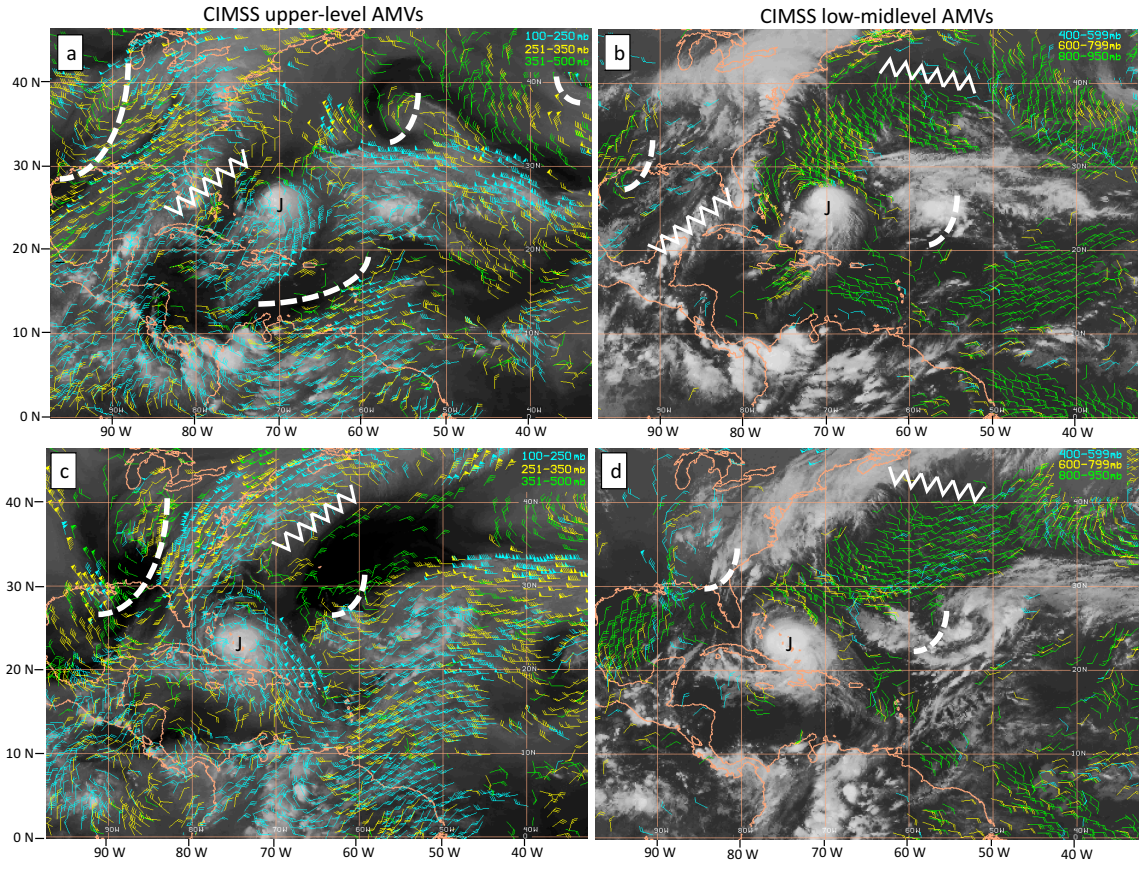

Figure 2.1 Atmospheric motion vectors (AMVs) valid at 0000 UTC 30 Sep 2015, superimposed over GOES-13 water vapor imagery, with Joaquin denoted by the "J" symbol. Upper and lower levels are shown in (a) and (b), respectively, with vectors color-coded by height. (c),(d) As in (a),(b) but for 0000 UTC 02 Oct 2015. The AMVs are derived from the University of Wisconsin-Madison Cooperative Institute for Meteorological Satellite Studies (UW-CIMSS) and these images were obtained from http://tropic.ssec.wisc.edu/archive/.

After 1800 UTC 01 Oct, Joaquin's intensity reached a steady state as it slowly meandered westward through the Bahamas, causing extensive destruction. Around 1200 UTC 02 Oct, the storm began to accelerate to the northeast, steered by southwesterly winds surrounding the eastern U.S. trough. Six hours later, Joaquin began an 18-h re-intensification leading to peak intensity, with its V_{MAX} increasing from 57 to 69 m s^{-1}. The storm weakened thereafter as it encountered lowering SSTs and increasing VWS.

2.3 Methodology

2.3.1 WRF model settings

The 114-h CTL simulation uses a two-way interactive, nonhydrostatic, quadruply nested, 27/9/3/1 km configuration of the Advanced Research core (ARW) WRF Version 3.6.1 (Skamarock et al. 2008). Figure 2.2 shows the domain setup, where the outer 3 domains are fixed and the innermost nest moves, following the 700-hPa vortex center at 15-minute intervals. The 27, 9, 3, and 1-km domains, hereafter Domains 1, 2, 3, and 4, use the Mercator projection and have (x,y) dimension grid sizes of (300,190), (421,322), (514,514) and (601,601), respectively. The model top is set to 30 hPa, and Domains 1-4 use the 55-vertical-level configuration from Chen et al. (2011), with the highest resolution in the boundary layer and near the model top. All four domains are initialized at 0600 UTC 29 Sep, when Joaquin begins its 60-h RI as a tropical storm with an 18 m s^{-1} V_{MAX}. Initial conditions for the 27- and 9-km domains are generated using a 30-h WRF Data Assimilation (WRFDA) hybrid 3DVAR data assimilation cycle, hereafter the WRFDA-hybrid cycle (see chapter 3). Neither vortex bogusing nor relocation techniques are used in generating hybrid analyses from the background WRF forecasts. The 114-h CTL forecast

covers the observed RI, steady-state, and re-intensification episodes. Lateral and lower boundary conditions are taken from the NCEP 1-degree Final Analysis (hereafter 1°-FNL), except for the SSTs. Initial SSTs are interpolated from the NOAA daily 0.25-degree resolution OI-SST dataset, which blends Advanced Very High Resolution Radiometer (AVHRR) and in-situ observations using optimal interpolation (Reynolds et al. 2007).

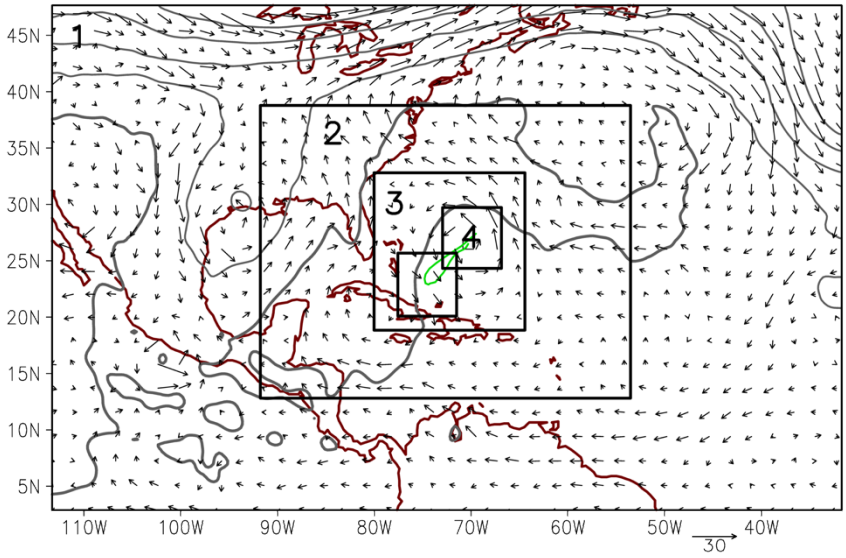

Figure 2.2 Model domain configuration, superimposed over 500-hPa geopotential height (5720, 5760, 5800, 5840 m, thin gray contours; 5880 m, thick gray contour) and 700-hPa horizontal wind vectors (m s^{-1}), both from the 29 Sep 0600 UTC NCEP 0.25°-FNL. Domains 1, 2, 3, and 4 have 27, 9, 3, and 1-km resolutions, respectively. Domain 4 follows the storm center, with the upper-right and lower-left positions shown here corresponding to the initial time and southwestern apex of the looping track, respectively. The green line shows Joaquin's best-track motion over the CTL simulation period (0600 UTC 29 Sep – 0000 UTC 04 Oct).

We use a simple ocean mixed layer physics scheme developed for WRF-ARW (Davis et al. 2008) to parameterize the wind-induced SST cooling. This scheme neglects pressure gradients and horizontal advections but retains the Coriolis force, and it generates mixed-layer currents and upwelling-induced cooling using the model-output surface winds, an initial mixed layer depth (set to 30 m) and deep-layer lapse rate (set to 0.14 K m^{-1}) as inputs. Other physics options used are (i) the Thompson et al. (2004, 2008) microphysics scheme,

which contains 5 hydrometeor species (rain, cloud water, cloud ice, snow, and graupel); (ii) the Kain-Fritsch cumulus parameterization for the outer 2 domains (Kain and Fritsch 1990); (iii) the YSU planetary boundary layer (PBL) parameterization with the revised MM5 Monin-Obukhov surface layer physics (Hong et al. 2006); and (iv) the Rapid Radiative Transfer Model (RRTM, Mlawer et al. 1997) longwave and Dudhia (1989) shortwave radiation schemes. Surface drag coefficients are taken from Donelan (2004).

We found that the most accurate track forecast could be achieved by applying analysis nudging (Stauffer and Seaman 1990) to the three fixed domains, whereby horizontal winds and temperature above the PBL are relaxed toward the 1°-FNL using a nudging coefficient of 3×10^{-4} s^{-1}. Through the full simulation period, nudging is applied to winds and temperature for Domains 1 and 2 and to winds for Domain 3.

2.3.2 Perturbed initial condition WRF sensitivity tests

A series of sensitivity tests is designed to perturb features in the CTL analysis that may be responsible for Joaquin's southwest motion, one at a time. WRF simulations are run from each perturbed analysis with nudging turned off, but with other model settings kept identical to CTL, using the same unperturbed NCEP 1°-FNL boundary conditions outside of the 27-km domain. The CTL initial conditions are perturbed by assimilating synthetic observations, in addition to the real observations previously used for CTL, into the 0600 UTC 29 Sep WRFDA-hybrid cycle (see chapter 3) background forecast 27-km and 9-km domains. We follow Brennan and Majumdar (2011) as a general guide, adapting their methodology to a regional data assimilation system.

To perturb large-scale features (i.e., ridges and troughs), we assimilate synthetic temperature observations at a higher level that have either +4 K or –4 K departures from

the background temperature field. Synthetic temperature observation errors are set to 0.1 K. The objective is to generate a temperature anomaly that modifies the geopotential height field above and below through hydrostatic adjustment both in the data assimilation, though the multivariate hybrid background error covariances, and in the subsequent WRF integration. For example, assimilation of 300 hPa temperature observations with -4 K departures from the background would be expected to reduce thicknesses in the layer surrounding 300 hPa, causing heights over a deeper layer below to rise. These tests, to be described in section 2.5.2, are named using the prefixes PERT-R or PERT-T, with the letters R and T indicating whether a ridge or trough is to be perturbed.

An additional sensitivity test, PERT-V, tests the impact of a weakened vortex on Joaquin's track. Two types of synthetic vertical soundings, in addition to real observations, are assimilated into the WRFDA-hybrid cycle background forecast: (i) a single column, centered on Joaquin's upper-level warm core, where the background temperature is reduced by 6 K every 50 hPa over the 500-200 hPa layer; and (ii) concentric rings, centered on the best-track fix, where the background relative humidity is reduced by 50% every 50 hPa over the 1000-700 hPa layer. Observation errors for (i) and (ii) are set to 0.1 K and 10%, respectively.

2.3.3 Steering flow diagnostics

For a given pressure level p, we define the environmental winds within a disk bounded by radius r as the area-averaged horizontal flows that remain after removing the symmetric TC vortex. Following Hanley et al. (2001), we compute the modeled environmental wind $\boldsymbol{v}_{env,m}(r, p)$ vector components after interpolating the Cartesian winds to cylindrical coordinates, using

$$u_{env,m}(r,p) = \frac{1}{A}\sum_{i=1}^{I_r}\left\{\frac{\overline{u_m}(p)_{i-1}+\overline{u_m}(p)_i}{2}\right\}A_i \qquad (2.1)$$

$$v_{env,m}(r,p) = \frac{1}{A}\sum_{i=1}^{I_r}\left\{\frac{\overline{v_m}(p)_{i-1}+\overline{v_m}(p)_i}{2}\right\}A_i, \qquad (2.2)$$

where u_m and v_m are the interpolated Cartesian winds, overbars denote azimuthal averages, i is the radial index, I_r indexes vortex removal radius r, A_i is the annular area between radial indices i and i-1, and $A = \pi r^2$. We take the NCEP 0.25-degree Final Analysis (hereafter 0.25°-FNL) as a proxy for the true atmosphere and compute the "observed" environmental wind $\boldsymbol{v}_{env,o}(r,p)$ using Eqs. (2.1) and (2.2), with the m subscripts replaced with o. GFS forecast and 0.25°-FNL horizontal winds are re-gridded to a storm-centered Cartesian regional domain with 25-km horizontal resolution. Steering flow analysis for WRF simulations is performed on the 9-km resolution domain. We define the vortex center at every pressure level as the gridpoint surrounded by the largest circulation, or area-averaged vorticity, within a 90-km radius,[4] after Cavallo et al. (2013). All computed centers are visually checked against horizontal wind and vorticity fields, and they are corrected if necessary.

Vertical wind shear vector components are computed by setting r = 500 km and differencing the environmental winds between the 200 and 850 hPa levels:

$$u_{VWS,m} = u_{env,m}(r, 200\ hPa) - u_{env,m}(r, 850\ hPa), \qquad (2.3)$$

$$v_{VWS,m} = v_{env,m}(r, 200\ hPa) - v_{env,m}(r, 850\ hPa). \qquad (2.4)$$

We adopt the methodology developed by GD13 and define the *optimal steering flow* as the volume-averaged environmental wind that minimizes the vector difference from the

[4] The 850-hPa center is located first, using the geopotential height centroid as a first-guess, and the higher-level centers are then found in order of increasing height, using the previously found center as the first-guess.

simulated storm speed $\boldsymbol{V}_m$. This difference, which we call the *steering flow residual*, results from errors in computing the environmental wind and storm speed, as well as from storm-scale processes such as the redistribution of convection relative to the storm center in response to vertical shear. For model output, we test 72 combinations of vortex removal radii, every 100 km ranging from 200-700 km, and steering layer top levels above p_b = 850 hPa, every 50 hPa up to 250 hPa, in order to find the optimal radius r_m and steering layer top level $p_{t,m}$ yielding the smallest steering flow residual. The optimal steering flow $\boldsymbol{V}_{opt,m}$ is the pressure-weighted vertically averaged environmental wind vector:

$$U_{opt,m} = \frac{1}{p_b - p_{t,m}} \int_{p_{t,m}}^{p_b} u_{env,m}(r_m, p)dp, \qquad (2.5)$$

$$V_{opt,m} = \frac{1}{p_b - p_{t,m}} \int_{p_{t,m}}^{p_b} v_{env,m}(r_m, p)dp. \qquad (2.6)$$

The optimal observed steering flow $\boldsymbol{V}_{opt,o}$, radius r_o, and steering layer top level $p_{t,o}$ can similarly be found for the 0.25°-FNL using $\boldsymbol{v}_{env,o}(r, p)$ and the observed storm speed $\boldsymbol{V}_o$. To compute $\boldsymbol{V}_m$ ($\boldsymbol{V}_o$), 24-h centered differences of 850-hPa center (NHC best-track) fixes are used. Thus, we can write the steering flow residuals for model and 0.25°-FNL data as

$$\boldsymbol{V}_{resid,m} = \boldsymbol{V}_{opt,m} - \boldsymbol{V}_{m,} \qquad (2.7)$$

$$\boldsymbol{V}_{resid,o} = \boldsymbol{V}_{opt,o} - \boldsymbol{V}_o. \qquad (2.8)$$

Environmental wind profiles are evaluated at the optimal radius, with

$$\boldsymbol{v}_m(p) = \boldsymbol{v}_{env,m}(r_m, p), \qquad (2.9)$$

$$\boldsymbol{v}_o(p) = \boldsymbol{v}_{env,o}(r_o, p). \qquad (2.10)$$

Finally, we define

$$\widehat{\boldsymbol{v}}_m(p) = \boldsymbol{v}_{env,m}(r_o, p), \qquad (2.11)$$

which enables us to compare the model-output and 0.25°-FNL environmental wind profiles for the same disk region surrounding their respective centers.

Model steering flow errors are quantified using the diagnostic equation derived in GD13:

$$\underbrace{\boldsymbol{V}_m - \boldsymbol{V}_o}_{TC\ MOTION\ ERROR} = \underbrace{\frac{1}{p_b - p_{t,o}} \int_{p_{t,o}}^{p_b} (\widehat{\boldsymbol{v}}_m - \boldsymbol{v}_o) dp}_{ENVIRONMENTAL\ WIND\ ERROR} + \underbrace{\frac{1}{p_b - p_{t,m}} \int_{p_{t,m}}^{p_b} -(\widehat{\boldsymbol{v}}_m - \boldsymbol{v}_m)\, dp}_{REMOVAL\ RADIUS\ ERROR}$$

$$+ \underbrace{\frac{1}{p_b - p_{t,m}} \left[\int_{p_{t,o}}^{p_b} \left(\frac{p_{t,m} - p_{t,o}}{p_b - p_{t,o}} \right) \widehat{\boldsymbol{v}}_m dp + \int_{p_{t,m}}^{p_{t,o}} \widehat{\boldsymbol{v}}_m dp \right]}_{VORTEX\ DEPTH\ ERROR}$$

$$+ \boldsymbol{V}_{resid,m} + \boldsymbol{V}_{resid,o}. \qquad (2.12)$$

The left-hand side approximates the error in simulated TC motion, provided that $\boldsymbol{V}_{resid,m}$ and $\boldsymbol{V}_{resid,o}$ are both small. The right-hand side terms from left to right are the environmental wind error, vortex removal radius error, vortex depth error, and residuals in the model and observations, respectively. The first term approximates the error in model-output environmental winds, averaged over the observed optimal steering volume. The removal radius and vortex depth errors arise from the optimal steering flow calculation yielding different vortex removal radii and steering layer depths, respectively, for the model and the true storm. Physically, the removal radius (vortex depth) errors are related to model misrepresentation of vortex size (depth) when the environmental winds vary substantially in the horizontal (vertical) direction. For example, a northerly-directed vortex depth error would result when a model simulates an environment with northerly steering flow reasonably well but fails to develop a vortex deep enough to interact with the upper-level northerly steering winds.

2.4 Validation of the CTL simulation

Before addressing the causes of Joaquin's unusual track, it is necessary to validate CTL against observations. Figure 2.3 compares the CTL forecast track to the NHC best-track positions. The southwestward motion toward the Bahamas, slow clockwise motion around the loop apex, and recurvature are all reproduced. The observed RI is well captured by CTL (Fig. 2.4a). The end of simulated RI (1200 UTC 01 Oct) coincides with significant slowing in the storm's forward speed, by which time the Davis et al. (2008) parameterization has cooled mean inner-core SSTs along and to the right of the simulated track by ~ 0.5 °C relative to 24 h previously (Fig. 2.4c). Observational and modeling studies have shown that a 1°C reduction in inner-core SSTs can induce substantial weakening or preclude further intensification in an otherwise favorable environment, due to lowered surface enthalpy fluxes (Cione and Uhlhorn 2003; Zhu and Zhang 2006). The simulated P_{MIN} begins to re-intensify around 1200 UTC 02 Oct, although the intensification rate is modest compared to the observations. As the storm accelerates northeastward away from its self-generated "cold pool", local SSTs are warming while northwesterly VWS is increasing (cf. Figs. 2.3 and 2.4), as an upper-level low approaches from the east (not shown).

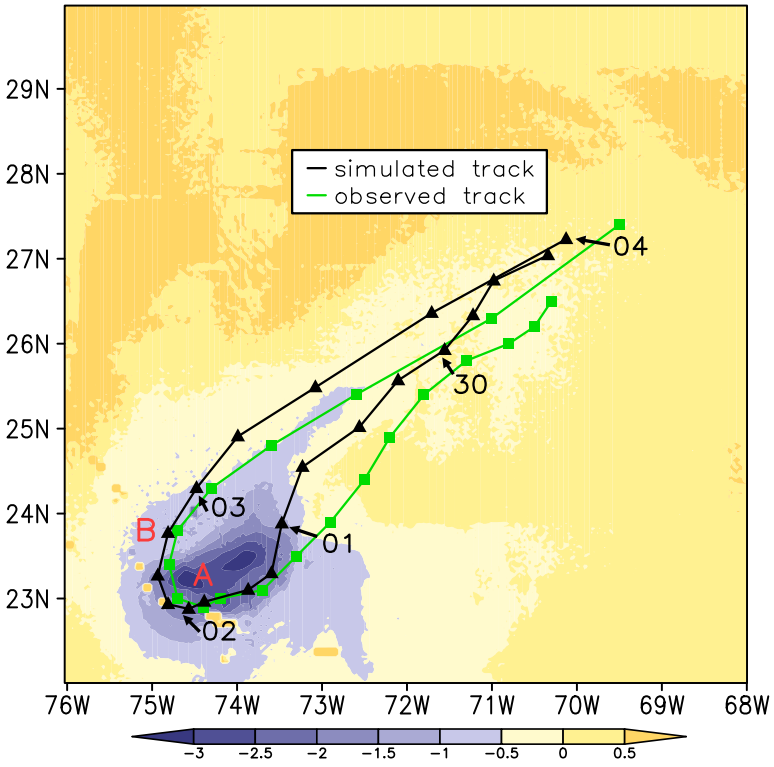

Figure 2.3 Six-hourly best-track (green) and model-simulated (black) Joaquin sea-level center positions plotted on a subset of the 3-km domain, with the WRF parameterized SST differences (K) between 1800 UTC 02 Oct and the initial time shown in shaded colors. Number labels indicate calendar days and show 0000 UTC best-track positions, with arrows pointing to the corresponding simulated positions. Letter labels "A" and "B" mark the simulated storm positions at the end of the observed RI and beginning of the observed re-intensification periods, respectively.

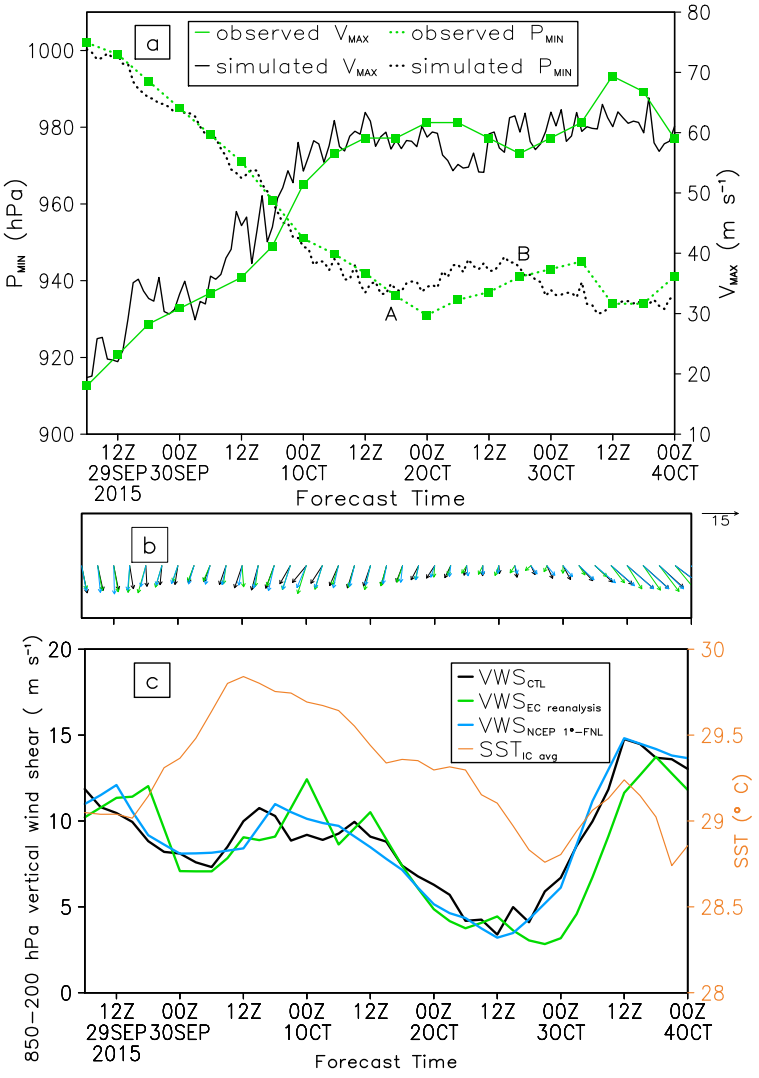

Figure 2.4 Time series of (a) best-track and simulated storm intensity in terms of the minimum central pressure (P_{MIN}) and maximum 10-m wind (V_{MAX}), (b) VWS (m s^{-1}), and (c) VWS magnitude with inner-core parameterized SSTs averaged within 120 km of the simulated storm center. Letter labels "A" and "B" in (a) correspond to the storm positions shown in Fig. 2.3. In (b) and (c), black colors show model-derived VWS, while green and blue colors show VWS computed from the ECMWF reanalysis and NCEP 1°-FNL, respectively.

Figure 2.5 compares model-simulated radar reflectivity against microwave satellite imagery for a few selected times. Five hours after initialization, the inner core remains highly asymmetric, with convection displaced south of the low-level circulation center in both the observations and the simulation (Figs. 2.5a,b). Previous TC modeling and

observational studies have shown that RI can be accompanied by an increasingly axisymmetric inner-core structure, with convection wrapping around the center (Rogers 2010; Chen et al. 2011; Zagrodnik and Jiang 2014; Rogers et al. 2015; Rios-Berrios et al. 2016; Fischer et al. 2018; Rios-Berrios et al. 2018); a similar trend can be seen for Joaquin as RI progresses (Figs. 2.5c-f). Nevertheless, a balanced vortex response to the northerly VWS (Jones 1995; Wang and Holland 1996; Molinari et al. 2006; Nguyen and Molinari 2015) may have helped focus vigorous convection south of the storm center throughout RI (Figs. 2.5a-f). Dry air at the mid-to-upper levels north of the storm may have further suppressed convection in that region (Figs. 2.6a-c). The environment south of the eyewall, on the other hand, is nearly saturated from the PBL to the upper troposphere (Fig. 2.6d). Some erosion of the northern eyewall occurs during steady-state (not shown), and re-intensification is accompanied by a re-invigoration of eyewall convection and the development of new convection underneath the upper-level low to Joaquin's northeast (Figs. 2.5g,h).

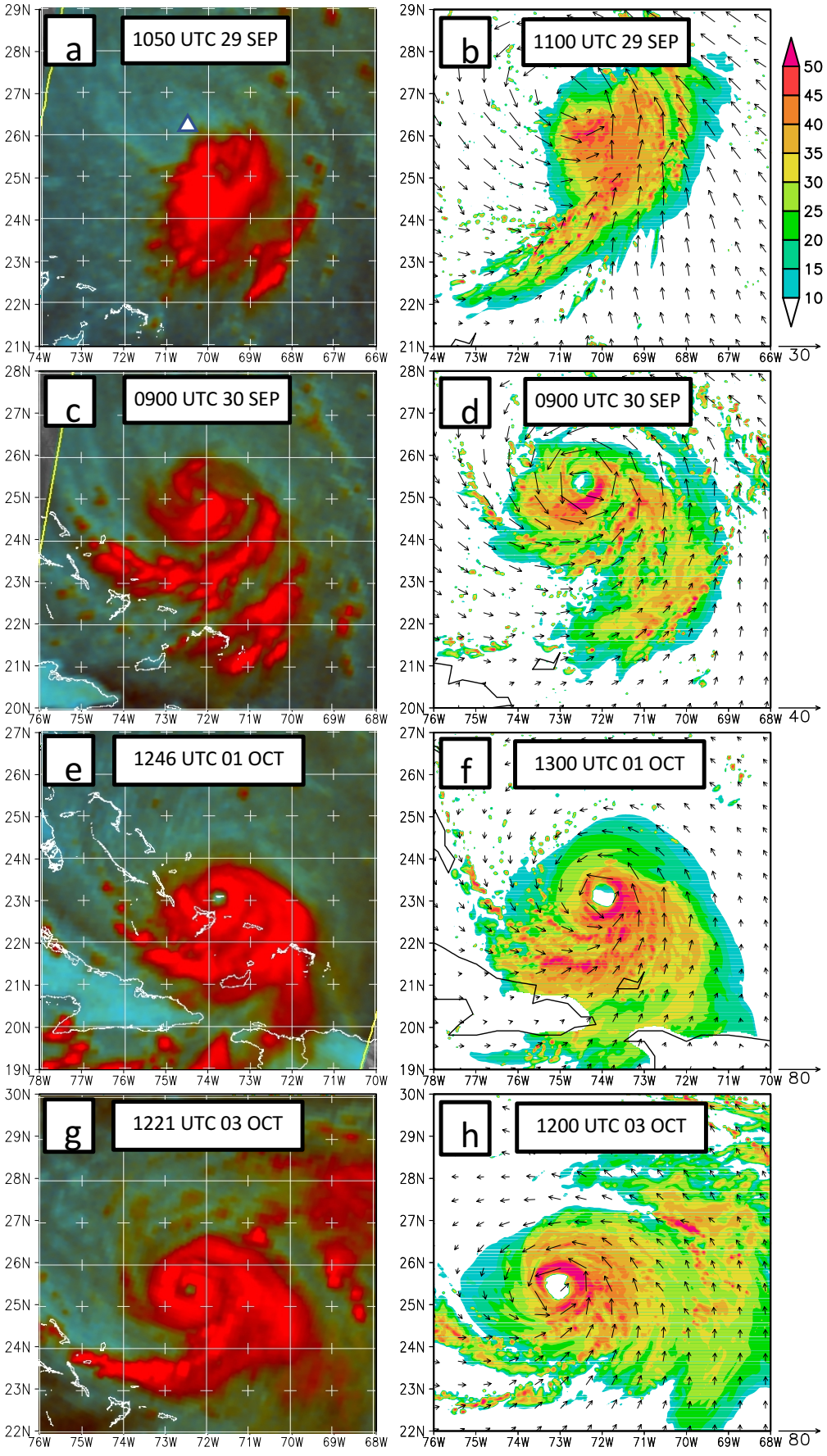
a
1050 UTC 29 SEP
b
1100 UTC 29 SEP
50
45
40
35
30
25
20
15
10
30
c
0900 UTC 30 SEP
d
0900 UTC 30 SEP
40
e
1246 UTC 01 OCT
f
1300 UTC 01 OCT
80
g
1221 UTC 03 OCT
h
1200 UTC 03 OCT
80

← **Figure 2.5** Left panels: 85-GHz satellite imagery for (a) 1050 UTC 29 Sep, (c) 0900 UTC 30 Sep, (e) 1246 UTC 1 Oct, and (g) 1221 UTC 3 Oct, obtained from the Naval Research Laboratory TC pages https://www.nrlmry.navy.mil/tc_pages/tc_home.html. Red colors show areas of deep convection while cyan bands indicate shallow convection and/or enhanced low-level relative humidity. Right panels: Model-simulated composite reflectivity (shaded, dBz) with 10-m flow vectors valid at (b) 1100 UTC 29 Sep, (d) 0900 UTC 30 Sep, (f) 1300 UTC 1 Oct, and (h) 1200 UTC 3 Oct. White triangle in (a) marks the 1200 UTC 29 Sep best-track center location.

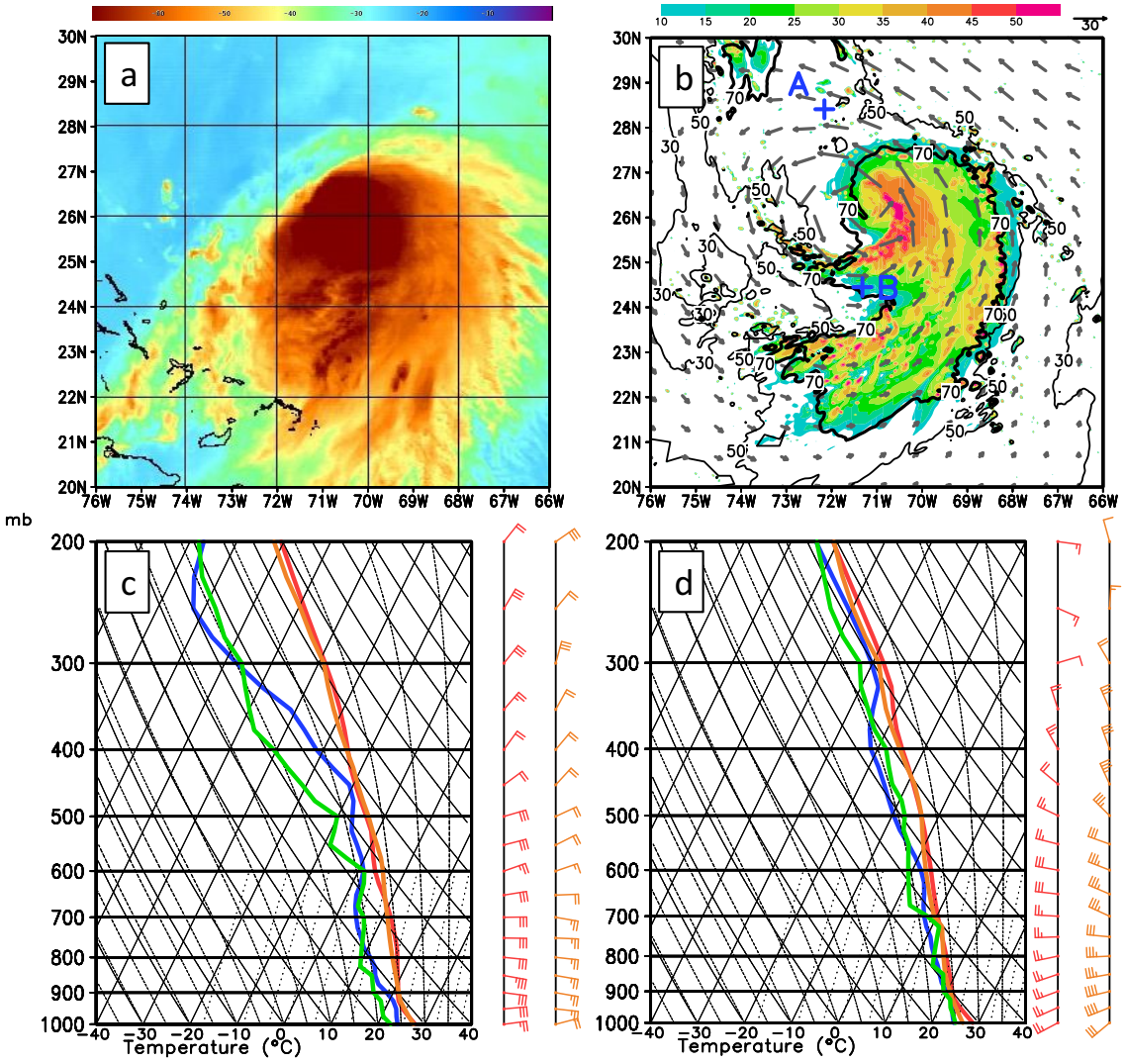

Figure 2.6 (a) GOES-13 water vapor satellite brightness temperature (°C) compared against (b) the simulated composite radar reflectivity (shaded, dBz), 700-200 hPa layer-averaged relative humidity (contoured) and 850-hPa horizontal flow vectors, with both (a) and (b) valid at 2000 UTC 29 Sep. Symbols "A" and "B" mark release positions of G-IV dropsondes falling during the 2000-2100 UTC 29 Sep period, and their corresponding skew *T*-log *p* diagrams are compared against model soundings at the same locations in (c) and (d), respectively. In (c) and (d), simulated winds and temperature are plotted in red, with dropsonde winds and temperature shown in orange. Simulated (dropsonde) dewpoint is plotted in blue (green).

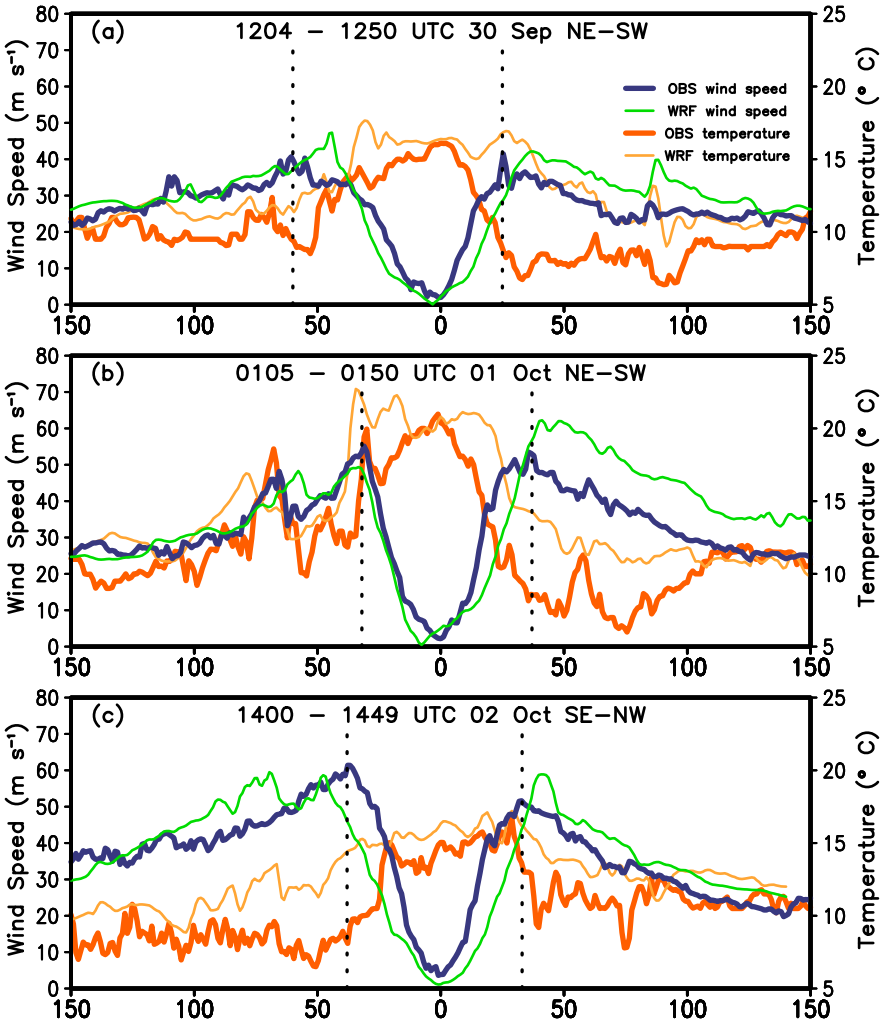

Figure 2.7 (a)-(c) Air Force C-130 flight-level (~ 700-hPa) wind speed (blue) and temperature (dark orange) recorded during transect legs at various times during Joaquin's lifecycle. Simulated wind (green) and temperature (light orange) at 700 mb along the same transects, horizontally translated to align with the simulated storm center, are shown for comparison. Abscissa shows distances (km) from storm center along the flight legs.

Zooming into the inner core, we next examine flight-level wind and temperature profiles from the Air Force Reserve 53rd Weather Reconnaissance Squadron C-130 aircraft missions flown during Joaquin's southwest movement period, comparing them to cross-sections taken through CTL (Fig. 2.7). The model reproduces the sharpening tangential

wind profile and low-level eye warming observed during RI (Figs. 2.7a,b), and also the weakened low-level warm anomaly for the steady-state period (Fig. 2.7c).

2.5 Steering flow analysis

2.5.1 GFS forecast errors

We begin our steering-flow analysis by examining two operational GFS forecasts, initialized at 1200 UTC on 29 and 30 Sep, respectively, and diagnosing their track error sources using the GD13 budget equation. When analyzing the large-scale steering environment, we use the 0.25°-FNL rather than CTL as the "truth dataset" because, as discussed in section 2.3.1, analysis nudging was used to force winds in the outer three CTL domains toward the 1°-FNL. The 1200 UTC 29 Sep GFS forecast, initialized 6 h after CTL, tracks the low-level center westward for 48 h before turning it sharply north and eventually northeast into the western Atlantic (Fig. 2.8a). It also fails to intensify Joaquin (Figs. 2.8b,c). Whereas the CTL upper-level center becomes aligned with the surface center within 18 h (Fig. 2.8a), the 29 Sep GFS upper-level center drifts slowly west-southwest during the first 60 h, maintaining ~200 km of separation from the low-level center (not shown). The GFS vortex, initialized 24 h later (i.e., at 1200 UTC 30 Sep), is now vertically aligned (not shown), despite being 10 m s^{-1} weaker in V_{MAX} compared to the best-track data (Figs. 2.8b,c). Although it initially tracks southwestward, it ceases this motion 24 h earlier than the observed storm, turning due west and then north (Fig. 2.8a), eventually making landfall on the North Carolina coast (not shown).

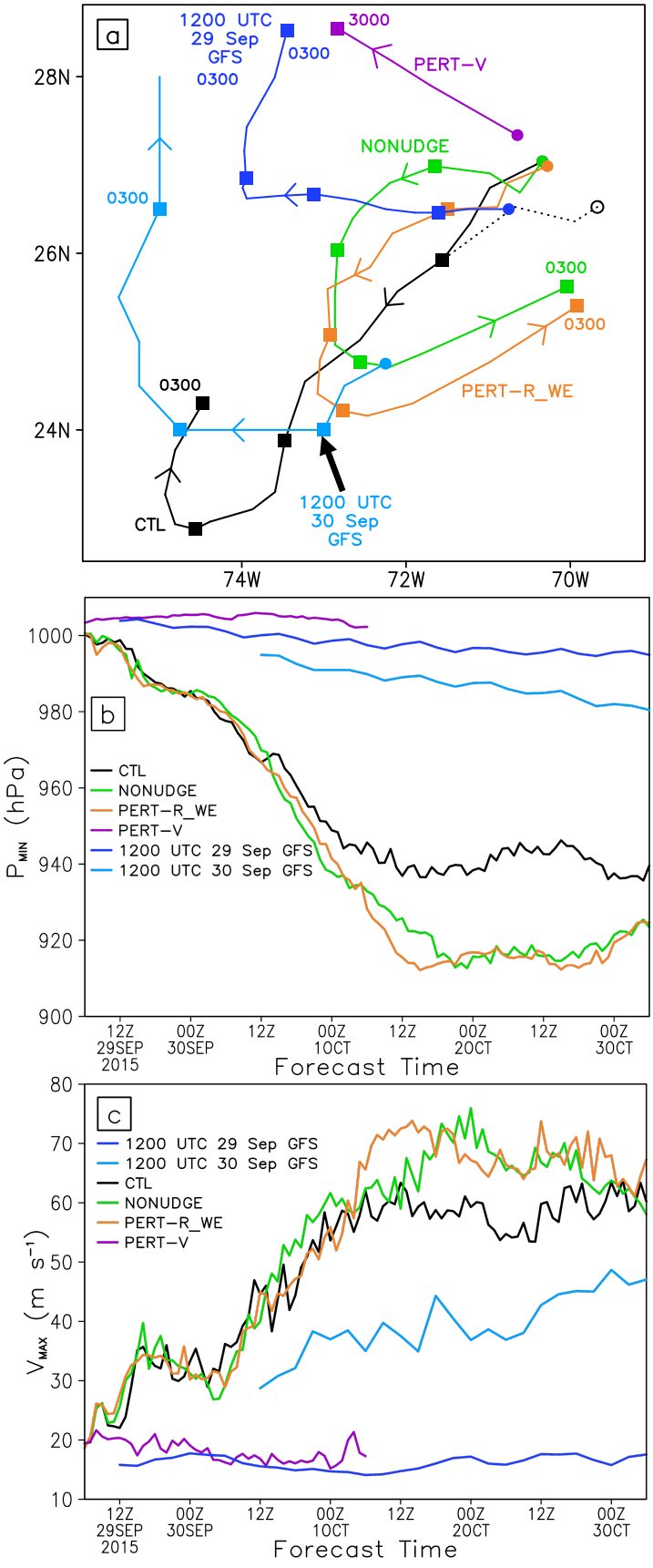
a
1200 UTC
29 Sep
GFS
0300
3000
PERT–V
NONUDGE
0300
0300
0300
0300
PERT–R_WE
0300
1200 UTC
30 Sep
GFS
CTL
28N
26N
24N
74W
72W
70W
b
CTL
NONUDGE
PERT–R_WE
PERT–V
1200 UTC 29 Sep GFS
1200 UTC 30 Sep GFS
P_MIN (hPa)
1000
980
960
940
920
900
12Z 29SEP 2015
00Z 30SEP
12Z
00Z 1OCT
12Z
00Z 2OCT
12Z
00Z 3OCT
Forecast Time
c
1200 UTC 29 Sep GFS
1200 UTC 30 Sep GFS
CTL
NONUDGE
PERT–R_WE
PERT–V
V_MAX (m s^-1)
80
70
60
50
40
30
20
10
12Z 29SEP 2015
00Z 30SEP
12Z
00Z 1OCT
12Z
00Z 2OCT
12Z
00Z 3OCT
Forecast Time

← **Figure 2.8** (a) Track forecasts for CTL and the initial condition sensitivity WRF runs, with the 1200 UTC 29 Sep and 1200 UTC 30 Sep operational GFS forecasts also shown. Closed circles show initial sea-level center positions and squares show sea-level center positions for each subsequent 0000 UTC time. Time labels are given in ddhh format, where dd and hh denote the two-digit calendar day and hour, respectively. The open circle and dotted line show the initial position and track of the CTL upper-level center prior to the vortex becoming vertically aligned. Minimum central pressure (P_{MIN}) and maximum 10-m wind (V_{MAX}) forecasts are shown in (b) and (c), respectively.

Figure 2.9 plots time series of the 0.25°-FNL environmental steering wind *u* and *v* profiles, along with their differences from the 1200 UTC 29 and 30 Sep cycle GFS forecasts. The FNL environmental winds show substantial VWS over the 48-h period beginning 1200 UTC 29 Sep that coincides with Joaquin's southwestward motion (Figs. 2.9a,b). Northeasterly environmental winds, associated with the height gradient between the upper-level ridge to the northwest and the upper-level trough to the southeast (Fig. 2.1a), intensify above 600 hPa. Joaquin's northeastward motion out of the Bahamas after 1200 UTC 02 Oct coincides with southwesterly environmental winds developing over the 850-500 hPa layer (Figs. 2.9c,d). This is consistent with anticyclonic deep-layer winds west of Joaquin becoming cyclonic as the digging eastern U. S. trough erodes the upper-level ridging northwest of Joaquin and lower-level ridging over Cuba (Fig. 2.1c,d).

Compared to the 0.25°-FNL, the 1200 UTC 29 Sep GFS initialized environmental winds have a 1-2 m s^{-1} easterly wind speed bias below 400 hPa and a 1-2 m s^{-1} southerly wind speed bias in the 550-750 hPa layer (Figs. 2.9a,b). Twelve hours later, the GFS southerly wind speed bias has increased to ~2 m s^{-1} in a deep layer. This bias grows larger in the upper levels after 24 h (Fig. 2.9b), although by this time the environmental wind differences may be more strongly related to the GFS-forecast Joaquin moving into a different large-scale flow environment, given its substantial track divergence from observations (cf. Figs. 2.3 and 2.8a). The 1200 UTC 30 Sep cycle GFS environmental

winds show less difference from the 0.25°-FNL over the first 30 forecast hours, consistent with the smaller track errors over this period, but they have the same general easterly and southerly biases (Figs. 2.9c,d).

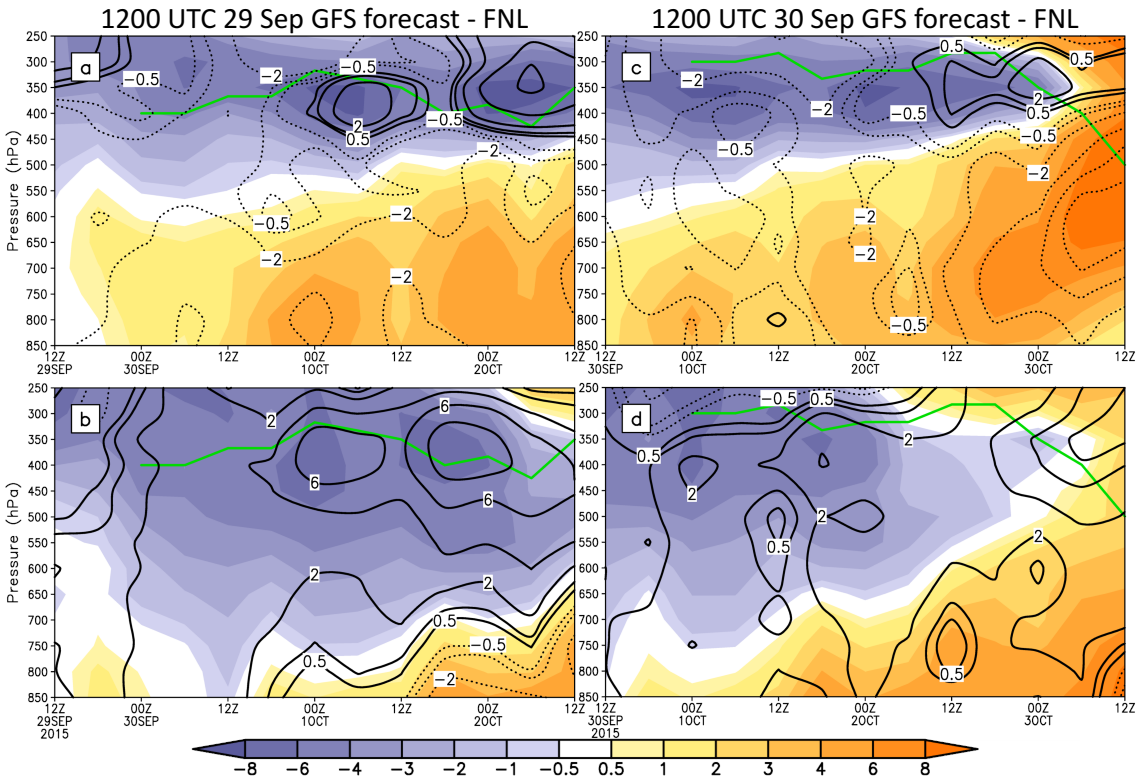

Figure 2.9 (a) Environmental *u*-wind profile time series for the 0.25°-FNL (shaded, m s^{-1}), with differences in environmental *u*-winds from the 1200 UTC 29 Sep cycle operational GFS forecast (GFS – 0.25°-FNL; dot-contoured for -8, -6, -4, -2, -1, -0.5 m s^{-1}, and solid-contoured for 0.5, 1, 2, 4, 6, 8 m s^{-1}). Green line denotes the top of the GFS forecast optimal steering layer, computed as a running mean over the 12-h period centered on the current time. (b) As in (a), but for environmental *v*-winds. (c) and (d) As in (a) and (b), but for differences between the 0.25°-FNL and the 1200 UTC 30 Sep cycle operational GFS. Environmental winds for (a)-(b), and (c)-(d) are computed using 400-km and 500-km vortex removal radii, respectively, corresponding to the mean optimal steering radii for the respective GFS forecasts over the periods shown. Note that an optimal steering depth is not shown for the first 12-h GFS forecast periods because this calculation uses 24-h centered differences in forecast storm position.

Figure 2.10 shows large-scale geopotential height differences between the 1200 UTC 30 Sep cycle GFS forecast and the 0.25°-FNL, averaged over the lower, middle, and upper

portions of the 850-250 hPa FNL optimal steering layer for two representative times. The 12-h GFS forecast turns Joaquin west, while CTL and the observed storm continue moving southwest for another 24 h (cf. Figs. 2.3 and 2.8a). For the 850-650 hPa layer (Fig. 2.10a), the 12-h GFS forecast generates 5-10 m lower heights around the base of the eastern U.S. trough and stronger low-level ridging northeast of the frontal wave centered near 27°N, 60°W. The GFS-forecast mid to upper level environment similarly has a low (high) height bias west (northeast) of Joaquin (Figs. 2.10b,c) due to its stronger eastern U.S. trough, weaker downstream ridging northwest of Joaquin, and weaker mid-to-upper level low well northeast of the storm near 33°N, 55°W. Twenty-four hours later, the 36-h GFS forecast is turning Joaquin onto a long-term northward heading, eventually bringing it to a U.S. landfall, while the observed storm is located over 100 km further south and slowly moving westward (cf. Figs. 2.3 and 2.8a). Compared to the 12-h forecast, the 36-h GFS forecast heights show similar, albeit more pronounced, differences from the 0.25°-FNL. The more strongly positive GFS zonal near-storm height anomaly gradient is consistent with the increased southerly GFS environmental wind anomaly through a deep layer (cf. Figs. 2.9d and 2.10d-f). The largest differences from the 0.25°-FNL are found above 650 hPa over Florida and adjacent Atlantic waters, where the GFS-forecast eastern U. S. trough is deeper, and near 24-33°N, 55°W where the GFS-forecast mid-to-upper-level trough, along with its lower-level reflection, are weaker. N18 showed similar differences in 24-h forecast large scale 700 hPa height patterns between their deterministic WRF simulation that captured the looping track and a composited group of U.S. landfalling ensemble members (see their Fig. 15f).

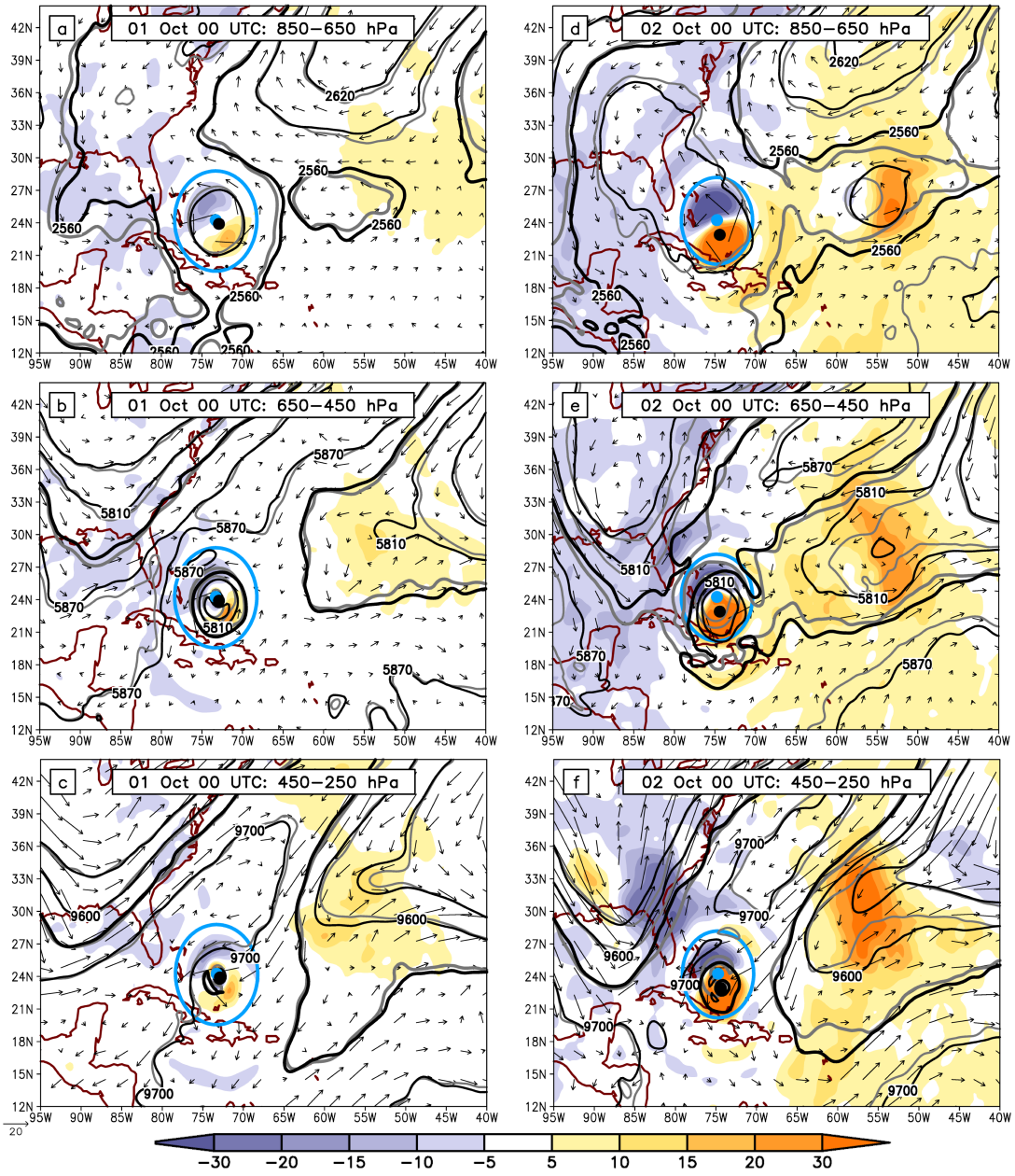

Figure 2.10 (a) Geopotential height difference (m, shaded) between the 1200 UTC 30 Sep cycle operational GFS 12-h forecast and the NCEP 0.25°-FNL valid at the same time (GFS – FNL), computed at each diagnostic pressure level and then averaged over the 850-650 hPa layer. FNL and GFS-forecast 750-hPa geopotential height for this time are contoured in black and gray, respectively, over the range 2530/2560/2590/2620 m. FNL horizontal winds (m s^{-1}) are also shown. Black (blue) closed circles denote the best-track (GFS forecast) storm centers. (b) As in (a) but for height differences averaged over the 650-450 hPa layer, with 500-hPa height (contoured at 5780/5810/5840/5870 m) and winds. (c) As in (a) but for height differences averaged over the 450-250 hPa layer, with 300-hPa height (contoured at 9550/9600/9650/9700 m) and winds. (d)-(f) As in (a)-(c), but for the 1200 UTC 30 Sep cycle operational GFS 36-h forecast and 0.25°-FNL valid at the same time. Blue open circles in (a)-(c) and (d)-(f) denote 500-km and 433-km GFS optimal steering radii respectively computed for the times shown. Thickened contours emphasize the troughs approaching Joaquin from the northwest and east.

Next, we apply the GD13 TC motion error budget equation to both representative GFS forecasts to determine whether model misrepresentation of the vortex size or depth also contributes to the track forecast error (Fig. 2.11). As in GD13, we restrict this analysis to the first 24-h forecast, so that the modeled and observed storm steering environments are not too far apart relative to the scale of the flow features being studied. For the forecast initialized on 29 Sep, the northwesterly-directed environmental wind error and northeasterly-directed vortex depth error vectors both contribute significantly toward a ~2 m s^{-1} northerly TC motion error. The vortex depth error results from the shallower GFS 12-24 h forecast optimal steering layer, which extends up to ~400 hPa (Figs. 2.9a,b), compared to the 850-250 hPa 0.25°-FNL optimal steering layer for the period of Joaquin's southwest movement (not shown). This calculation implies that the GFS forecasts a shallower vortex that is less affected by northeasterly steering winds above 400 hPa (Figs. 2.9a,b), as compared to the true storm. In contrast, the GFS forecast initialized on 30 Sep has a 12-24 h northerly motion error of ~1 m s^{-1}, which results primarily from the environmental wind error, as the steering layer is now deeper, extending up to ~300 hPa (cf. Figs. 2.9c,d and 2.11). Both the vortex removal radius error and residual remain relatively small for these GFS forecasts.

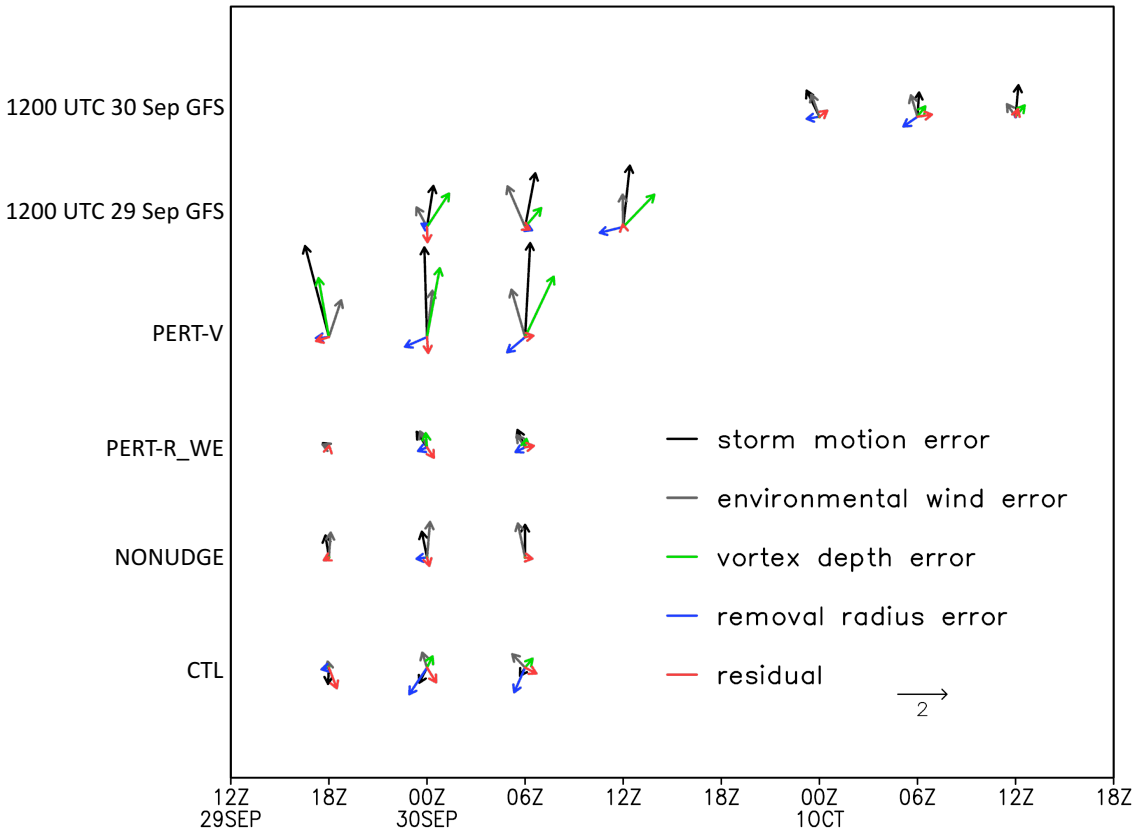

Figure 2.11 Time series of Galarneau and Davis (2013) TC motion equation error budget terms (m s^{-1}) for selected model forecasts, with *u*- and *v*- components combined into vector form.

2.5.2 Sensitivity tests to WRF initial conditions

To examine to what extent the large-scale flow and vortex depth errors diagnosed above contribute to track forecast errors, several sensitivity simulations are run from perturbed analyses with nudging turned off while all other settings are kept identical to CTL. The first sensitivity test is termed as NONUDGE, in which nudging is turned off but the CTL analysis is not perturbed. Although NONUDGE also captures the looping track, with southwestward motion followed by a northeast turn (albeit in the wrong direction), it fails to generate sustained southward motion during the first 24 h (Fig. 2.8a). The track differences between CTL and NONUDGE may result from a combination of (i) model physics error in the outer three domains, and (ii) biases in the CTL initial conditions with

respect to the 1°-FNL, shown in Fig. 2.12. In the lower levels, we find a CTL low-height bias over a broad region extending northward, southward, and westward from Joaquin that encompasses much of the continental U.S. east of the Rockies, Gulf of Mexico, and Central America; particularly notable are the > 6 m lower CTL heights immediately northwest of Joaquin that extend from the Cuba ridge to the southwest corner of the north Atlantic ridge centered near 37°N, 55°W (Fig. 2.12a). The central portion of the latter ridge is also stronger in CTL. In the mid-to-upper levels (Fig. 2.12b), the subtropical ridge directly northwest of Joaquin and the upper-level trough centered near 35° N, 55° W are both weaker in CTL. Overall, the CTL initial conditions and GFS 12-h forecast valid 42 h later (Fig. 2.10a-c) share similar differences from the 0.25°-FNL in their representation of large-scale features surrounding Joaquin.

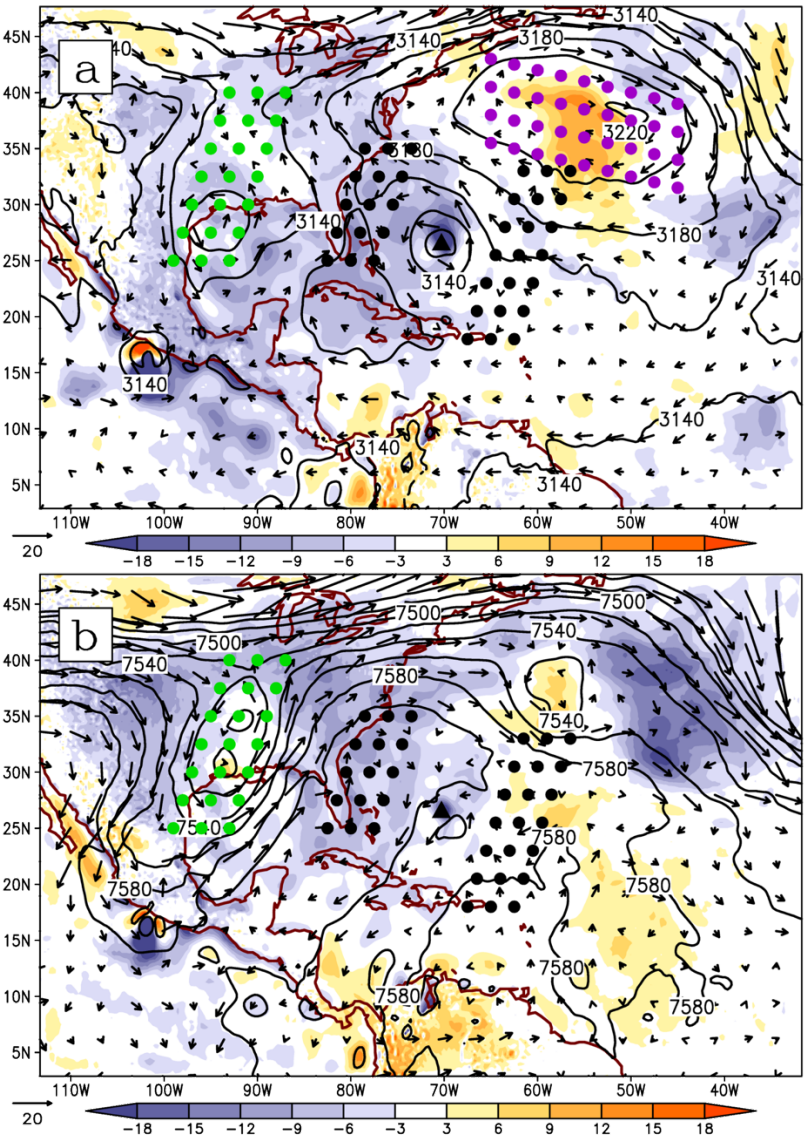

Figure 2.12 (a) Geopotential height differences between the 0600 UTC 29 Sep NCEP 0.25°-FNL and the CTL initial conditions (CTL - FNL), computed at each pressure level and then averaged over the 850-600 hPa layer (shaded, m) with 700-hPa FNL geopotential height (contoured, m) and horizontal flow vectors (m s^{-1}). (b) As in (a) but for geopotential height differences averaged over the 600-250 hPa layer, with 400-hPa FNL geopotential height and winds. Black triangle denotes the 0600 UTC 29 Sep best-track Joaquin position. Black, purple and green dots show the respective synthetic observation locations for the PERT-R_WE, PERT-R_ATL, and PERT-T experiments.

Using the CTL initial condition and GFS forecast biases as a starting point, we now identify features in Joaquin's environment that may be important to its steering. We perturb

these features in the CTL analysis, one at a time, using the methods of section 2.3.2 and re-run CTL without nudging (Table 2.1; Figs. 2.12, 2.13). The first three tests are designed to strengthen the northerly geostrophic winds across Joaquin's near-storm environment. PERT-R_W enhances mid-to-upper level ridging immediately west of Joaquin, PERT-R_E weakens mid-to-upper level ridging immediately to the east, and PERT-R_WE combines the impacts of PERT-R_W and PERT-R_E. In PERT-R_WE, for example, generating a 300 hPa cold anomaly along the axis of the ridge northwest of Joaquin increases heights by ~ 4-10 m over a deep layer below, with the greatest impacts between 400 and 700 hPa (Figs. 2.13a,c). The next two experiments test the sensitivity of Joaquin's southwest motion to perturbations in more distant features. PERT-R_ATL weakens the central portion of the northern Atlantic 700-hPa ridge – here the intention is to weaken the low-level anticyclonic flows on its southwestern periphery. PERT-T investigates whether weakening the eastern U.S. trough might strengthen (or at least delay the weakening of) the downstream subtropical ridge northwest of Joaquin. PERT-V tests the sensitivity of Joaquin's motion to a weakened vortex. Compared to CTL, the PERT-V-analyzed upper-level warm temperature anomaly is weakened by ~ 50% and 850-hPa water vapor mixing ratios are reduced by >3 g/kg inside of a 2° latitude radius (Figs. 2.13b,d). The multivariate hybrid background error covariances have also slightly weakened and broadened the 800-400 hPa layer vortex circulation (Fig. 2.13d).

Table 2.1 Summary of the perturbed initial condition WRF sensitivity tests. Synthetic observation pressure levels and perturbation strengths are shown here for each experiment, and their locations are shown in Figs. 2.12 and 2.13. For all layer soundings, observations are assimilated every 50 hPa. *T* and *RH* denote temperature and relative humidity, respectively.

Name	Objective	Level (hPa)	Type	Strength
PERT-R_W	strengthen 850-300 hPa layer ridging northwest of Joaquin	300	*T*	-4 K
PERT-R_E	weaken 850-300 hPa layer ridging southeast of Joaquin	300	*T*	4 K
PERT-R_WE	combine the impacts of PERT-R_W and PERT-R_E	300	*T*	-4 and 4 K
PERT-R_ATL	weaken 850-600 hPa layer ridging in north-central Atlantic	600-400	*T*	4 K
PERT-T	weaken eastern U.S. trough over 850-300 hPa layer	300	*T*	-4 K
PERT-V	weaken TC Joaquin vortex	500-200	*T*	-6 K
		1000-700	*RH*	-50 %

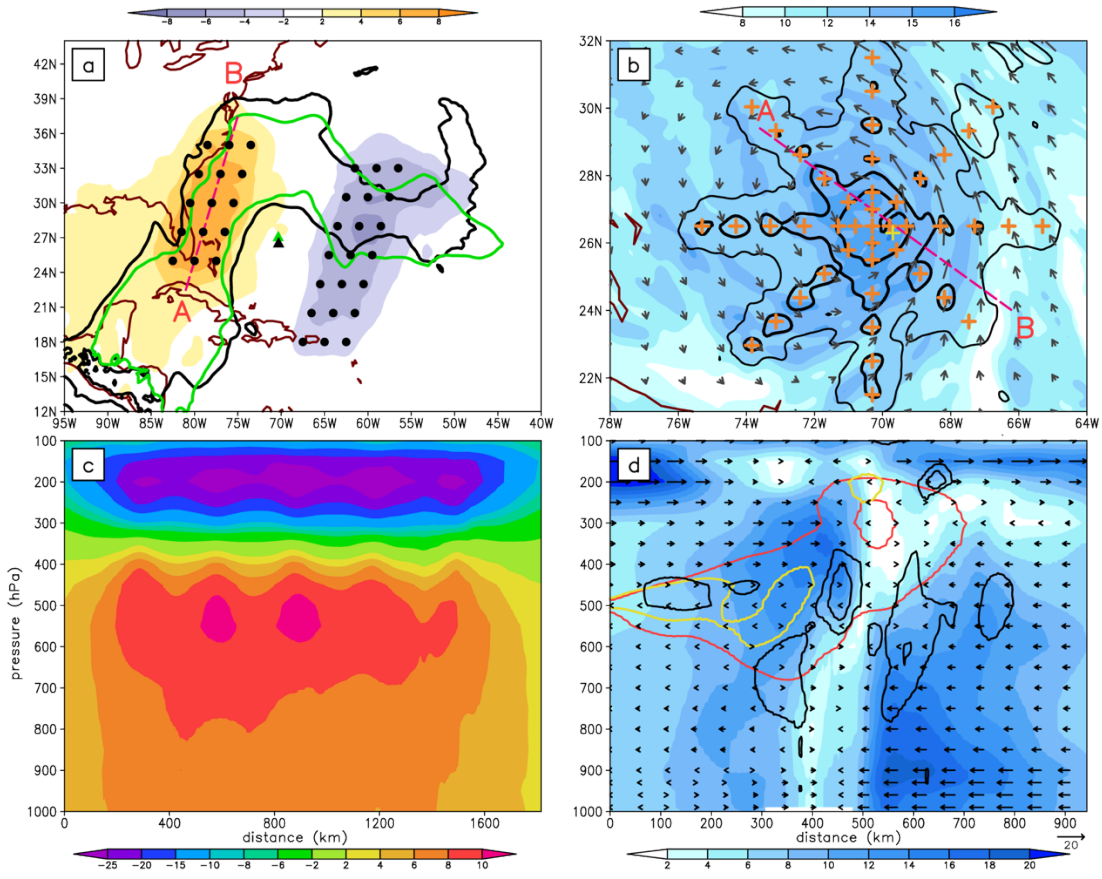

Figure 2.13 Perturbed initial conditions used for WRF sensitivity tests. (a) Geopotential height differences (shaded, m) between the PERT-R_WE and CTL analyses (PERT-R_WE – CTL), averaged over the 850-350 hPa layer. Green (black) contours show the CTL (0600 UTC 29 Sep 0.25°-FNL) 5880-m 500-hPa geopotential height. Green (black) triangles mark the current CTL surface (best-track) storm center, while black dots mark the locations

of synthetic 300-hPa temperature observations used in generating the PERT-R_WE analysis. (b) Differences in 850-hPa water vapor mixing ratio between the PERT-V and CTL analyses (PERT-V – CTL; g/kg; -1, thin contours and -3/-5, thick contours), with CTL analyzed 850-hPa water vapor mixing ratio (shaded, g kg^{-1}) and horizontal winds (vectors, m s^{-1}). Orange (yellow) crosses mark synthetic moisture (temperature) sounding locations used in generating the PERT-V analysis. (c) Geopotential height differences (shaded, m) between the PERT-R_WE and CTL analyses (PERT-R_WE – CTL), averaged along a 36-km wide vertical cross-section taken along the line running from A to B in (a). (d) Vertical cross-section of the CTL analyzed horizontal wind speed (shaded, m s^{-1}), with analysis horizontal wind speed differences (PERT-V – CTL, -2/-4 m s^{-1}, contoured in black), taken along a 36-km wide line running from A to B in (b). Red (yellow) contours denote CTL (PERT-V) temperature anomalies (T′(z), 3/5 K; calculated with respect to a 500-1500 km annular averaged CTL reference profile). Horizontal in-plane flow vectors for the CTL analysis are also shown.

Among all sensitivity experiments, PERT-R_WE yields the most significant increase in southward motion, with its forecast track falling roughly halfway between those of NONUDGE and CTL over the first 48 h (Fig. 2.8a). The GD13 TC motion error budget confirms that the PERT-R_WE track forecast improvement results from a ~70% smaller northerly-directed environmental wind error (Fig. 2.11). The PERT-R_WE analysis perturbations persist after 18-h model integration, when ridging west (east) of Joaquin remains stronger (weaker) compared to NONUDGE at both 700 and 500 hPa (Fig. 2.14). Notably, the 18-h PERT-R_WE forecast removes the anomalous NONUDGE ridging immediately east of Joaquin that is not present in the 0.25°-FNL (Figs. 2.14a,b). The PERT-R_W and PERT-R_E forecast tracks are similar, and they fall roughly halfway between the NONUDGE and PERT-R_WE tracks (not shown). By contrast, PERT-R_ATL and PERT-T yield no track forecast improvement compared to NONUDGE (also not shown). While it is tempting to conclude, based on these results, that Joaquin's southwest motion is less sensitive to the north Atlantic 700-hPa ridge and eastern U.S. trough compared to the near-storm environment, it is possible that a different experiment design that perturbed the former two features more strongly and/or from an earlier forecast start time could have

elicited a stronger track response. Nevertheless, our results are consistent with N18 and Torn et al. (2018), who found that Joaquin's early southwest motion was more sensitive to the near-storm environment than to more distant synoptic-scale features. PERT-V, on the other hand, steers Joaquin's lower-level center due northwest (Fig. 2.8a). It also fails to intensify the storm (Figs. 2.8b,c) and align the lower-level and upper-level centers (not shown). The GD13 error budget analysis confirms that the largest contributor to the ~ 4 m s^{-1} PERT-V northward motion error is the vortex depth error, which had been near zero for NONUDGE (Fig. 2.11).

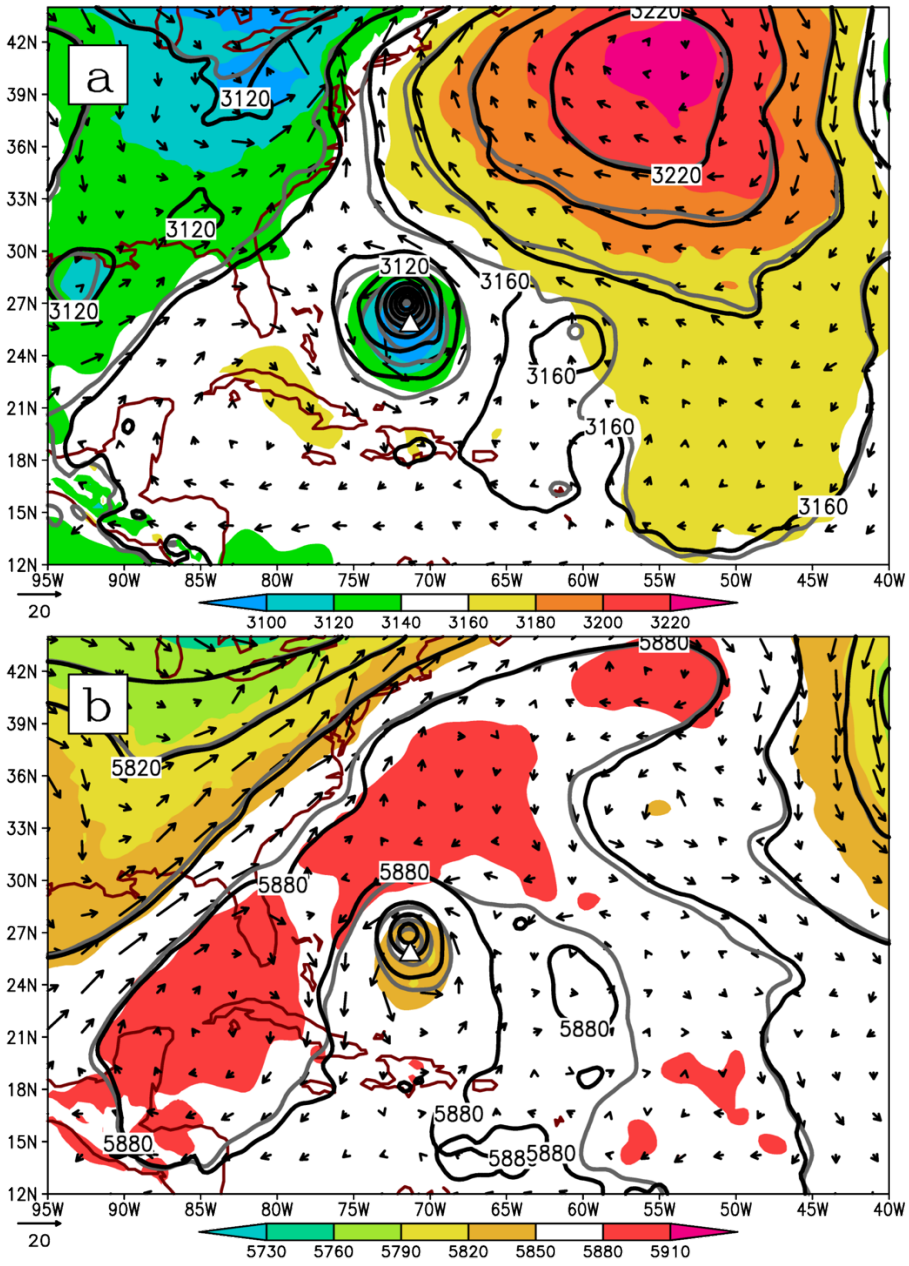

Figure 2.14 (a) Geopotential height (shaded, m) and horizontal flow vectors (m s^{-1}) from the 0000 UTC 30 Sep NCEP 0.25°-FNL with NONUDGE 18-h forecast geopotential height (m) contoured in black at 20-m intervals and PERT-R_WE 18-h forecast geopotential height contoured in gray over the same interval range, all from the 700-hPa level. (b) As in (a), but from the 500-hPa level, with NONUDGE and PERT-R_WE geopotential height contoured at 30-m intervals. White triangles denote the 0000 UTC 30 Sep best-track Joaquin position.

2.5.3 Impact of vortex structural changes on Joaquin's motion

It is possible that changes to Joaquin's vortex structure may have also helped draw the center southward during the early CTL simulation period, i.e., prior to 0000 UTC 30 Sep. That is, Joaquin's vortex undergoes two simultaneous processes that have been well documented in observational, modeling, and theoretical studies of TCs intensifying under moderate VWS (Reasor et al. 2013; Rogers et al. 2015; Nguyen and Molinari 2015; Rios-Berrios et al. 2016; Rios-Berrios et al. 2018): (i) axisymmetrization, as convection that had previously been focused south of the center wraps into the upshear quadrants (Fig. 5a-d); and (ii) reduction in the vertical tilt (Fig. 8a). For some moderately sheared TCs, particularly those in early stages of development, these two processes may be driven by downshear vortex reformation. For example, explosive deep convection on the downshear (eastern) side of Tropical Storm Gabrielle (2001) facilitated the concentration of low-level cyclonic vorticity through convergence and stretching; the new vortex grew vertically deep while absorbing the parent circulation over a 4-h period prior to landfall in southwest Florida (Nguyen and Molinari 2015). This process likely accounted for Gabrielle having a best-track speed that was nearly double the mean environmental flow speed over this period (Molinari et al. 2006).

Figure 2.15 shows the evolution of the CTL radar reflectivity, sea-level pressure (SLP) field, and 850- and 500-hPa level circulations over the first 18 h. At the CTL initial time, the vortex tilts downshear-left, and deep convection is confined to the downshear quadrants (Figs. 2.15a,b). Six hours later, a local SLP minimum has developed where the downshear-left corner of a larger, elliptically shaped low-level circulation intersects the northwest edge of the deep convection (2.15c). The local SLP minimum is co-located with enhanced low-

level cyclonic vorticity, and it lies beneath the upper-level center (Fig. 2.15d). By 1800 UTC 29 Sep, deep convection has wrapped cyclonically into the upshear-left quadrant and the low-level circulation has contracted and intensified (Fig. 2.15e). While both the upper-level and lower-level centers have continued moving southwestward (Fig. 2.8a), the former is now positioned upshear-left relative to the latter, and the tilt is reduced to ~30 km, compared to ~80 km 6-h prior (Figs. 2.15d,f). Six hours later the vortex is vertically aligned and a closed circular eyewall has formed (Figs. 2.15g,h). The CTL vortex structural changes over the 0600 UTC 29 – 0000 UTC 30 Sep period bear some similarity to the Tropical Strom Gabrielle downshear reformation process (see Figs. 7, 9 and 15 in Nguyen and Molinari 2015); however, unlike for Gabrielle, the developing downshear circulation in Joaquin never fully "takes over" from the parent circulation. Rather, both centers merge in concert with the vortex vertical alignment (Figs. 2.15b,d,f). A deeper investigation of the dynamical and thermodynamic processes driving these structural changes, and of how they relate to Joaquin's RI, warrants further study.

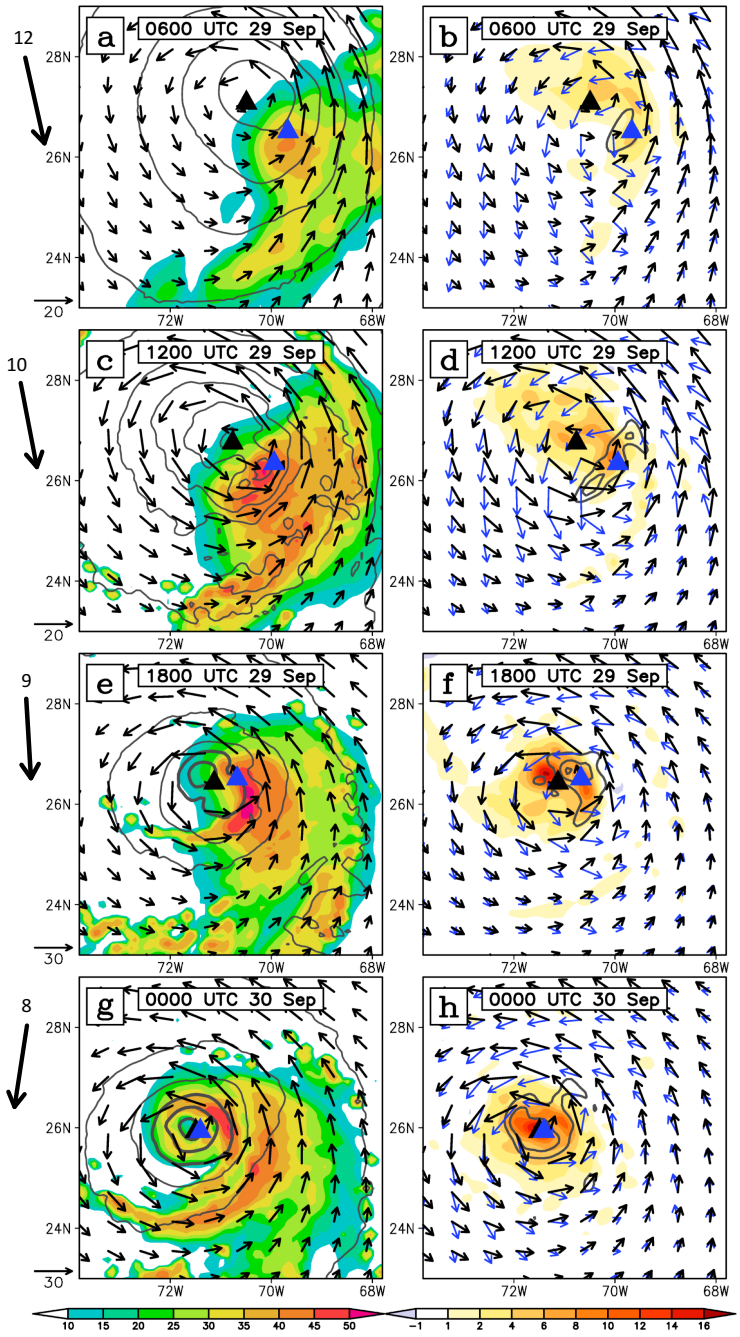

Figure 2.15 (a) CTL analyzed composite reflectivity (dBz, shaded) with sea-level pressure (hPa; thick gray contours below 1000 hPa, thin gray contours for 1000 hPa and above) and 850-hPa horizontal winds (m s^{-1}), valid at 0600 UTC 29 Sep. Thick black arrow to the left of the panel denotes the 850-200 hPa VWS vector, with its magnitude (m s^{-1}) labeled above. (b) As in (a), but with relative vorticity ($\times 10^4$ s^{-1}) at 850 hPa (shaded) and at 500 hPa (contoured for 4/8/12). Black (blue) vectors show 850-hPa (500-hPa) horizontal winds (m s^{-1}), scaled to the vector length from (a). Black (blue) triangles show the 850-hPa (500-hPa) circulation center. (c),(d) As in (a),(b) but for the 6-h CTL forecast, valid at 1200 UTC 29 Sep. (e),(f) As in (a),(b) but for the 12-h CTL forecast, valid at 1800 UTC 29 Sep. (g),(h) As in (a),(b) but for the 18-h CTL forecast, valid at 0000 UTC 30 Sep. Sea-level pressure is contoured at 2 hPa intervals for (a),(c) and 4 hPa intervals for (e),(g). All variables are taken from the 9-km model domain.

To what extent did the contraction and vertical alignment of Joaquin's vortex cause additional southward motion in the low-level center that cannot be accounted for by the environmental winds? Between 0600 and 1800 UTC 29 Sep, the CTL 850-hPa center moves southwest with motion vector (u, v) = (-1.46, -1.67) m s^{-1}. Applying the optimal steering flow calculation (see section 2.3.3) to CTL at 1200 UTC 29 Sep yields the vertically-averaged environmental wind vector (U_{opt}, V_{opt}) = (-1.86, -0.87) m s^{-1}, with a steering depth and vortex removal radius of 850-250 hPa and 700 km, respectively. Despite being a rough estimate[5], this calculation implies that vortex reorganization over the first 12 h causes a 0.4 m s^{-1} eastward and 0.8 m s^{-1} southward deviation from the environmental steering winds in the CTL motion – a significant contribution.

2.5.4 Vortex-scale response to steering environment

The steering flow analysis in sections 2.5.1-2.5.3 above has explored the sensitivity of Joaquin's motion to environmental steering features, vortex intensity and depth, and vortex reformation. In reality, TC steering is controlled by the interaction between the cyclonic circulation and the environmental flow. Let us now take a closer look at how Joaquin's circulation interacts with the steering environment using vertical cross sections taken through five representative 12-h forecasts. All cross sections are taken in the NW-SE direction, which is approximately orthogonal to Joaquin's observed motion during these times.

The 12-h CTL vortex, now near-vertically aligned, has a notable circulation asymmetry, with stronger (weaker) northeasterly (southwesterly) winds northwest

[5] This calculation assumes that the environmental steering winds, vortex depth, and vortex size at 1200 UTC 29 Sep remain constant over the +/- 6 h window surrounding this time.

(southeast) of the center. This pattern is evident both in the 500-hPa planar view (Fig. 2.16a) and in winds orthogonal to the cross-section inside of the ~333 km optimal steering radius, especially above 600 hPa (Fig. 2.16b). Removal of the azimuthally averaged tangential winds would yield residual northeasterly winds in the northwestern circulation that may be important in steering Joaquin southwestward. In contrast, the westward-moving NONUDGE storm (Fig. 8a) circulation is more symmetric through a deep layer (Figs. 2.16c,d). Nudging wind and temperature on the three fixed domains towards the 1°-FNL has re-aligned the strongest 500-hPa ridging, denoted by the 5890 m contour, from northeast of the center in NONUDGE to due north of the center in CTL (Figs. 2.16a-d). PERT-R_WE, which has partially recovered the observed southwest motion (Fig. 2.8a), shows a near-storm 500-hPa environment more like CTL, with enhanced ridging north and west of the center (Fig. 2.16e). Compared to NONUDGE, PERT-R_WE has restored the northwest-southeast inner core circulation asymmetry found in CTL, especially over the 700-400 hPa layer, where height perturbations in the initial conditions are largest (cf. Figs. 2.13c and 2.16e,f). Compared to the other three simulations, the PERT-V and 1200 UTC 29 Sep GFS 12-h forecasts both have considerably weaker vortices that tilt southeastward with height, and their highest cyclonic potential vorticity is concentrated below 650 hPa (Figs. 2.16g-j), which is consistent with their significantly larger vortex depth errors (Fig. 2.11).

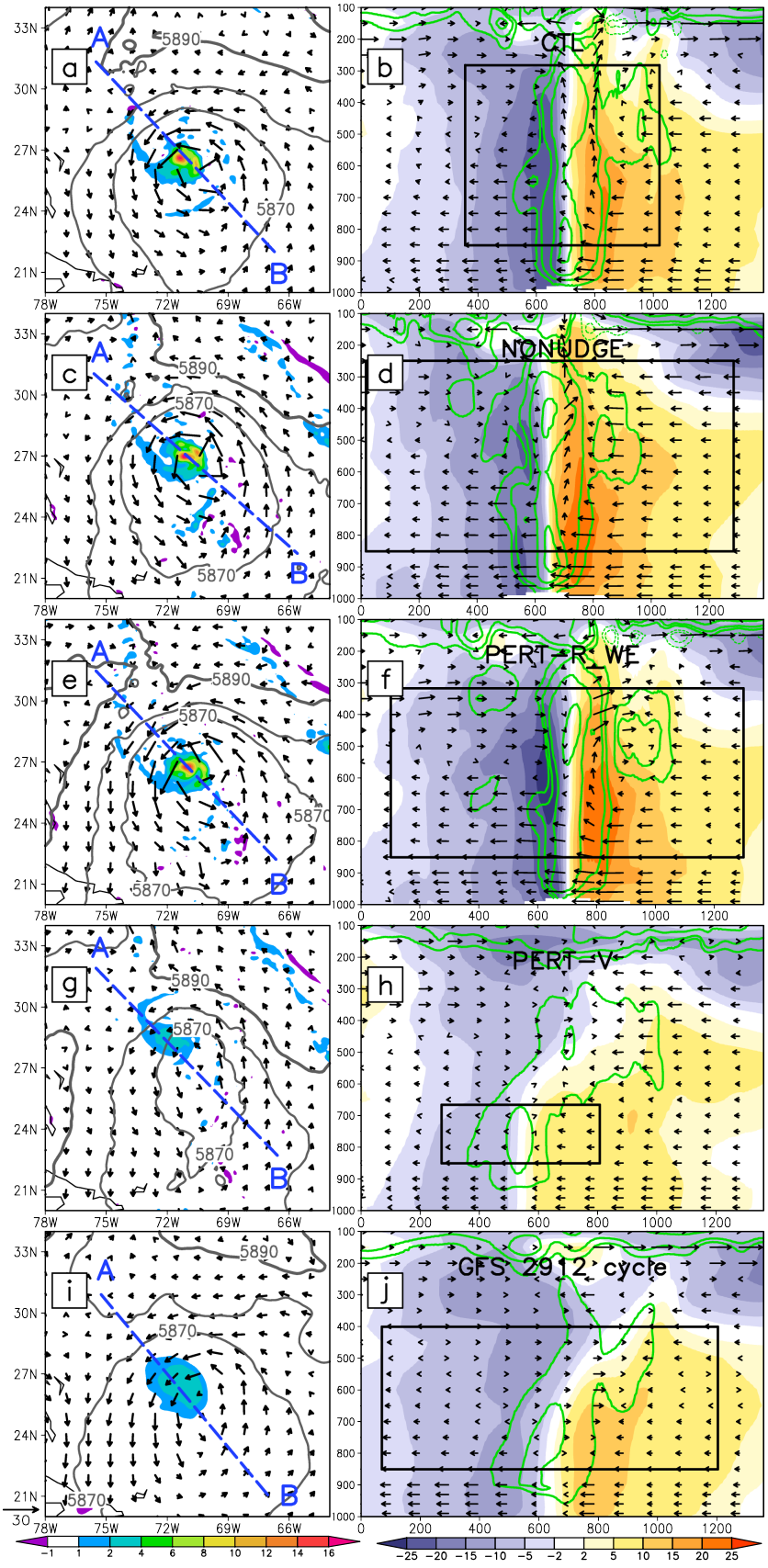
a
b
CTL
c
d
NONUDGE
e
f
PERT_R_WE
g
h
PERT_V
i
j
GFS_2912_cycle
A
B
5890
5870
33N
30N
27N
24N
21N
78W
75W
72W
69W
66W
0
200
400
600
800
1000
1200
−1
1
2
4
6
8
10
12
14
16
−25
−20
−15
−10
−5
−2
2
5
10
15
20
25

← **Figure 2.16** (a) CTL 12-h forecast 500-hPa horizontal wind vectors (m s^{-1}) with geopotential height (contoured every 10 m over the 5870-5890 m range), superimposed over 850-hPa relative vorticity ($\times 10^4$ s^{-1}). (b) Vertical cross-section, 90-km wide, taken along the line running from A to B in (a), with distances (km) marked on the abscissa. Horizontal winds normal to the cross-section are shaded (m s^{-1}), with positive (negative) values assigned to winds directed into (out of) the page. Green contours plot Ertel potential vorticity [-2/-1/1/2/4/8/12 Potential Vorticity Units (PVU), dotted for negative values]. In-plane flow vectors (m s^{-1}; vertical motions multiplied by 5) are also shown. Black rectangles show the optimal steering flow volume centered on the low-level storm center, with dimensions averaged over the 6-18 h period. (c,d), (e,f), (g,h), and (i,j) As in (a,b) but for the 12-h NONUDGE, PERT-R_WE, PERT-V, and 1200 UTC 29 Sep cycle GFS forecasts. For (b,d,f,h,j), flow vectors are scaled to 20 m s^{-1} for the same unit vector length used for (a,c,e,g,i).

Returning to CTL and examining a few later times during its southwest movement period, we find that the strongest 500-hPa ridging remains northwest of the storm, consistent with the 500-hPa circulation being stronger on the northwest side and weaker on the southeast side of the center (Figs. 2.17a,c,e). Vertical cross sections show this circulation asymmetry to be prominent above 600 hPa (Figs. 2.17b,d,e). These results suggest that Joaquin interacted with its steering environment over a broad radial band that extended deep into the inner-core region, to < 100 km from the storm center. Other high-resolution case studies (Marks et al. 1992; Liu et al. 1999) similarly found that TC steering could be largely explained by translational flows within the inner-core region.

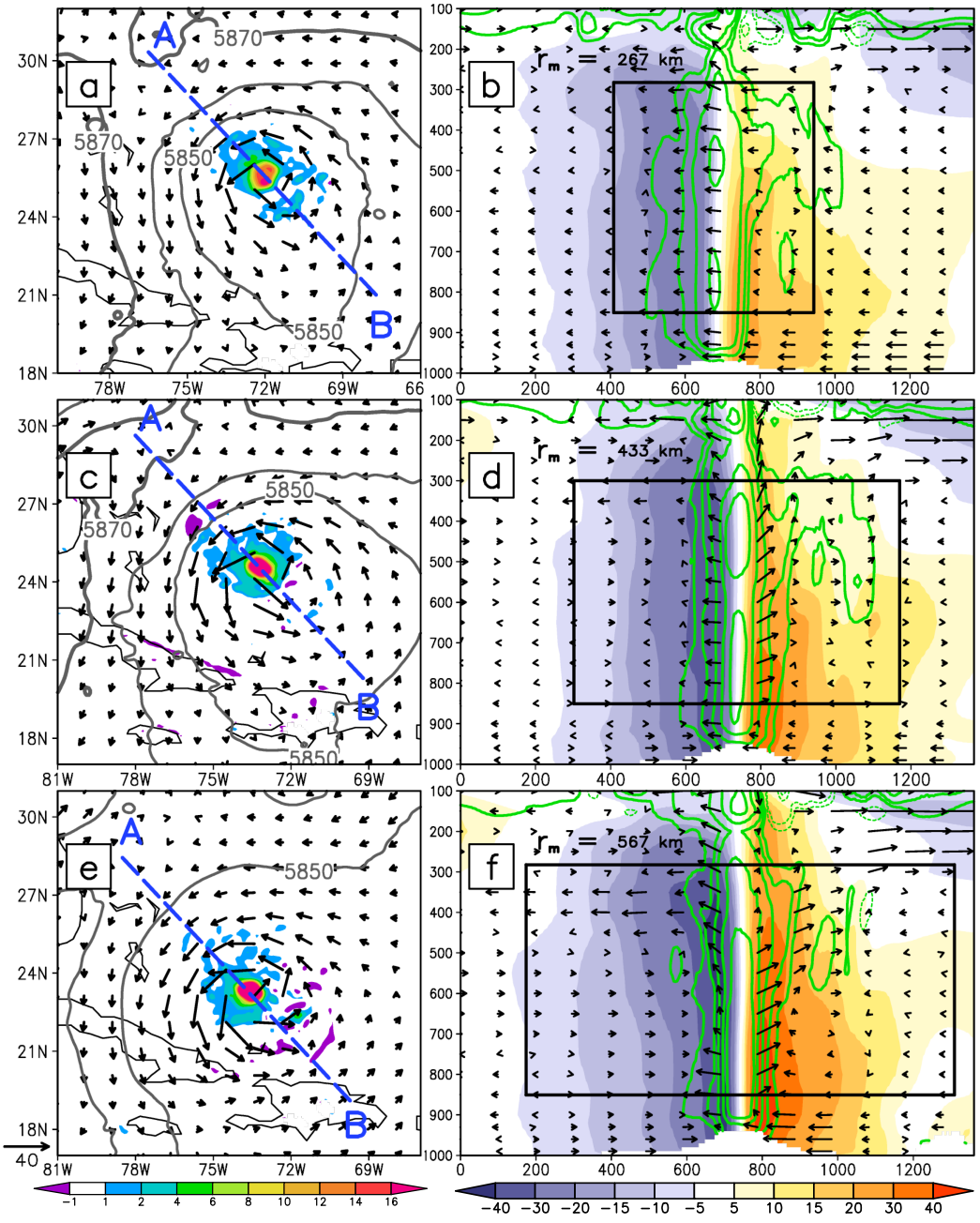

Figure 2.17 As in Fig. 2.16, but for the CTL 24-h forecast (a,b), 36-h forecast (c,d), and 48-h forecast (e,f). For (a,c,e), the 5850, 5860, and 5870 m 500-hPa geopotential height contours are shown. Note the different vector length scale used for (a,c,e) compared to Fig. 2.16 (a,c,e,g,i). This length scales to 20 m s^{-1} for (b,d,f). Also note the different shading scale used for (b,d,f), compared to Fig. 2.16 (b,d,f,h,j).

2.6 Summary and Concluding Remarks

This chapter has examined the atmospheric features that steered Hurricane Joaquin (2015) onto its climatologically unusual looping track, where the storm tracked southwestward for several days followed by slow clockwise turning and recurvature to the northeast. We focused on the period of Joaquin's southwest motion because (i) many early-cycle operational forecasts struggled to capture the persistence of this motion, and (ii) this steering positioned the storm far enough south relative to a southeast U. S. mid-to-upper level low such that it could be steered out to sea rather than be pulled towards the U. S. coast by the winds surrounding the low.

We began by validating the 1-km resolution WRF CTL simulation against observations. CTL initialized Joaquin as a weak tropical storm and reproduced its RI and looping track. The WRFDA-hybrid generated CTL initial conditions were biased relative to the 0.25°-FNL, whereby deep-layer ridging was too weak northwest of Joaquin; nudging of horizontal winds (temperature) towards the 1°-FNL on the outer three (two) domains adjusted the WRF large-scale conditions such that by 24 h they were quite similar to those of the 0.25°-FNL (not shown).

Next, we analyzed steering flows for two representative operational GFS forecasts. Using the GD13 TC motion error budget equation, we found that the 1200 UTC 29 Sep cycle forecast failed to generate any sustained southward motion due to (i) a deep-layer southerly wind bias in the storm steering environment that was present in the initial conditions and grew larger over time and (ii) an insufficiently deep vortex that did not strongly interact with northeasterly environmental steering flows above 400 hPa. The 1200 UTC 30 Sep cycle GFS forecast, on the other hand, initialized a stronger, vertically aligned

vortex that responded to a deeper steering layer. Here, northerly-directed motion errors after 12 h resulted primarily from a deep-layer southerly environmental wind forecast bias relative to the 0.25°-FNL, which was shown to be consistent with inadequately strong ridging west of the storm at 12 h, as well as with the GFS digging the eastern U.S. trough further south and east over Florida at 36 h. Berg (2016) compared 72-h GFS and ECMWF forecasts and similarly found a deeper vortex and a less progressive eastern U.S. trough in the ECMWF forecast, which had significantly lower track errors (see his Fig. 10).

A unique contribution from this study was to show, using WRF initial condition sensitivity tests, that Joaquin's southwest motion was sensitive to both track error sources diagnosed from the early-cycle GFS forecasts: namely, the environmental wind and vortex depth errors. *In order to simulate Joaquin's southwest motion, the WRF model must generate both a sufficiently strong mid-to-upper level ridge northwest of the storm and a sufficiently deep vortex to interact with the geostrophic flows around the east side of the ridge.* Cross sections taken from CTL during Joaquin's southwest-moving period show stronger mid-to-upper level winds northwest of the center, relative to the southeastern quadrant, which is consistent with the strongest nearby mid-to-upper level ridging being located northwest of the vortex center. These findings are consistent with N18 and Torn et al. (2018), who similarly found that Joaquin's early southwest motion was most sensitive to small geopotential height and wind changes in the near-storm environment and less sensitive to more distant features, such as the eastern U.S. trough. Like N18, we also find that Joaquin's motion after 0000 UTC 02 Oct may have become sensitive to the position of the eastern U.S. trough as it was evolving into a closed low, having by now moved closer to the storm.

Unlike N18, however, we found that Joaquin's southwest motion could also be dependent on the vortex having sufficient depth. In part, these differences may stem from N18 finding the environmental flow uncertainty to be maximized in the lower troposphere, near 700 hPa, which should affect the motion of both deep and shallow TCs. However, we found vortex depth to be an important factor only for the "extreme case" forecasts that initialized Joaquin as a weak tropical storm and failed to intensify it - namely, the 1200 UTC 29 Sep cycle GFS and the PERT-V sensitivity test. GD13 similarly found insufficient vortex depth to be a significant contributor to Advanced Hurricane WRF (AHW) track errors during the early development of Hurricane Earl (2010). Our findings suggest that model misrepresentation of vortex depth may be an important track error source for some TC cases, especially for weaker, developing storms that are embedded in vertically sheared environmental flows. We also showed how Joaquin's vortex contraction and tilt reduction over the 0600 UTC 29 Sep – 0000 UTC 30 Sep period may have helped to draw the low-level center southward.

Despite marked improvements in TC track forecasting over the past few decades, operational model forecasts can still contain large track errors, particularly for climatologically unusual cases (Zhang et al. 2018). Assimilating additional data over ocean regions, to include both satellite radiances and aircraft dropsondes sampling the synoptic environment, together with improved model physics, may lead to better model representation of large-scale flow features (Brennan and Majumdar 2011; GD13; Bassill 2014; Torn et al. 2015,2018). Our results further suggest that for TCs developing in vertically sheared environments, improved inner-core sampling by means of cloudy radiances and aircraft reconnaissance missions may reduce track forecast errors by

improving the model estimate of vortex depth in the initial conditions. Given that vortex depth is generally correlated with intensity, improvements in track forecasting may be partly contingent on more accurate intensity forecasts for these cases.

Chapter 3. Data Assimilation Methods Used for Generating the Hurricane Joaquin (2015) Control and Sensitivity Simulations

3.1 Cycling strategy

A 30-h WRF spinup cycle, herein the WRFDA-hybrid cycle, assimilates observations every 3 h using WRF Data Assimilation (WRFDA) V3.9 hybrid 3DVAR software (Wang et al. 2008a,b) with the purpose of generating accurate and dynamically balanced initial conditions for the Hurricane Joaquin (2015) Control (CTL) and sensitivity simulations described in chapter 2 (Fig. 3.1). WRF is run at 27/9/3-km resolution with the CTL 2-way nesting configuration (Fig. 2.2) and physics schemes, except that the Davis et al. (2008) SST parameterization is turned off. The WRFDA-hybrid cycle begins with a 3-h WRF forecast initialized from the 0000 UTC 28 Sep 1°-FNL, which becomes the background for the first hybrid analysis. The cycle continues, with hybrid analyses initializing 3-h WRF simulations. Data assimilation is performed separately on the 27 and 9-km domains. The 3-km nest is interpolated from the 9-km analyses, except for 1800 and 2100 UTC 28 Sep, when inner-core reconnaissance flight data are available, and data assimilation is performed on the 3-km background. To filter out noisy and potentially unbalanced features from the analyses, digital filter initialization (DFI, Lynch and Huang 1992) with a twice-DFI scheme and a Dolph Filter (Lynch 1997) is applied at the beginning of all cycled WRF runs, using 2-h backward and forward integrations. The DFI-processed 0600 UTC 29 Sep analysis is used to initialize CTL.

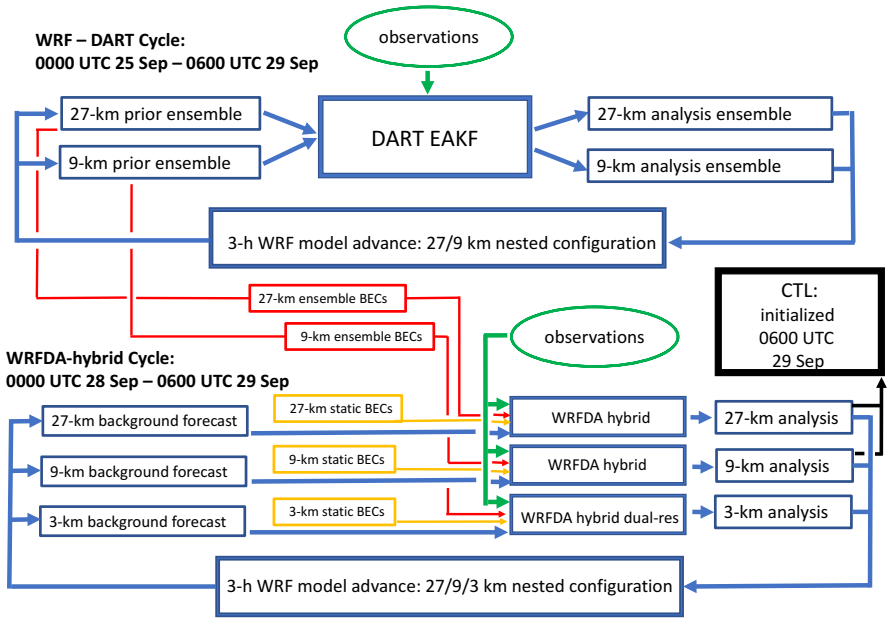

Figure 3.1 Schematic summarizing the cycled data assimilation methodology used for generating the CTL analysis.

An 80-member 27/9-km WRF forecast ensemble, herein the WRF-DART cycle (Fig. 3.1), provides ensemble-based "errors of the day" to the hybrid 3DVAR algorithm. The ensemble initial conditions are seeded at 0000 UTC 25 Sep by adding random Gaussian draws taken from the 27-km domain static "CV5" background error field to the 1°-FNL (Torn et al. 2006). Lateral boundary conditions for the 27-km domain are perturbed similarly. Following an initial 6-h WRF ensemble forecast[6], observations are assimilated every 3 h using the Data Assimilation Research Testbed (DART) Ensemble Adjustment Kalman Filter (EAKF; Anderson 2001, 2009). The WRF-DART cycle is initialized three days prior to the first hybrid analysis so that the system has sufficient time to develop spread representative of the flow-dependent errors.

[6] Except for the omission of the 3-km nest, WRF model settings are the same as those for the WRFDA-hybrid cycle. DFI is also not used for WRF-DART model advances.

3.2 Data assimilation algorithms

The WRFDA-hybrid 3DVAR algorithm can perhaps most intuitively be understood when the variational cost function *J*, which is minimized to solve for the analysis increment $\mathbf{x}'$, is expressed in the form derived by Wang et al. (2007):

$$J(\mathbf{x}') = \frac{1}{2}\mathbf{x}'^{\mathbf{T}}\left(\frac{1}{\beta_1}\mathbf{B} + \frac{1}{\beta_2}\mathbf{P}^{e}\circ\mathbf{S}\right)^{-1}\mathbf{x}'$$

$$+\frac{1}{2}\left(\mathbf{y}^{o\prime} - \mathbf{H}\mathbf{x}'\right)^{\mathrm{T}}\mathbf{R}^{-1}\left(\mathbf{y}^{o\prime} - \mathbf{H}\mathbf{x}'\right), \qquad (3.1)$$

where the static background error covariance (BEC) **B**, observation error covariance **R**, innovation vector $\mathbf{y}^{o\prime} = \mathbf{y}^{o} - H(\mathbf{x}^{b})$, and linear observation operator **H** are all familiar terms from the ordinary 3DVAR cost function. The innovation is the difference between the observations $\mathbf{y}^{o}$ and the background forecast $\mathbf{x}^{b}$ transformed to observation space using the nonlinear observation operator *H*. Equation (3.1) differs from ordinary 3DVAR only in the first right-hand side term, were the static BEC is replaced by the expression in parentheses, which is a linear combination of static and ensemble BEC contributions, controlled by the weighting factors β_1 and β_2, where

$$\frac{1}{\beta_1} + \frac{1}{\beta_2} = 1. \qquad (3.2)$$

For $k = 1,\ldots, K$ ensemble members, the *k*th ensemble forecast $\mathbf{x}_k$ normalized perturbation about the mean $\bar{\mathbf{x}}$ is

$$\mathbf{x}_k^{e} = \frac{(\mathbf{x}_k - \bar{\mathbf{x}})}{\sqrt{(K-1)}}, \qquad (3.3)$$

and the ensemble covariance $\mathbf{P}^{e}$ becomes

$$\mathbf{P}^{e} = \sum_{k=1}^{K} \mathbf{x}_k^{e}\,(\mathbf{x}_k^{e})^{\mathrm{T}}. \qquad (3.4)$$

The ensemble, or "errors of the day" BEC in (3.1), is the Schur product of $\mathbf{P}^e$ and the localization matrix **S**. The latter smoothly spreads the ensemble covariances through model space while at the same time limiting sampling error by driving the covariances towards zero at large distances, making use of a recursive filter with a Gaussian response function.

Wang et al. 2008a describe the WRFDA hybrid 3DVAR algorithm in detail. Here, equal weighting between the static and ensemble BECs is used, and the horizontal length scale of the recursive filter used to localize the ensemble BECs in model space is set to 750 km, which corresponds to an e-folding distance of ~ 2100 km. Two "outer loops" are used to minimize the Eq. (3.1) cost function (Schwartz et al. 2013). When assimilating observations into the 3-km domain, ensemble perturbations are interpolated from the 9-km WRF-DART forecast using the WRFDA hybrid "dual resolution" algorithm (Schwartz et al. 2015). The "NMC method" (Parrish and Derber 1992) is used to generate the static BECs (CV5 option) from differences in 12 and 24-h WRF forecasts verifying at the same time, gathered over a 40-day period prior to the start of the WRFDA-hybrid cycle.

The DART EAKF ingests observations with the purpose of adjusting the analysis ensemble mean toward the truth while maintaining a spread representative of the flow-dependent errors. The EAKF is one commonly used flavor of Ensemble Kalman Filter (EnKF), a more general class of algorithms that are all fundamentally based on the following equations:

$$\boldsymbol{x}^a(t) = \boldsymbol{x}^f(t) + \mathbf{K}[\boldsymbol{y^o} - H\boldsymbol{x}^f(t)], \qquad (3.5)$$

$$\mathbf{K} = \mathbf{P}^f H^T (H\mathbf{P}^f H^T + \mathbf{R})^{-1}, \qquad (3.6)$$

$$\boldsymbol{x}^f(t+1) = M[\boldsymbol{x}^a(t)]. \qquad (3.7)$$

Equation (3.5) adjusts a forecast vector $\boldsymbol{x}^f(t)$ at time t using the Kalman gain matrix $\mathbf{K}$ multiplied by the innovation vector to generate the analysis $\boldsymbol{x}^a(t)$. Although Eqs. (3.5)-(3.7) can be applied to a single forecast, here we let $\boldsymbol{x}^f(t)$ and $\boldsymbol{x}^a(t)$ denote a forecast and analysis ensemble respectively. As in Eq. (3.1), the innovation vector is the difference between the observations and $\boldsymbol{x}^f(t)$, transformed to observation space using the nonlinear observation operator H. Equation (3.6) shows that $\mathbf{K}$ is computed from the background error covariance $\mathbf{P}^f$ and the observation error covariance $\mathbf{R}$; EnKFs compute $\mathbf{P}^f$ through covariances in ensemble perturbations about the mean. Thus, Eqs. (3.5) and (3.6) show that observations will have a higher impact on state variables that have larger covariances with the observed state variables in the background forecast. The analysis is subsequently advanced to time $t + 1$ using the nonlinear model integration M. The various types of EnKFs differ in how they approximate $\mathbf{K}$ and apply Eqs. (3.5)-(3.7) to an ensemble of forecasts (Houtekamer and Zhang 2016).

The DART EAKF approximates Eqs. (3.5) and (3.6) in a two-step process, assimilating each observation one at a time or in small batches. In the first step, the observation operator H is applied to every ensemble member to generate a *prior observation ensemble* for a given observation T that has an observed value T_o. The prior observation ensemble is then fit to a Gaussian probability estimate for T given the state of the system in the background forecast. Next, the prior observation ensemble distribution is transformed into the *posterior observation ensemble* Gaussian estimate for T that minimizes the combined background forecast uncertainty and observation error, the latter accounting for both instrument errors and errors stemming from representing the observations in model space. Larger prior ensemble spread and smaller observation errors

both act to adjust the posterior estimate of T closer to the observed value T_o. In the second step, unobserved state variables for the ensemble members are adjusted by linear regression against the posterior observation ensemble. Two important limitations in this algorithm are worth noting. First, the analysis can be altered simply by changing the order of observation assimilation. Second, errors in the prior ensemble and observations are both assumed to be Gaussian.

We employ several strategies to prevent "filter divergence" whereby the forecast ensemble spread collapses, causing the observations to have little influence and the state to evolve away from the truth. For brevity, we mention only key settings, which follow previous successful studies (Torn 2010; Cavallo et al. 2013; Wu et al. 2014, 2015). To compensate for spread deficiency, which can result from a finite-sized ensemble not capturing model error and other sources of uncertainty, inflation (with an initial standard deviation of 0.6) is applied to the background ensembles prior to assimilation and allowed to vary in time and space (Anderson 2009). Densely observed regions evolve higher inflation values. To prevent unnecessarily high inflation for later periods, should the local observation density decrease, the inflation fields are damped by 10% every cycle. Horizontal and vertical localization is applied, which limits the spatial influence that observations have on the model state, thereby mitigating analysis degradations caused by distant spurious correlations. We use a bell-shaped polynomial correlation function (Gaspari and Cohn 1999) that reaches zero 1910 km in the horizontal and 10 km in the vertical around each observation. The size of this ellipsoid is reduced if necessary by adaptive localization (Torn 2010) to limit the number of observations contained within it to approximately 1600.

3.3 Observations

Table 3.1 summarizes the observations assimilated into the WRF-DART and WRFDA-hybrid cycles. They are assumed valid at the analysis times and taken from +/- 1.5-h time windows, except for the C-130 flight-level winds and temperature, which are taken from +/- 30-min windows. Conventional observations include radiosondes, atmospheric motion vectors (AMVs), and aircraft reports. The AMV winds are derived by tracking moving cloud and water vapor features in geostationary satellite imagery. The University of Wisconsin-Madison Cooperative Institute for Meteorological Satellite Studies (UW-CIMMS) AMVs are a high spatial resolution hourly dataset, available for the period beginning at 0000 UTC 28 Sep, whereas the NOAA-NESDIS AMVs are processed for global analyses and have a coarser resolution. Velden et al. (2017) describe the quality control algorithms used in processing the UW-CIMMS AMVs, which include the removal of all AMVs in the 400-700 hPa layer, where the vector height assignments have been found to be less accurate. To minimize uncorrelated observation errors, not accounted for in the data assimilation, all AMVs are averaged, or "superobbed," over 81-km wide and 25-hPa deep boxes. The "obserr.txt" table supplied with the WRFDA V3.9.1 software provides most observation errors. AMV errors are taken from Velden et al. (2017). C-130 flight-level wind and temperature errors are set to 2 m s^{-1} and 0.5 K, respectively, following Aksoy et al. (2013). National Hurricane Center (NHC) Advisory position and P_{min} errors are set to 0.2 deg and 3 hPa, respectively.

Table 3.1 Observations assimilated into the WRFDA-hybrid and WRF-DART cycles.

Table 1. Assimilated observations

Platform	Observation type	Assimilated in DART EAKF	Assimilated in WRFDA-hybrid	Notes
Radiosondes	*u*, *v*, *T*, *q*	yes	yes	*q* assimilated as relative humidity in WRFDA-hybrid, specific humidity in DART EAKF
Satellite AMVs	*u,v*	yes	yes	superobbed into 81 km x 81 km x 25 hPa boxes
Aircraft	*u*,*v*,*T*	yes	yes	superobbed into 81 km x 81 km x 25 hPa boxes
U.S. Air Force C-130 Recon Flight-level data	*u*,*v*,*T*	yes	yes	28 Sep 1800 UTC and 2100 UTC analyses only; for DART EAKF, thinned to 18-km along-track intervals, for WRFDA hybrid, thinned to 6-km along-track intervals
AMSU-A	radiance	no	yes	thinned to 108 km, 36 km, and 18-km mesh for WRF domains 1, 2, and 3, respectively
Bogus	*q*	no	yes	assimilated as relative humidity over the 1000 – 700 hPa layer in 25-hPa intervals, in concentric arcs S of storm center
NHC Advisory lat, lon, P_{min}	-	yes	no	Data are linearly interpolated in time to 3-h analyses between 6-h advisories

The WRFDA-hybrid cycle assimilates Advanced Microwave Sounding Unit-A (AMSU-A) radiances from the NOAA-15, NOAA-18, NOAA-19, and METOP-2 satellites. Only the temperature-sensitive channels 5, 6, and 7 are assimilated. These channels are not sensitive to surface emissivity and do not heavily sample regions above the model top. The WRFDA Variational Bias Correction (VARBC) routines are used to correct for biases in the quality-controlled radiances; they add a correction term to the radiance forward operator consisting of a constant "offset" added to a linear combination of seven channel-dependent predictors, which are related to field variables and the scan geometry, all multiplied by coefficients. The predictor coefficients are updated every cycle as part of the cost function minimization. To spin up the coefficients, WRFDA is run for a 40-day period prior to 0000 UTC 28 Sep in an "offline mode," following Liu et al. (2012), with the NCEP 1°-FNL used as the reference field.

We examine the impact of assimilating AMSU-A radiances on the 0600 UTC 29 Sep CTL analysis by re-running the 30-h WRFDA-hybrid cycle with these observations removed. Figure 3.2 shows that the resulting NORADIANCES analysis differs most significantly from the CTL analysis in terms of the former having higher mid-to-upper level geopotential heights northeast of Joaquin. This is not too surprising, given that (i) maritime regions are less well sampled by conventional observations and that (ii) the AMSU-A channel 5-7 weighting functions peak in the middle and upper troposphere. The upper-level low centered near 37˚ N, 58˚ W is not well captured by the NORADIANCES analysis, as evidenced by the fact that the closed 7540-m 400-hPa geopotential height contour that delineates this feature in the 0600 UTC 29 Sep 0.25°-FNL is missing in NORADIANCES (cf. 2.12, 3.2). AMSU-A radiance assimilation lowers heights in its vicinity (Fig. 3.2), although this low is still too weak in the CTL analysis relative to the 0600 UTC 29 Sep 0.25°-FNL (Fig. 2.12). Compared to NONUDGE, a 48-h WRF forecast run from the NORADIANCES analysis with nudging turned off but all other model settings identical to CTL shows (i) an initialized vortex positioned further north and (ii) even less southward motion (Fig. 3.3), and its intensity forecast resembles that of NONUDGE (not shown).

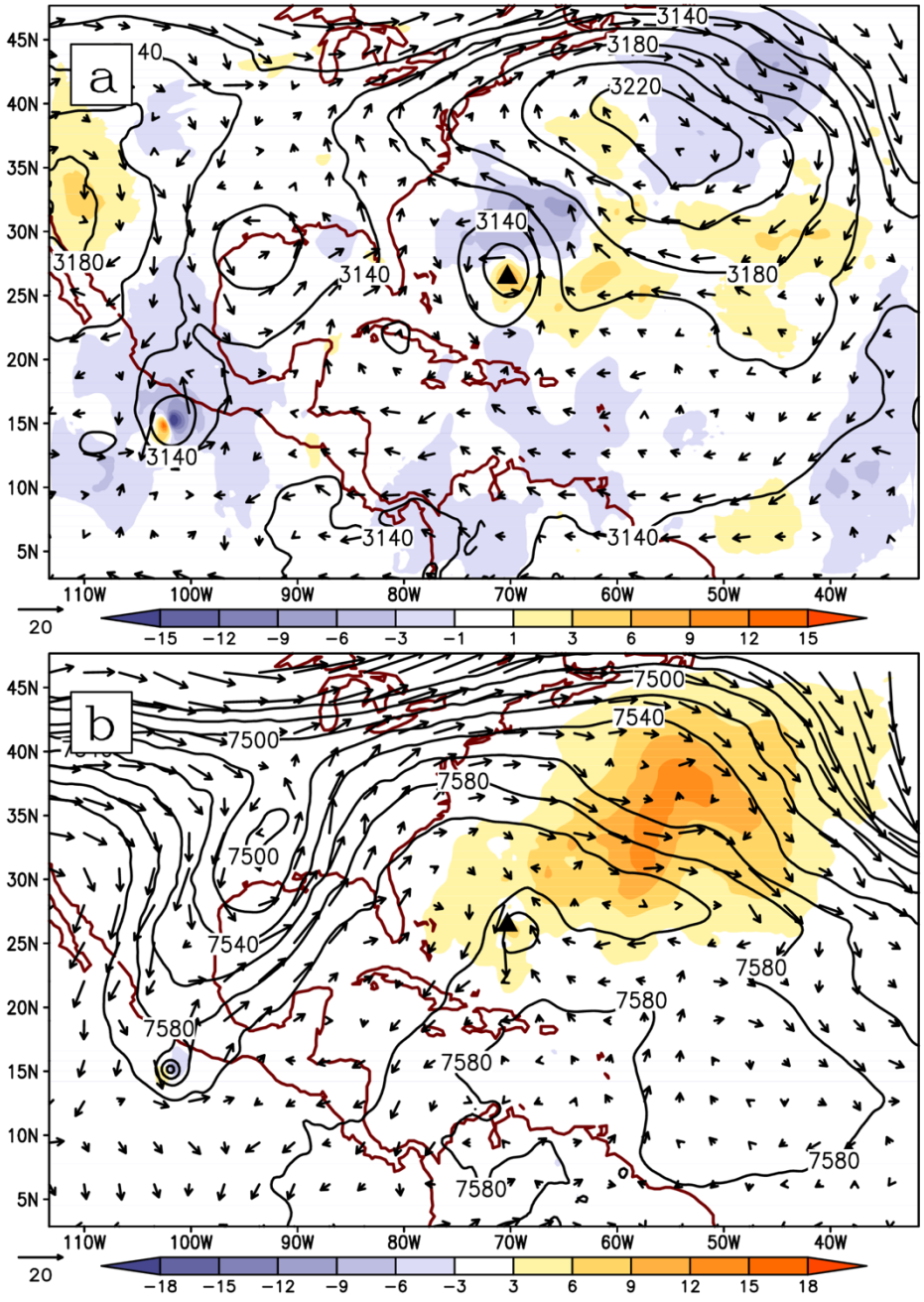

Figure 3.2 (a) Geopotential height differences between the 0600 UTC 29 Sep NORADIANCES and CTL analyses (NORADIANCES - CTL), computed at each pressure level and then averaged over the 850-600 hPa layer (shaded, m) with 700-hPa NORADIANCES geopotential height (contoured, m) and horizontal flow vectors (m s^{-1}). (b) As in (a) but for geopotential height differences averaged over the 600-250 hPa layer, with 400-hPa NORADIANCES geopotential height and winds. Black triangle denotes the 0600 UTC 29 Sep best-track Joaquin position.

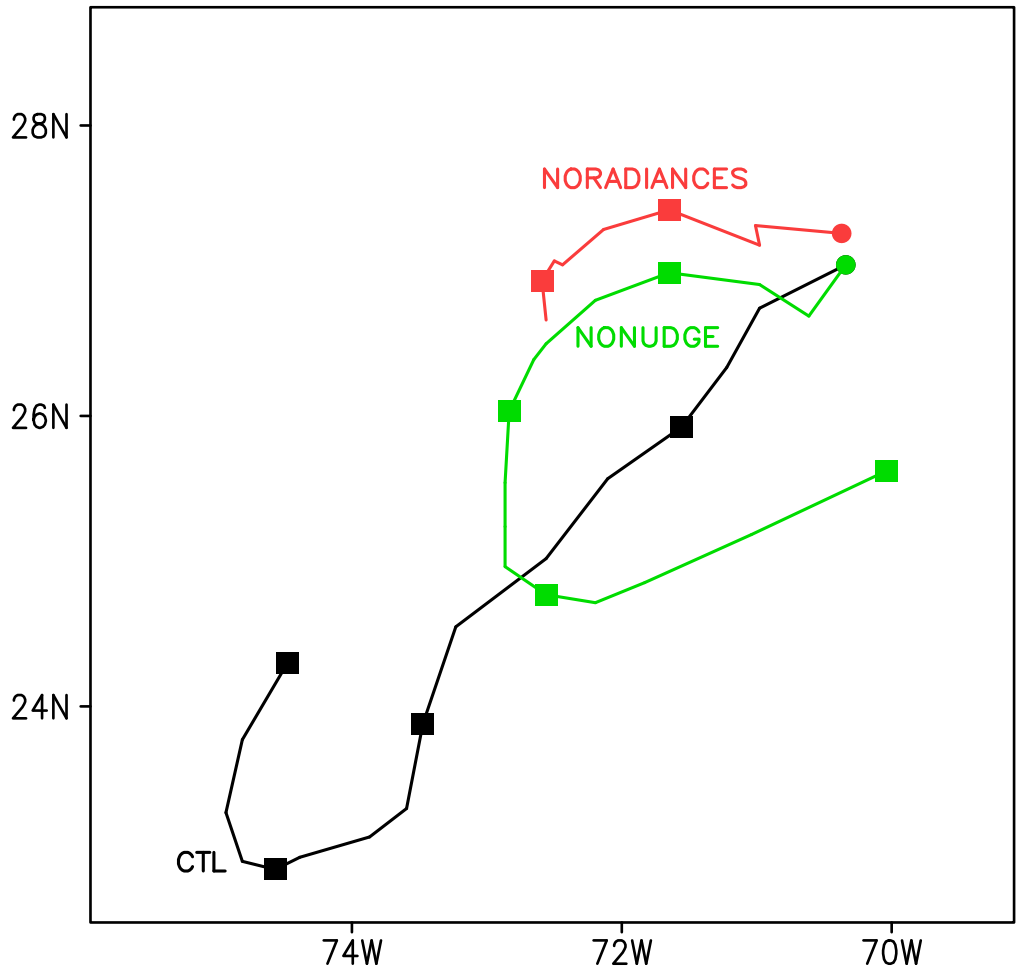

Figure 3.3 Hurricane Joaquin (2015) track for a 48-h WRF simulation run at 1-km resolution from the NORADIANCES analysis (red line), superimposed over 96-h CTL and NONUDGE track forecasts (black and green lines, respectively). Circles denote initial positions and squares denote 0000 UTC positions for all subsequent days.

Except for flight-level wind and temperature observations from one C-130 mission, inner-core observations are not available prior to the CTL initialization time. Previous studies have used bogus moisture soundings to enhance the background relative humidity near a developing TC (Hsiao et al. 2010; Schwartz et al. 2013, 2015). Microwave satellite observations (not shown) indicate that deep convection is displaced south of the surface low center during the WRFDA-hybrid cycling period. To help focus simulated convection in that region, bogus moisture soundings are seeded in concentric semicircles south of the

NHC best-track center extending out to 6 degrees of latitude. Figure 2.13 shows the same sounding configuration, except over a full 360-degree circle. Each sounding increases relative humidity in the 1000-700 hPa layer by a factor of 1.1[7] above the background.

3.4 Validation of the WRF-DART ensemble

As discussed in section 3.2, cycled EnKF systems are vulnerable to filter divergence, whereby the mean evolves away from the truth and the spread collapses. Houtekamer et al. (2005) showed that a properly calibrated prior ensemble mean root mean square error (RMSE), evaluated against observations, should approximately equal the *total spread*, defined as the square root of the sum of the observation error and the spread in the prior ensemble representation the observation. It is important to perform this comparison using the prior, or background, ensemble forecasts because the EnKF can reject any observations that are too far removed from the ensemble mean estimate. For this DART configuration, observations are passed through an "outlier check" prior to assimilation, which rejects any observation that differs from the prior ensemble mean by more than three times the square root of the total spread. Thus, it is possible for an analysis ensemble mean that has drifted far from the true atmospheric state to have a low RMSE against the small fraction of observations that were actually assimilated. Since the ensemble covariances in WRFDA-hybrid are taken from the WRF-DART ensemble forecast spread, it is highly desirable that this spread is representative of the "errors of the day."

[7] Larger factors were tested and found to over-intensify the storm during the WRFDA-hybrid Cycle.

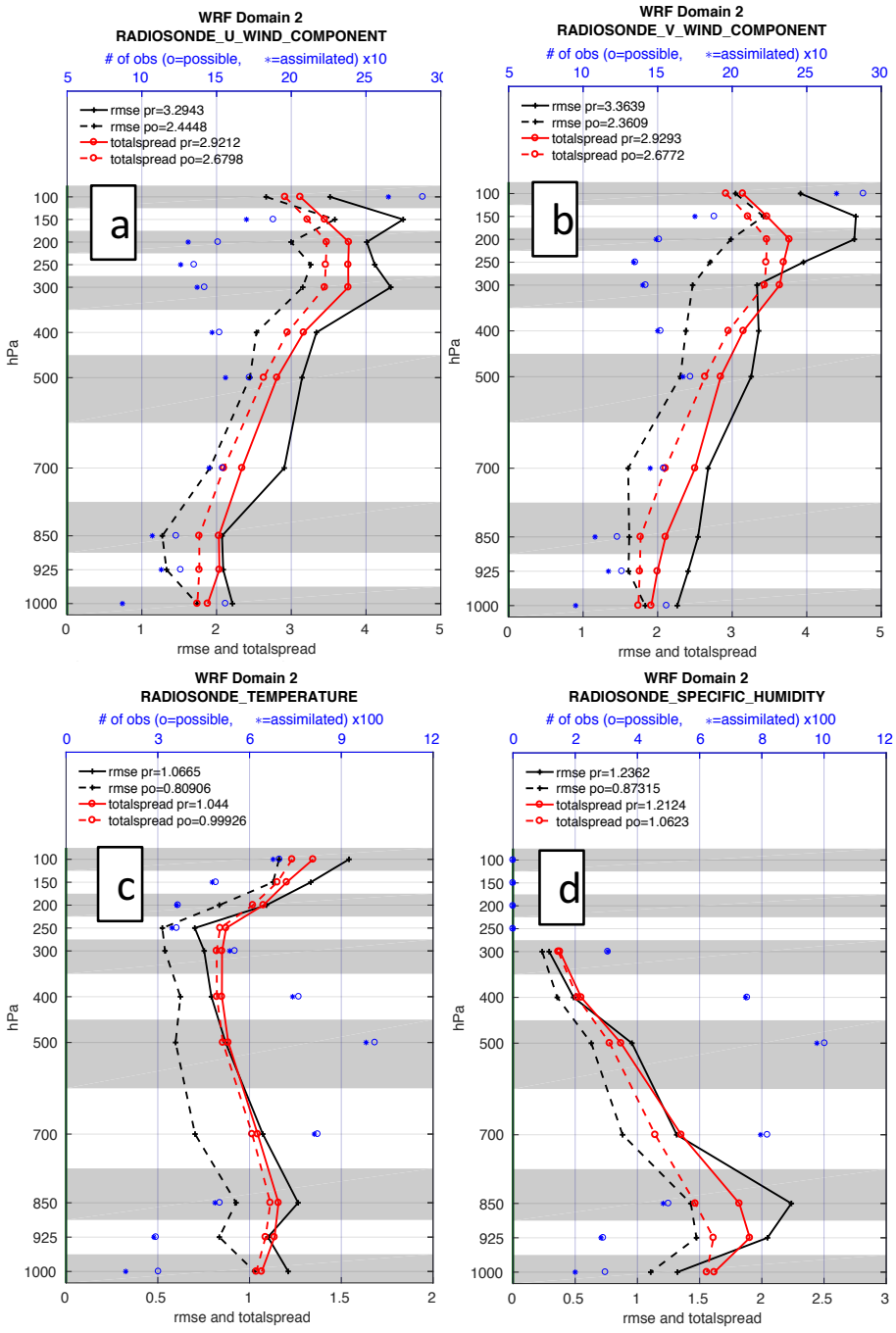

Figure 3.4 Vertical profiles comparing the prior (i.e., background) and posterior (i.e., analysis) WRF-DART ensemble mean RMSE (black) with the total spread (red, see text for definition). These statistics are computed over the WRF 9-km domain for radiosonde (a) *u*-winds, (b) *v*-winds, (c) temperature, and (d) specific humidity. Solid and dashed lines represent the prior and posterior statistics, respectively. Also shown for each height bin are the number of observations processed (open circles) and number of observations that were assimilated (asterisks). The abscissa units are m s^{-1} for (a) and (b), K for (c), and g kg^{-1} for (d).

Here we show vertical profiles of prior and posterior RMSE and total spread, binned over height and over the 0000 UTC 28 Sep – 1200 UTC 29 Sep period, for radiosondes (Figure 3.4) and AMVs (Figure 3.5). For the radiosonde horizontal winds, the ensemble is somewhat underdispersive for most heights, with the ratio of the prior total spread to the prior mean RMSE being around 0.8 – 0.9 (Figs. 3.4a,b). Although this fit appears to be reasonable, when comparing against similar observation space diagnostics shown in Wang et al. (2008b) and Torn and Hakim (2008), Schwartz et al. (2015) showed a somewhat better fit between radiosonde *u* and *v* RMSE and total spread for their WRF-DART ensemble run at 15-km resolution (their Fig. 7). Our RMSE-to-total spread fit could have possibly been improved by tuning the radiosonde *u* and *v* observation errors, but that was not done here. The RMSE-to-total spread ratio is close to 1 for temperature at all heights and for specific humidity above 850 hPa (Figs. 3.4c,d). The prior ensemble mean RMSEs shown for *u,v,t,* and *q* are comparable to those shown in Schwartz et al. (2015). For these four observation types, at least 80 percent of available observations survive the rejection outlier test, with the exception of the lowest height bin around 1000 hPa. It is not surprising that the rejection rate is higher for the boundary layer, given the large vertical temperature and wind gradients that exist here.

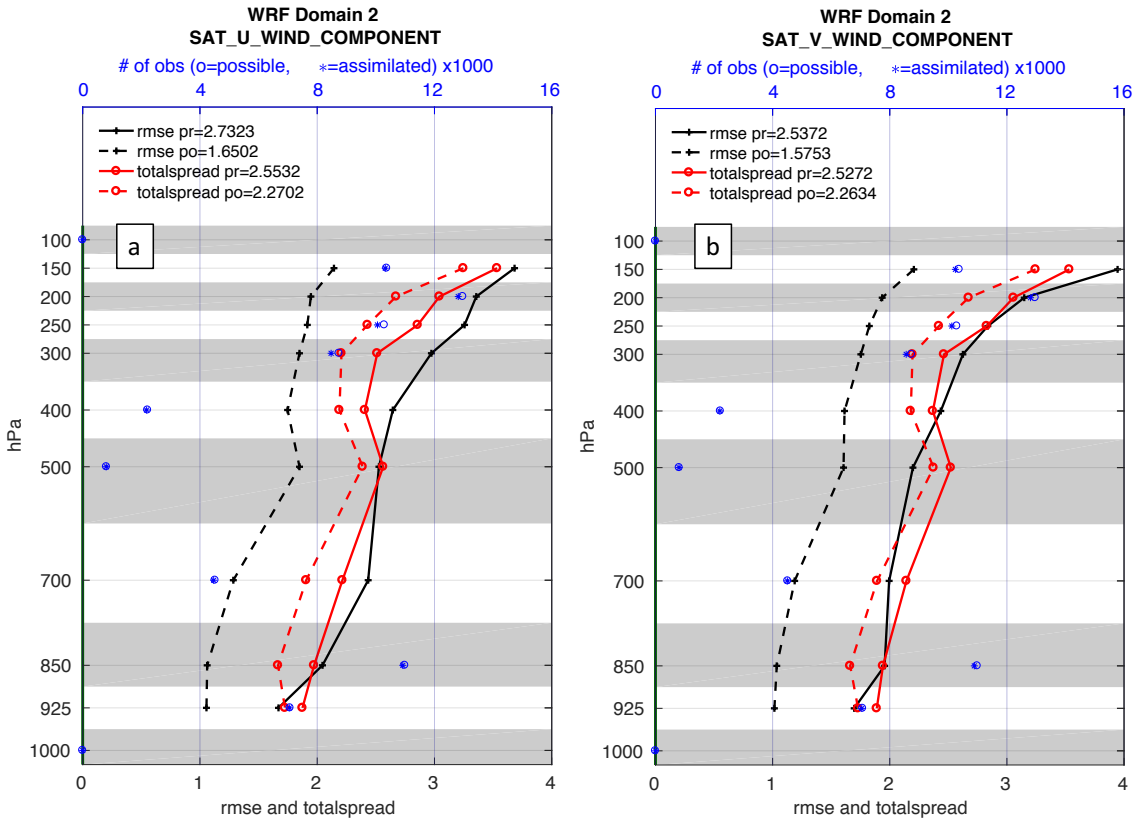

Figure 3.5 As in Fig. 3.4, but for AMV (a) *u*-winds and (b) *v*-winds.

The ensemble is well calibrated with respect to the AMVs (Figs. 3.5a,b), with a rejection rate < 3% at all heights and strong agreement between prior mean RMSE and total spread. This is an encouraging result, given that the AMVs provide the bulk of the EAKF observations over the ocean regions surrounding Joaquin. Figure 3.5 also shows that the AMV vertical distribution is highly bimodal, with large numbers in the upper levels (150-300 hPa) and lower levels (700-925 hPa). These regions have cloud features that can be more reliably tracked, as discussed in section 3.3.

Chapter 4. A Three-dimensional Trajectory Model with Advection Correction for Tropical Cyclones: Algorithm Description and Tests for Accuracy

Material presented in this chapter has been published in Monthly Weather Review as Miller and Zhang (2019b)

4.1 Introduction

A Lagrangian, or parcel-following, analysis is a powerful tool for studying a wide variety of atmospheric processes. Applications include the tracking of ash clouds following volcanic eruptions (Kristiansen et al. 2012), studying ozone and water vapor exchange between the troposphere and stratosphere (Homeyer et al. 2011), pollutant transport and dispersion analysis (Stohl and Kromp-Kolb 1994; Stohl 1996; Brankov et al. 1998; Baker 2010), and investigating sources of updraft buoyancy in tropical maritime convection (Fierro et al. 2009, 2012). Some atmospheric models have a built-in capability to compute forward parcel trajectories during run-time with the same computational timestep used for integrating the prognostic governing equations (Fierro et al. 2009, 2012; Dahl et al. 2012). Nevertheless, for many problems, or if backward trajectories are needed, the four-dimensional (4D) gridded winds must be supplied by analyses or offline model runs. A fluid parcel may be uniquely identified by its position $\mathbf{x}_0$ at any initial, or "seed" time, t_0. The parcel position $\mathbf{x}(\mathbf{x}_0,t)$ at any time t_f may be found by integrating

$$D\mathbf{x}/Dt = \mathbf{u}(\mathbf{x},t) \tag{4.1}$$

using the Lagrangian derivative with respect to time (D/Dt) over the time interval $[t_0 , t_f]$, where $\mathbf{u}(\mathbf{x},t)$ is the parcel velocity. Since parcels are free to travel between the grid vertices, $\mathbf{u}(\mathbf{x},t)$ is obtained by interpolating the Eulerian gridded winds to the parcel position at every computational timestep. A sub-class of trajectory models, commonly referred to as

Lagrangian dispersion models, account for parameterized subgrid scales of motion when solving for $\mathbf{u}(\mathbf{x},t)$; however, this study focuses on trajectory applications where the unresolved motion scales may be neglected.

Model output temporal resolution is often limited by disk storage constraints; for these cases, Eq. (4.1) is typically integrated using a considerably smaller timestep to minimize numerical truncation errors. Temporal interpolation of the gridded wind field to the computational times has been shown to be a significant trajectory error source (Kuo et al. 1985; Rössler et al. 1992; Stohl et al. 1995; Dahl et al. 2012).[8] For example, Dahl et al. (2012) simulated a supercell thunderstorm using the Bryan Cloud Model 1 (CM1) and generated forward "truth" trajectories during model run-time that passed through the near-surface mesocyclone. They ran backward trajectories from the forward trajectory end-points using varying model output time intervals and found that applying linear time interpolation (LI) to the confluent, nonlinearly evolving flow resulted in fictitious low-level inflow trajectories for the temporally coarser input data. Trajectory models have traditionally used LI to estimate $\mathbf{u}(\mathbf{x},t)$ from gridded input (Bowman et al. 2013). This method should be well suited for any velocity field with an approximately linear evolution between sampling times.

Shapiro et al. (2015, hereafter S15) tested an alternative time interpolation technique using advection correction (AC) on two-dimensional (2D) trajectories run from a high-resolution (30-m) CM1 supercell simulation. AC algorithms have been extensively used in

[8] Other sources of trajectory error include the spatial interpolation of the gridded winds, numerical truncation errors accumulated from integrating Eq. (4.1), and inaccuracies in the gridded input winds themselves.

Doppler radar data processing when an analysis reflectivity or wind field must be constructed from nonsimultaneous beam scan observations; they essentially re-define the observations in a reference frame moving with the pattern translation velocity (Gal-Chen 1982, hereafter GC82; Zhang and Gal-Chen 1996; Dowell and Bluestein 2002; Shapiro et al. 2010). Let us now illustrate, in a simple example, how AC can be applied to the time interpolation of the vertical velocity field; this concept can be extended to any scalar or Cartesian velocity vector component translating through three-dimensional (3D) space at constant velocity. Consider a wavelike updraft pattern $w(x, t)$ moving in the positive-x direction with a speed U (m s^{-1}), as shown in Fig. 4.1; w is perfectly resolved in space but not in time. Suppose that w can be sampled at data input times $t = t_0$ and $t = t_0 + \Delta t$, and we wish to find $w(p, t_0 + \Delta t/2)$ for $x = p$. Although the updraft peak passes p at time $t = t_0 + \Delta t/2$, it is displaced away from p at both data input times, and hence LI between $w(p, t_0)$ and $w(p, t_0 + \Delta t)$ yields an erroneously low estimate. Let us now re-define p in a reference frame moving with velocity U that is co-located with the fixed frame only for $t = t_0 + \Delta t/2$. For times $t = t_0$ and $t = t_0 + \Delta t$, the positions of p in the fixed reference frame, p_{t0} and $p_{t0+\Delta t}$ respectively, are

$$p_{t0} = p - U\Delta t/2 \qquad (4.2a)$$

$$p_{t0+\Delta t} = p + U\Delta t/2. \qquad (4.2b)$$

For this simple case, $Dw/Dt = 0$, and therefore $w(p, t_0 + \Delta t/2)$ is exactly equivalent to both $w(p_{t0}, t_0)$ and $w(p_{t0+\Delta t}, t_0 + \Delta t)$. On the other hand, if the waveform were to grow or decay, LI between $w(p_{t0}, t_0)$ and $w(p_{t0+\Delta t}, t_0 + \Delta t)$ could still improve the estimate of $w(p, t_0 + \Delta t/2)$ compared to LI from $x = p$, provided that the waveform retains its general shape. Herein

LI will refer to linear time interpolation in the traditional sense, i.e., with no advection correction of the fixed frame coordinate position.

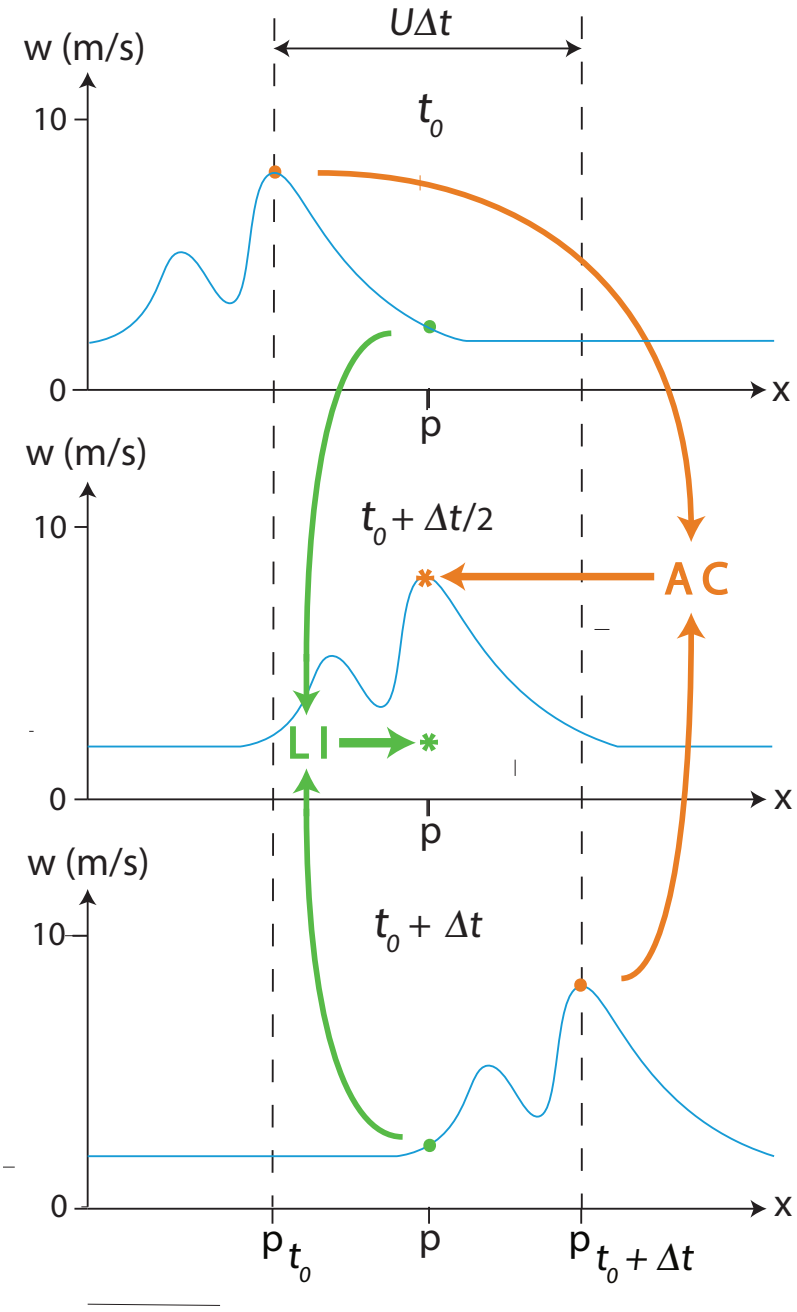

Figure 4.1 Illustration of the advection correction principle for an updraft waveform $w(x,t)$ translating in the positive-x direction with velocity U. For $x = p$, the waveform amplitude at time $t = t_0 + \Delta t / 2$ is estimated by temporal interpolation between data input times $t = t_0$ and $t = t_0 + \Delta t$. Simple linear interpolation (LI) in time from $x = p$ in the fixed reference frame substantially underestimates w, whereas advection correction (AC) time interpolation from $x = p'$ in the reference frame translating with velocity U yields the true w amplitude.

S15 found that advection-correcting the 2D wind field improved the accuracy of most trajectories in their samples, relative to LI. However, they cautioned that defining the pattern translation velocities for realistic atmospheric flows could be a nontrivial task. According to the "frozen turbulence hypothesis" (Taylor 1938), a two-dimensional fluid vector field (u, v) may be idealized in terms of a complex turbulent pattern (u', v') that retains its shape over sufficiently short time intervals while translating with an "advective" flow vector (U, V). Recognizing that many atmospheric features have advective flow patterns with spatiotemporal variation, S15 divided their model output domain into a checkerboard pattern of non-overlapping "subdomains" and defined U and V for each subdomain and model output time interval. They tested two methods for determining the advective flows: (i) averaging the model-output winds over the subdomain, and (ii) using an "iterative Gal-Chen procedure" developed by GC82 that yielded an advection-corrected u field with the smallest departure from Lagrangian conservation following U and V. The latter method minimized a cost function that penalized deviations from the frozen turbulence constraint, yielding linear equations for U and V in terms of local u gradients and time tendencies integrated over the subdomain. AC using U and V determined by this method yielded the most accurate trajectories. S15 also showed how the iterative Gal-Chen procedure could converge on spurious U and V solutions if the input data temporal resolution became too coarse.

The major objective of this chapter is to assess the utility of AC in reducing time interpolation errors for trajectories computed from TC simulation output. To accomplish this, we extend the 2D AC algorithm developed by S15 to 3D. Unlike S15, we define the advection velocities in cylindrical coordinates (r, λ, z), where r, λ, and z are radius,

azimuthal angle, and height; this is a convenient framework for analyzing the swirling wind circulations of TCs. Radial velocity $u_r = \mathrm{d}r/\mathrm{d}t$ and angular velocity $\omega = \mathrm{d}\lambda/\mathrm{d}t$ can be expressed as

$$u_r = U_r + u_r' \tag{4.3a}$$

$$\omega = \Omega + \omega', \tag{4.3b}$$

where capital letters and primes denote advective and perturbation components, respectively. Here, advective flows are defined over non-overlapping subdomains on the computational grid for every model output time interval. We evaluate how AC impacts trajectory accuracy with U_r and Ω determined by either (i) a gridpoint spatiotemporal average over each subdomain or (ii) a modified version of the S15 iterative Gal-Chen procedure that solves for the advective flows U_r and Ω based on the absolute angular momentum (AAM) conservation principle. For axisymmetric TCs, it is well established that AAM, defined in terms of radius r measured from the vortex center, tangential wind $v_t = \omega r$, and Coriolis parameter f

$$\mathrm{AAM} = r(v_t + fr/2), \tag{4.4}$$

is nearly conserved following the flow above the maritime boundary layer (MBL), where friction and diffusion may be neglected (Zhang et al. 2001; Montgomery and Smith 2014; Qin et al. 2018). Here we invoke the additional assumption that the pressure torque $\partial p/\partial \lambda$ (Zhang et al. 2001) is small enough such that AAM can be treated as a "quasi-conserved" variable following 3D flows over sufficiently short time intervals:

$$\frac{D\,AAM}{Dt} = \frac{\partial AAM}{\partial t} + U_r \frac{\partial AAM}{\partial r} + \Omega \frac{\partial AAM}{\partial \lambda} + W \frac{\partial AAM}{\partial z} \approx 0. \tag{4.5}$$

We will test this algorithm on trajectories run from Weather Research and Forecasting - Advanced Research core (WRF-ARW) model simulations of Hurricanes Joaquin (2015) and Wilma (2005).

TC simulations offer a promising testbed for trajectory AC algorithms. Advances in observing systems and high-resolution modeling over the past twenty years have revealed that TC eyewall swirling winds have a rich and complex kinematic structure, with various types of embedded flow disturbances, even for mature, relatively axisymmetric cases. Outbreaks of deep convection, known as hot towers or *convective bursts* (CBs), have been shown to precede or accompany TC intensification episodes (Heymsfield et al. 2001; Guimond et al. 2010; Chen and Zhang 2013; Rogers et al. 2015). A few previous studies have examined TC dynamical processes in a Lagrangian framework. Perhaps Liu et al. (1999) was the first to show the long residence of air parcels in the eye of their MM5-simulated Hurricane Andrew (1992) through forward and backward trajectories that were calculated by interpolating hourly model outputs into 3-min intervals. Using trajectories run from his MM5-simulated Hurricane Bob (1991) outputs at 2-min intervals, Braun (2002) showed that perturbation pressure gradient forces lifted air parcels above the eyewall MBL, with the parcels acquiring thermal buoyancy at higher levels. Cram et al. (2007) studied mixing between the eyewall, eye, and outer regions using trajectories computed from a Hurricane Bonnie (1998) MM5 simulation output at 3-min resolution. Their analysis revealed that while high-equivalent potential temperature (θ_e) air parcels from the low-level eye can be mixed into eyewall updrafts, providing a source of enhanced buoyancy, this sheared TC also experienced a ~ 1 K mean eyewall θ_e reduction due to extensive mixing of low-θ_e parcels from outer regions. Stern and Zhang (2013)

investigated eye warming in an idealized WRF simulation using backward trajectories generated by the RIP4 post-processing software (Stoelinga 2009) from 1-min and 6-min output data. They found that once a threshold intensity of ~ 40 m s^{-1} is reached, stirring between the eye and eyewall becomes reduced to the extent that upper-level parcels originating near the eye center can remain there for several days and descend 5-10 km, even in the presence of moderate VWS. Onderlinde and Nolan (2016) used trajectories computed from 1-min resolution WRF idealized simulation output to show how the faster (slower) intensification rate of a vertically sheared TC with positive (negative) TC-relative environmental helicity resulted in part from a larger (smaller) percentage of boundary layer parcels being lofted into deep convective updrafts in upshear quadrants.

The next section describes the WRF simulation datasets and trajectory computation, AC, and trajectory error diagnostics methods. Section 4.3 shows a series of analytical trajectory tests to make sure that our codes are free of errors. Sections 4.4 and 4.5 compare the impacts of AC and LI on trajectories using the Hurricanes Joaquin (2015) and Wilma (2005) simulations, respectively. A summary and concluding remarks are given in the final section.

4.2 Datasets and methodology

4.2.1 WRF simulation datasets

Hurricane Wilma (2005) underwent a record-breaking 18-hour RI episode on 18-19 Oct that culminated in a peak intensity in terms of P_{MIN} and V_{MAX} of 882 hPa and 82 m s^{-1}, respectively (Pasch et al. 2006; Chen et al. 2011). RI is defined herein by the V_{MAX} intensification exceeding 15 m s^{-1} (24 h) $^{-1}$ (Kaplan and DeMaria 2003). At peak intensity,

Wilma (2005) was also the strongest hurricane ever recorded in the Atlantic basin. Wilma intensified in the western Caribbean under near-ideal environmental conditions with low VWS and high SSTs of 29-30 °C. Chen et al. (2011) simulated this storm using the WRF-ARW model with a quadruply-nested 27/9/3/1 km two-way interactive grid, 55 vertical σ-levels, and a 30-hPa model top. The 1-km nest, with (x,y) grid dimensions of 451 × 451, followed the vortex center. This simulation captured the timing and rate of Wilma's RI reasonably well, and two subsequent papers (Chen and Zhang 2013, hereafter CZ13; Miller et al. 2015) showed how extreme upper-level CB updrafts exceeding 15 m s^{-1} may have contributed to Wilma's RI by directing subsidence warming into the developing upper-level warm core.

Hurricane Joaquin (2015) differed markedly from Wilma (2005), mainly due to its looping track that was poorly forecast by most operational models (Berg 2016; Doyle et al. 2017). The storm began a 60-h RI period on 0600 UTC 29 Sep, with its V_{MAX} increasing from 18 to 61 m s^{-1}. High SSTs exceeding 29 ºC appear to have facilitated the RI, despite moderate northerly VWS. Microwave satellite observations showed an asymmetric inner-core structure throughout Joaquin's early-to-middle RI period. Following RI, Joaquin slowly moved westward through the Bahamas, maintaining its intensity. Around 1800 UTC 02 Oct, soon after beginning its acceleration to the northeast, Joaquin began an 18-h re-intensification, with its V_{MAX} increasing from 57 to 69 m s^{-1}. Thereafter the storm weakened as it encountered lowering SSTs and increasing VWS. Miller and Zhang (2019a) simulated Joaquin with WRF-ARW using a 27/9/3/1 km two-way interactive grid, 55 vertical σ-levels, and a 30-hPa model top. The innermost domain, with (x,y) dimensions of 601 × 601, followed the vortex center. WRF is initialized at RI onset with initial

conditions generated from cycling hybrid data assimilation, and the outer three domains are nudged with a large-scale analysis. Results show that the model reproduces the RI rate and asymmetric inner-core structures reasonably well.

4.2.2 General procedures for trajectory computations

Aside from the AC algorithms, basic numerical elements of our trajectory calculations follow previous studies (Cram et al. 2007; Dahl et al. 2012; S15). The 1-km WRF moving nest from the Wilma (2005) and Joaquin (2015) simulations supplies the input data for all numerically-simulated data trajectories. ARWpost[9] software is used for de-staggering and vertically interpolating WRF-output winds and desired scalars from their native Mercator projection C-grid to a computational A-grid, where scalars and all velocity components are defined at the vertices. The computational grid has a constant horizontal grid cell length $\Delta x = \Delta y = 1000$ m and a vertical resolution Δz set to 250-m (50-m) above (below) z=1 km. Model-output 10-m horizontal winds and $w = 0$ populate the ground level. Lateral boundaries are set to the edges of the de-staggered WRF grid, and the top boundary is set to 20 km. Map scale factors m_x and m_y relate Δx and Δy to their corresponding distances on the spherical Earth surface (Skamarock et al. 2008):

$$m_x = \frac{\Delta_x}{R_e \cos(\phi)|\Delta\lambda|} \tag{4.6a}$$

$$m_y = \frac{\Delta_y}{R_e \Delta\phi}\,, \tag{4.6b}$$

[9] Documentation is for the ARWpost postprocessing package is available at http://www2.mmm.ucar.edu/wrf/users/docs/user_guide_V3.9/users_guide_chap9.htm#_ARWpost_3.

where ϕ and λ are the latitude and longitude in radians, respectively, and R_e is the mean radius of the Earth. To correct for map distortion effects, the WRF-output u and v winds are transformed to the grid-relative winds

$$u_{grid} = u(m_x) \tag{4.7a}$$

$$v_{grid} = v(m_y). \tag{4.7b}$$

Eq. (4.1) is integrated using a second order Runge-Kutta (RK2) scheme (Press et al. 1992) with a 10-s computational time step. The parcel velocity at computational times is estimated from gridded winds at the nearest input times using either LI or AC in time and trilinear interpolation in space. Any parcel arriving at the grid top or lateral boundaries is flagged as having left the domain and its trajectory integration is terminated.

For the two numerically-simulated data cases, an additional complication arises from the fact that the WRF vortex-following nest translates horizontally by several gridpoints between some output times. Prior to trajectory runtime, the grid translation vectors for the x- and y-directions, x_{TRANS} and y_{TRANS} respectively, are determined for every output time interval using the WRF-output latitude and longitude and map scale factors[10]; for output intervals where the domain remains stationary, x_{TRANS} and y_{TRANS} are set to zero. These vectors have units of (number of gridpoints) $\times \Delta x$, with a positive (negative) sign for northward and eastward (southward and westward) domain shifts, in the time direction of model integration. Trajectory calculations are kept in an Earth-relative framework by adding a correction term to Eq. (4.1) that opposes the effect of domain translation on parcel

[10] For both the Wilma (2005) and Joaquin (2015) trajectory integration periods, the 1-km domain moved in increments of 3 grid cells in one or both horizontal directions. This distance corresponds to 1 grid length in the parent nest.

movement. For the i_{th} RK2 iteration, equations for parcel displacement in the respective x- and y-directions, δx_i and δy_i, are

$$\delta x_i = u_{\text{grid},i}\,\delta t - x_{\text{TRANS}}\frac{\delta t}{\Delta t} \tag{4.8a}$$

$$\delta y_i = v_{\text{grid},i}\,\delta t - y_{\text{TRANS}}\frac{\delta t}{\Delta t}, \tag{4.8b}$$

where $u_{\text{grid},i}$ ($v_{\text{grid},i}$) are the local u-winds (v-winds), the computational timestep δt is positive (negative) for forward (backward) trajectories, and Δt is the model output time interval.

4.2.3 Advection correction overview

AC of model-output winds and scalars is performed in the horizontal plane, one vertical level at a time. Our rationale for defining the horizontal advective flows U_r and Ω in cylindrical coordinates is the fact that on the vortex scale, TCs are often analyzed in terms of a swirling quasi-axisymmetric horizontal wind or "primary circulation," and a "secondary circulation" consisting of a low-level inflow, eyewall updraft core, and upper-level outflow (Liu et al. 1999; Montgomery and Smith 2014). Appendix A describes the methods used to determine the vortex center, and Figure 4.2a summarizes the AC algorithm used for numerically-simulated data cases; modifications for the analytical tests will be noted in section 4.3. Prior to running trajectories, the computational grid is divided into non-overlapping horizontal subdomains, and U_r and Ω are computed for each subdomain, one level at a time, for all model output time intervals Δt using either the procedure described in section 4.2.4 or as subdomain-averaged u_r and ω. Each level is divided into concentric annuli that extend outward from the storm center to a specified outer radial boundary; these annuli are further subdivided into arcs. Similar subdomain configurations are used for the two hurricane cases. For Wilma (Joaquin), 2-km (3-km) wide annuli are

subdivided into 24° wide arcs over an AC region extending out to a 60-km (180-km) radius beyond the azimuthal mean radius of maximum wind (RMW) over the z = 0-16 km (z = 0-10 km) layer. Standard LI is used in lieu of AC outside of this region.

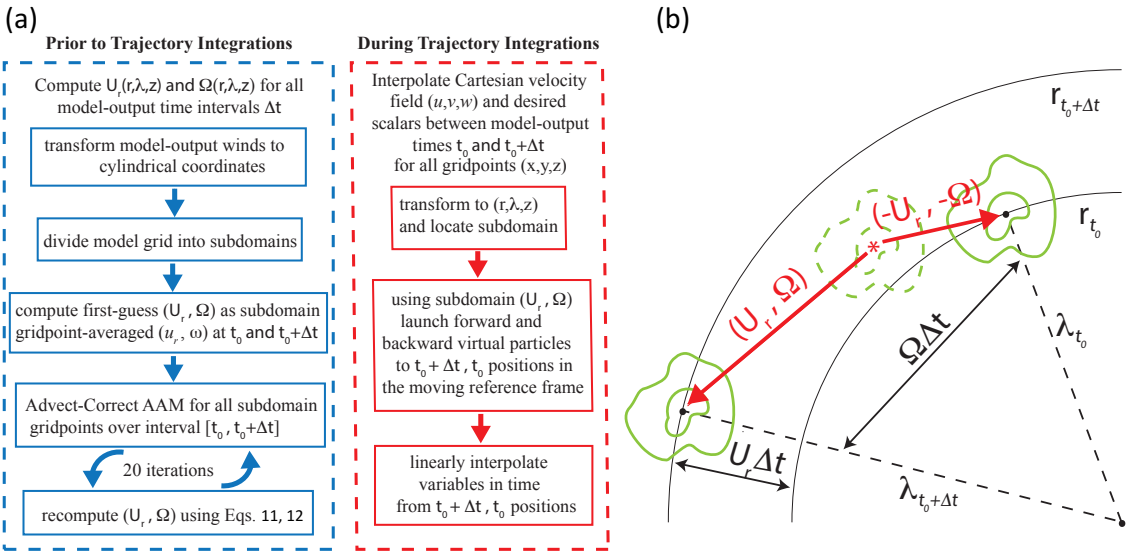

Figure 4.2 (a) Block diagram outlining the keys steps of the advection correction algorithm. (b) Schematic illustrating advection correction in a cylindrical coordinate framework. An updraft element (solid green contours) translates counterclockwise with angular velocity Ω and radially outward with linear velocity U_r between times $t = t_0$ and $t = t_0 + \Delta t$, where its amplitude is known. Assuming Ω and U_r are also known, the updraft amplitude at an arbitrary intermediate time (dashed green contours) can be estimated by launching virtual particles (red arrows) to the moving reference frame coordinates (r',λ') at times $t = t_0$ and $t = t_0 + \Delta t$ and then linearly interpolating the updraft amplitude in time from these two positions.

During trajectory integrations, 3D arrays of Cartesian velocity vector components u, v, w and desired scalars are generated at every computational time by temporally interpolating model data from the nearest output times. Virtual particles (borrowing S15's terminology) are launched backward and forward in time[11] with velocity ($-U_r$, $-\Omega$) and (U_r

[11] Here "time" refers to real, or simulation time, which of course is opposite to the time direction for integrating backward trajectories.

, Ω), respectively, from every gridpoint (x, y, z) within the AC subdomain configuration. They are free to leave their subdomains, and their "landing positions" are the advection-corrected coordinates of (x, y, z) at the nearest model output times (Fig. 4.2b). Model output data are bilinearly interpolated in space to the landing positions; subsequently, data from the landing positions are linearly interpolated in time to yield values for (x, y, z) at the computational time. How reasonable, one may ask, is the assumption that perturbations in 3D flows and thermodynamic variables all maintain their amplitudes as they are advected by a mean flow pattern? For a given trajectory, are there cases where AC of *w* improves accuracy, but AC of *u* and *v* has negative impacts, and vice versa? We shall revisit these questions in sections 4.4 and 4.5 when we compare numerically-simulated data trajectories run using AC of the full Cartesian vector (*u, v, w*) versus the *w*-component only.

4.2.4 Solving for the subdomain advective flows U_r and Ω

Our iterative method for obtaining U_r and Ω on each subdomain closely follows the "iterative Gal-Chen based procedure" used by S15 to solve for their *U* and *V*, but with the following modifications: (i) applying the frozen turbulence constraint to AAM instead of the *u* field; (ii) tracking the pattern advection in cylindrical rather than Cartesian coordinates; and (iii) adding a vertical advection constraint on the solution. Let us define a cost function *J* that penalizes deviations from AAM conservation following the flow (i.e., the condition of D AAM/Dt = 0):

$$J(U_r, \Omega) = \iiint \left(\frac{\partial AAM}{\partial t} + \overline{w} \frac{\overline{\partial AAM}}{\partial z} + U_r \frac{\partial AAM}{\partial r} + \Omega \frac{\partial AAM}{\partial \lambda} \right)^2 r dr d\lambda dt, \qquad (4.9)$$

where the integration extends over all subdomain gridpoints and computational times within the model output interval Δt. U_r and Ω are treated as constants over each subdomain. Here vertical AAM advection is not explicitly solved for but instead treated as a constant

penalty term, parameterized as $\overline{w}\,\overline{\frac{\partial AAM}{\partial z}}$, with overbars denoting subdomain gridpoint averages. Horizontal advections U_r and Ω that minimize *J* can be found by setting $\partial J/\partial U_r$ = 0 and $\partial J/\partial \Omega = 0$ to yield the system of equations

$$\mathrm{A}U_r + \mathrm{B}\Omega = \mathrm{D} \tag{4.10a}$$

$$\mathrm{B}U_r + \mathrm{C}\Omega = \mathrm{E}, \tag{4.10b}$$

where

$$A = \iiint \left(\frac{\partial AAM}{\partial r}\right)^2 r dr d\lambda dt \qquad B = \left(\frac{\partial AAM}{\partial r}\right)\left(\frac{\partial AAM}{\partial \lambda}\right) r dr d\lambda dt$$

$$C = \iiint \left(\frac{\partial AAM}{\partial \lambda}\right)^2 r dr d\lambda dt \quad D = -\iiint \left(\frac{\partial AAM}{\partial t} + \overline{w}\,\overline{\frac{\partial AAM}{\partial z}}\right)\left(\frac{\partial AAM}{\partial r}\right) r dr d\lambda dt$$

$$E = -\iiint \left(\frac{\partial AAM}{\partial t} + \overline{w}\,\overline{\frac{\partial AAM}{\partial z}}\right)\left(\frac{\partial AAM}{\partial \lambda}\right) r dr d\lambda dt, \tag{4.11}$$

with all integrations being performed over the subdomain and Δ*t*.

The equations for U_r and Ω then become

$$U_r = \frac{CD - EB}{AC - B^2} \text{ and } \Omega = \frac{AE - BD}{AC - B^2} \tag{4.12}$$

Taking the second derivatives $\partial^2 J/\partial {U_r}^2$, $\partial^2 J/\partial \Omega^2$, and $\partial^2 J/\partial U_r \partial \Omega$, and invoking the second derivative test (Stewart 1999, p. 974) with the Cauchy-Schwarz-Buniakowski inequality for integrals (Gradshteyn and Ryzhik 2007, p. 1064) reveals that the solution corresponds to a minimum (rather than a maximum) in *J*.

Following GC82 and S15, we minimize *J* iteratively. The procedure is initialized with "first-guess" advections, which are set to the subdomain-averaged u_r and ω. They define the velocities of the virtual particles used for temporally interpolating the model-output AAM field to all computational timesteps spanning Δ*t*, as described in the preceding subsection. Integrals *A*-*E* in Eq. (4.11) are then computed from the advection-corrected

AAM field, and U_r and Ω are updated using Eq. (4.12). This cycle is run for 20 iterations, and the code is flagged for instances of nonconvergence, defined here as either $\Delta U_r \geq 0.1$ m s^{-1} or $\Delta\Omega \geq 0.001$ ° s^{-1} between the 19th and 20th iterations. We forego this iterative procedure for the boundary layer (z < 1 km) subdomains where large departures from AAM material conservation can be expected due to friction. Here, the advective flows are set to the subdomain-averaged first guesses, and they are blended with the z = 1 km Gal-Chen advections over the upper portion.

Unfortunately, solution uniqueness for U_r and Ω cannot be guaranteed. Shapiro et al. (2010) and S15 showed how this problem is inherent to any Gal-Chen based procedure used in determining advective flows from scalar fields available at discrete input times. Although the partial derivatives $\frac{\partial AAM}{\partial t}$, $\frac{\partial AAM}{\partial r}$, and $\frac{\partial AAM}{\partial \lambda}$ are treated as constants when differentiating Eq. (4.9) with respect to U_r and Ω, they are actually implicit functions of the advective flows, causing Eqs. (4.10a,b) to become nonlinear. Shapiro et al. (2010) showed analytically how an infinite family of U solutions could be retrieved by a Gal-Chen based procedure for a wave pattern translating with constant velocity U_{true}, with the nearest spurious solutions moving closer to U_{true} as the data input time interval increases. S15 found a similar result in their numerically-simulated data tests, although they also found that choosing reasonable first-guess U and V values reduced the likelihood of convergence to spurious solutions. Solution nonuniqueness will be explored herein in sections 4.3 and 4.4.

4.2.5 Calculation of trajectory errors

Trajectory errors are quantified in terms of position differences from LI "reference trajectories" seeded from the same locations and model output times and run using higher-temporal resolution input data. Horizontal and vertical position errors are defined

separately due to the fact that TC vertical length scales are ~*O*(10 km) smaller than horizontal length scales. Borrowing the S15 notation, the horizontal individual displacement error (IDE_{HORIZ}) for trajectory *i* is defined as

$$IDE^{i}_{HORIZ,\,EXP} = \sqrt{\left(x^{i}_{EXP} - x^{i}_{R}\right)^{2} + \left(y^{i}_{EXP} - y^{i}_{R}\right)^{2}}, \tag{4.13}$$

where endpoint position (x, y) is evaluated at a specified integration time and subscripts EXP and R denote the experiment, either LI or AC, and reference trajectory, respectively. Likewise, we may define a vertical individual displacement error (IDE_{VERT})

$$IDE^{i}_{VERT,EXP} = |z^{i}_{EXP} - z^{i}_{R}| \tag{4.14}$$

at endpoint position z. The impacts of AC are measured in terms of the change in horizontal and vertical position errors when a sample of LI trajectories is re-run from the same temporal input resolution using AC. Differenced horizontal individual displacement errors (ΔIDE_{HORIZ}) and vertical individual displacement errors (ΔIDE_{VERT}) are defined for trajectory *i* as

$$\Delta IDE^{i}_{HORIZ} = IDE^{i}_{HORIZ,LI} - IDE^{i}_{HORIZ,AC} \tag{4.15}$$

and

$$\Delta IDE^{i}_{VERT} = IDE^{i}_{VERT,LI} - IDE^{i}_{VERT,AC}\,. \tag{4.16}$$

Therefore, a positive (negative) ΔIDE_{HORIZ} indicates reduced (increased) horizontal position errors for trajectory *i*, relative to the reference trajectory, when AC is used in lieu of LI; likewise for ΔIDE_{VERT} and vertical position errors.

4.3 Analytical tests of trajectory computation

Our first analytical test runs LI trajectories on a steady-state flow field in order to verify that the RK2 time integration and trilinear interpolation modules are functioning properly. The computational grids have (x, y, z) dimensions of 121 × 121 × 41, with horizontal and vertical lengths set to $\Delta x = \Delta y = 1$ km and $\Delta z = 0.25$ km, respectively. Horizontal flows are invariant with height, and they are based on the Taylor-Green (1937) vortex initial conditions, in which

$$u(x, y) = V_{max} \sin\left(\frac{\pi x}{L}\right) \cos\left(\frac{\pi y}{L}\right) \tag{4.17}$$

and

$$v(x, y) = -V_{max} \cos\left(\frac{\pi x}{L}\right) \sin\left(\frac{\pi y}{L}\right), \tag{4.18}$$

where V_{max} = 100 m s^{-1} and L = 120 km. Horizontal components of this inviscid and incompressible flow field can be described by a streamfunction ψ, where $u = \partial\psi/\partial y$ and $v = -\partial\psi/\partial x$:

$$\psi(x, y) = \frac{V_{max} L}{\pi} \sin\left(\frac{\pi x}{L}\right) \sin\left(\frac{\pi y}{L}\right). \tag{4.19}$$

The horizontally uniform vertical velocity field is defined by $w(z) = kz$, with k = 0.001 s^{-1}. A batch of 984 backward trajectories is seeded in a concentric circular pattern[12] from the z = 9 km level and run for 30 min, and selected horizontal projections are shown in Fig. 4.3a, superimposed upon the horizontal flow field. Since the horizontal winds are steady-state, trajectories should follow contours of ψ. Visual inspection of Fig. 4.3a suggests that trajectories are closely following streamlines, and deviations of ψ from its initial value

[12] Trajectories are seeded at 15° azimuthal intervals for every radius between r = 10 km and r = 50 km.

along all trajectories run are found to be less than 0.02% (not shown). Backward trajectory height-versus-time traces follow the function $z = z_0 e^{-kt}$ with z_0 = 9 km (not shown) - this is the exact solution to the differential equation for parcel height along all backward trajectories.

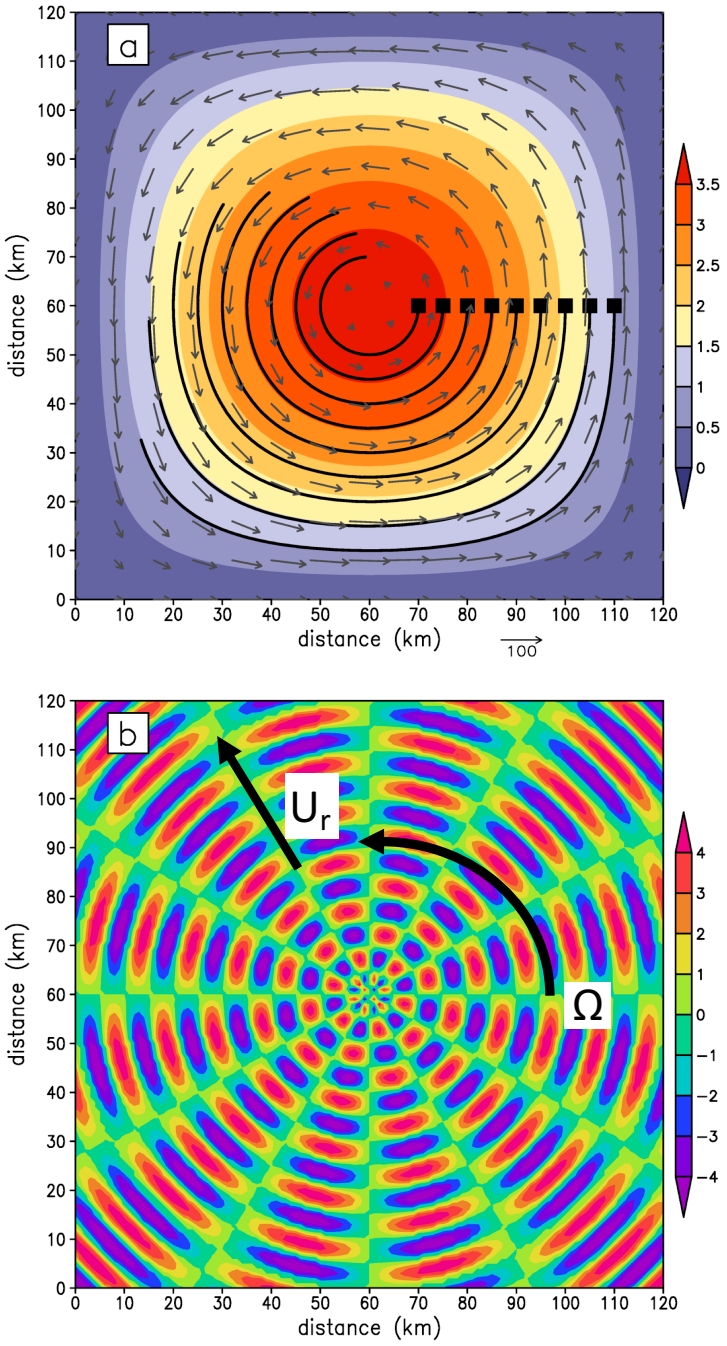

← **Figure 4.3** (a) Horizontal flow field used for the analytical tests, with streamfunction (shaded, $\times 10^{-3}$ m^2 s^{-1}) and flow vectors (m s^{-1}). Representative 30-m backward trajectories for the first analytical test are shown in black, with squares denoting their seeded initial positions. (b) Horizontal variation of vertical motion at the initial time (shaded, m s^{-1}) used for the second analytical test. This vertical motion pattern translates azimuthally counterclockwise and radially outward over time, as shown by the black arrows.

The second test is designed to verify that the AC algorithms are free of code errors. It uses the same computational grid and horizontal flows employed for the first test, but with the steady-state $w = kz$ field replaced with a horizontally-varying pattern (Fig. 4.3b) that rotates cyclonically and translates radially outward. We keep w constant with height. In cylindrical coordinates, it can be expressed as

$$w(r, \lambda, t) = w_{max} \sin\left(2\pi \frac{\lambda - \Omega t}{L_\lambda}\right) \sin\left(2\pi \frac{r - U_r t}{L_r}\right), \qquad (4.20)$$

with azimuthal angle λ measured counterclockwise from the positive x axis, radius r measured from the domain center, and parameters $w_{max} = 5$ m s^{-1}, $L_\lambda = 60°$, $L_r = 10{,}000$ m, $\Omega = 0.1°$ s^{-1}, and $U_r = 8.33$ m s^{-1}. Using the product rule, Eq. (4.20) can be shown to satisfy $\frac{\partial w}{\partial t} + U_r \frac{\partial w}{\partial r} + \Omega \frac{\partial w}{\partial \lambda} = 0$; thus, w is conserved for a parcel following the advection flow vector (U_r, Ω). The 984 30-min backward trajectories from the first test are re-launched from $z = 5$ km, using both LI and AC, on flows with varying temporal resolution Δt: 5 min, 2.5 min, 1 min, and 30 s. The 30-s LI experiment supplies the "reference trajectories." AC is applied to the w-field only. For AC experiments, each level is divided into subdomain arcs with (r, λ) resolutions of 4-km × 30°. Since w is conserved following the advective flow by design, we replace AAM in Eqs. (4.9) and (4.11) with w when solving for U_r and Ω. The AC algorithm otherwise follows the one described in sections 4.2.3 and 4.2.4.

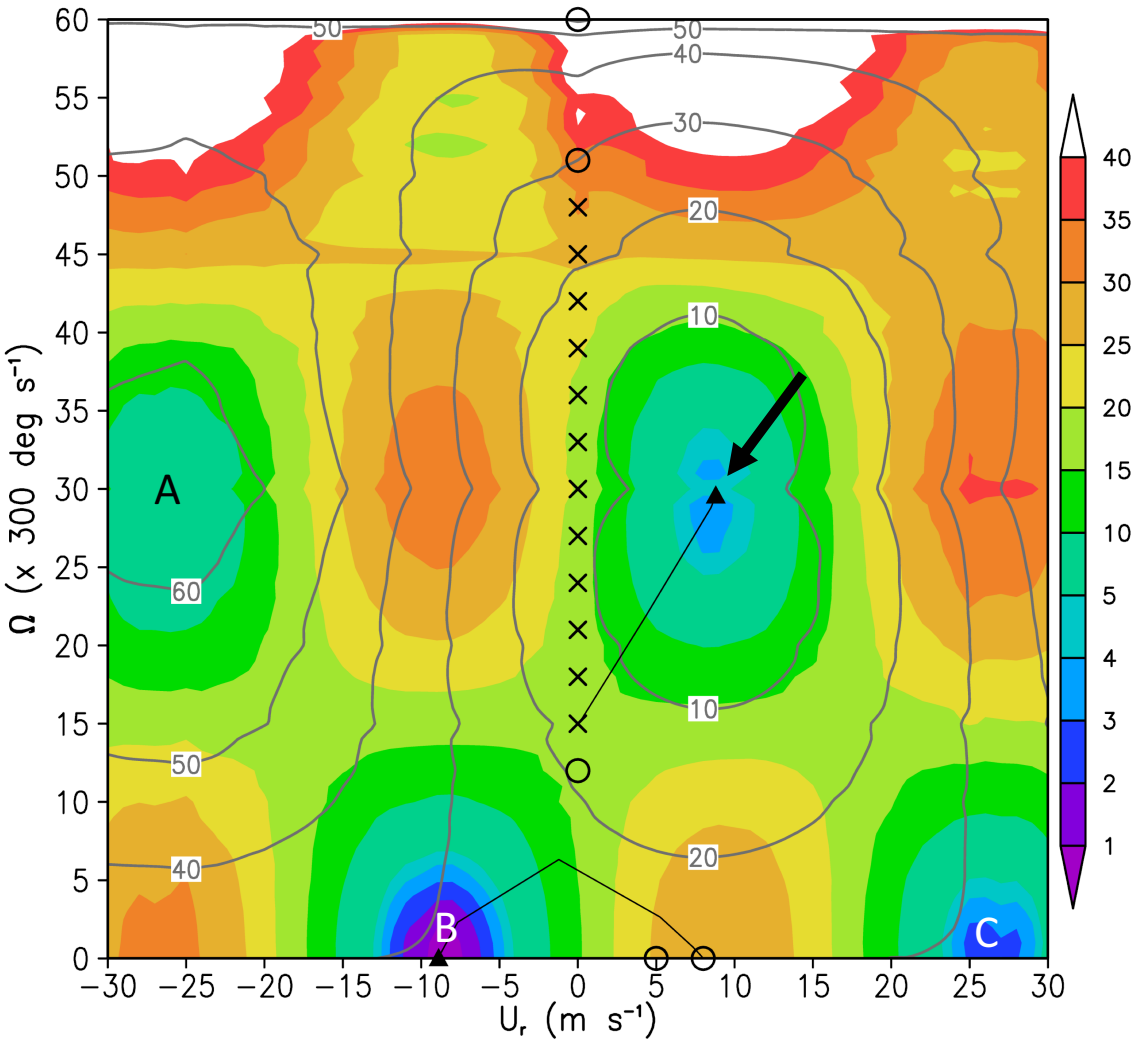

Figure 4.4 Cost function $J(U_r, \Omega)$ (shaded, $m^4 s^{-3} \times 1.8/\pi \times 10^5$) evaluated for a selected subdomain on the analytical flow field shown in Fig. 4.3b for the 5-min data input interval (shaded) and the 2.5-min data input interval (gray contours) ending at t = 30 min. To compute J, Eq. 4.9 is solved using a range of input U_r and Ω values, with AAM replaced by w. Black arrow points to the local minimum corresponding to the true advective flows (i.e. $U_r = 8.33$ m s^{-1}, $\Omega = 0.1$ deg s^{-1}). Letters A, B, and C label spurious local minima (see text). Black ×-symbols (open circles) show first-guess (U_r, Ω) combinations that converged to values close to the true advective flows (converged to spurious solutions) using the iterative Gal-Chen procedure with 5-min input data. Black line segments connect intermediate (U_r, Ω) solutions found over the 20 iterations leading to the final (U_r, Ω) solution, denoted by black triangles, for two selected first-guesses.

Before examining trajectory errors, let us first verify that the iterative Gal-Chen based procedure can converge upon the true Ω and U_r, given different first-guess values.

Figure 4.4 shows the cost function $J(U_r, \Omega)$ computed by "brute force" for a selected subdomain from the 5-min output data for a range of U_r and Ω inputs. For each U_r and Ω pair, the subdomain w-field is advection-corrected over a Δt = 5-min period using a 10-s computational timestep, and then Eq. (4.9) is evaluated. As expected, a local minimum can be found for the "true" advections (U_r = 8.33 m s^{-1}, Ω = 0.1° s^{-1}). Note, however, the regularly-spaced pattern of additional local minima A, B, and C located at ($U_r \sim$ -25.0 m s^{-1}, $\Omega \sim 0.1°$ s^{-1}), ($U_r \sim$ -9.0 m s^{-1}, $\Omega \sim 0.0°$ s^{-1}), and ($U_r \sim$ 26.0 m s^{-1}, $\Omega \sim 0.0°$ s^{-1}), respectively; this is consistent with J being nonunique in U_r and Ω, as discussed in section 4.2.4. To understand the physical basis for these spurious minima, consider $w(r, \lambda, t)$ at two data input times $t = 0$ and $t = T$, denoted by w_0 and w_T, respectively:

$$w_0 = w_{max} \sin\left(2\pi \frac{\lambda}{L_\lambda}\right) \sin\left(2\pi \frac{r}{L_r}\right) \qquad (4.21a)$$

$$w_T = w_{max} \sin\left(2\pi \frac{\lambda - \Omega_{true} T}{L_\lambda}\right) \sin\left(2\pi \frac{r - U_{r,true} T}{L_r}\right), \qquad (4.21b)$$

where Ω_{true} and $U_{r,true}$ represent the true advection velocities. Due to $w(r, \lambda, t)$ being doubly periodic in r and λ (Fig. 4.3b), Eqs. 4.21(a,b) can also be satisfied by any w_T phase-shifted by integer multiples of (i) one wavelength in either r or λ or (ii) one-half wavelength in both r and λ. Thus, Ω_{true} and $U_{r,true}$ may be replaced with two families of infinite solutions:

$$U_r = U_{r,true} + \frac{m_1 L_r}{T},\ m_1 = 0, \pm 1, 2, 3, \ldots$$

$$\Omega = \Omega_{true} + \frac{m_2 L_\lambda}{T},\ m_2 = 0, \pm 1, 2, 3, \ldots \qquad (4.22),$$

and

$$U_r = U_{r,true} + \frac{n_1 L_r}{T},\ n_1 = \pm \frac{1}{2}, \frac{3}{2}, \frac{5}{2}, \ldots$$

$$\Omega = \Omega_{true} + \frac{n_2 L_\lambda}{T},\ n_2 = \pm n_1 \pm 0, 1, 2, \ldots \qquad (4.23).$$

Local minima A, B, and C from Fig. 4 are close to the Eq. (4.22) ($m_1 = -1$; $m_2 = 0$), Eq. (4.23) ($n_1 = -\frac{1}{2}$; $n_2 = -\frac{1}{2}$), and Eq. (4.23) ($n_1 = +\frac{1}{2}$; $n_2 = -\frac{1}{2}$) solutions, respectively, for $T = 300$ s. Eqs. (4.22) and (4.23) show how the spurious solutions become more distant from ($U_{r,\text{true}}$, Ω_{true}) as the data input interval T decreases. Thus, only the local minimum ($U_{r,\text{true}}$, Ω_{true}) remains over the input (U_r, Ω) range shown in Fig. 4.4, when Δt is reduced to 2.5 min. The iterative Gal-Chen solver initialized with a range of first-guess (U_r, Ω) pairs converges on ($U_{r,\text{true}}$, Ω_{true}) as long as the first-guesses are closer to ($U_{r,\text{true}}$, Ω_{true}) than to any of the spurious nodes (Fig. 4.4).

Figure 4.5a shows traces of $w(r, \lambda, t)$ interpolated along a representative trajectory using LI and AC over a range of Δt. All AC experiments use the iterative Gal-Chen procedure initialized with $U_r = 0$ m s^{-1} and $\Omega = 0.06°$ s^{-1}. LI estimates move increasingly far from the reference trajectory trace within data input intervals as Δt increases, with w errors growing as large as 3 m s^{-1} for $\Delta t = 5$ min; AC estimates, on the other hand, remain close to the reference solution, even for coarser Δt. Figure 4.5b compares the growth of $\text{IDE}^i_{\text{VERT,LI}}$ and $\text{IDE}^i_{\text{VERT,AC}}$ along all 984 backward trajectories for the different Δt experiments. A substantial spread in $\text{IDE}^i_{\text{VERT,LI}}$ among the trajectories develops over time for the coarser data input intervals ($\Delta t = 2.5$ min and 5 min), as indicated by orange and magenta lines in Fig. 4.5b; this reflects the fact that w, translating with tangential velocity Ωr, becomes locally less stationary in time with increasing radius and hence LI becomes an increasingly poorer w-estimator for large radii.[13] Applying AC in lieu of LI reduces the

[13] Recall that the backward trajectories follow the steady-state horizontal traces shown in Fig. 4.3a. Therefore, each of them remains at a nearly constant radius, although they are seeded over a large radial range.

2.5-min and 5-min $IDE^{i}_{VERT,LI}$ by up to an order of magnitude, as shown by green and blue colored lines in Fig. 4.5b.

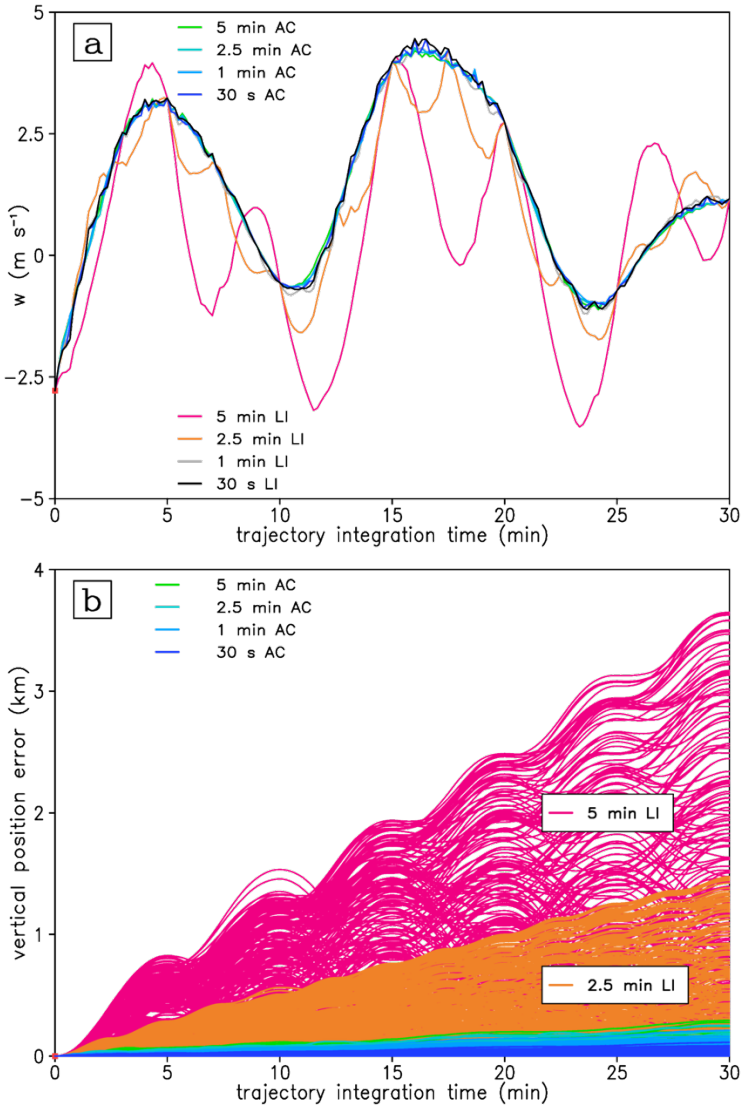

Figure 4.5 Results of the second analytical test showing (a) vertical velocity along a representative backward trajectory, with linear interpolation (LI) and advection correction (AC) time interpolation methods both tested for 5-m, 2.5-m, 1-m, and 30-s data input times and (b) individual height displacement errors as a function of time along all 984 backward trajectories from the experiments shown in (a). The 1-m LI trajectory error growth pattern (not shown here) closely resembles that of the 5-m AC trajectories. Reference trajectories are computed from the 30-s input data using LI.

Results of the analytical tests described above suggest that the major components of our trajectory model can function properly when applied to a simple flow field containing perturbations that are perfectly conserved while translating through space. In the next section, we must determine whether AC can reduce trajectory errors for realistic TC flows, given several potential pitfalls that may become more problematic with coarser input data resolutions. They include the validity of the frozen-turbulence hypothesis and the potential for the iterative Gal-Chen procedure to retrieve spurious (U_r, Ω) solutions.

4.4 Hurricane Joaquin (2015) tests

The Hurricane Joaquin (2015) WRF simulation is output at 5-min and 1-min temporal resolutions for the forecast period 24:00-28:00 (hh:mm denotes hours and minutes). During this period, the Category 1 hurricane is undergoing RI while the inner-core radar reflectivity structure remains relatively asymmetric, with the strongest convection in the southeastern eyewall (see Figs. 2.5c,d). Each experiment runs 4-h backward trajectories from every gridpoint over a 100 km × 100 km horizontal section of the inner core at z = 6 km height and time 28:00 (10,201 total). Table 4.1 summarizes the three AC implementations run from 5-min output that are tested against LI from 5-min output (hereafter LI-5). Both AC_W and AC_{UVW} solve for U_r and Ω using the iterative Gal-Chen based procedure described in section 4.2.4; AC_W advection-corrects only vertical velocity, using LI for horizontal winds, while AC_{UVW} advection-corrects the full 3D velocity vector (u, v, w). AC-MW_{UVW} modifies AC_{UVW} by setting U_r and Ω to the subdomain-averaged "first-guess" radial and angular velocities. Error statistics are

computed after 2 h of backward integration using reference LI trajectories run from the 1-min output data (hereafter LI-1).

Table 4.1 Advection correction experiments

Name	Wind Vector Components Interpolated	Procedure for Finding U_r and Ω
AC_W	w	iterative Gal-Chen
AC_{UVW}	u, v, w	iterative Gal-Chen
AC-MW_{UVW}	u, v, w	use subdomain-averaged flows

4.4.1 Trajectory error statistics

Figure 4.6 plots ΔIDE_{HORIZ} and ΔIDE_{VERT} as a function of trajectory seed position for the AC_W and AC_{UVW} experiments. Note that ΔIDE_{HORIZ} and ΔIDE_{VERT} measure the change in horizontal and vertical 2-h position errors, respectively, for the i^{th} LI-5 trajectory when it is re-run using AC, with positive (negative) values indicating improved (worsened) accuracy relative to the i^{th} reference LI-1 trajectory. As expected, replacing LI-5 with AC_W primarily impacts trajectory accuracy in regions where the vertical motion field is highly variable in space (Figs. 4.6a,b) and nonstationary in time (not shown): namely, near and downstream of larger-scale ascent in the eastern eyewall and in portions of the outer circulation. The AC_W ΔIDE_{HORIZ} and ΔIDE_{VERT} patterns show some spatial correlation, which is not surprising, given that parcel vertical velocity corrections should lead to horizontal position corrections in this vertically sheared tangential wind circulation (not shown). Although AC_W has some positive impact around the edges of the southeastern eyewall updraft core, it degrades a substantial percentage of the LI-5 trajectories seeded from the northeast eye-eyewall interface region. By contrast, AC_{UVW} reduces LI-5 errors over a larger portion of the sample, as evident in the more widespread blue shading, and it performs particularly well in the inner northeast eyewall (Figs. 4.6c,d). For example, consider the boxed area where AC_{UVW} reduces many LI-5 horizontal (vertical) trajectory

errors by > 30 km (> 3 km). Many backward trajectories seeded in this box originate from the boundary layer via eyewall ascent, as well as from the outer environment via a descending mid-to-upper-level inflow channel (Fig. 4.7). Confluent flows present a challenging scenario for backward trajectory calculations, where relatively small uncertainties in the local wind estimation can lead to large position errors (Dahl et al. 2012).

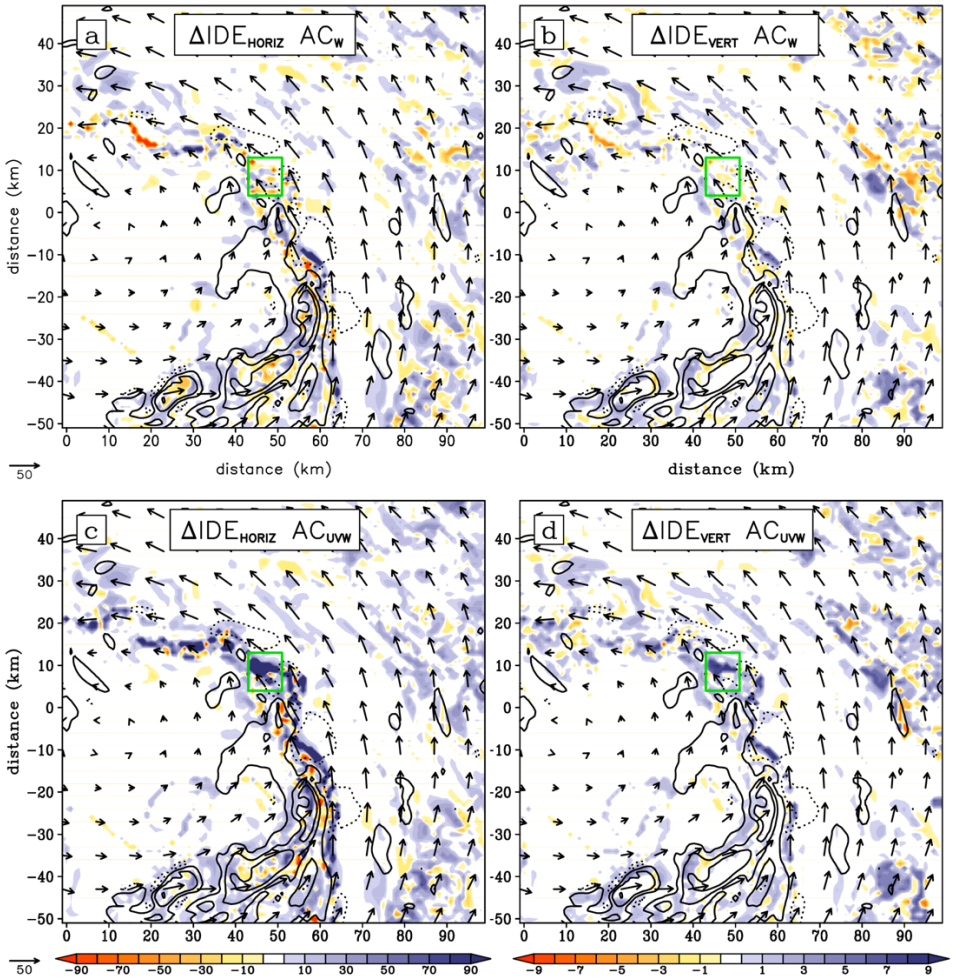

Figure 4.6 Distribution of vertical velocity (black-solid contours at 1/5/10 m s^{-1}; black-dotted contours at -2 m s^{-1}) and horizontal storm-relative flow vectors (m s^{-1}) taken from the WRF-simulated Hurricane Joaquin (2015) 1-km resolution domain at z = 6 km and t = 28:00. Four-hour backward trajectories are seeded from this time at every 1-km gridpoint, for a total of 10201 trajectories. (a) Differenced 2-h horizontal individual displacement errors (ΔIDE_{HORIZ}) (shaded, every 10 km except every 5 km for $|\Delta IDE_{HORIZ}| < 10$ km) plotted as a function of seed position for AC_W. (b) As in (a) but for differenced vertical individual displacement errors (ΔIDE_{VERT}) (shaded, every 1 km except every 0.5 km for $|\Delta IDE_{VERT}| < 1$ km). (c),(d) As in (a) and (b), respectively, but for the AC_{UVW} experiment. Horizontal distances shown here and for all subsequent figures, unless otherwise noted, are measured in km from the domain center, with negative values for regions south and west of the domain center.

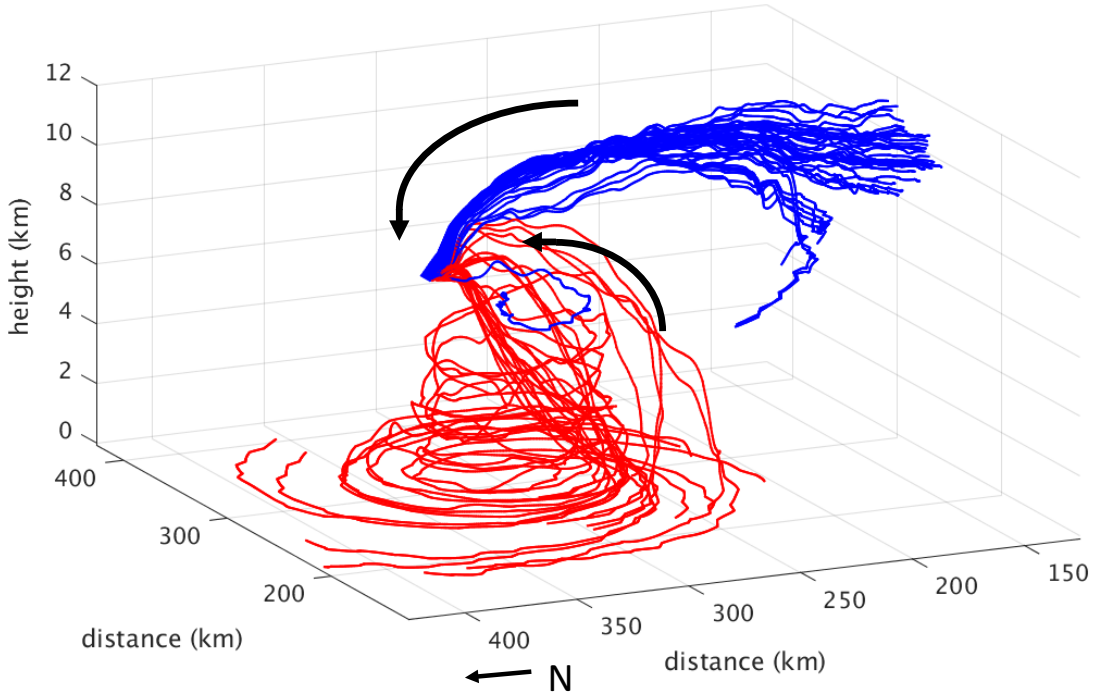

Figure 4.7 Three-dimensional 4-h backward trajectories computed from the Hurricane Joaquin (2015) WRF simulation 5-min output using advection correction of the horizontal and vertical velocity fields (AC_{UVW}). All trajectories shown here are seeded at z = 6 km, forecast hour 28:00, and they are selected from within the rectangular region shown in Fig. 4.6. They are stratified by final (i.e. forecast hour 24:00) height, with red colors showing trajectories originating below z = 1 km (23 total) and blue colors showing trajectories originating from above z = 6 km (40 total). Black arrows highlight the convergent flowpaths of the two backward trajectory clusters. Horizontal distances are measured from the 1-km domain southwest corner.

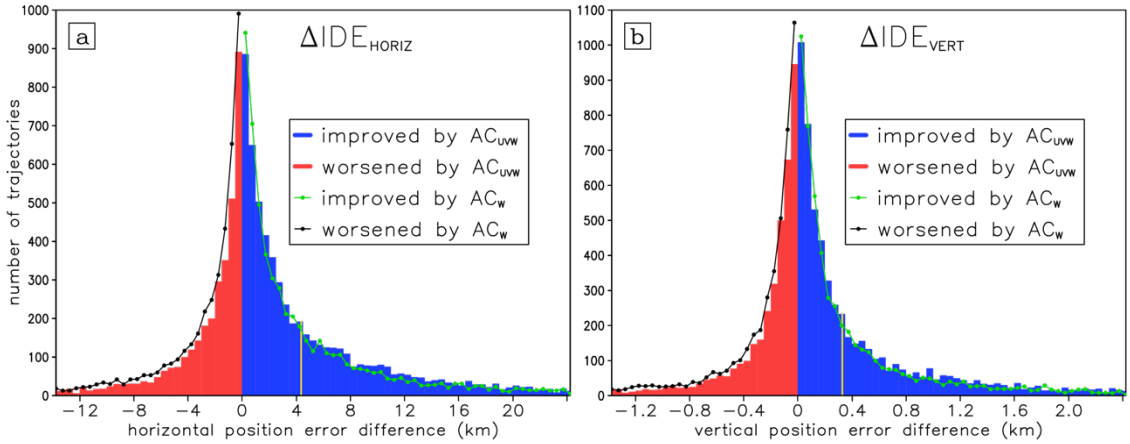

Figure 4.8 (a) Histogram of Differenced horizontal individual displacement errors (ΔIDE_{HORIZ}) for the 10,201 AC_{UVW} trajectories, using a 0.25-km bin width. Blue (red) bars show trajectories with improved (worsened) accuracy, as measured by a reduced (increased) IDE_{HORIZ} compared to the same trajectories run from the 5-m model output using LI. Lines connect the histogram bin heights for the 10,201 AC_W trajectories, with green (black) denoting improved (worsened) accuracy. (b) As in (a) but for ΔIDE_{VERT}. Yellow vertical lines denote the sample mean values.

These results are supported by histograms of ΔIDE_{HORIZ}, given in Fig. 4.8a, which show a rightward (positive) shift in the AC_{UVW} distribution relative to AC_W. The ΔIDE_{VERT} distribution differs less between the two experiments; however, AC_{UVW} overwhelmingly outperforms AC_W for the extreme distribution tails ($|\Delta IDE_{VERT}| > 1$ km) not shown on these histograms (cf. Figs. 4.6b,d and 4.8b). By replacing AC_W with AC_{UVW}, the mean ΔIDE_{HORIZ} increases from 1.42 to 4.44 km, and the number of trajectories with $\Delta IDE_{HORIZ} > 10$ km increases from 1030 to 1581 (Table 4.2). Interestingly, AC-MW_{UVW} slightly outperforms AC_{UVW} in these statistics; similar trends can be found for ΔIDE_{VERT} (Table 4.2).

Table 4.2 Summary statistics for the AC_W, AC_{UVW}, and AC-MW_{UVW} experiments using the Hurricane Joaquin (2015) simulation dataset. Italicized values highlight the experiment with the most improved trajectory accuracy for each statistic.

	ΔIDE_{HORIZ}			ΔIDE_{VERT}		
Statistic	AC_W	AC_{UVW}	AC-MW_{UVW}	AC_W	AC_{UVW}	AC-MW_{UVW}
Mean ΔIDE (km)	1.42	4.44	*4.97*	0.11	0.33	*0.39*
% Left-Tail[14]	5.3	4.0	*3.8*	5.4	*3.6*	*3.6*
% Right-Tail[15]	10.1	15.5	*16.2*	8.7	13.1	*13.9*

4.4.2 Evaluation of the iterative U_r and Ω solver

Let us now examine the advective flows U_r and Ω retrieved by the iterative Gal-Chen based solver for the 5-min and 1-min Joaquin (2015) input data. In particular, we are interested in (i) how often the algorithm fails to converge, (ii) the solution nonuniqueness threats, and (iii) how these flows might differ from the model-output local winds. Considering all subdomains over the 24:00 – 28:00 period, the nonconvergence frequency is 3.28 % for 5-min data and near zero (< 0.01 %) for 1-min data; for cases of nonconvergence, U_r and Ω are set to the subdomain-averaged flows.[16]

Taking a horizontal plan view of 28:00 model-output winds at z = 6 km, we find a markedly asymmetric pattern, with ω stronger in the northern eyewall (Fig. 4.9a), and a wavenumber-2 inflow-outflow pattern in u_r (Fig. 4.9e). U_r and Ω retrieved from the 5-min data (Figs. 4.9b,f) are generally similar to u_r and ω, although they contain a number of sharp local discontinuities that likely represent spurious solutions. Many of these

[14] Percentage of all trajectories with $\Delta IDE_{HORIZ} < -10$ km, $\Delta IDE_{VERT} < -1$ km

[15] Percentage of all trajectories with $\Delta IDE_{HORIZ} > 10$ km, $\Delta IDE_{VERT} > 1$ km

[16] Subdomain advections are also set to the first-guess values when the iterative Gal-Chen based procedure converges upon physically unreasonable solutions, where U_r exceeds 40 m s^{-1}; these instances are quite rare, however, with a ~ 0.1 % occurrence rate for the 5-min data.

discontinuities are eliminated using a filter applied to the 3D U_r and Ω fields (Figs. 4.9c,g). In the first pass, the filter identifies all subdomains where either U_r or Ω differ by more than 20% from a local average computed from the 26 surrounding subdomains in (r, λ, z) space. The flagged "discontinuity subdomains" are then assigned U_r and/or Ω values averaged from surrounding non-flagged subdomains in the second pass. All AC_W and AC_{UVW} experiments described here use filtered advective flows. Finally, note the smoother unfiltered U_r and Ω patterns retrieved from the 1-min data, compared to the 5-min data (cf. Figs. 4.9b,f, and 4.9d,h). These differences are consistent with our analytical tests (section 4.3) showing that spurious solutions move farther away from the true solution for smaller data input intervals; therefore, the iterative Gal-Chen based procedure should be less likely to converge upon them, given reasonable first-guesses. S15 found a similar result in their numerically-simulated data tests (see their Figs. 16 and 18).

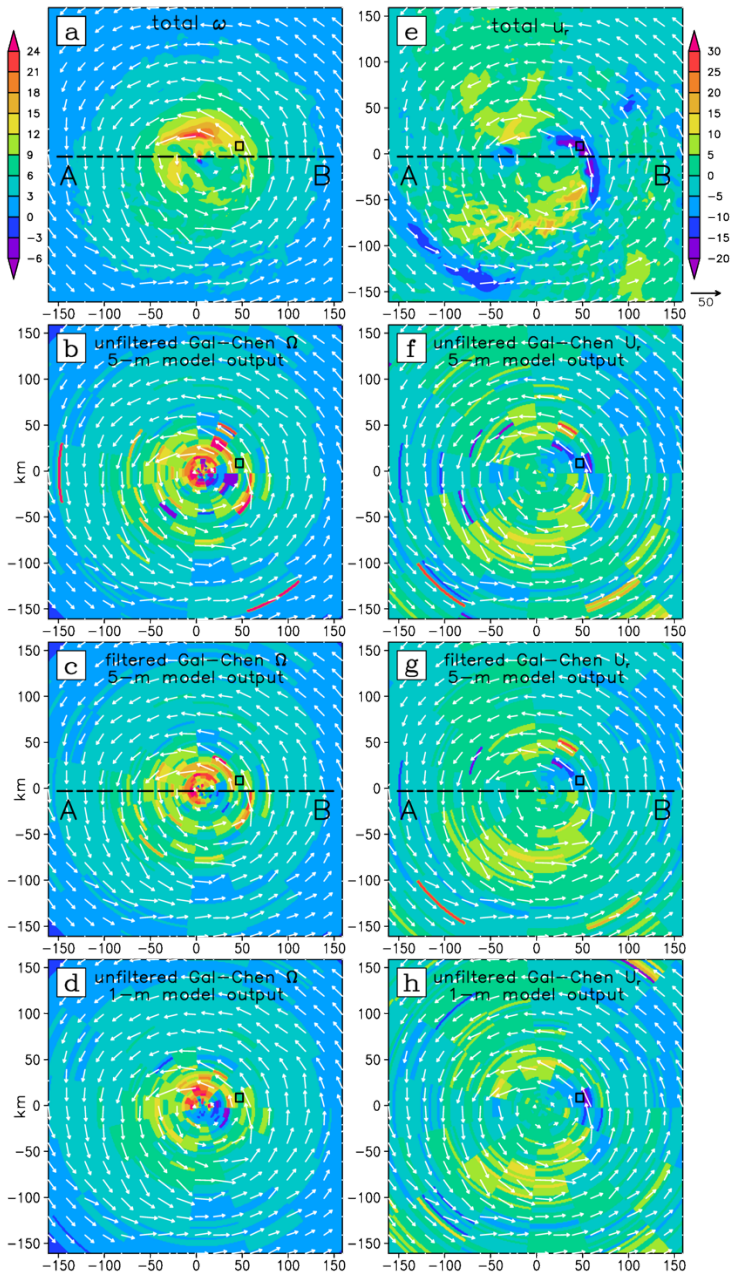

Figure 4.9 (a) Distribution of the model-output total angular velocity (ω) (shaded, × 300° s^{-1}) with storm-relative horizontal flow vectors (m s^{-1}) at z=6 km from the Hurricane Joaquin (2015) simulation at 28:00; (b) as in (a) but for the advective component of angular velocity (Ω) found by the iterative Gal-Chen procedure using 5-min data output data; (c) as in (b) but after applying a filter to the Gal-Chen Ω field to remove local discontinuities, and (d) as in (b) but from the iterative Gal-Chen procedure using 1-m data. (e) As in (a) but for the total radial velocity (u_r) (m s^{-1}). (f)-(g) As in (b)-(d) but for the advective component of the radial velocity (U_r) (m s^{-1}). Dashed lines in (a),(c),(e), and (g) denote the vertical cross section shown in Fig. 4.10, and the black rectangular box corresponds to the region highlighted in Fig. 4.6.

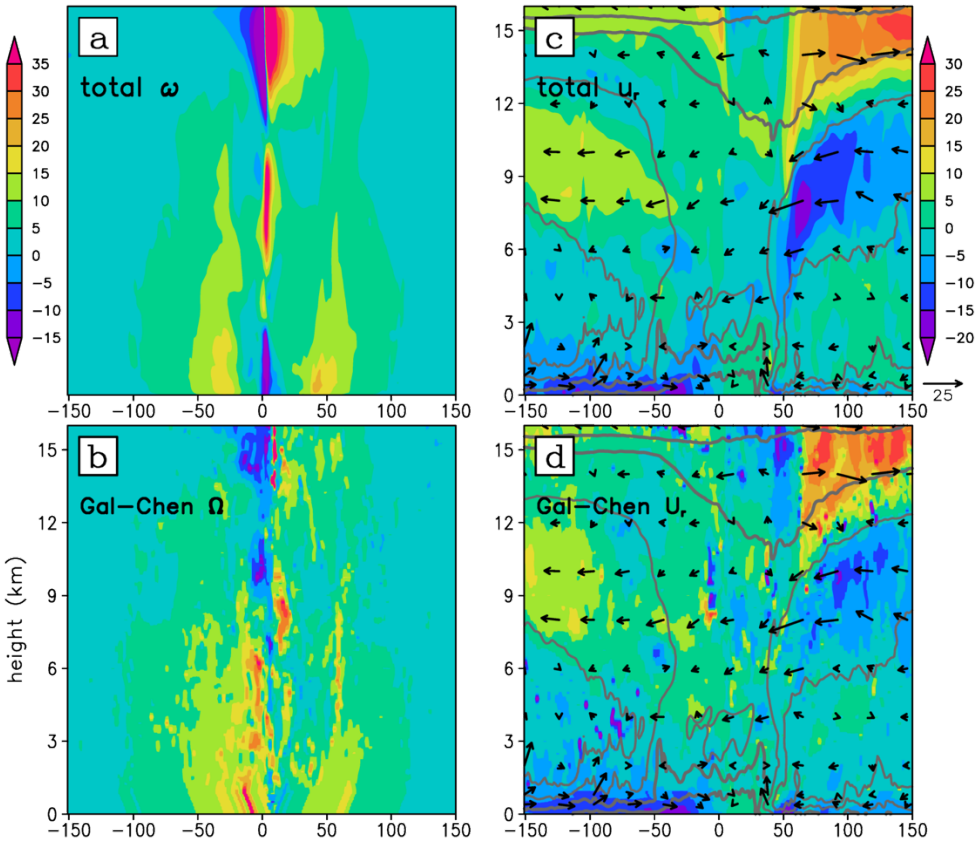

Figure 4.10 (a) East-west vertical cross section of the model-output total angular velocity (ω) (shaded, × 300° s^{-1}) at the forecast time 28:00 of the simulated Hurricane Joaquin (2015), running along the line AB shown in Fig. 4.9. (b) As in (a) but for the advective component of the angular velocity (Ω) found using the iterative Gal-Chen procedure over the preceding 5-m data output interval and then applying a filter to remove local discontinuities. (c) As in (a) but for the model-output total radial velocity (u_r) (shaded, m s^{-1}), with in-plane flow vectors (m s^{-1}; vertical velocity multiplied by 5) and θ_e (K; 350/354 thin-contoured, 358/362 thick-contoured). (d) As in (b) but for the advective component of the radial velocity (U_r) (m s^{-1}). Distances from the 1-km model domain center (km) are shown on the abscissa.

A vertical cross section taken through the 5-min filtered U_r and Ω fields (Fig. 4.10) indicates that the advective flow structures are (i) vertically coherent despite being solved for one level at a time, and (ii) generally similar in structure to the total flows in terms of the primary (Figs. 4.10a,b) and secondary circulations (Figs. 4.10c,d). One exception to (ii) is the aforementioned descending inflow channel for r = 50-100 km, z = 6-10 km. Here,

$|U_r|$ is smaller than $|u_r|$, suggesting that local perturbation inflows u_r' may be present. Examining $J(U_r, \Omega)$ computed for a representative subdomain in this region (Fig. 4.11), we see that the global J-minimum does in fact correspond to a $|U_r|$ roughly 50% smaller than the first-guess $|u_r|$, and that the iterative Gal-Chen based procedure successfully locates this global minimum. No problematic spurious local minima are present nearby.

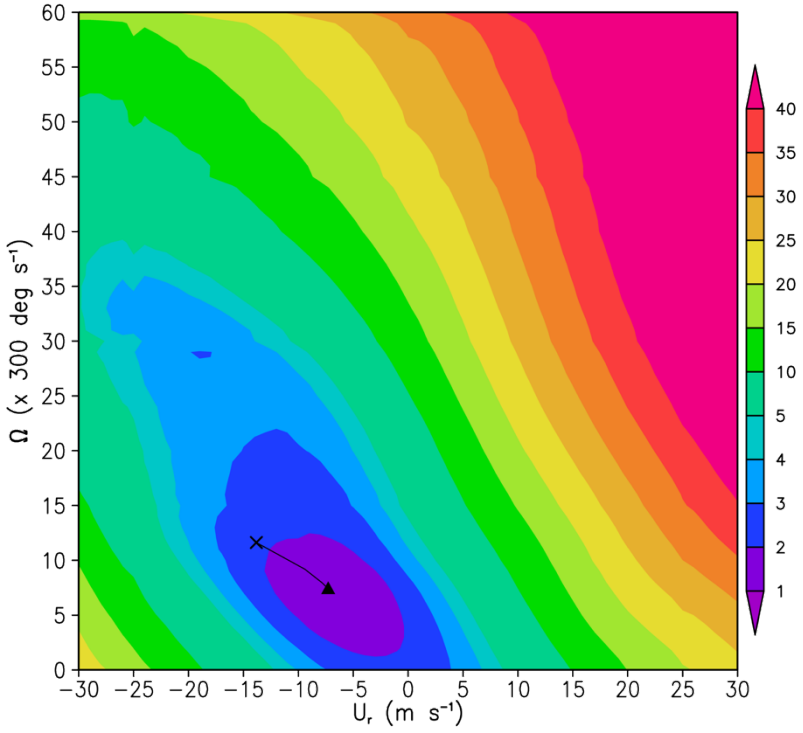

Figure 4.11 As in Fig. 4.4 but the cost function $J(U_r, \Omega)$ ($m^6s^{-3} \times 9/\pi \times 10^{15}$) evaluated for a z = 6 km subdomain enclosed within the boxed region shown in Fig. 4.6, computed over the 5-min time interval preceding forecast time 28:00.

4.4.3 Remarks

To better understand why LI-5 trajectory errors in the northeastern inner eyewall are substantially reduced by AC_{UVW} but not by AC_W (Figs. 4.6a,c), let us examine the time evolution of Joaquin's z = 6 km horizontal winds over three successive 5-min output times, as shown in Fig. 4.12. Wind and relative vorticity anomalies are computed with respect to

local time averages over the 1-h period centered on 28:00. We find three distinct positive vorticity anomalies rotating cyclonically around the inner eyewall; these structures resemble the mesovortices found in the simulated Hurricane Bonnie (1998) by Braun et al. (2006). They translate between model output times over distances similar to their ~ 10 km horizontal scale. The horizontal velocity field otherwise remains quite stable over the 27:30-28:30 period. $IDE_{HORIZ,LI}$ is largest in the region transited by these disturbances, where it ranges from 10 km to as high as 70 km locally (not shown), suggesting that LI-5 is poorly estimating the local winds here. The widespread AC_{UVW} error reduction found here suggests that AC of the horizontal winds improves the local wind estimates.

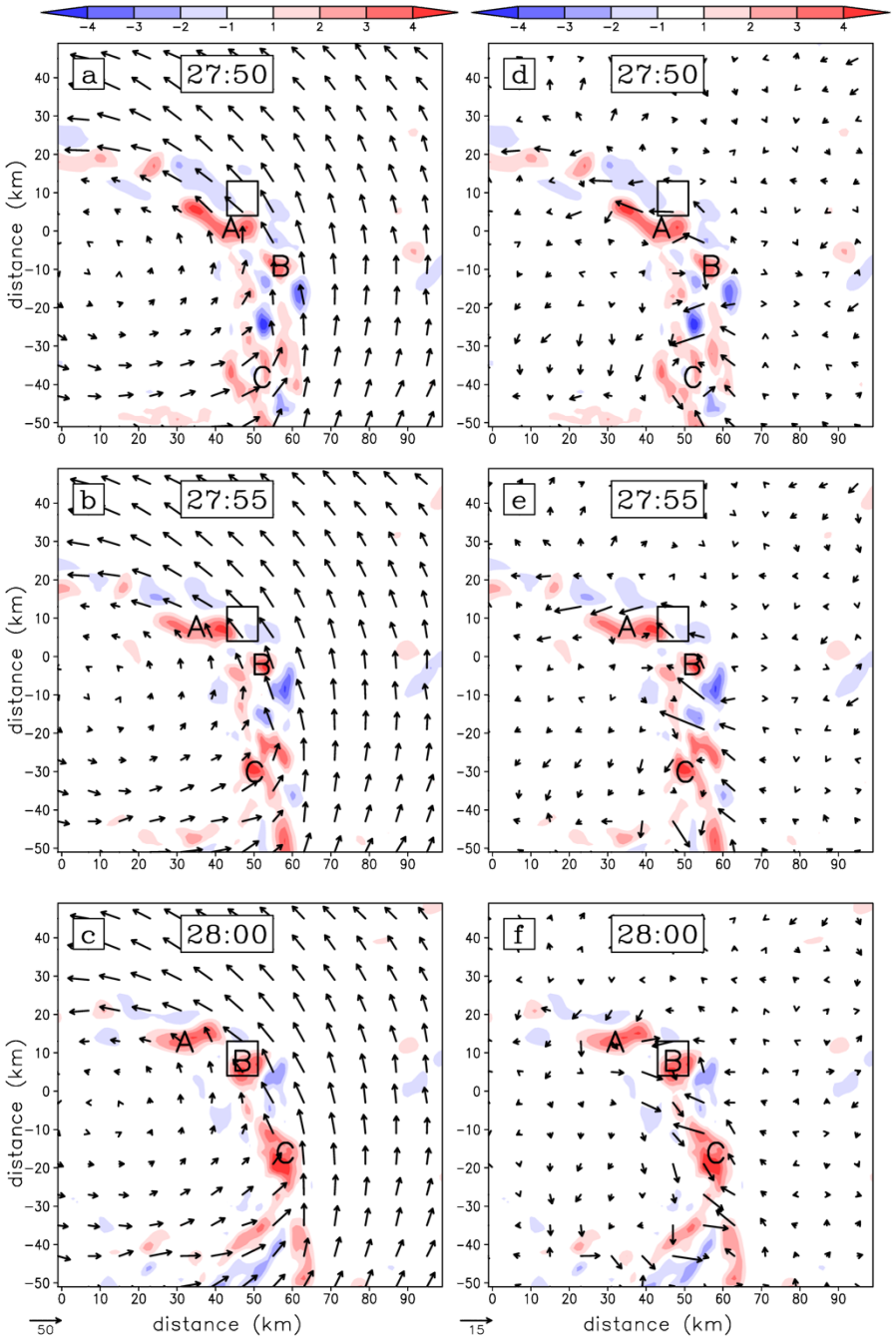

Figure 4.12 (a) Distribution of the horizontal storm-relative flow vectors (at forecast time 27:50), and the vertical component of relative vorticity anomaly ($\partial v/\partial x - \partial u/\partial y$)′ (shaded, $\times 10^{-3}$ s^{-1}), measured with respect to the local temporal average over the forecast period 27:30 – 28:30 from the Hurricane Joaquin (2015) WRF simulation 1-km resolution grid at z = 6 km. (b) and (c) As in (a) but for forecast times 27:55 and 28:00, respectively. (d)-(f) As in (a)-(c) but with perturbation flow vectors measured with respect to the local temporal average over the forecast period 27:30 – 28:30. Letter labels track cyclonic flow perturbations embedded in the mean flow.

The slight improvement of AC-MW_{UVW} over AC_{UVW} in terms of bulk sample statistics (Table 4.2) suggests that the subdomain-averaged flows are a reasonably good estimate of the advective flows for most portions of the simulated Joaquin (2015) circulation. Horizontal and vertical cross sections comparing (u_r, ω) and (U_r, Ω) support this conclusion (Figs. 4.9 and 4.10). However, we might expect the relative performance of the AC-MW_{UVW} and AC_{UVW} methods to depend on a number of factors, including the TC case, region of interest, subdomain size, and model output time resolution. For example, even though S15 found that AC and AC-MW yielded similar mean trajectory errors when the subdomains were kept sufficiently small, they also found that AC-MW performed quite poorly in the mesocyclone inflow region, where the local and pattern-translation u-wind speeds differed by 25 m s^{-1}.

4.5 Hurricane Wilma (2005) tests

In this section, we investigate the utility of AC for computing trajectories through TC updraft cores, using the WRF-simulated Hurricane Wilma (2005) 5-min output data (Chen et al. 2011). Wilma's RI onset and upper-level warm core development coincide with an outbreak of particularly intense, well-defined CBs (w > 15 m s^{-1}) that rotate around the eyewall with lifetimes of ~ 30 min (see Fig. 5 in CZ13). Only 5-min output was available for this case. However, an analysis of the advective flows retrieved by the Gal-Chen procedure over the 4-h backward trajectory computation period (not shown) indicates that they were generally similar to the local winds, with an overall nonconvergence rate of 5.7 %. To compare the same trajectories generated using LI and AC, we examine along-

trajectory traces of w and θ_e. Assuming saturated conditions, parcel θ_e is conserved after neglecting mixing, hydrometeor heat retention, and the latent heat of fusion. Our objective here is to show how artificial oscillations in parcel w and θ_e result when LI is applied to rotating updraft cores sampled at less-than-ideal temporal resolution, and how AC can mitigate this problem.

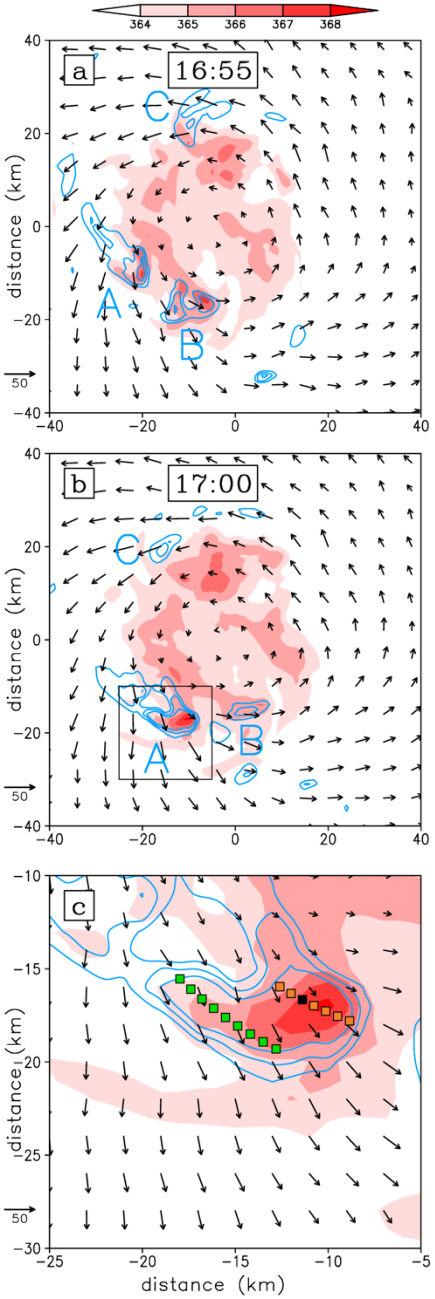

← **Figure 4.13** (a) Distribution of θ_e (shaded, K), vertical velocity (contoured at 5/10/15 m s^{-1}), and in-plane flow vectors (m s^{-1}) taken from the Hurricane Wilma (2005) prediction at z = 14 km for forecast time 16:55. Letter labels denote convective burst elements. (b) As in (a) but for forecast time 17:00. (c) As in (b) but zoomed in to show the seed positions (colored squares) of the convective burst trajectories. Horizontal distances are measured from the 1-km resolution model domain center.

Consider CB "A" shown in Figure 4.13. While rotating about 30° counterclockwise over the 16:55-17:00 period, the updraft has broadened and intensified; note how the strongest portion moves in concert with a positive θ_e anomaly - possibly an artifact of intense fusion latent heat release (LHR) (Miller et al. 2015). Figure 4.14a shows a cluster of 4-h forward and 4-h backward AC trajectories seeded from inside CB "A" at z = 14 km (Fig. 4.13c). For comparison, a few trajectories representative of the background secondary circulation, with maximum w not exceeding 7.5 m s^{-1}, are shown in Fig. 4.14b. Both CB and "non-CB" updrafts originate from MBL parcels spiraling inward, with their θ_e increasing due to wind-induced ocean surface latent and sensible heat fluxes, consistent with the WISHE hypothesis (Emanuel 1986). CB and non-CB parcels both experience a θ_e reduction with ascent into the middle levels, likely from dry air entrainment (Cram et al. 2007), followed by a θ_e recovery in the upper troposphere, possibly on account of fusion heating (Fierro et al. 2009, 2012; Miller et al. 2015). Note the more pronounced θ_e "dip" extending through a deeper layer for the secondary circulation cluster; this is consistent with reduced upper-level fusion LHR in their comparatively weaker updrafts.

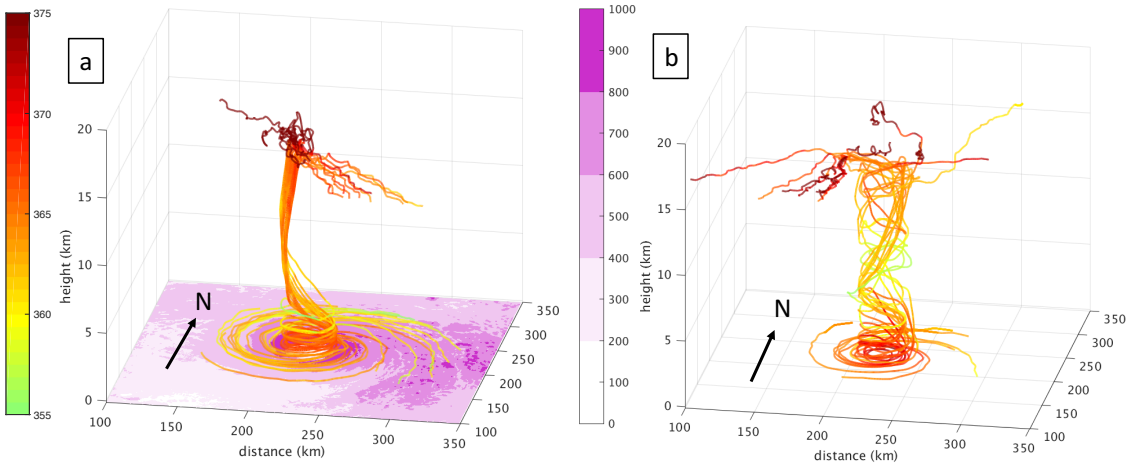

Figure 4.14 Three-dimensional plots showing 8-h trajectories run from the Hurricane Wilma (2005) WRF prediction 5-min output, using advection correction time interpolation of the vertical velocity field (AC_W). Four-hour forward and four-hour backward trajectories are seeded from z=14 km at 17:00. Panel (a) shows a cluster of 16 trajectories seeded from inside convective burst "A" in Fig. 4.13, while (b) shows 13 representative background secondary circulation trajectories. Lines are colored by θ_e (K) interpolated along each trajectory. Purple shading in (a) shows the total (latent + sensible) heat flux (W m^{-2}) from the ocean surface at forecast time 15:00. Horizontal distances are measured from the southwestern corner of the 1-km resolution model domain.

To evaluate the impacts of AC, in Figure 4.15 we compare w, θ_e and AAM along the CB "A" backward trajectories computed using LI, AC_W, and AC_{UVW}. Note the prominent w and θ_e oscillations above z=6 km for the LI trajectories (Figs. 4.15b,c). The AC trajectories, on the other hand, show a more gradual decrease in w and θ_e with downward extent (cf. Figs. 4.15f,g and 4.15j,k). AAM is reasonably well-conserved along most trajectories above z = 3 km (z = 1 km) for LI (AC) (Figs. 4.15d,h,l). Previous TC AAM budgets using azimuthally-averaged variables have found friction and turbulence forcing to be small above the MBL (Zhang et al. 2001; Qin et al. 2018b). Our results suggest that the 3D AAM material conservation assumption used for the Gal-Chen based U_r and Ω solver was reasonable for this CB.

Figure 4.16 re-plots w and θ_e as a function of time along the first 10 minutes of the LI backward CB trajectories. Note how the oscillations of w and θ_e generally stay in phase along each trajectory. Furthermore, w and θ_e minima tend to occur in between the model output times, suggesting that they may be unphysical artifacts of the LI damping mechanism illustrated in Fig. 4.1. Between 16:55 and 17:00, the ~10° wide CB "A" core region (w > 15 m s^{-1}) near r = 20 km rotates from ~215° to ~245° azimuth (Figs. 4.13a,b). The large "dip" in w estimated along the LI trajectories around backward integration time t = 150 s (Fig. 4.16a) is consistent with w(r = 20 km, λ = 230°) being small for the two nearest model output times (Figs. 4.13a,b).[17] This is simply a consequence of CB "A" having a relatively small horizontal scale relative to its translation speed. The absence of any significant local minima in the upper-level AC_W w profiles (Fig. 4.15j), on the other hand, results in AC_W bringing the parcels ~2.5-km lower compared to LI after 20 minutes of backward integration (not shown).

[17] Azimuthal-height plane cross-sections (not shown) reveal that the CB "A" updraft core remains nearly upright above the melting level at both 16:55 and 17:00.

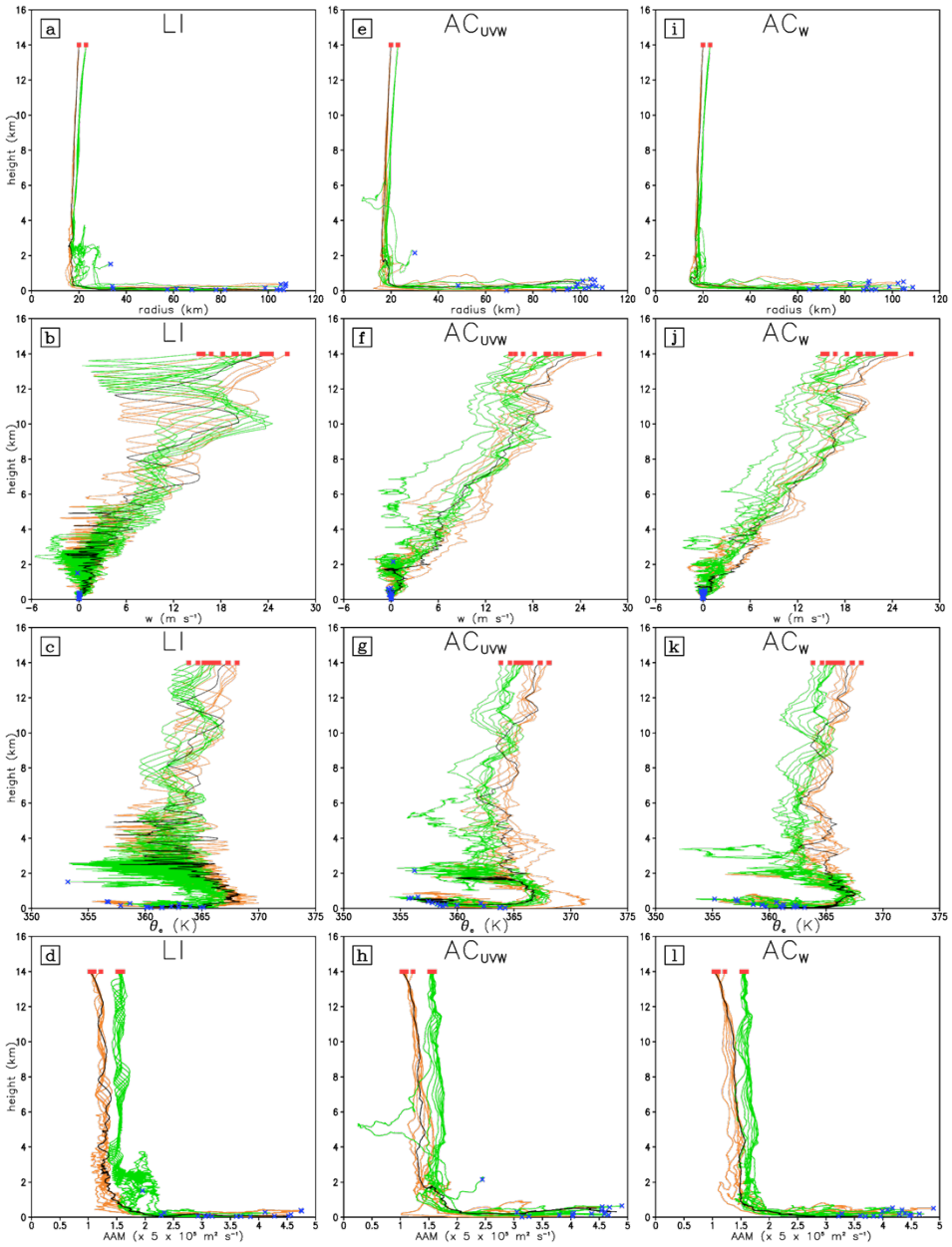

Figure 4.15 (a) Radius-height projections of the 4-h backward CB "A" trajectories from the Hurricane Wilma (2005) WRF simulation (Fig. 4.13c), computed using linear interpolation (LI) in time. Orange (green) trajectories are seeded from the r = 20 km (r = 23 km) radius, and they correspond to the colored seed positions in Fig. 4.13c. Trajectory #3 is outlined in black. Red squares (blue crosses) denote seeded (final) positions. (b) Vertical velocity (m s^{-1}) interpolated along the LI backward trajectories shown in (a). (c) As in (b), but for θ_e (K). (d) As in (b), but for AAM ($\times$ 5 $\times$ 10^5 m^2 s^{-1}). (e)-(h) As in (a)-(d) but for the same trajectories re-run using advection correction of the horizontal and vertical velocity fields (AC_{UVW}). (i)-(l) As in (a)-(d) but for the same trajectories re-run using advection correction of the vertical velocity field (AC_W).

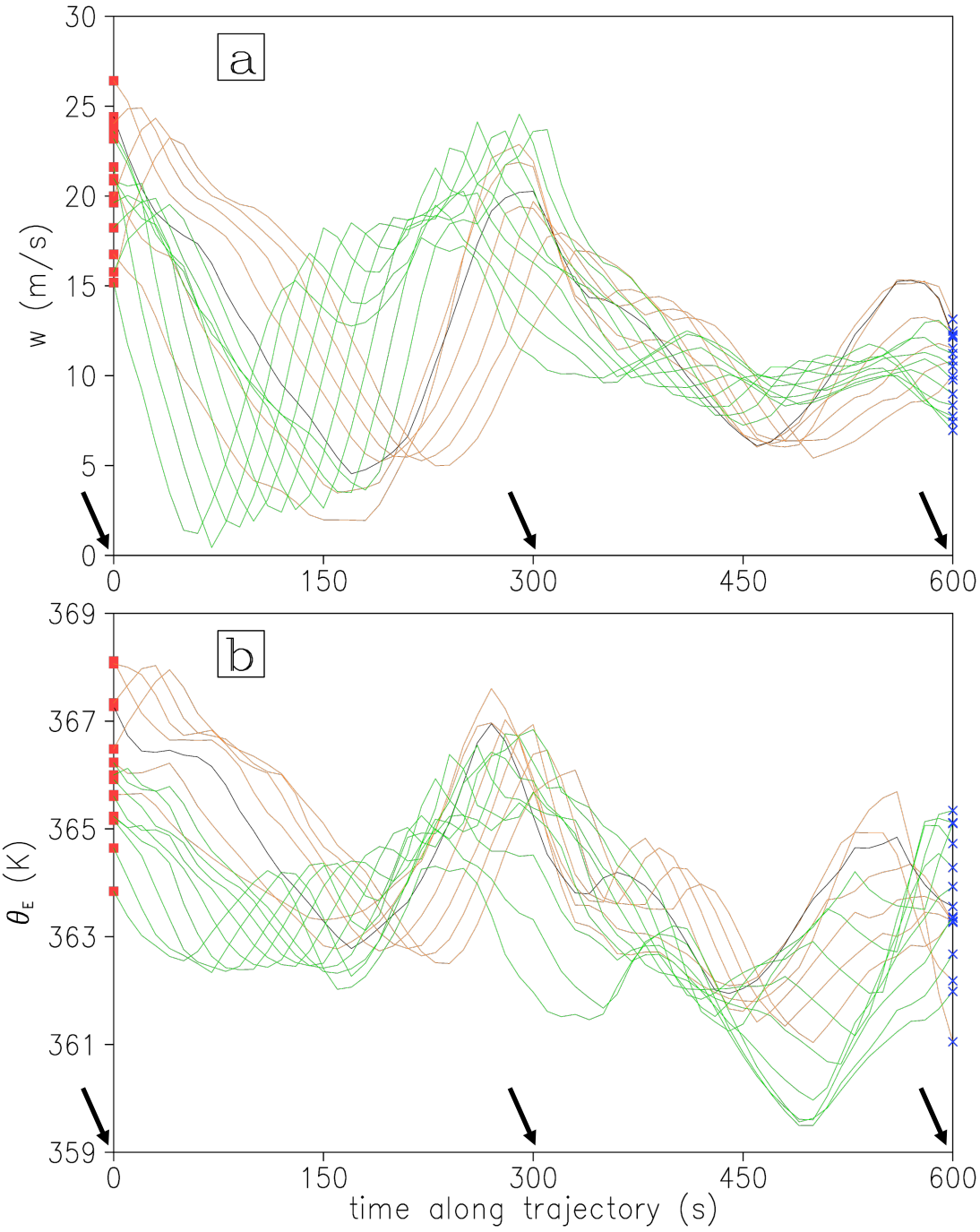

Figure 4.16 (a) Vertical velocity (m s^{-1}) plotted as a function of integration time for the CB "A" backward trajectories computed using LI, color coded as in Fig. 4.15. Arrows label model data output times. (b) As in (a) but for θ_e (K).

4.6 Summary and conclusions

In this chapter, we present a new algorithm for computing trajectories from simulated TC data that interpolates the gridded winds in time using AC in lieu of traditional LI. Our goal is to reduce trajectory errors that result from inaccurate estimates of the wind field at the computational timestep, which is typically smaller than the model output time resolution due to computational stability constraints. AC algorithms interpolate variables in time from a reference frame that moves with the advective flow velocity.

Our AC method extends the techniques previously developed in GC82 and S15 by (i) extending them to 3D flow fields, (ii) applying the frozen turbulence constraint to AAM, and (iii) defining the advective flows in cylindrical rather than Cartesian coordinates. We first tested our trajectory computation algorithms on an analytical flow field and determined that they are likely free of code errors. Next, we tested several alternate AC algorithms against LI using a batch of 10,201 backward trajectories run from Hurricane Joaquin (2015) WRF simulation 5-min output, with 1-min output reserved for computing reference, or "truth" trajectories. While AC of only w led to little overall improvement over LI, AC of the full 3D wind vector (u, v, w) improved trajectory accuracy more substantially, especially in the inner eyewall region where eyewall mesovortex structures were being advected by the tangential winds. Unlike S15, we obtained slightly better results when we defined the advective flows as gridpoint averages local to each subdomain, as opposed to using an iterative algorithm that minimized a cost function penalizing deviations from material conservation of AAM. This result was consistent with our findings that the iterative algorithm (i) retrieved advective flows that did not differ substantially from the model-output total winds over much of the model domain, and (ii) occasionally converged

on spurious solutions, the likelihood increasing with coarser data input resolution. Finally, we showed how AC could eliminate along-trajectory *w* oscillations that appear when LI is applied to rotating deep convective updrafts in a Hurricane Wilma (2005) WRF simulation; these oscillations likely result from the model output frequency being too coarse relative to the horizontal scale and translation speed of the updraft disturbances.

These results suggest that AC can improve the accuracy of trajectories computed from TC simulation output, particularly in regions where flows are unsteady over time, such as in eyewall mesovortices and convective bursts. Like S15, we recommend that AC be applied with caution, as there may be some TC cases, or at least portions of their circulations, where neither subdomain-averaged winds nor the iterative Gal-Chen based procedure could yield reasonably accurate advective flows. Ideally, AC should be tested against LI using a set of reference trajectories computed at model runtime, or from higher-resolution data. Otherwise, the quality of the advective flow solution may be examined using analyses similar to those shown in section 4.4.2 herein.

More generally, our findings motivate the testing of AC in trajectory calculations for meteorological applications beyond TCs. For these cases, better results would likely be obtained if the horizontal advective flows were defined in Cartesian rather than cylindrical coordinates, as in S15. It may also be worthwhile to test the impact of advection-correcting variables in the vertical direction. Here, vertical advections could be defined either by minimizing a cost function with respect to 3D flows, as in Zhang and Gal-Chen (1996), or simply by setting them to a locally-averaged vertical velocity. In chapter 5, we will apply this 3D trajectory algorithm to a variety of flow structures using high-resolution WRF simulated TCs.

Chapter 5. Applying the Trajectory Model to Rapidly Intensifying Hurricane Wilma (2005): Tracing the Roots of Convective Bursts in the Eyewall

Material presented in this chapter has been submitted to Monthly Weather Review as Miller and Zhang (2019c) and is currently under review

5.1 Introduction

Observations of TCs over recent decades have shown that outbreaks of inner-core deep convection, the so-called "convective bursts" (CBs), often precede or coincide with episodes of RI, defined for Atlantic TCs as a V_{MAX} intensification rate exceeding 15 m s^{-1} (24 h)$^{-1}$ (Kaplan and DeMaria 2003). Gentry et al. (1970) identified these features as localized cold brightness temperature anomalies in satellite imagery and recognized their potential significance in the TC intensification process. Subsequent studies used airborne Doppler radar and flight-level temperature instrumentation to analyze CB three-dimensional kinematic structure and thermodynamics (Rodgers et al. 1998; Heymsfield et al. 2001; Molinari et al. 2006; Houze 2009; Guimond et al. 2010). Convection-resolving numerical TC simulations have captured similar features (Chen and Zhang 2013; Chen and Gopalakrishnan 2015; Nguyen and Molinari 2015).

Previous studies have proposed several mechanisms through which inner-core CBs may facilitate TC intensification. According to one hypothesis, compensating subsidence flanking the inner edges of CB updrafts enhances development of the warm core. Heymsfield et al. (2001) showed how a cluster of CB subsidence currents originating near the tropopause may have contributed up to 3° C of midlevel eye warming in Hurricane Bonnie (1998). Provided that adiabatic warming offsets evaporative cooling in subsidence

currents, the high inertial stability inside the radius of maximum wind (RMW) may help to "trap" subsidence-induced heating in the eye (Hack and Schubert 1986). CBs or "hot towers" may also facilitate tropical cyclogenesis by moistening the inner-core midtroposphere, thereby "priming" it for the subsequent development of sustained convection (Nolan 2007; Montgomery et al. 2006). Other studies have shown how CBs embedded in a developing TC circulation can spin up the tangential wind V_T by collectively aggregating and stretching low-level cyclonic vorticity anomalies (Nguyen et al. 2008; Montgomery and Smith 2014; Nguyen and Molinari 2015).

Hurricane Wilma (2005) underwent a record-breaking 12-hour RI event on 18-19 Oct, featuring a P_{MIN} deepening rate of 83 hPa $(12\ h)^{-1}$ with a P_{MIN} and V_{MAX} of 882 hPa and 82 m s^{-1}, respectively. Wilma intensified in the western Caribbean under near-ideal environmental conditions with low VWS and high SSTs of 29-30 °C. The storm subsequently underwent an eyewall replacement cycle and weakened to Saffir-Simpson Category 4 intensity before making landfall near Cozumel Island on Mexico's Yucatan Peninsula on 21 Oct; see Pasch et al. (2006) for more details.

Chen et al. (2011, hereafter CZ11) generated a cloud-permitting prediction of Hurricane Wilma (2005) using the Weather Research and Forecasting (WRF) model. Using this dataset, Zhang and Chen (2012) demonstrated how upper-tropospheric eye warming accounted for the largest portion of Wilma's hydrostatically-induced P_{MIN} falls during RI. Chen and Zhang (2013, hereafter CZ13) showed how CBs, which they defined as updraft grid columns with $w \geq 15$ m s^{-1} above $z = 11$ km, directed subsidence currents into the developing upper-level warm core around RI onset; Figure 5.1 shows an example of this process. Miller et al. (2015, hereafter M15) found that turning off the latent heat of fusion

resulted in a storm with fewer CBs, reduced upper-level warming, and a less extreme RI rate. They also used a heat budget to show that Wilma's upper-level eye warming occurred primarily under adiabatic conditions.

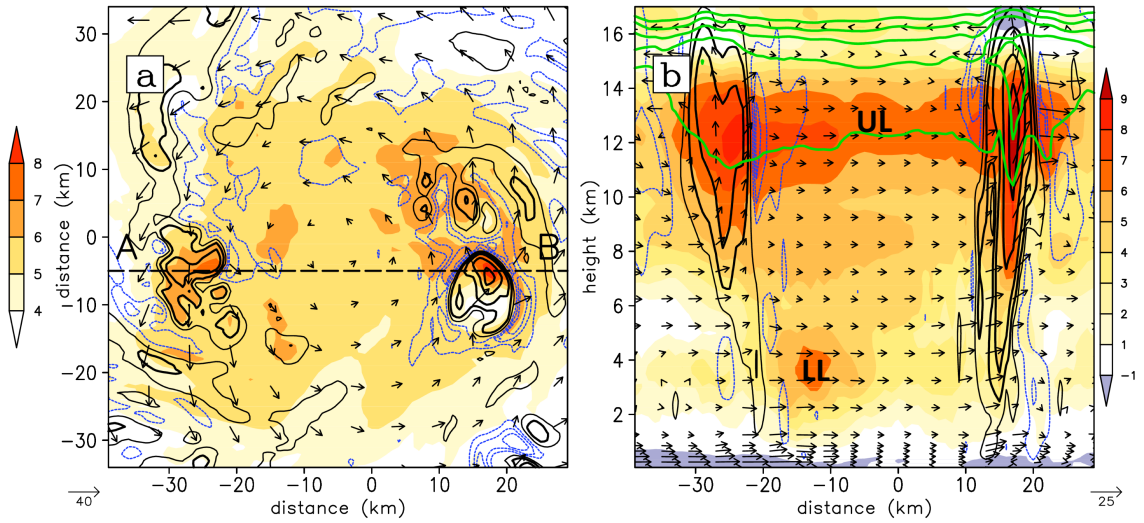

Figure 5.1 (a) WRF-predicted 16:10, z = 14 km temperature anomaly $T'(z,t)$ (shaded, K), computed with respect to the 1000 km × 1000 km area-averaged temperature profile centered on the storm at the initial time $\overline{T(z,t=0)}$. Vertical velocity (m s^{-1}) is contoured (thin black at 2; thick black at 5/10/20/30; dotted blue at -5/-3/-1) and horizontal storm-relative flow vectors (m s^{-1}) are also shown. (b) Vertical cross section, taken along the dashed line A-B, given in (a), of θ (K, green-contoured every 5K over the range 360-380K, vertical velocity contoured as in (a), with in-plane storm-relative flow vectors (m s^{-1}). Symbols LL and UL highlight the locations of the lower-level and upper-level warm cores, respectively. Note the different shading scales used for $T'(z,t)$ in (a) and (b).

On the vortex scale, eyewall vertical ascent connects the low-level radial inflow to the upper-level outflow, thus comprising the middle branch of the TC "secondary circulation". Early theories of TC intensification (Charney and Eliassen 1964; Ooyama 1969,1982; Shapiro and Willoughby 1982; Hack and Schubert 1986) recognized the significance of the secondary circulation in converting latent heat energy released by inner-core deep convection into the swirling winds' kinetic energy; however, they generally assumed eyewall ascent to be relatively weak, horizontally uniform, and constrained by

balanced vortex dynamics. Over recent decades, however, observations and high-resolution modeling of TC eyewalls have found considerable horizontal variation in the vertical velocity (w) fields, even for mature cases (Jorgensen 1984; Jorgensen et al. 1985; Marks and Houze 1987; Black et al. 1996; Braun 2002; Eastin et al. 2005a,b; Braun et al. 2006; Hogsett and Zhang 2009; Rogers 2010; Rogers et al. 2015). All of these studies reported localized "cores" of stronger updrafts, as well as downdrafts being embedded within a weaker background ascent. Furthermore, Braun (2002) and Eastin et al. (2005a,b) showed that the updraft cores could be positively buoyant relative to the mesoscale eyewall environment, which implies the existence of conditional instability in the eyewall. M15 found that azimuthally-averaged slantwise convective available potential energy (SCAPE) computed along constant-AAM surfaces exceeded 400 J/kg in their simulated Hurricane Wilma (2005) eyewall during RI. Assuming pseudoadiabatic thermodynamics and undilute ascent, SCAPE of this magnitude would support a theoretical maximum updraft speed $w_{MAX\text{-}UNDILUTE} \cong \sqrt{2SCAPE} = 28$ m s^{-1}, which is comparable to the strongest CB updrafts found in their prediction. By contrast, the wind-induced surface heat exchange (WISHE) theory of TC intensification (Rotunno and Emanuel 1987; Emanuel 1997) is based upon the steady-state Emanuel (1986) model that assumes the TC eyewall to be everywhere neutral to moist pseudoadiabatic ascent. Perhaps most significantly, WISHE theory re-focused attention on heat and moisture fluxes from the ocean surface as the primary source of high equivalent potential temperature (θ_e) air in a TC maritime boundary layer (MBL). Further work is clearly needed toward developing a more comprehensive model of TC intensification that incorporates the impacts of buoyant deep convection with insights gained from older models based on balanced dynamics (Charney and Eliassen 1964;

Ooyama 1982; Emanuel 1986) and moist neutral thermodynamics (Emanuel 1986).

The major objective of this chapter is to better understand the thermodynamics and three-dimensional structure of CBs associated with the RI of Hurricane Wilma (2005). It is still unclear how a mid-to-upper level TC eyewall can support large parcel buoyancy. Although wind-induced heat and moisture fluxes above warm SSTs provide an ample source of high θ_e air to a TC MBL (Emanuel 1986; Braun 2002; Zhang et al. 2002; Cram et al. 2007), excessive hydrometeor loading due to the moist tropical environment (Zhang et al. 2000), warming from latent heat release (LHR) (Shapiro and Willoughby 1982; Emanuel 1986), and the midlevel entrainment of environmental low-θ_e air (Cram et al. 2007) could all render the eyewall a less favorable environment for maintaining buoyant updrafts. A few other questions are worth addressing. Given the rapidly rotating flows, to what extent can CB updraft roots be traced to portions of the MBL where ocean surface heat fluxes are locally higher? How do CB updrafts interact with the locally sheared (both horizontally and vertically) swirling winds? How do local pressure perturbations from hydrostatic balance affect CB updraft accelerations? For instance, Braun (2002) found that the vertical perturbation pressure gradient acceleration (PGA) was downward-directed everywhere except in the MBL along a trajectory computed from his simulated Hurricane Bob (1991).

Unlike in many previous studies, this chapter's objective will be achieved in a Lagrangian framework – that is, by using the Miller and Zhang (2019, hereafter MZ19) trajectory model to run a large batch of backward trajectories from the CZ11 Wilma (2005) WRF prediction that samples both CB updraft cores and the background secondary circulation. We focus more on the 12:00-20:00 (hh:mm format) prediction period, which

features intense inner-core CB activity, RI onset at 15:00, and the subsequent RI in V_{MAX} from 38 to 58 m s^{-1}. Wilma undergoes significant structural changes over this period, e.g., the axisymmetrization and contraction of the eyewall convection (see Figs. 12a-c in CZ11) and the intensification of the upper-level warm core (see Fig. 1a in CZ13). Our study combines a detailed analysis of the three-dimensional structure and thermodynamics of a selected CB with a statistical comparison of thermodynamic variables interpolated along samples of trajectories binned by updraft intensity.

The next section describes the Hurricane Wilma (2005) WRF prediction, trajectory computation methods, experiment design, and statistical methods used for analyzing trajectory output data. Section 5.3 presents an analysis of a selected CB, and section 5.4 compares a larger sample of CBs to the background secondary circulation in terms of their thermodynamic properties, environmental air entrainment, and vertical accelerations. A summary and concluding remarks are given in the final section.

5.2 Datasets and methodology

5.2.1 Hurricane Wilma (2005) WRF prediction

CZ11 describe their Wilma (2005) WRF prediction configuration and observation validations in detail. They integrated the WRF Advanced Research core (ARW) for 72 hours beginning at 0000 UTC 18 Oct 2005, using a two-way interactive, quadruply-nested (27/9/3/1 km) grid, 55 vertical σ-levels and a 30-hPa model top. This prediction captures the timing, location, and rate of Wilma's observed RI and subsequent eyewall replacement cycle reasonably well, along with the associated inner-core structural changes.

5.2.2 Trajectory computations

Trajectories are computed from the Wilma WRF prediction 5-min output flow fields using the algorithm developed by MZ19. First, WRF 1-km domain 12:00-20:00 output is de-staggered and vertically interpolated to height coordinates using ARWpost software.[18] The resulting "computational grid" has a vertical resolution of 250-m (50-m) above (below) z = 1 km, with a top boundary of z = 20 km and a ground level populated with WRF-output 10-m horizontal winds and zero w. The MZ19 model integrates parcel positions using a second order Runge-Kutta (RK2) scheme with a 10-s computational time step. Gridded winds are interpolated to the parcel positions trilinearly in space; time interpolations from the two nearest WRF output times use advection correction (AC, Gal-Chen 1982; Shapiro et al. 2015; MZ19), a technique that interpolates data in a reference frame that follows the mean flow, rather than from a fixed position as in traditional linear time interpolation (LI). More specifically, time interpolations use the AC_W algorithm described in MZ19, where AC is used for scalars and w, while LI is used for the u- and v-components. Choice of AC_W is motivated by the fact that Wilma's inner-core horizontal winds (deep convective updrafts) remain relatively steady (translate considerable azimuthal distances; to be shown in section 5.3.2) between 5-min output times over the analysis period. Any backward trajectories arriving at the computational grid top or lateral boundaries are flagged and their integration is terminated early. Scalar variables interpolated to the 10-s trajectory positions (Table 5.1) are saved for analysis.

[18] Documentation for the ARWpost software package is available at http://www2.mmm.ucar.edu/wrf/users/docs/user_guide_V3.9/users_guide_chap9.htm#_ARWpost_3.

Table 5.1 Diagnostic variables interpolated from the postprocessed WRF grid during trajectory computations

Symbol	Description	Units
T	temperature	K
p	pressure	hPa
θ_e	equivalent potential temperature (Bolton 1980)	K
q_V	water vapor mixing ratio	g kg^{-1}
q_{LIQ}	combined liquid hydrometeor (cloud + rain water) mixing ratio	g kg^{-1}
q_{FRZ}	combined frozen hydrometeor (ice + snow + graupel) mixing ratio	g kg^{-1}
RH	relative humidity (with respect to ice for $T < 273.15$ K)	%
H_S	sensible surface heat flux	W m^{-2}
H_L	latent surface heat flux	W m^{-2}

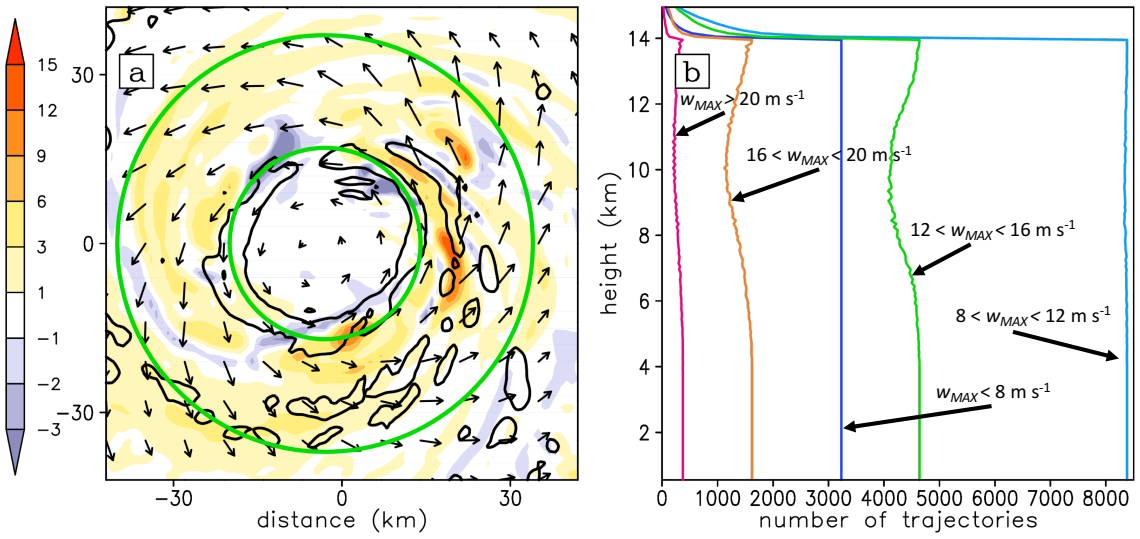

Fig. 5.2 (a) WRF-predicted z = 14 km vertical motion (w, shaded, m s^{-1}) and horizontal wind vectors (m s^{-1}) with z = 6 km w (2 m s^{-1} contoured in black) at 18:00. Green circles bound the annular region that backward trajectories are seeded from, as described in the text. (b) Number of trajectories in sub-samples of w_{MAX}-8, w_{MAX}-12, w_{MAX}-16, w_{MAX}-20, and w_{MAX}-CB with at least one output data point contained within the 100-m vertical layer bin configuration used for the vertical momentum budget analysis in section 5.4.4, as shown on the y-axis.

5.2.3 Trajectory experiment design and analysis techniques

For each WRF output time between 16:00 and 20:00, a set of 1,980 4-h backward trajectories is seeded from z = 14 km over the region where the eyewall updraft core flares outward, forming the roots of the main outflow. Seed points are positioned at 2º azimuthal intervals on concentric rings radially spaced every 2 km over a 20-km wide annulus centered on the z = 14 km RMW (Fig. 5.2a). Of all 97,020 backward trajectories, only the ~ 45% that can be traced to the MBL - hereafter the MBL-Origin sample, are further analyzed. Herein the MBL is defined as the region below z = 0.5 km, which generally aligns with the azimuthally-averaged low-level inflow inside of r = 40 km over the analysis period (not shown). The remaining trajectories fall into two broad categories: (i) those entrained into updrafts from the midlevel eye, eyewall, or outer environment; and (ii) those originating from the outflow layer or higher levels.[19] The MBL-Origin trajectories are further stratified into subsamples binned by w_{MAX}, defined for each trajectory as its maximum w. These subsamples are respectively named w_{MAX}-8, w_{MAX}-12, w_{MAX}-16, w_{MAX}-20, and w_{MAX}-CB, for $w_{MAX} \leq 8$ m s^{-1}, 8 m s^{-1} < $w_{MAX} \leq 12$ m s^{-1}, 12 m s^{-1} < $w_{MAX} \leq 16$ m s^{-1}, 16 m s^{-1} < $w_{MAX} \leq 20$ m s^{-1}, and $w_{MAX} > 20$ m s^{-1}. Herein we define CBs as any updrafts containing one or more w_{MAX}-CB trajectories. Each MBL-Origin trajectory is assigned an "updraft period" running backward in time, beginning with the first 10-s output time for which w averaged over the next 1-min interval exceeds zero (possibly the seed point) and ending with the parcel reaching the z = 0.5 km level.

[19] Trajectories that do not meet the MBL-Origin criterion may be useful for analyzing other TC processes and they will be reserved for a future study.

Table 5.2 Diagnostic variables computed at the parcel position from trajectory output variables after completion of trajectory integrations

Symbol	Description	Units
ρ	density	kg m^{-3}
θ_v	virtual potential temperature	K
q_{HYD}	total hydrometeor mixing ratio ($q_{LIQ} + q_{FRZ}$)	g kg^{-1}
q_{TOT}	total water mixing ratio ($q_{HYD} + q_V$)	g kg^{-1}
RH	relative humidity (with respect to ice for $T < 273.15$ K)	%
V_R	radial wind component	m s^{-1}
d_{EDGE}	smallest distance to updraft edge among the four Cardinal directions	km
D_{AVG}	mean updraft diameter	km
$\theta_{e,ENV}$	environmental θ_e (see section 2e)	K
RH_{ENV}	environmental RH (see section 2e)	%

Table 5.2 lists additional diagnostic variables derived from trajectory output data. Perturbations from the azimuthal mean are denoted with the prime superscript and "360" subscript. For example, $\theta'_{v,360} = \theta_v - \overline{\theta_{v,360}}$, where $\overline{\theta_{v,360}}$ is the azimuthally-averaged virtual potential temperature, interpolated linearly in time and bilinearly in space to the parcel (r, z) coordinates. All diagnostic variables are averaged over trajectory output times that fall within 250-m height bins k=1, k_{TOP} spanning the z = 0.25 - 14 km layer. Mean profiles of any variable a for a given w_{MAX}–binned subsample may be then computed as:

$$\bar{a}(k) = \frac{\sum_{i=1}^{n} a_i(k)}{n}, \qquad (5.1)$$

where trajectories i = 1, … n belong to the subsample and contain at least one output data point within bin k, and $a_i(k)$ is a along i^{th} trajectory, averaged over bin k. Variance and standard deviation profiles of a are respectively given by

$$\hat{a}(k) = \frac{\sum_{i=1}^{n} [a_i(k) - \bar{a}(k)]^2}{n-1} \qquad (5.2)$$

and

$$s_a(k) = [\hat{a}(k)]^{1/2}. \qquad (5.3)$$

Differences in $\bar{a}(k)$ between different subsamples are evaluated for statistical significance at the two-sided 95% confidence interval using the Student's-*t* test for independent samples (Wilks 2011, pp. 142-144). The Pearson correlation coefficient $\rho_{a,b}$ between variables *a* and *b* is computed as

$$\rho_{a,b}(k) = \frac{\sum_{i=1}^{n}[a_i(k)-\bar{a}(k)][b_i(k)-\bar{b}(k)]}{(n-1)s_a(k)s_b(k)}. \quad (5.4)$$

5.2.4 Computation of vertical accelerations along trajectories

Parcel vertical accelerations $Dw/Dt = \frac{\partial w}{\partial t} + u\frac{\partial w}{\partial x} + v\frac{dw}{dy} + w\frac{\partial w}{\partial z}$ along backward trajectories are computed using 1-min centered time differences of *w* previously smoothed using a 2-min running mean[20]. The anelastic vertical momentum equation can be written as (Houze 1993 p. 36; Braun 2002; Fierro et al. 2012):

$$\frac{Dw}{Dt} \approx \underbrace{-\frac{1}{\bar{\rho}}\frac{\partial p'}{\partial z}}_{PGA} + \underbrace{g\left[\frac{\theta_v'}{\overline{\theta_v}} + (\kappa-1)\frac{p'}{\bar{p}} - q_{HYD}'\right]}_{BA} + mixing, \quad (5.5)$$

where overbars (primes) denote horizontal averages over (perturbations from) a hydrostatic height-dependent horizontal base state, g is the gravitational constant, $\kappa = 0.286$, and other symbols are defined in Tables 5.1 and 5.2. From left to right, the Eq. (5.5) forcing terms on *Dw/Dt* are the PGA, buoyant acceleration (BA), and subgrid-scale turbulent momentum mixing. The BA can be decomposed into three components: (i) thermal buoyancy $g\frac{\theta_v'}{\overline{\theta_v}}$, (ii) a "pressure-buoyancy term" $g(\kappa-1)\frac{p'}{\bar{p}}$ that absorbs p' contributions to ρ', and (iii) hydrometeor loading gq_{HYD}'. Vertical acceleration profiles are generated for MBL-origin

[20] Smoothing trajectory output *w* in this manner improves the agreement between the left and right-hand sides of Eq. (5.5), presumably because it helps smooth out spurious parcel *w* tendencies resulting from errors in the spatiotemporal interpolation of parcel winds from the model grid.

trajectories seeded over the 16:00-18:00 period using the methods described in section 5.2.3, except that the vertical bin k width is reduced to 100 m to minimize the residual difference between parcel Dw/Dt and its forcing terms. Figure 5.2b shows the number of trajectories from each w_{MAX}-binned subsample used for computing vertical acceleration statistics as a function of height.[21]

Previous studies have used different basic-state definitions when computing the Eq. (5.5) right-hand terms from model output because of no unique definition of buoyancy (Zhang et al. 2000; Braun 2002; Fierro et al. 2012). Here, the hydrostatic base states for p, θ_v and q_{HYD} are defined in cylindrical (r, λ, z) coordinates as their respective horizontal averages over the 180° azimuthal arc centered on the parcel – for example:

$$\overline{\theta_v}(r,\lambda,z,t) = \frac{\sum_{j=\lambda-90}^{j=\lambda+90} \theta_v(r,j,z,t)}{n_j}, \qquad (5.6)$$

where λ is measured in degrees counterclockwise and n_j is the number of points used in the azimuthal sum. This definition rests on the assumptions that (i) nearby air radially inside (outside) of an eyewall air parcel should be warmer (cooler), due to the warm core structure; and (ii) the wavenumber-0 and -1 components of the V_T and θ_v fields are in thermal wind balance. Braun (2002) similarly defined departures from the base state as wavenumber-2 and higher perturbations. As in Braun (2002), the base state hydrometeor mixing ratio is excluded in Eq. (5.5) since it contributes to hydrostatic balance between $\overline{\theta_v}$ and $\bar{p}$.

[21] Statistics for all diagnostic variables other than the Eq. (5.5) terms use the full MBL-origin sample. The relatively large computational expense incurred from computing the hydrostatic base state at all trajectory positions motivated use of the smaller trajectory sample size for vertical momentum budgets.

The Fig. 5.3 schematic summarizes the numerical method used for computing the PGA along trajectories. First, hydrostatic base state pressures are defined using Eq. (5.6) applied to the pressure field at heights $z \pm \delta z$ relative to the parcel (r, λ, z) position, where $\delta z = 500$ m. Next, perturbation pressures p'_{ABOVE} and p'_{BELOW} are computed as the local p' averaged over a 2° arc centered on the parcel over the z to $z + \delta z$ and z to $z - \delta z$ layers, respectively. Finally, we compute PGA = $(p'_{ABOVE} - p'_{BELOW})/\bar{\rho}\delta z$.

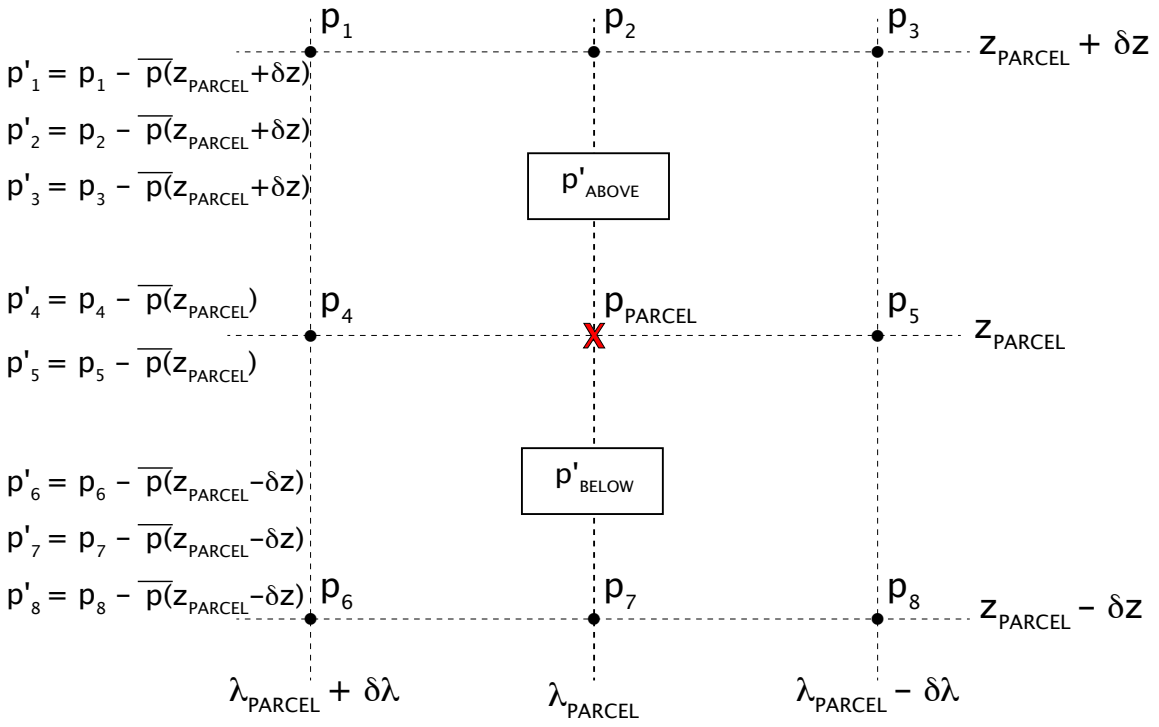

Fig. 5.3 Schematic illustrating the numerical technique used for computing the PGA. For a given parcel at coordinates ($r_{PARCEL}, \lambda_{PARCEL}, z_{PARCEL}$), perturbation pressures p'_{ABOVE} and p'_{BELOW} are computed as 6-gridpoint averages over the $\pm$ 1° arc surrounding λ_{PARCEL} and the vertical layer of thickness δz = 500 m above and below z_{PARCEL} respectively. Overbars denote basic state pressures computed using Eq. (5.6) applied to pressure and p-symbols denote local pressure values at gridpoints identified by subscripts. Therefore, $p'_{ABOVE} = (p'_1 + p'_2 + p'_3 + p'_4 + p'_5 + p'_{PARCEL}) / 6$ and $p'_{BELOW} = (p'_4 + p'_5 + p'_6 + p'_7 + p'_8 + p'_{PARCEL}) / 6$.

5.2.5 Updraft entrainment analysis

Previous theoretical and idealized modeling studies have identified two basic processes driving the entrainment of environmental air into cloudy updrafts: (i) turbulent mixing across the updraft outer edge; and (ii) local[22] radial inflow into the updraft region as required by mass continuity to balance the updraft acceleration, i.e. "dynamic entrainment" (Houze 1993; Morrison 2017). For simplicity, it is often assumed that mixing is sufficiently rapid such that a cloudy "updraft region" can be treated as a homogenous mass of air parcels with a well-defined boundary differentiating it from a subsaturated environment[23]. Here we follow Jorgensen et al. (1985) and define an "updraft element" surrounding trajectory positions where w exceeds 0.5 m s^{-1} and RH exceeds 95%. Rather than attempt to quantify dynamic and turbulent mixing processes, we instead define four new variables along trajectories that impact the trajectory parcel entrainment rate, as shown schematically in Fig. 5.4: (i) d_{EDGE} – the smallest distance in any Cardinal direction to the updraft element boundary; (ii) D_{AVG} – the mean updraft element diameter; (iii) $\theta_{e,ENV}$ – environmental θ_e; and (iv) RH_{ENV} – environmental RH. The latter two variables are averaged over a six-gridpoint line extending outward from d_{EDGE}.

[22] We use the term "local" here to describe lateral inflow into the updraft core driven by convective-scale mass continuity, which is different from the vortex-scale radial inflow that constitutes a portion of the TC secondary circulation.

[23] As discussed in Houze (1993) pp. 239-247, laboratory and field experiments have shown that mixing of cloudy air with its environment can occur in discrete "gulps" on slow enough timescales to render the updraft region thermodynamically inhomogenous to some degree.

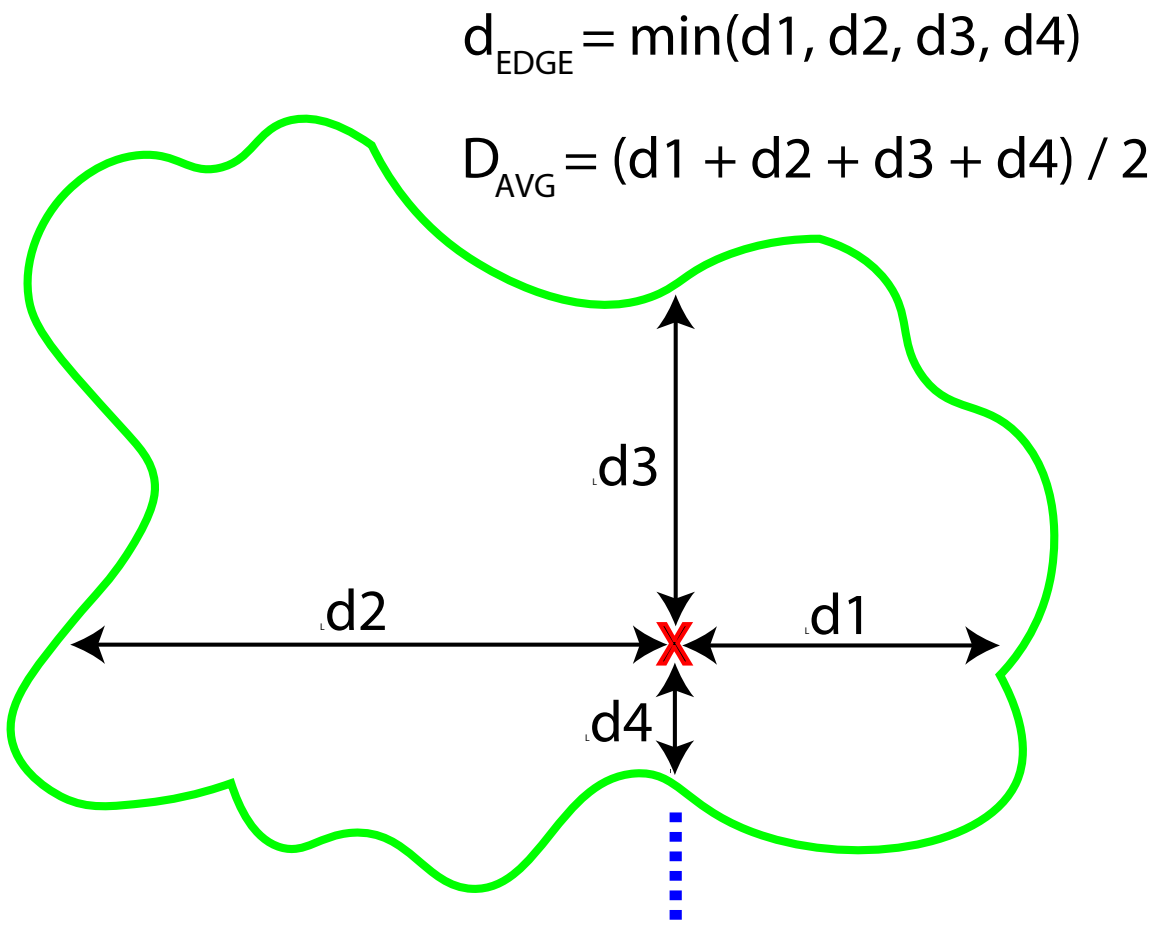

Fig. 5.4 Schematic showing the basic parameters used to study the impacts of entrainment on trajectory updrafts. The green curve marks the outer boundary of the local updraft element, defined by $w > 0$ m s^{-1} and relative humidity > 95%. Distances d1, d2, d3, and d4 are measured in the four Cardinal directions from the parcel position, denoted by the red "X" symbol, to the updraft element boundary. Symbols "d_{EDGE}" and "D_{AVG}" denote the smallest distance in any Cardinal direction to the updraft element boundary and the mean updraft element diameter, respectively. Environmental θ_e ($\theta_{e,ENV}$) and relative humidity (RH_{ENV}) are averaged along the blue dashed line segment.

5.3 Analysis of convective burst structure and thermodynamics

We begin by examining the time evolution of CB updraft element "CB-E1", shown in Figure 5.1 near its peak intensity at WRF prediction time 16:10. In the upper troposphere, the updraft is roughly 10 km wide and surrounded by subsidence currents, with the peak intensity of $|w| > 5$ m s^{-1} directed northwestward and southeastward (Fig. 5.1a). The

northwestward-directed subsidence current originates near the tropopause, roughly denoted by the 375K isentrope (Fig. 5.1b), and it may contribute to the development of the upper-level warm core by entraining stratospheric air that adiabatically warms while descending (Zhang and Chen 2012; CZ13). A vertical cross section taken through CB-E1 reveals a ~ 3 km-wide core of extreme w exceeding 30 m s^{-1} that extends over the z = 10-14 km layer (Fig. 5.1b). The local potential temperature (θ) anomaly co-located with the updraft core may result from LHR exceeding adiabatic cooling.

5.3.1 Three-dimensional trajectory

To better understand the thermodynamics contributing to the extreme w found in Wilma's CBs, let us follow the history of a parcel that passes through CB-E1 at 16:10, identified herein as Trajectory-CB1. Figures 5.5a and 5.5b show its three-dimensional path, beginning in the MBL at t = 14:00 and ending at its seed position at z = 14 km, t = 18:00. Between 14:00 and 15:40, the parcel remains in the MBL while spiraling cyclonically inward. After 15:40, Trajectory-CB1 accelerates upward monotonically, completing just one half circle transit around the western and southern eyewall before achieving its 30.6 m s^{-1} w_{MAX} around z = 13 km, t = 16:10. By comparison, Trajectory-SC, which leaves the MBL at a similar time but is more representative of the background secondary circulation with w_{MAX} = 8.9 m s^{-1}, completes one and a half loops around the eyewall during ascent to z = 14 km (Figs. 5.5c,d). Returning to Trajectory-CB1, we find a rapid upward deceleration after 16:10; by 16:15 its w approaches zero at z ~ 15.5 km. Thereafter the parcel translates cyclonically around the upper-level eyewall (Figs. 5.5a,b) while its w oscillates roughly sinusoidally between +/- 2 m s^{-1} with a ~ 45 min period (not shown) – possibly forced by convectively-generated gravity waves. One notable exception is a 5-min window after

16:39 when the parcel executes a sharp anticyclonic loop while descending from a $z \sim 17.5$ km peak height (Figs. 5.5a,b) that it reached after having been lofted by a 4 m s^{-1} updraft (not shown).

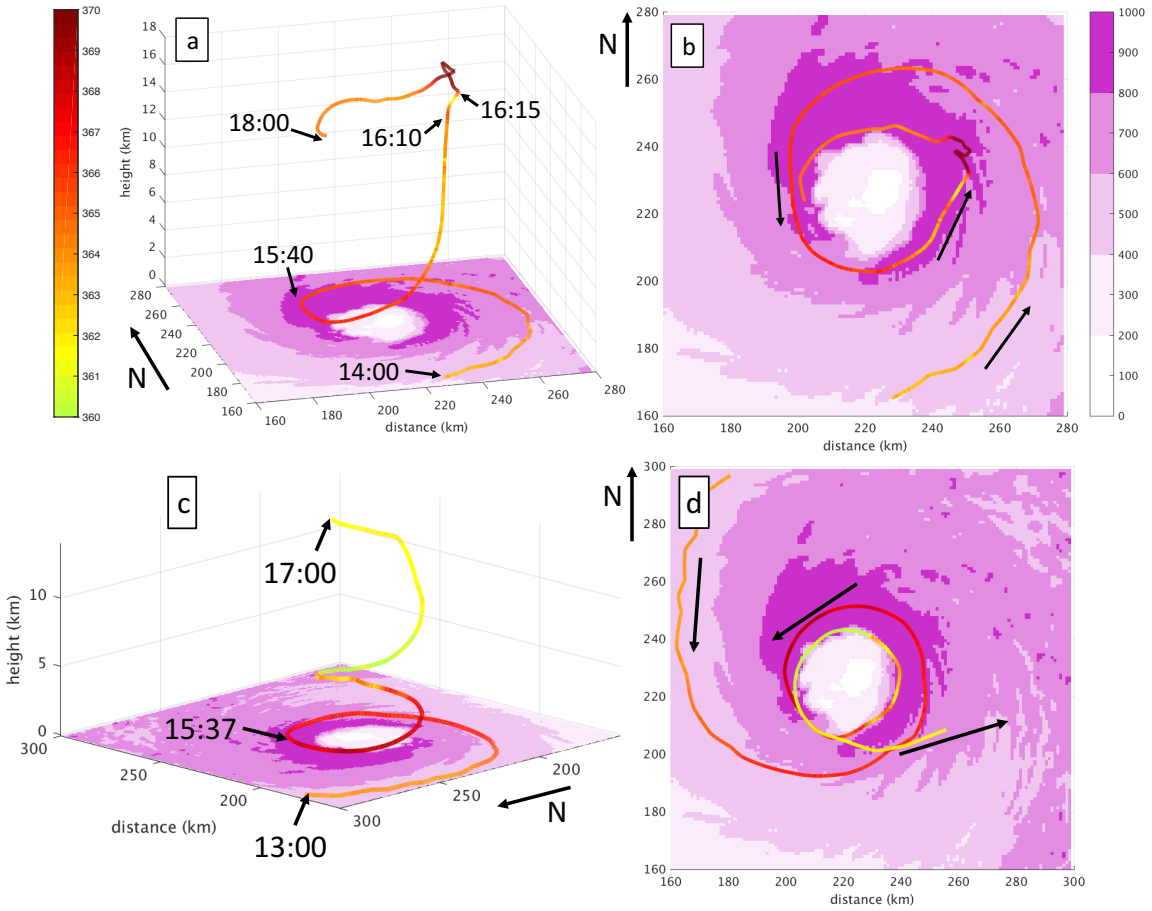

Fig. 5.5 (a) Three-dimensional and (b) x-y planar projection of Trajectory-CB1, color-coded by θ_e (K). WRF prediction times (hh:mm format) for selected points along the trajectory described in the text are also shown in (a), with arrows in (b) pointing in the direction of parcel movement in WRF model time. Purple shading denotes the sum of latent and sensible ocean surface heat fluxes (W m^{-2}) at 15:00. (c),(d) As in (a),(b) but for Trajectory-SC.

5.3.2 Parcel θ_e evolution

A parcel's θ_e is conserved under inviscid pseudoadiabatic ascent; however, for real TC updrafts it is not strictly conserved because Lagrangian θ_e sources and sinks include the latent heat of fusion, cloud-radiative interactions, mixing, and ocean surface heat fluxes (Bolton 1980; Zhang et al. 2002). While transiting the MBL between 14:00 and 15:40, Trajectory-CB1 experiences a 2.96K θ_e increase. This agrees closely with the 2.79K $\Delta\theta_e$ value predicted by Liu et al. (1999) to result from upward ocean surface sensible and latent heat fluxes, using the parcel $\overline{\theta_e}$, $\bar{T}$, $\bar{p}$, ΔT, Δp, and Δq_v from 14:00-15:40 (see their Footnote 1). Notably, the Trajectory-CB1 parcel moves over locally maximized ocean surface heat fluxes around 15:00 (Figs. 5.5a,b). In section 5.4.2 we will revisit the question of whether CB parcels, on average, experience higher ocean surface heat fluxes compared to the background secondary circulation prior to ascent.

At 15:40, when the Trajectory-CB1 parcel ascends out of the MBL, we find it on the northwestern edge of the eyewall updraft core where the radial inflow is locally enhanced, as indicated by a green triangle in Figs. 5.6a,b. Inner-core MBL θ_e is maximized along the eye-eyewall interface, perhaps originating from the surface layer at the eye center and then being drawn into the eyewall updraft (Liu et al. 1999; Braun 2002). An azimuth-height cross section, slanted outward to align with the *r-z* planar projection of Trajectory-CB1 above the MBL, reveals the parcel to be near an updraft element "E1" that extends from the MBL upward to $z \sim 2.5$ km; E1 is also co-located with a local column of higher θ_e air (Fig. 5.7a)[24]. Most columns in this cross section exhibit potentially unstable

[24] While it is true that the azimuthal-height cross-section shown in Fig. 5.7a is taken several km radially inside of the Trajectory-CB1 location at 15:40, the parcel is still

conditions, i.e., with θ_e rapidly decreasing above the MBL, reaching a minimum around z = 4 km and increasing with height above (Fig. 5.7a). Although other TC modeling studies have documented a midtropospheric eyewall θ_e minimum (Liu et al. 1999; Braun 2002), the reader should note that for most azimuths, this cross section is taken just outside of the eyewall updraft core due to asymmetry in the latter (Fig. 5.7a-d).

moving radially inward at this time. By 15:45 the parcel has moved inside the 2-km wide region used for averaging the variables shown in Fig. 5.7b-f (not shown).

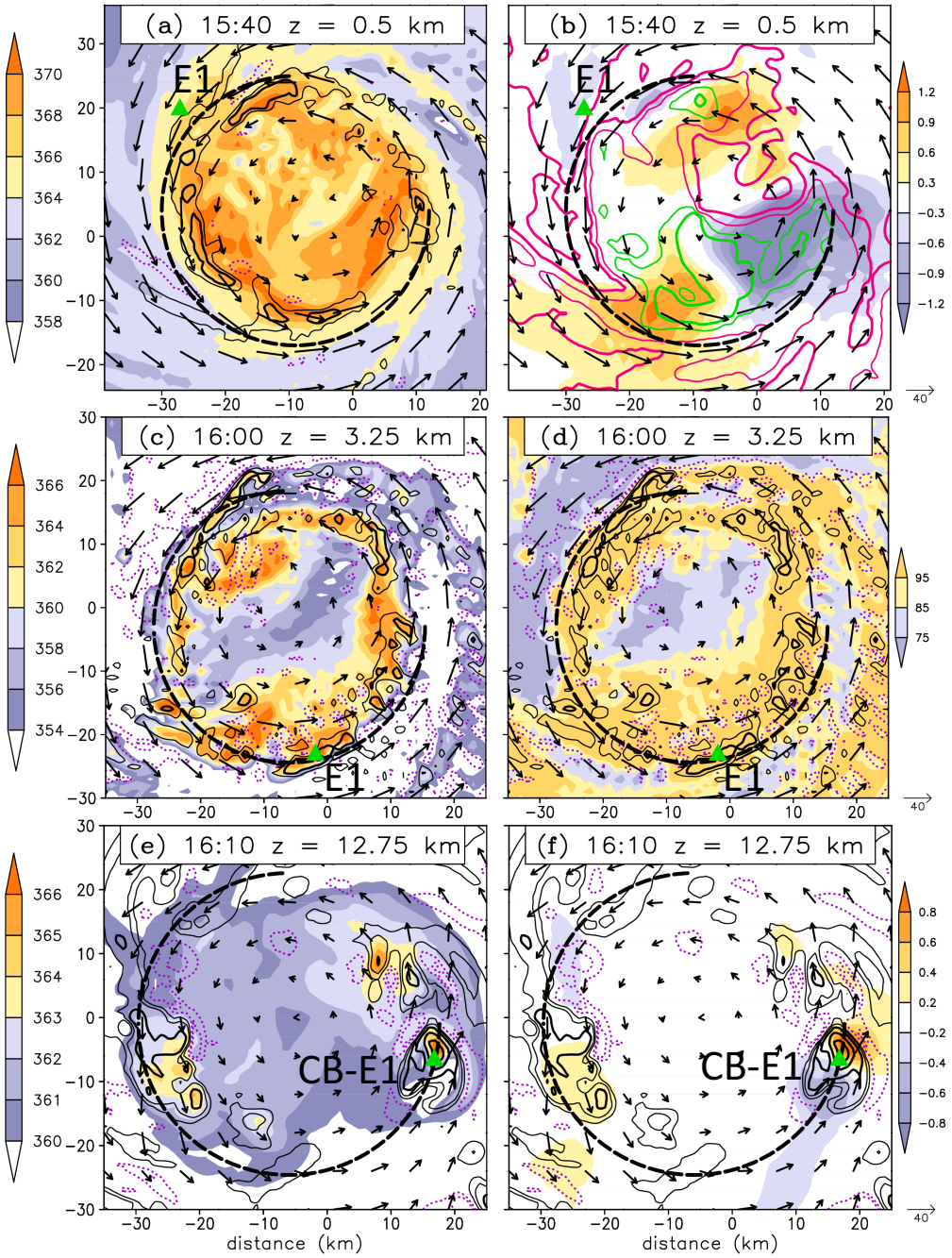

Fig. 5.6 (a) WRF-predicted t = 15:40 and z = 0.5 km θ_e (shaded, K), horizontal storm-relative flow vectors (m s^{-1}) and vertical motion (w, black contoured for 1 and 2 m s^{-1}, purple dotted contoured for -1 m s^{-1}). Green triangle denotes the Trajectory-CB1 position, currently at z = 0.45 km. (b) As in (a) but with the z = 0.5 km p' field (shaded, hPa) and radial winds (green contoured for 2, 5 and 10 m s^{-1}; magenta contoured for -10,-5 and -2 m s^{-1}). (c) and (d) As in (a) and (b) but for t = 16:00 and z = 3.25 km, with the current z = 3.27 km Trajectory-CB1 position. In (c) and (d), w is thin-black (thick-black) contoured for 2 (5) m s^{-1} and purple-dotted contoured for -3/-1 m s^{-1}; relative humidity (%) is shaded in (d). (e) and (f) As in (a) and (b) but for t = 16:10 and z = 12.75 km, with the current z = 12.83 km Trajectory-CB1 position. For (e) and (f), w (m s^{-1}) is contoured (thin solid black, 2/5; thick solid black, 10/20/30; dotted purple, -4/-2) and (f) shows the z = 15 km p' field (shaded, hPa). Dashed arc denotes the azimuthal-height section shown in Fig. 5.7. Letter labels E1 and CB-E1 denote the updraft elements discussed in the text.

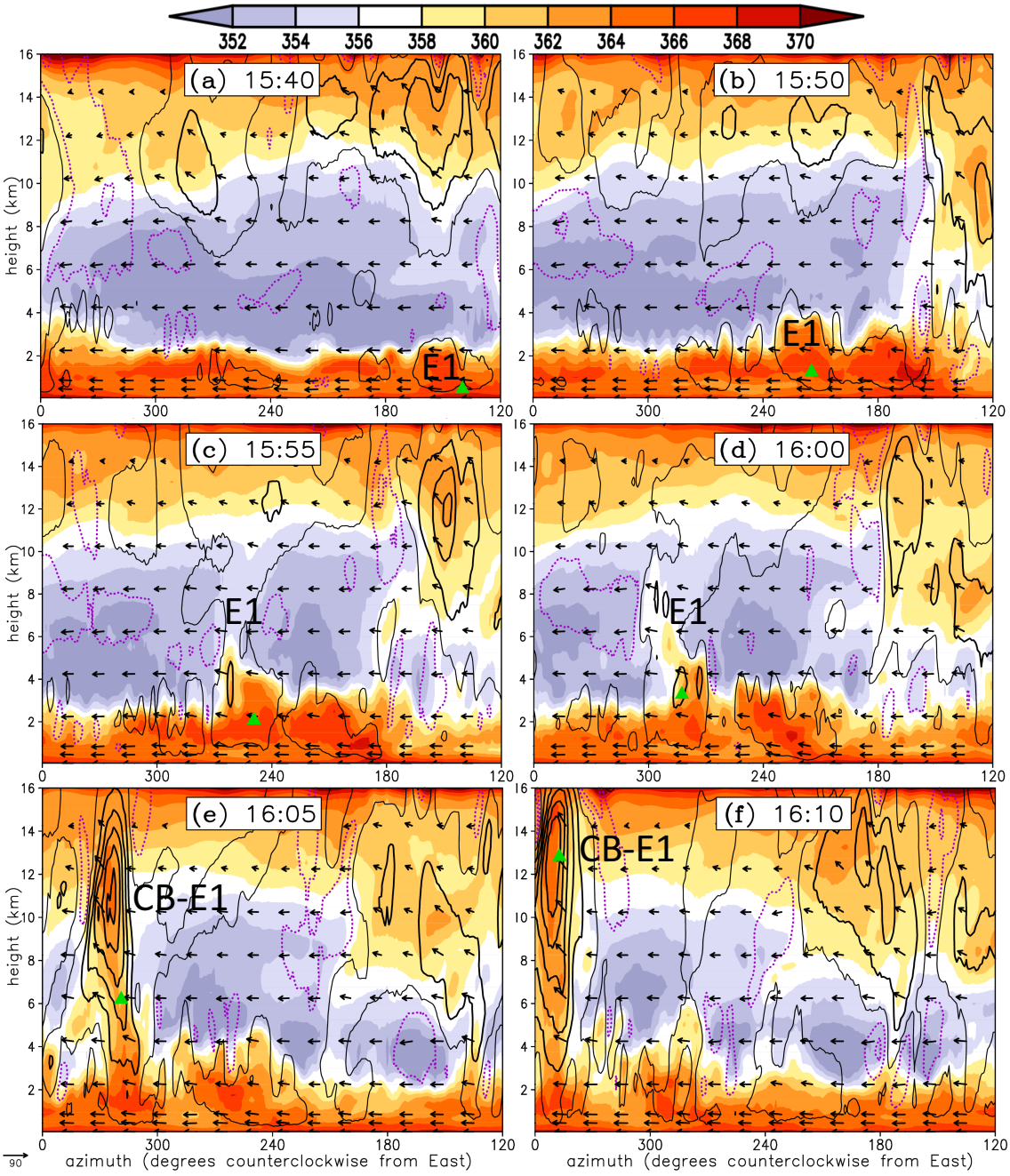

Fig. 5.7 (a) Time series of the azimuth-height cross sections of WRF-predicted θ_e (shaded, K) and w (thin black contour for 1 m s^{-1}; thick black contours for 5/10/15/20/25/30 m s^{-1}; purple dotted contours for -1/-3 m s^{-1}) with in-plane flow vectors (m s^{-1}; vertical motions multiplied by 3) at 15:40. (b),(c),(d),(e),(f) As in (a) but for WRF prediction times 15:50, 15:55, 16:00, 16:05, and 16:10. The conical surface defined for this cross-section slopes outward from r = 21 km, z = 1 km to r = 24 km, z = 15 km, and all variables shown here are averaged over a 2-km wide radial band centered on the cross section. Letter labels E1 and CB-E1 denote the updraft elements discussed in the text, and the green triangle marks the position of Trajectory-CB1.

Trajectory-CB1 θ_e decreases from 366 to 363 K over the next 25 minutes while the parcel ascends to z = 6 km (Fig. 5.5a), likely a consequence of some environmental entrainment. The parcel remains embedded within E1 as it rotates cyclonically with a phase speed close to the 35.6° (5 min^{-1}) mean angular velocity obtained by averaging V_t in the outwardly-sloping cross-section over λ = 120° – 360°, z = 0 – 6 km, t = 15:40-16:05 (Figs. 5.6a-d and 5.7a-e). Between 15:40 and 15:50, E1 remains confined to the low-to-middle troposphere while gradually deepening (Figs. 5.7a,b). By 15:55, E1 has deepened – now extending through the full troposphere, although its intensity remains relatively modest (Fig. 5.7c). Meanwhile, the higher θ_e anomaly inside E1 grows upward while remaining rooted in the MBL (Figs. 5.7a-c); in some aspects, the evolution of E1 resembles Morton et al. (1956)'s analytical model of a plume growing above a steady buoyancy source (Morrison 2017). E1 therefore appears to "precondition" the local environment above the rising Trajectory-CB1 parcel with higher θ_e air relative to the midlevel mesoscale environment, where θ_e < 356 K; this may at least partially explain why Trajectory-CB1 experiences significantly less θ_e reduction in the midtroposphere, compared to background secondary circulation trajectories such as Trajectory-SC (cf. 5.5a,c) and others (not shown) that are also saturated throughout ascent. We shall examine updraft entrainment more systematically in section 5.4.3 using the full trajectory sample.

E1 explosively intensifies between 16:00 and 16:05, particularly in the upper troposphere where peak w increases from < 5 m s^{-1} to > 25 m s^{-1} (Figs. 5.7e,f). Convective burst element "CB-E1" has been born. At 16:05 it extends from near the top of the MBL to above z = 16 km, tilting cyclonically downwind below z = 8 km and becoming vertically upright for higher levels (Fig. 5.7e). Over the next 5 minutes, as CB-E1 approaches its peak

intensity, the height of maximum *w* shifts upward from z ~ 11 km to z ~ 13 km while CB-E1 becomes vertically aligned through the entire troposphere – perhaps a consequence of the lower (upper) portion being advected cyclonically downwind by a stronger (weaker) layer-mean V_T (Figs. 5.7e,f). The Trajectory-CB1 parcel accelerates upward through the CB-E1 core between 16:05 and 16:10, ascending from z = 6 km to z = 13 km (Figs. 5.7e,f). The parcel's θ_e increases by ~ 1 K over this period, likely due to a combination of (i) fusion LHR from ice-phase microphysical processes inside the parcel (Fierro et al. 2012; M15); and (ii) mixing with adjacent higher-θ_e air previously warmed by fusion LHR in other parcels (Figs. 5.6e and 5.7e,f).

5.3.3 Parcel vertical momentum budget

The positive θ_e anomaly inside the intensifying CB-E1 relative to nearby areas at the same height (Figs. 5.6c,e and 5.7a-f) suggests that the aggregate mass of parcels comprising CB-E1 is thermally buoyant relative to the hydrostatic base state (section 5.2.4) and experiences upward acceleration. To confirm this, and to better understand the relative impacts of hydrometeor loading and the PGA, we now compute vertical acceleration terms from Eq. (5.5) along Trajectory-CB1, with a focus on the period of continuous parcel ascent through the z = 0.25 - 15.5 km layer.

Figure 5.8a shows vertical profiles along Trajectory-CB1 of *w*, BA, PGA, as well as the thermal ($g\frac{\theta_v'}{\overline{\theta_v}}$) and hydrometeor loading (gq_{HYD}') contributions to the BA. We find a positive BA that increases nearly monotonically with height from the upper MBL (z = 0.25 - 0.5 km) to a maximum value of ~ 250 m s^{-1} h^{-1} near z = 11.5 km except for a brief dip below zero around z = 1.5 km. The Eq. (5.5) $g(\kappa - 1)\frac{p'}{\bar{p}}$ term (not shown) is positive and

similar in magnitude to $g\frac{\theta_v'}{\overline{\theta_v}}$ below z = 1.5 km - consistent with the parcel originating from a region of negative low-level p' (Fig. 5.6b), whereas for higher levels it becomes 1-2 orders of magnitude smaller than $g\frac{\theta_v'}{\overline{\theta_v}}$. Although the $g\frac{\theta_v'}{\overline{\theta_v}}$ and gq_{hyd}' terms are comparably strong within an order or magnitude, the downward-directed hydrometeor loading is insufficient to offset the very large thermal buoyancy anywhere between z = 2 km and z = 15 km. Two positive BA spikes near z = 0.4 and z = 0.9 km, resulting from nearly equal ~ +15 m s^{-1} h^{-1} contributions from $g\frac{\theta_v'}{\overline{\theta_v}}$, $g(\kappa-1)\frac{p'}{\bar{p}}$, and gq_{hyd}', appear to have lifted the parcel out of the MBL, given the generally negative PGA below z = 2 km. Between z = 3 km and z = 12.5 km, the PGA is alternately positive and negative while remaining significantly weaker than the BA. Note, however, the sharp negative PGA spike in the upper troposphere, which we shall examine shortly. Figure 5.8b shows that the sum BA + PGA is in generally good agreement with Dw/Dt; the lower WRF vertical resolution in the upper troposphere (CZ11) may partially explain the greater residual above z = 8 km between the left- and right-hand sides of Eq. (5.5), excluding the mixing term.

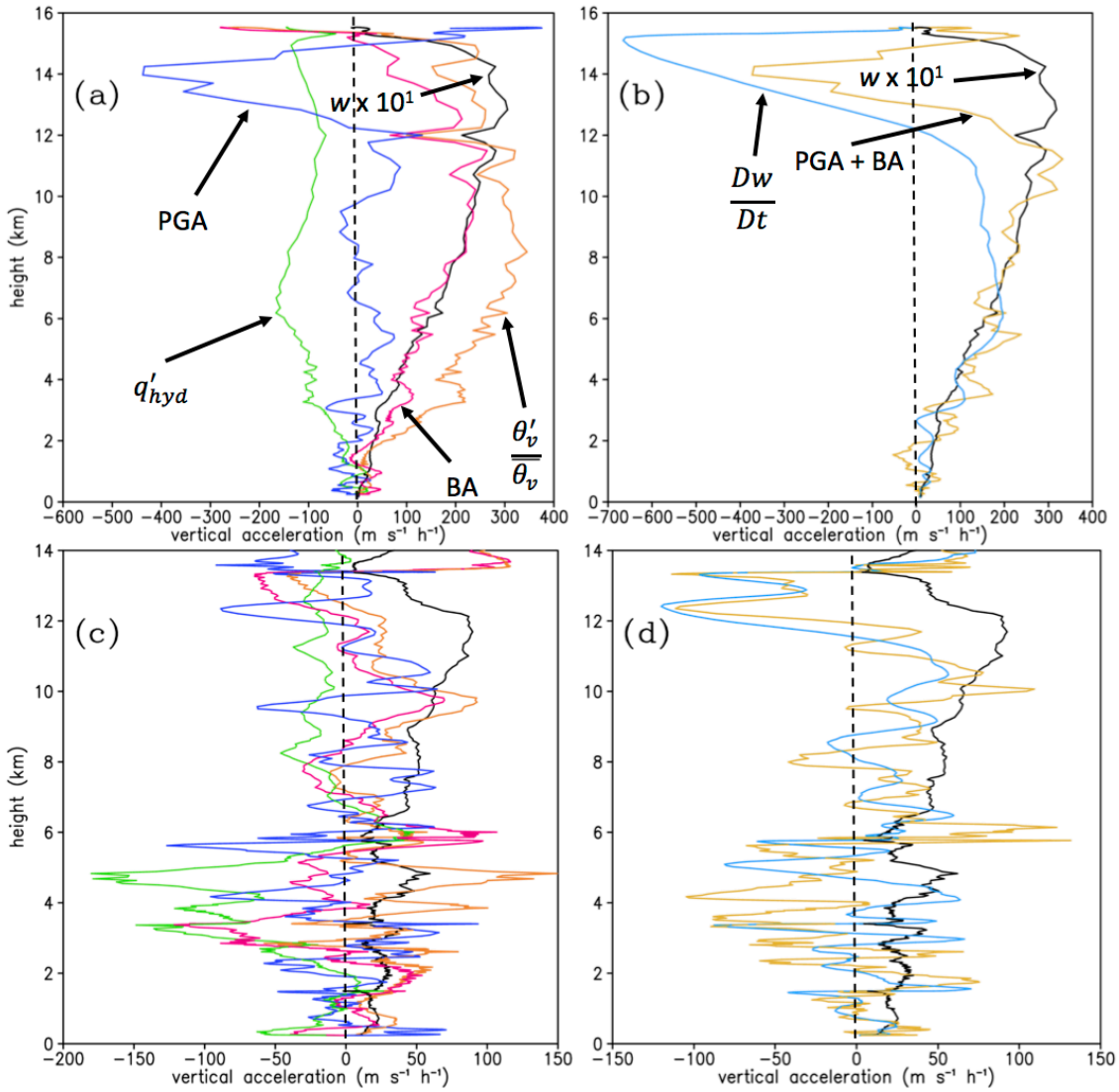

Fig. 5.8 (a) BA (m^{-1} s^{-1} h^{-1}; magenta line), with its thermal (m^{-1} s^{-1} h^{-1}; orange line) and hydrometeor loading (m^{-1} s^{-1} h^{-1}; green line) components, PGA (m^{-1} s^{-1} h^{-1}; blue line), and w (× 10 m s^{-1}; black line, all plotted as a function of height along a portion of Trajectory-CB1. (b) As in (a), but with vertical acceleration Dw/Dt (m^{-1} s^{-1} h^{-1}; light blue line) and the sum of the buoyant and vertical perturbation pressure gradient acceleration (m s^{-1} h^{-1}; light orange line). (c) and (d) As in (a) and (b) but for Trajectory-SC. Note the different magnitudes of the budget terms between the two trajectories [see the horizontal axes between (a), (b); and (c), (d)].

To better understand the physical origins of the Trajectory-CB1 vertical acceleration terms, let us examine the distribution of θ_v', q_{HYD}', and p' in an azimuthal-height cross section through CB-E1 and its environment, shown in Figure 5.9. The large

positive θ_v' and q_{HYD}', co-located with the mid-to-upper level CB-E1 core (Figs. 5.9a,b), strongly suggest that LHR from condensation and fusion generates the positive deep-layer thermal buoyancy responsible for the parcel's extreme w_{MAX} (Fig. 5.8a). Unfortunately, microphysical heating tendency output variables are not available for this WRF prediction, and therefore we cannot further study the relative contributions of liquid-phase (i.e. condensation) and ice-phase (i.e. freezing, riming, and deposition) processes toward parcel θ_v'.

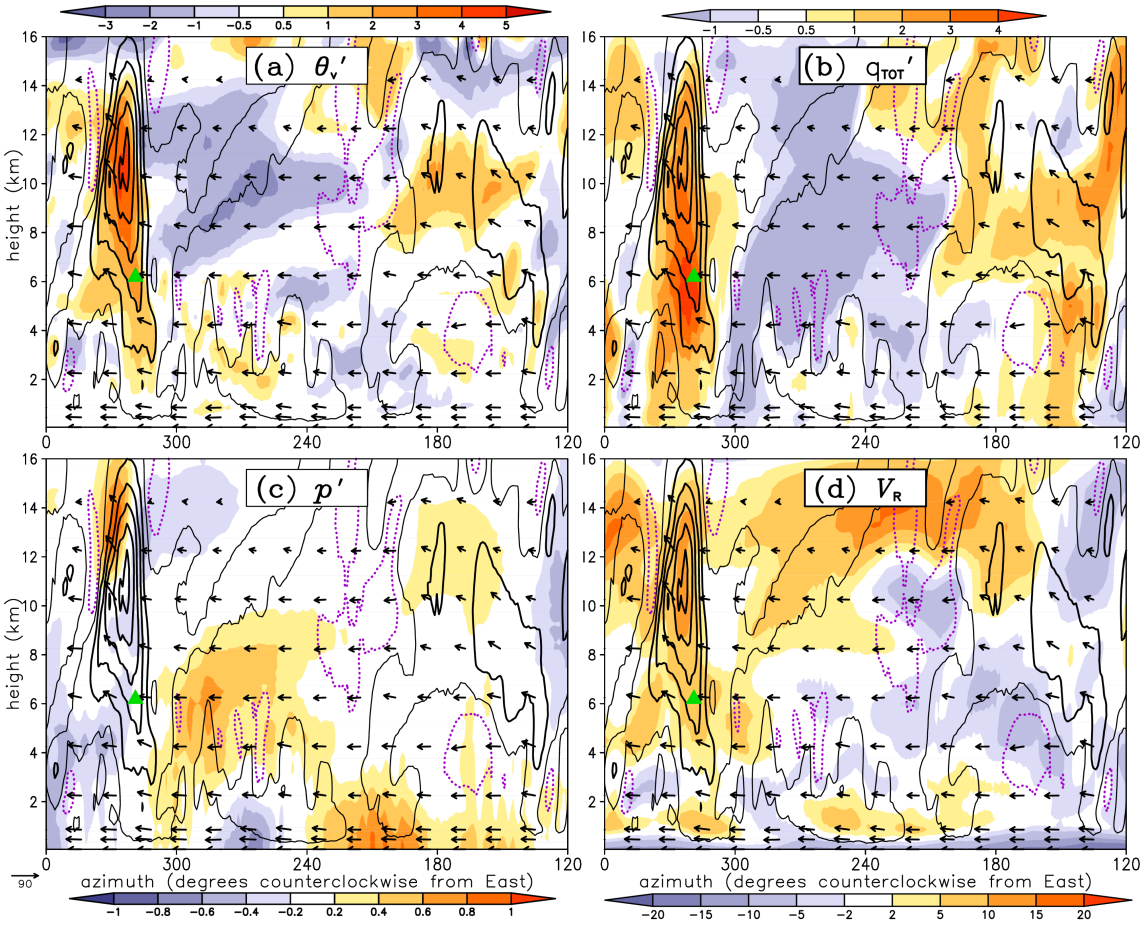

Fig. 5.9 (a) As in Fig. 5.7 but for WRF prediction time 16:05, with perturbation virtual potential temperature (θ_v', shaded, K). (b) As in (a) but with perturbation total hydrometeor mixing ratio (q_{TOT}', shaded, g kg^{-1}). (c) As in (a) but with perturbation pressure (p', shaded, hPa). (d) As in (a), but for radial wind (V_R, shaded, m s^{-1}). All perturbation variables shown here are defined with respect to the hydrostatic base state (section 5.2.4).

Our finding of a comparatively weak PGA through much of this parcel's ascent differs from Braun (2002), who computed an upward (downward) PGA that offset (nearly offset) a(n) downward (upward) BA within (above) the MBL along a trajectory rising through simulated Hurricane Bob (1991)'s eyewall (see his Fig. 17). Idealized simulations of upright nonrotating buoyant updrafts predict a downward-directed PGA opposing the BA (Markowski and Richardson 2010; Morrison 2016), provided that VWS – and therefore dynamic contributions to the p' field - is small. Conceptually, this can be understood from a mass continuity perspective, where a positive p' at the updraft top is needed to push surrounding air laterally outward and a negative p' at the updraft bottom is needed to draw surrounding air inward to fill its wake. Using similar assumptions, Morrison (2016) developed an analytical updraft model in which the downward PGA magnitude is proportional to the updraft width-to-height ratio; thus it is possible that the full-tropospheric depth of CB-E1 may have helped to keep the PGA relatively weak below z = 12.5 km. Nevertheless, a p' field consistent with Morrison's (2016) analytical model surrounds the CB-E1 $w > 25$ m s^{-1} core, with positive (negative) p' above (below) it (Fig. 5.9c). This local p' couplet generates the strongly negative PGA over the z = 12.5-15 km layer (confirmed by replotting Fig. 5.9c for 16:10, not shown) that forces rapid vertical deceleration of the Trajectory-CB1 parcel (Figs. 5.8a,b). The positive p' anomaly found above and cyclonically downwind of CB-E1 (Figs. 5.6f, 5.9c) resembles the "meso-high" structures observed above continental mesoscale convective systems (Fritsch and Maddox 1981), albeit on a smaller scale. It may be hydrostatically forced by a cold anomaly directly above it (cf. Figs. 5.1b and 5.6f), with the latter perhaps generated by adiabatic cooling in parcels overshooting the equilibrium level. Dynamic contributions to the p' field around

CB-E1 may also result from the interaction of the updraft with the horizontal (Zhang et al. 2000) and vertical (Rotunno and Klemp 1982) shear of V_T, and they could be examined in a future study.

By contrast, Trajectory-SC has a bimodal *w* profile, with maxima of ~ 5 m s^{-1} and ~ 9 m s^{-1} near z = 5 km and z = 12 km, respectively (Fig. 5.8c). Comparing its vertical acceleration terms in the upper MBL (z = 0.25-0.5 km) with Trajectory-CB1, we find a similarly weak positive $g\frac{\theta_v'}{\overline{\theta_v}}$. However, unlike Trajectory-CB1, MBL gq_{HYD}' is negative and MBL PGA is positive[25] (cf. Figs. 5.8a,c). Over the z = 0.5 – 5 km layer, thermal buoyancy is positive but considerably weaker than that of Trajectory-CB1. As a result, the BA becomes negative over the z = 3-5.5 km layer due to $g\frac{\theta_v'}{\overline{\theta_v}}$ being unable to offset gq_{HYD}', which helps to decelerate parcel *w* to near zero around z = 6 km (Fig. 5.8c). The recovery of upward motion at higher levels results in part from rapid hydrometeor unloading, given the modest thermal buoyancy in the upper troposphere. The left- and right-hand sides of Eq. (5.5) show fairly good agreement for this parcel (Fig. 5.8d). In several aspects, Trajectory-SC resembles the tropical oceanic squall line updraft trajectory shown in Fierro et al. (2012, see their Fig. 9); similarities include the PGA lifting the parcel out of a heavy-precipitating portion of the MBL and the bimodal *w* profile. Interestingly, both Trajectory-SC and Trajectory-CB1 begin their eyewall ascent with similarly high θ_e (cf. Figs. 5.5a,c). It is possible that the weaker mid-to-upper level thermal buoyancy in the former (cf. Figs. 5.8a,c) results at least in part from greater dilution by low-θ_e environmental air, as

[25] The Eq. (5.5) "pressure-buoyancy term" is also weakly positive in the MBL, averaging around 8 m s^{-1} h^{-1} (not shown).

discussed in section 5.3.2 (cf. Figs. 5.5a,c).

5.4 Trajectory updraft statistics

In the preceding section we compared vertical acceleration profiles between two of Wilma's updraft parcels: one from an intense CB and the other representative of the background secondary circulation. We found that the CB parcel's extreme ~ 30 m s^{-1} w_{MAX} results from large thermal buoyancy exceeding 200 m s^{-1} h^{-1} in the middle and upper troposphere. Thermal buoyancy in the secondary circulation parcel, by contrast, is considerably smaller, generally < 50 m s^{-1} h^{-1}. Although both parcels possess similar θ_e and thermal buoyancy while ascending out of the MBL, the secondary circulation parcel experiences more substantial θ_e reduction in the midtroposphere, suggesting that the entrainment of cooler and/or drier environmental air may have prevented it from achieving large thermal buoyancy. We now determine whether these results apply more generally to Wilma's CBs, using data from all 43,347 MBL-origin backward trajectories stratified by w_{MAX} into five subsamples per the procedure described in section 5.2.3.

5.4.1 General thermodynamic and microphysical characteristics

Figure 5.10a shows $\overline{w'_{360}}(k)$ profiles for the w_{MAX}-8, w_{MAX}-12, w_{MAX}-16, w_{MAX}-20, and w_{MAX}-CB trajectory subsamples, where $w'_{360,i}(k)$ is the perturbation from azimuthally averaged $w(r, \lambda, z, t)$ along the i^{th} trajectory, averaged over 250-m layer k, and the overbar denotes an average over all trajectories in the subsample. Note that the "360" subscript used for primed variables emphasizes that the perturbation is computed from the azimuthal average; primed variables without this subscript described elsewhere in this study are perturbations from the hydrostatic base state (section 5.2.4). Figure 5.10a also shows the number of trajectories in each subsample. The largest group, w_{MAX}-12 (19296), comprises

~ 45% of all MBL-origin updrafts, and we shall consider it representative of the background secondary circulation. Above z = 3 km $\overline{w'_{360}}(k)$ becomes larger with increasing subsample w_{MAX}, and the $\overline{w'_{360}}(k)$ spread among subsamples becomes maximized in the upper troposphere. Interestingly, this trend reverses over the z = 1.5 – 2.5 km layer, where w_{MAX}-CB trajectories have statistically significant smaller $\overline{w'_{360}}(k)$ compared to w_{MAX}-12 trajectories. The w_{MAX}-16, w_{MAX}-20, and w_{MAX}-CB $\overline{w'_{360}}(k)$ profiles are all unimodal with upper tropospheric maxima. These results imply that during early RI, localized stronger updrafts embedded in Wilma's eyewall tend to peak in the upper troposphere, consistent with the cumulative contoured frequency by altitude diagram (CCFAD) analysis of M15 (see their Fig. 8). On the other hand, the w_{MAX}-8 and w_{MAX}-12 $\overline{w'_{360}}(k)$ profiles are bimodal, like the Trajectory-SC1 w profile (cf. Figs. 5.8c, 5.10a). Previous modeling studies (Fierro et al. 2009; Wang 2014; M15) and observations (Hildebrand et al. 1996; May and Rajopadhyaya 1996) have found similar bimodal structures in modestly strong tropical oceanic convective updrafts, generally attributing the midlevel minimum to hydrometeor loading and enhanced static stability and the upper-level maximum to hydrometeor unloading and fusion LHR.

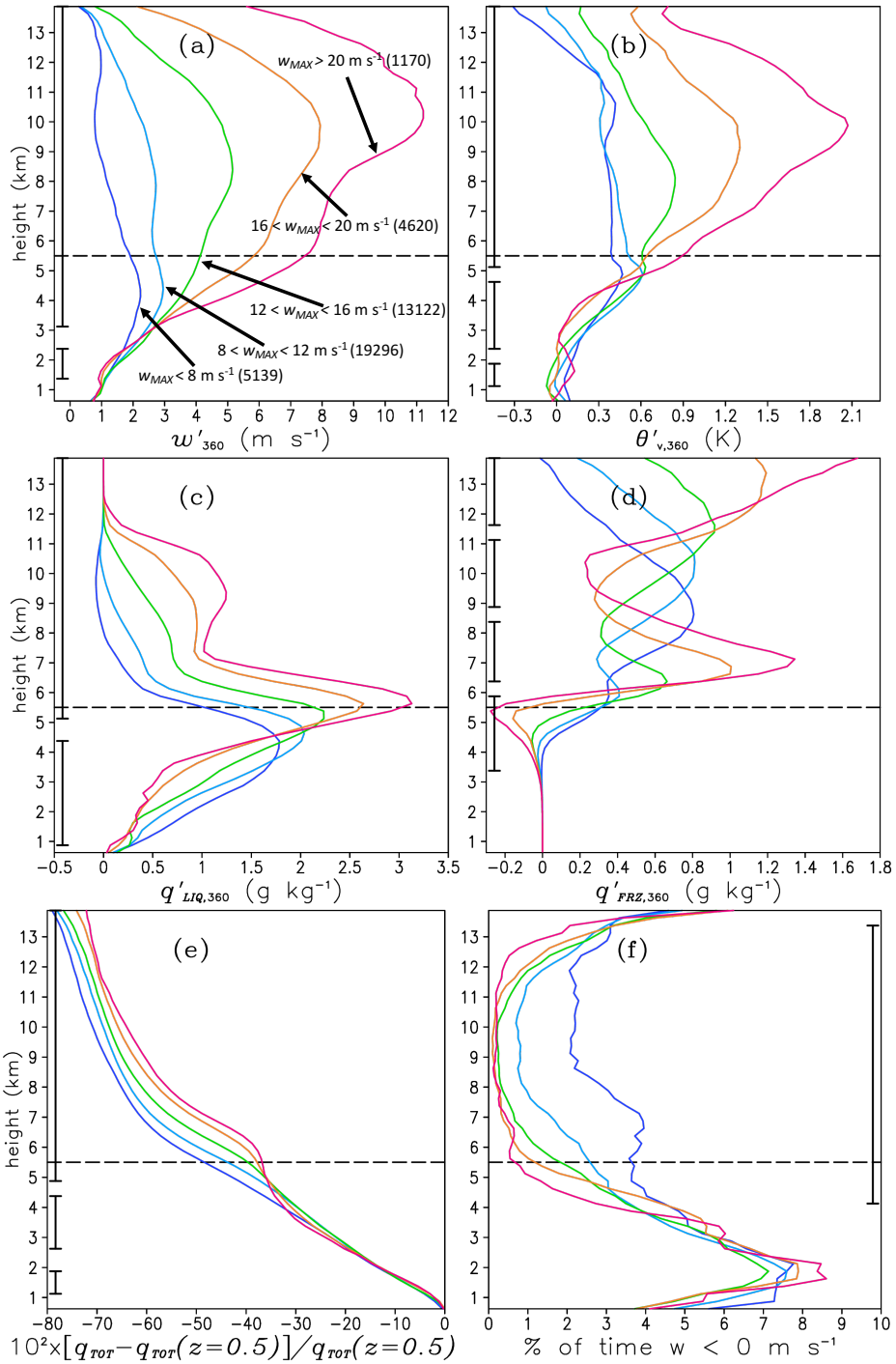

Fig. 5.10 Vertical profiles of the mean (a) perturbation vertical motion w'_{360} (m s^{-1}), (b) perturbation virtual potential temperature $\theta'_{v,360}$ (K), (c) perturbation liquid hydrometeor mixing ratio $q'_{LIQ,360}$ (g kg^{-1}), (d) perturbation frozen hydrometeor mixing ratio $q'_{FRZ,360}$ (g kg^{-1}), (e) water fallout percentage, and (f) percent of time over each 250-m vertical layer that parcel experiences downward motion. Mean values are computed for each sub-sample of updraft backward trajectories binned by w_{MAX}, as shown by arrows in (a), with the number of trajectories for each sub-sample given inside parentheses. Bracketed lines enclose vertical layers where the w_{MAX}-12 and w_{MAX}-CB sample mean differences are statistically significant at the 95% level. Perturbation variables shown in (a)-(d) are computed with respect to the azimuthal mean.

The w_{MAX}-16, w_{MAX}-20 and w_{MAX}-CB mean virtual potential temperature anomaly $\overline{\theta'_{v,360}}(k)$ profiles have similar shapes to their $\overline{w'_{360}}(k)$, with respective upper-tropospheric maxima of 0.8, 1.3, and 2.0K about 1 km lower than the heights of their respective maximum $\overline{w'_{360}}(k)$ (Fig. 5.10b). By comparison, the w_{MAX}-8 and w_{MAX}-12 $\overline{\theta'_{v,360}}(k)$ profiles are flatter, with broad maxima of ~ 0.5 K extending from the melting level to z = 11 km. Absolute differences in $\overline{\theta'_{v,360}}(k)$ between the subsamples are smaller below the melting level; in fact, $\overline{\theta'_{v,360}}(k)$ is statistically significantly smaller for w_{MAX}-CB compared to w_{MAX}-12 over the z = 2.4 – 4.7 km layer (Fig. 5.10b). The tendency for $\overline{w'_{360}}(k)$ and $\overline{\theta'_{v,360}}(k)$ to increase with subsample w_{MAX} above the melting level is consistent with positive anomalies of supercooled liquid water $\overline{q'_{LIQ}}(k)$ (Fig. 5.10c) and frozen hydrometers $\overline{q'_{FRZ}}(k)$ (Fig. 5.10d) also increasing with subsample w_{MAX} above the melting level. We also see that on average, the stronger updrafts experience greater hydrometeor retention above the melting level (Fig. 5.10e).

The results shown in Figs. 5.10a-f imply a "positive feedback" mechanism whereby stronger updrafts above z = 3 km loft greater quantities of supercooled water above the melting level, which in turn increase parcel thermal buoyancy through fusion LHR (Fierro et al. 2009, 2012; M15), leading to greater vertical accelerations in the upper troposphere. Next, we ask: what low- and mid-level processes give some parcels – including CBs - greater updraft speeds as they approach the melting level, compared to the background secondary circulation?

5.4.2 Boundary layer thermodynamics

Can a parcel's w_{MAX} be statistically related to its MBL thermodynamic history? At RI onset, Wilma's highest inner-core total (latent + sensible) ocean surface heat fluxes (H) are found in the northern eyewall, where surface V_T is strongest (Fig. 5.11a). Two hours later, maximum H has become symmetrically distributed throughout the eyewall, consistent with the axisymmetrization of Wilma's surface V_T (Fig. 5.11b). Here we consider only the 31,243 MBL-Origin trajectories that remain in the MBL for at least one hour prior to ascent but which are otherwise stratified by w_{MAX} in the same manner (section 5.2.3). Figure 5.12 shows time series of subsample $\overline{\theta_e(t)}$, $\overline{H(t)}$, and height $\overline{z(t)}$ during the final hour of parcel transit through the MBL, where overbars denote averages over all subsample trajectories t minutes prior to exiting the MBL. Compared to w_{MAX}-12 parcels, the w_{MAX}-CB parcels have statistically significant higher $\overline{\theta_e}(t)$ during their final 15 minutes in the MBL, statistically significant higher $\overline{H}(t)$ over their final 8 minutes in the MBL, and statistically significant lower $\bar{z}(t)$ over most of their final hour in the MBL (Figs. 5.12a,b). These results support CZ13's finding that higher SSTs contribute, generally, to higher numbers of CBs in Wilma. However, the lack of a more systematic relationship between w_{MAX}, MBL $\overline{\theta_e}(t)$, and MBL $\overline{H}(t)$ suggests that processes above the MBL might also be important to differentiating stronger updrafts from the background secondary circulation.

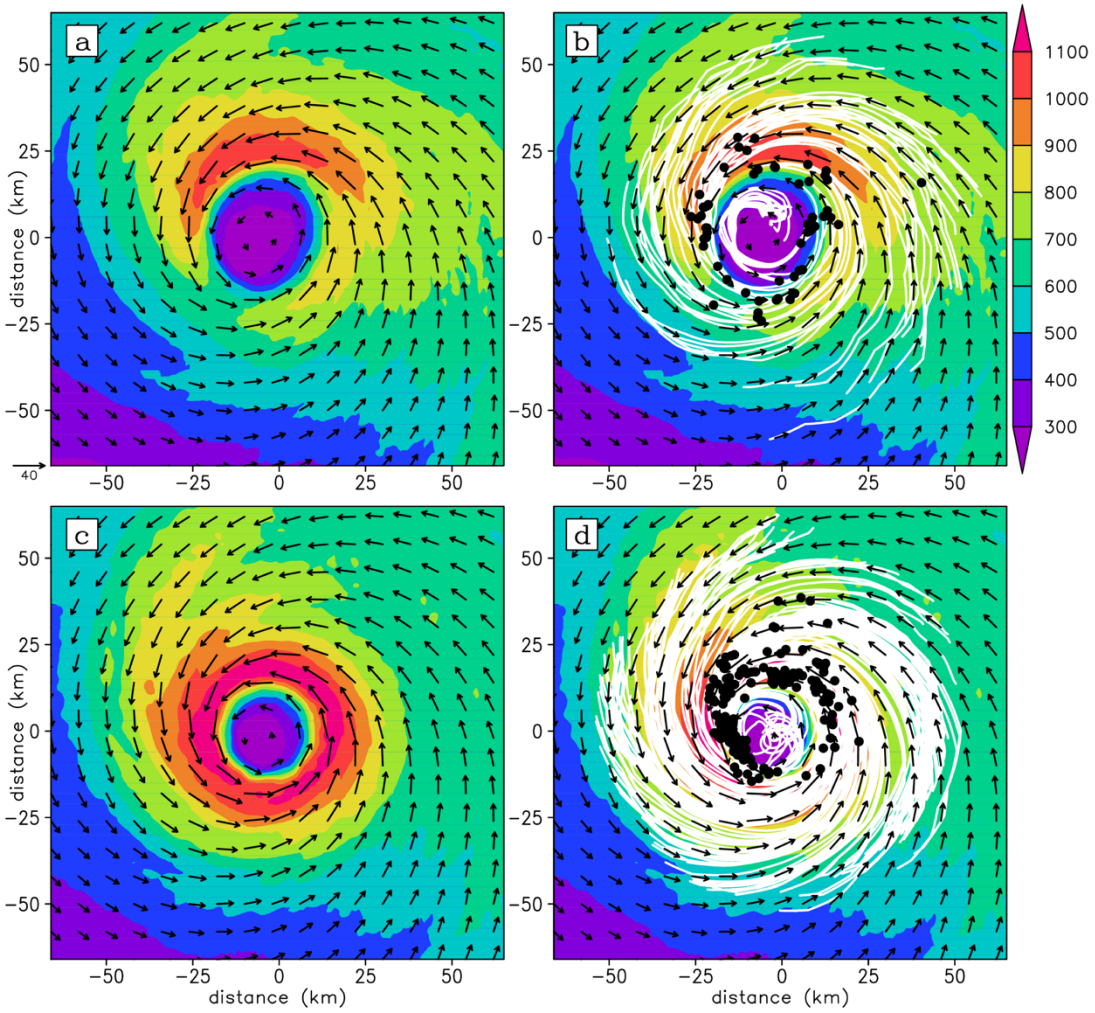

Fig. 5.11 (a) WRF-predicted total (latent + sensible) ocean surface heat flux (W m^{-2}) and 10-m horizontal flow vectors (m s^{-1}) averaged over the 1-h period ending at 15:00. (b) As in (a), but with black dots denoting the positions where w_{MAX}-20 and w_{MAX}-CB trajectories ascend above z = 0.5 km, and white lines showing x-y planar projections of these trajectories over the previous 1-h period. Only w_{MAX}-20 and w_{MAX}-CB trajectories ascending above z = 0.5 km over the +/- 5 min period surrounding 15:00 are plotted here. (c),(d) As in (a),(b) but for (c) model fields averaged over the 1-h period ending at 17:00 and (d) w_{MAX}-20 and w_{MAX}-CB updraft backward trajectories ascending above z = 0.5 km at 17:00 +/5 min.

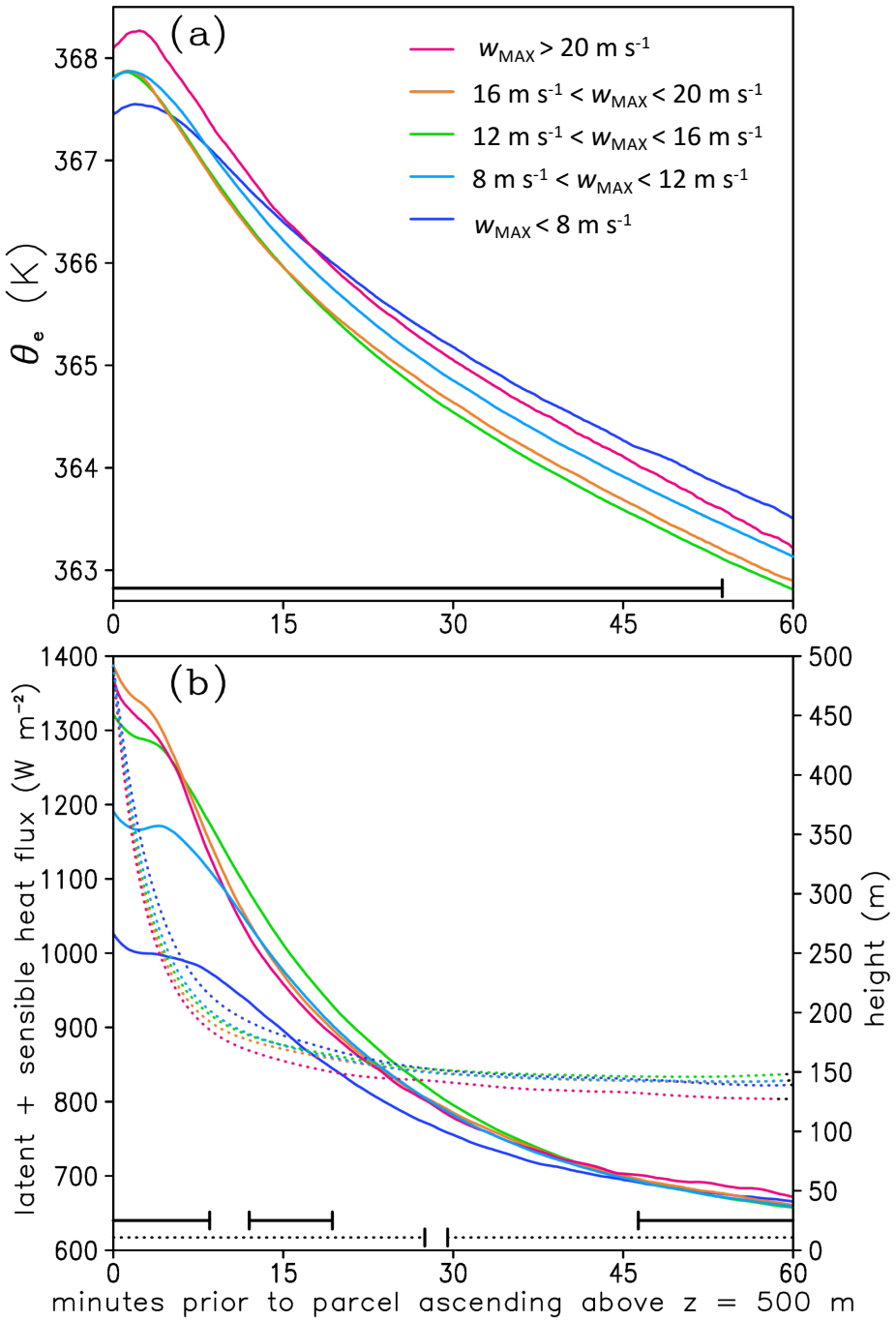

Fig. 5.12 (a) Mean θ_e (K) for sub-samples of backward trajectories binned by w_{MAX}, plotted as a function of time prior to their ascent above z = 0.5 km. (b) As in (a) but for mean total (latent + sensible) ocean surface heat flux (W m^{-2}; solid) and parcel height (m; dotted). Solid- or dot-bracketed lines denote time intervals where the difference between the w_{MAX}-12 and w_{MAX}-CB sample mean total surface heat flux (parcel height) are statistically significant at the 95% level.

5.4.3 Environmental air entrainment

Recall from section 5.3.2 that the CB parcel (i.e. Trajectory-CB1) experienced a ~3 K reduction in θ_e while ascending from the MBL to z = 6 km, whereas the secondary circulation parcel (i.e. Trajectory-SC) experienced an ~8 K θ_e decrease over the same layer despite having ~2 K higher θ_e when exiting the MBL. This leads us to ask: (i) are Wilma's CB updrafts, on average, characterized by less parcel θ_e dilution compared to the background secondary circulation? and (ii) if so, what processes might "protect" the CB parcels from being mixed with lower-θ_e air? Figure 5.13a shows $\overline{\theta_e}(k)$ profiles for the 5 w_{MAX}-binned subsamples. At z = 1 km, $\overline{\theta_e}$ increases with w_{MAX}, although $\overline{\theta_e}$ for w_{MAX}-CB is only ~0.5 K larger than that of w_{MAX}-12. Although $\overline{\theta_e}(k)$ decreases with height toward the melting level for all subsamples, the spread in $\overline{\theta_e}(k)$ among subsamples also increases with height, such that melting level $\overline{\theta_e}$ for w_{MAX}-CB is ~2.3 K larger than that of w_{MAX}-12. Above the melting level $\overline{\theta_e}(k)$ increases with height for all subsamples, likely due to fusion LHR (Fierro et al. 2009, 2012; M15).

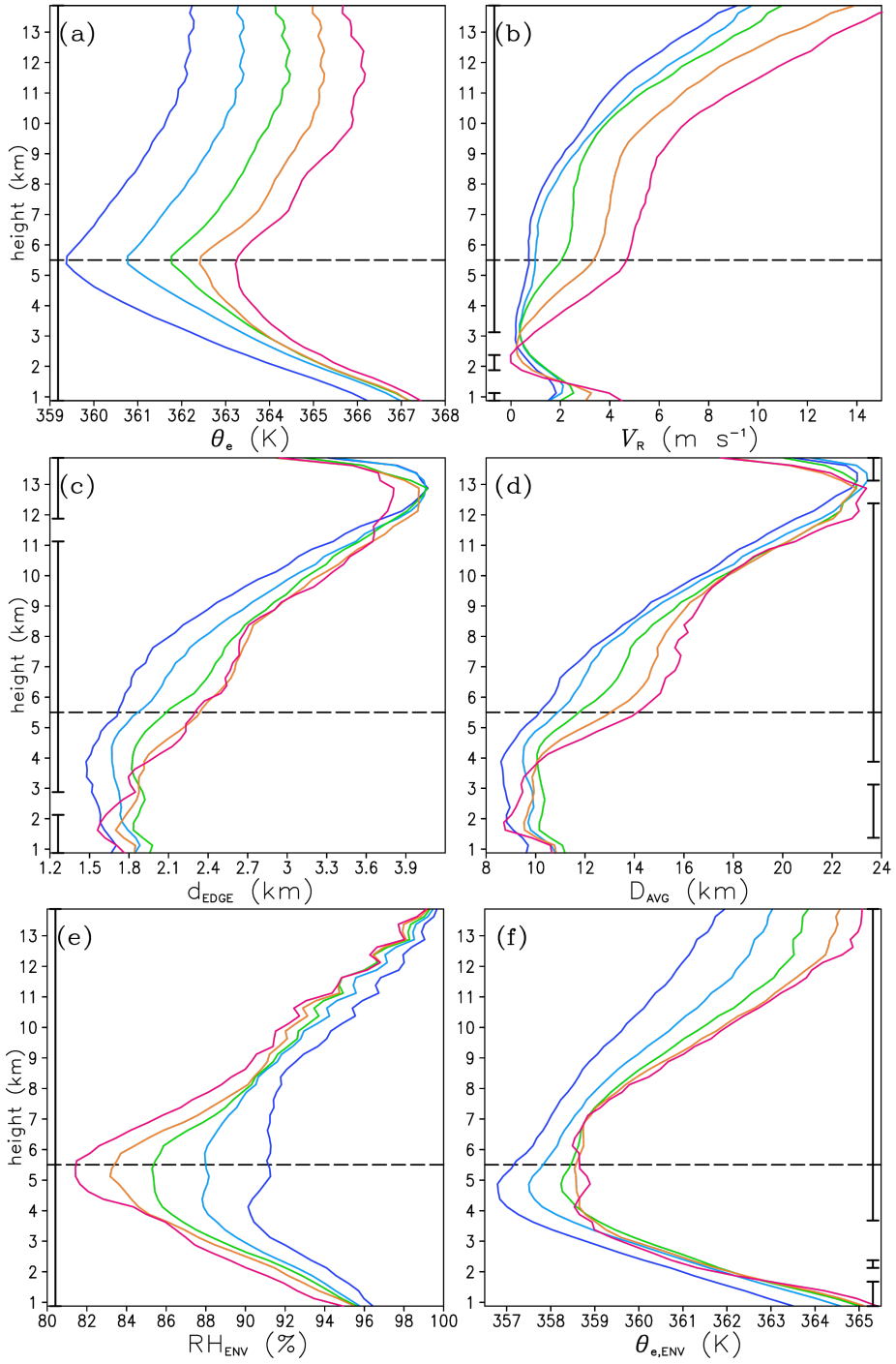

Fig. 5.13 (a) As in Fig. 5.10, but for the subsample mean θ_e (K). (b) As in (a), but for subsample mean radial wind interpolated to the parcel position (m s^{-1}). (c) As in (a), but for the subsample mean smallest distance in any Cardinal direction to the updraft element boundary (d_{EDGE}, km). (d) As in (a), but for the subsample mean updraft element diameter (D_{AVG}, km). (e) As in (a), but for subsample mean environmental relative humidity (RH_{ENV}, %). (f) As in (a), but for subsample mean environmental θ_e ($\theta_{e,ENV}$, K). See section 5.2.5 for the definitions of RH_{ENV} and $\theta_{e,ENV}$.

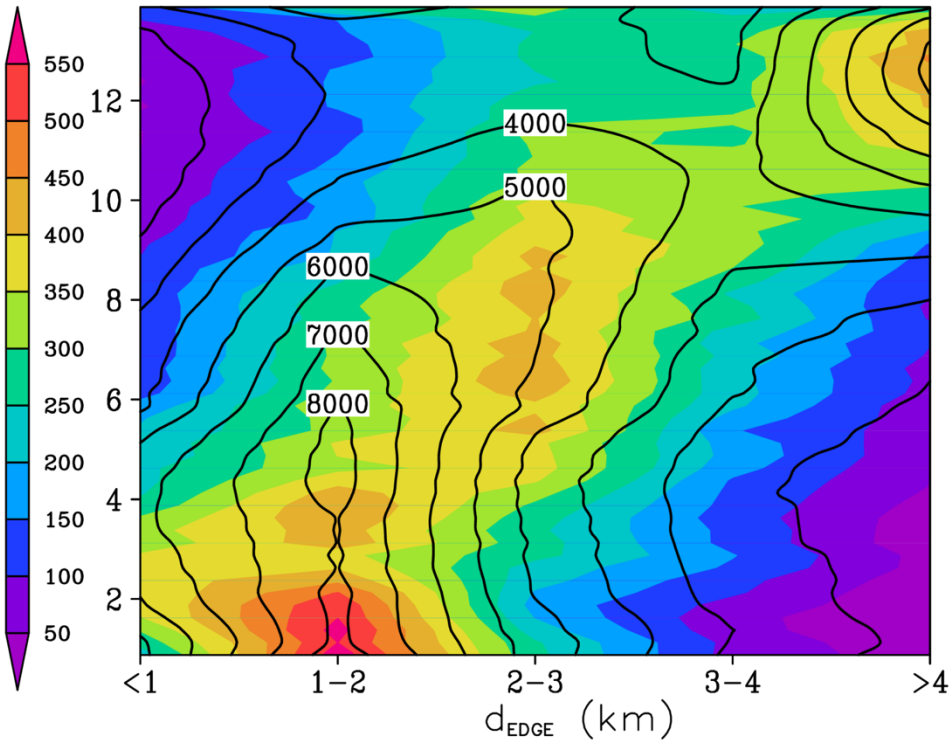

Fig. 5.14 (a) Histogram showing the number of updraft trajectories from the w_{MAX}-CB sub-sample (shaded), binned by distance to the updraft edge (km), as shown on the *x*-axis, and by height (km), as shown on the *y*-axis. Black contours show the number of updraft trajectories from the w_{MAX}-12 sub-sample, binned in the same manner.

These results confirm that CB parcels, on average, begin with higher θ_e in the MBL and experience less θ_e reduction while ascending into the upper troposphere, compared to the background secondary circulation. Might this result from lower rates of environmental air entrainment into CB parcels? It is worth reminding the reader that this study treats updrafts as aggregations of adjacent parcels that are distinguished from the surrounding environment by their having $w > 0.5$ m s^{-1} and $RH > 95\%$ (section 5.2.5). We assume that the updrafts are sufficiently horizontally homogenous, such that mixing with the environment modifies parcel thermodynamic properties much more strongly compared to mixing with adjacent updraft parcels. Additionally, we assume that parcel mass

exchange with the environment along trajectories is inversely proportional to the smallest distance from the parcel to the updraft edge (d_{EDGE}, see section 5.2.5). Figure 5.13c shows that the w_{MAX}-CB trajectories have statistically significant larger $\overline{d_{EDGE}}(k)$ compared to w_{MAX}-12 trajectories over the z = 3-11 km layer, with the largest absolute difference in their $\overline{d_{EDGE}}(k)$ being found over the z = 3-7.5 km layer. Examining how the histogram of w_{MAX}-CB and w_{MAX}-12 trajectories binned by d_{EDGE} varies with height in Fig. 5.14, we find that the low-level distribution peaks at d_{EDGE} = 1-2 km for both w_{MAX}-CB and w_{MAX}-12. However, the z = 4.5-8.5 km layer histogram peak shifts to d_{EDGE} = 2-3 km for w_{MAX}-CB while remaining at d_{EDGE} = 1-2 km for w_{MAX}-12. Figure 5.13d shows that the smaller $\overline{d_{EDGE}}(k)$ in w_{MAX}-12 is not merely a consequence of these parcels being located on the outer edge of stronger updraft cores; rather, compared to CB parcels they belong to narrower updrafts, on average, over the z = 4-12 km layer. These results agree with Morrison (2017), who used idealized WRF simulations to show that narrower (wider) updrafts experience more (less) dilution, leading to greater (less) reduction in buoyancy. Although our analysis has focused on the special characteristics of Wilma's CBs, the tendency for subsample $|\partial\overline{\theta_e}/\partial z|$ to become smaller with w_{MAX} while $\overline{d_{EDGE}}$ and $\overline{D_{AVG}}$ become larger with w_{MAX} over the z = 4-5.5 km layer (Figs. 5.13a,c-d) suggests that Wilma's eyewall updraft intensity may generally depend on the environmental air entrainment rate, which in turn may be partially governed by updraft width.

It is reasonable to expect that a parcel's θ_e dilution rate depends not only on the rate of mass exchange with the environment but also on the magnitude of the θ_e difference between the parcel and the environment (Morrison 2017). We find that w_{MAX}-CB trajectories have statistically significant higher mean environmental θ_e ($\theta_{e,ENV}$, section

5.2.5) compared to w_{MAX}-12 trajectories above z = 3.5 km (Fig. 5.13e). Given that $\overline{\theta_e - \theta_{e,ENV}}(k) > 0$ in the low-to-middle troposphere for all trajectory subsamples (not shown), it is possible that a higher ambient θ_e environment also contributes to the better θ_e conservation in CB parcels compared to background ascent (cf. Figs. 5.13a,e). Somewhat paradoxically, $\overline{RH_{ENV}}(k)$ becomes lower with increasing w_{MAX}, most markedly in the midtroposphere (Fig. 5.13f). Nevertheless w_{MAX}-CB $\overline{RH_{ENV}}(k)$ still exceeds 80% for all heights. Therefore, the higher midlevel $\overline{\theta_{e,ENV}}(k)$ for w_{MAX}-CB relative to w_{MAX}-12 must result from the former trajectories, on average, having a warmer (i.e., higher-θ) environment (cf. Figs. 5.13e,f).

During the trajectory analysis period, Wilma's midlevel eyewall is characterized by a negative radial θ_e gradient, with higher θ_e air pooled along the inner edge (Fig. 5.6c). Liu et al. (1999) first showed how the radial wind V_R could vary substantially with azimuth in a TC eyewall, with downdrafts generally aligned with local radial inflow (see their Fig. 10). Figure 5.9d shows a similar pattern in Wilma's eyewall; note how CB-E1 is co-located with anomalous radial outflow (i.e. positive V_R) exceeding 2 m s^{-1} through the depth of the troposphere, which suggests that outward advection of higher-θ_e air may have helped to locally enhance environmental θ_e near parcels rising through its updraft core (cf. Figs. 5.6c, 5.7e and 5.9d). In support of this hypothesis, we find that w_{MAX}-CB parcels are characterized by anomalous positive $\overline{V_R}(k)$ above z = 3 km that is statistically significantly larger than the w_{MAX}-12 $\overline{V_R}(k)$ (Fig. 5.13b). The above results therefore suggest two factors that may explain the smaller midlevel θ_e dilution rates characteristic to CB parcels: (i) reduced mixing with the environment due to wider updrafts and (ii) CBs tending to develop in higher local θ_e environments with anomalous radial outflow. However, a more rigorous

quantitative analysis of entrainment in TC eyewall updrafts – perhaps using passive tracer variables - warrants future study.

5.4.4 Statistical vertical momentum budget

Finally, let us extend the section 5.3.3 vertical momentum budget analysis to the full trajectory sample. Figure 5.15a shows that $\overline{BA}(k)$ increases with subsample w_{MAX} over the z = 2-9 km layer. Between z = 1.5 km and the melting level, w_{MAX}-12 (w_{MAX}-8) have very small (negative) $\overline{BA}(k)$ and positive $\overline{PGA}(k)$. Above the melting level, all subsamples have positive $\overline{BA}(k)$ and negative $\overline{PGA}(k)$ (Fig. 5.15a), consistent with idealized updraft simulations with minimal dynamic contributions to the p' field (Markowski and Richardson 2010; Morrison 2016). Interestingly, all subsamples have a similar $\overline{PGA}(k)$ magnitude between the melting level and z = 10.5 km. As a result, $\overline{BA}(k)$ and $\overline{PGA}(k)$ nearly cancel for w_{MAX}-8 and w_{MAX}-12, consistent with their near zero $\overline{Dw/Dt}(k)$ while $|\overline{BA}(k)| > |\overline{PGA}(k)|$ for the stronger updraft groups, consistent with their positive $\overline{Dw/Dt}(k)$ (cf. Figs. 5.15a,b). For individual trajectories, BA(k) and PGA(k) are generally anti-correlated over a deep layer (Figs. 5.16a,b), and a scatterplot of z = 10 km BA versus PGA further shows that BA + PGA > 0 for most w_{MAX}-CB trajectories but for only ~ 50% of w_{MAX}-12 trajectories (Fig. 5.16b).

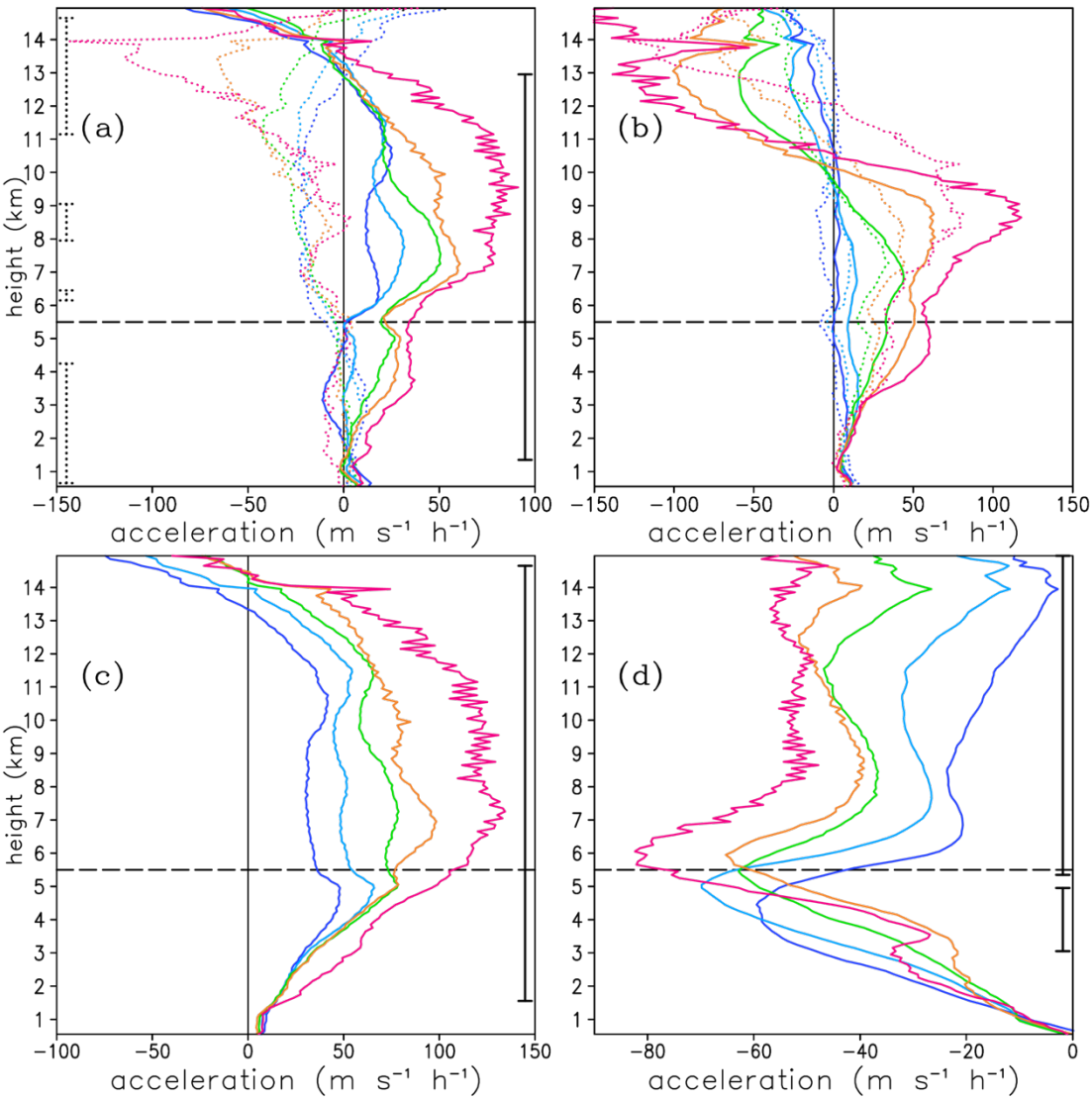

Fig. 5.15 (a) Vertical profiles of trajectory subsample mean BA (solid lines, m s^{-1} h^{-1}) and PGA (dotted lines, m s^{-1} h^{-1}), color coded by subsample w_{MAX} range as in Fig. 5.10. (b) As in (a), but for subsample mean parcel vertical acceleration *Dw/Dt* (solid lines, m s^{-1} h^{-1}) and sum of the subsample mean BA and PGA (dotted lines, m s^{-1} h^{-1}). (c) As in (a), but for subsample mean thermal buoyancy $g\theta_v'/\overline{\theta_v}$ (solid lines, m s^{-1} h^{-1}). (d) As in (b) but for subsample mean hydrometeor loading $gq_{HYD}{}'$ (solid lines, m s^{-1} h^{-1}). Dashed black line denotes the approximate melting level. Bracketed solid (dotted) lines in (a),(c),(d) [(a)] show height intervals over which differences in the w_{MAX}-12 and w_{MAX} -CB mean BA, $g\theta_v'/\overline{\theta_v}$, and $gq_{HYD,}{}'$ respectively, (PGA) are statistically significant at the 95% level.

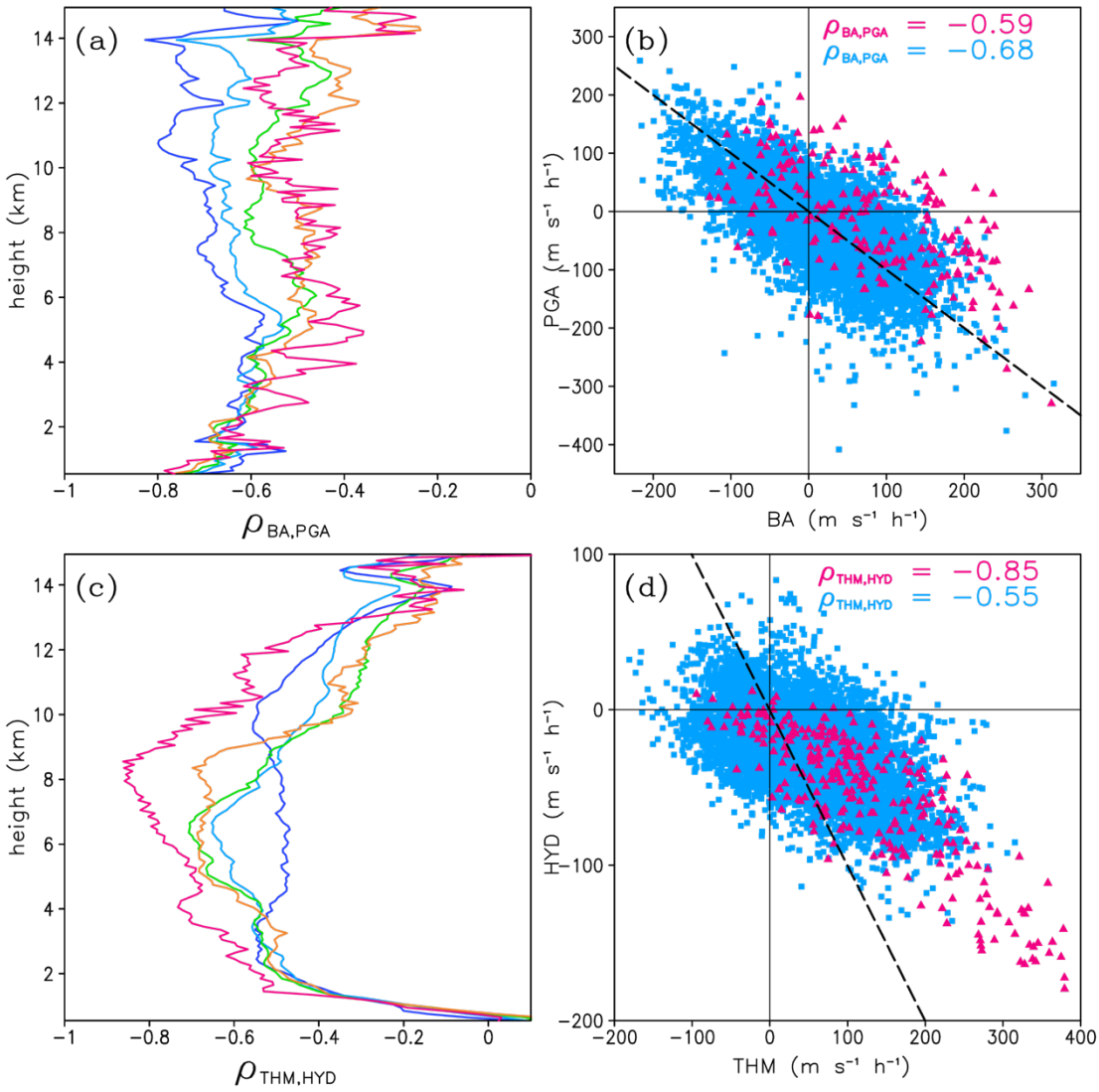

Fig. 5.16 (a) Pearson correlation coefficient between the BA and PGA ($\rho_{BA,PGA}$) plotted for each w_{MAX}-binned subsample as a function of height, with lines colored by subsample w_{MAX} range as in Figs. 5.10 and 5.15. (b) Scatterplot of BA versus PGA at z = 10 km for w_{MAX}-12 (light blue dots) and w_{MAX}-CB (magenta triangles). (c) As in (a) but for the correlation coefficient between thermal buoyancy (THM) and hydrometeor loading (HYD) ($\rho_{THM,HYD}$). (d) As in (b) but for the z = 8 km scatterplot of THM and HYD. Trajectories to the right of the dashed line in (b) have BA + PGA > 0 and trajectories to the right of the dashed line in (d) have THM + HYD > 0.

How do the relative contributions of thermal buoyancy and hydrometeor loading to the BA change with increasing w_{MAX}? Figure 5.15c shows that subsample mean $\overline{g\frac{\theta_v'}{\overline{\theta_v}}}(k)$ becomes more largely positive with increasing w_{MAX} over the z = 4-14 km layer, most

markedly between the melting level and z = 14 km. In the lower troposphere, between z = 1.5 and z = 3 km, w_{MAX}-CB trajectories are distinguished from all others by their larger positive $\overline{g\frac{\theta_v'}{\overline{\theta_v}}}(k)$, consistent with the fact that w_{MAX}-CB trajectories are also distinguished from all others by their higher $\overline{\theta_e}(t)$ upon exiting the MBL (cf. Figs. 5.12a and 5.15c). Another interesting CB trajectory characteristic is their statistically significant smaller $\overline{gq_{HYD}'}(k)$ magnitude relative to w_{MAX}-12 trajectories over the z = 3-5 km layer (Fig. 5.15d). Furthermore, the increasing BA with w_{MAX} among the remaining four subsamples over the z = 2-4 km layer primarily results from $|\overline{gq_{HYD}'}(k)|$ decreasing with w_{MAX}, since their respective $\overline{g\frac{\theta_v'}{\overline{\theta_v}}}(k)$ are quite similar (cf. Figs. 5.15a,c,d). These results suggest that local minima in lower-to-middle tropospheric hydrometeor loading such as those shown in Fig. 5.9b may help to differentiate the parcels that ultimately develop stronger upper-tropospheric w_{MAX} from others with similar thermal buoyancy. Above the melting level, individual trajectory $g\frac{\theta_v'}{\overline{\theta_v}}(k)$ and $gq_{HYD}'(k)$ become more strongly anti-correlated with increasing w_{MAX}, which makes intuitive sense given that stronger updrafts loft greater quantities of hydrometeors above the melting level, resulting in greater fusion LHR from ice-phase microphysical processes (cf. Figs. 5.15d and 5.16c,d). Nevertheless, positive $g\frac{\theta_v'}{\overline{\theta_v}}(k)$ still outweighs negative $gq_{HYD}'(k)$ for most CB trajectories in the upper troposphere, resulting in a positive BA (cf. Figs. 5.15a and 5.16d).

5.5 Summary and concluding remarks

This chapter has investigated the three-dimensional structure and thermodynamics of Hurricane Wilma (2005)'s CBs relative to their background secondary circulation from a Lagrangian perspective. For this purpose, we ran 97,020 4-h backward trajectories using winds output from a Wilma (2005) WRF prediction, which are seeded from its upper-tropospheric eyewall over a 4-h period shortly following RI onset. Of the 97,020 backward trajectories, the ~ 45% originating in the MBL are binned by w_{MAX} and saved for analysis in this study.

First, we compared an intense CB trajectory, with ~ 30 m s^{-1} w_{MAX}, against a background secondary circulation trajectory in terms of their three-dimensional structure, θ_e tendencies, and vertical momentum budgets. Key findings are:

- The CB parcel ascends from the MBL to z = 14 km in ~ 31 minutes, completing one half circle around the eyewall. By contrast, the secondary circulation parcel ascends the same vertical distance over ~ 83 minutes, completing 1.5 circles around the eyewall.
- Both the CB and secondary circulation parcels exit the MBL with high θ_e - 366 K and 368.5 K, respectively. Although both parcels experience some reduction in θ_e while ascending to the melting level followed by θ_e recovery in the upper troposphere, the low-to-middle tropospheric θ_e decline is significantly smaller for the CB parcel (~ -3 K) compared to the secondary circulation parcel (~ -8 K).
- A weakly positive BA lifts the CB parcel of the MBL. This positive BA becomes stronger with height into the upper troposphere, on account of positive thermal buoyancy more than offsetting hydrometeor loading – the former peaking at ~ 330

m s^{-1} h^{-1} near z = 8 km. As a result, w increases nearly monotonically with height toward a z ~ 13 km w_{MAX}. A strongly negative PGA rapidly decelerates w at higher levels.

- The secondary circulation parcel originates in a heavy-precipitating portion of the MBL, and a positive PGA helps to lift it into the eyewall free troposphere. Unlike the CB parcel, thermal buoyancy remains mostly positive but much weaker throughout ascent, generally < 50 m s^{-1} h^{-1}. Increasing hydrometeor loading, together with a negative PGA, offsets the weak positive thermal buoyancy as the parcel approaches the melting level, resulting in deceleration to near zero w. Rapid hydrometeor unloading above the melting level helps to accelerate this parcel vertically towards its upper-level w_{MAX}.

Next, we compared all CB trajectories against all secondary circulation trajectories – as well as all intermediate-strength updrafts - in terms of their respective mean θ_e, vertical momentum budgets, as well as other variables expected to impact the BA and θ_e conservation under saturated conditions. Wilma's CB parcels were most strongly distinguished from the secondary circulation by their (i) higher total (latent + sensible) heat fluxes from the ocean surface during their last 8 minutes transiting the MBL prior to ascent; (ii) higher θ_e during their last 15 minutes transiting the MBL prior to ascent; (iii) greater θ_e conservation (i.e., less θ_e reduction in the low-to-middle troposphere); (iv) belonging to wider updraft elements, especially in the midtroposphere; (v) updraft elements being surrounded by locally higher environmental θ_e; (vi) reduced hydrometeor loading over the z = 3-5 km layer; (vii) larger thermal buoyancy above the melting level; and (viii) higher supercooled liquid water and frozen hydrometeor mixing ratios above the melting level.

These results suggest that Wilma's CBs are rooted in portions of the MBL with locally enhanced θ_e and ocean surface heat/moisture fluxes. They support CZ13, who found that reducing SSTs[26] by 1 ºC significantly reduces Wilma's CB activity, upper level warming, and RI rate. They also support some aspects of Emanuel (1986, 1997)'s WISHE hypothesis – namely, that wind-induced ocean surface heat and moisture fluxes provide the thermodynamic heat source driving TC intensification. However, in identifying localized stronger updrafts (i.e., CBs) that are positively buoyant relative to the eyewall background state, this study supports other recent work (Heymsfield et al. 2001; Braun 2002; and Eastin et al. 2005a,b) in disagreement with WISHE's assumption that eyewall ascent is slantwise moist neutral everywhere. CZ13 and M15 also showed how CB compensating subsidence may have contributed to Wilma's upper level warm core development and resulting P_{MIN} intensification – a mechanism not accounted for in WISHE.

We have also identified two processes that may have helped differentiate Wilma's CB parcels from background secondary circulation parcels leaving the MBL with similarly high θ_e: midlevel entrainment and hydrometeor loading. Compared to the w_{MAX}-12 trajectories, the smaller CB parcel θ_e reduction between z = 3 km and the melting level suggests reduced mixing with the lower-θ_e eyewall midtropospheric air, given that θ_e is conserved under inviscid pseudoadiabatic ascent. This is consistent with CB updraft elements, on average, being wider and having higher local environmental θ_e compared to w_{MAX}-12 updraft elements over the z = 4-6 km layer. We showed how (i) prior development

[26] Technically speaking, ocean surface heat and moisture fluxes are proportional to the air-sea thermodynamic disequilbrium, which depends not only on SST but also on the temperature, pressure, and water vapor mixing ratio of the atmospheric surface layer. They also strongly depend on surface wind speeds, as shown in Fig. 5.11.

of a plume-like updraft structure and (ii) warm θ_e advection by local radial outflow may have "preconditioned" the environment above the rising CB parcel with higher θ_e air. In the midlevels, the CB parcels' higher mean θ_e relative to the background ascent is consistent with their higher mean thermal buoyancy. Higher midlevel thermal buoyancy, together with less hydrometeor loading in the z = 3-5 km layer, is consistent with CB parcels having stronger midlevel *Dw/Dt* relative to the background ascent. Wilma's CBs become most thermodynamically distinct from the background secondary circulation, in terms of their enhanced thermal buoyancy and *w*, in the upper troposphere. This is consistent with our finding that CBs, on average, are distinguished from the background ascent by their stronger midlevel updrafts that loft larger quantities of hydrometeors above the melting level, the latter in turn enhancing upper-tropospheric LHR from ice-phase microphysical processes.

As for any case study, future work is needed in order to determine how generally these results apply to CBs in other TCs. Hurricane Wilma (2005) may be considered a "prototype case" for TCs undergoing extreme RI under near-ideal environmental conditions. It may be particularly worthwhile to investigate how VWS affects CB structure and thermodynamics. Given the important role that CBs appear to play in TC intensification, it is necessary to develop a more complete understanding of the inner-core processes favoring their development.

Chapter 6. Summary, Concluding Remarks and Future Work

6.1 Summary and concluding remarks

This dissertation has investigated the atmospheric processes governing two TC phenomena that operational NWP models still struggle to predict: climatologically unusual motion and RI. In part, we are motivated to develop a more complete physical understanding of nature's most powerful storms, given our naturally curious nature as scientists. More importantly, we contend that better scientific understanding can lead to more accurate public forecasts. Recent studies have shown how TC unusual motion and RI may occur more frequently in the Atlantic and western Pacific basins than previously thought (Qin et al. 2016; Landsea and Cangialosi 2018; Zhang et al. 2018). TC forecasters are commonly faced with conflicting NWP guidance between different global deterministic models and between different ensemble members. For these situations, the forecasters' scientific understanding can be important in helping them to determine which models are better handling the current atmospheric state. When combined with retrospective case studies, an improved physical understanding of TC processes should also help pinpoint the source of NWP model errors, such as data assimilation and physical parameterization schemes.

Our chapter 2 analysis of unusual TC motion focused on Hurricane Joaquin (2015), which followed a particularly rare hairpin-shaped clockwise looping track, initially southwestward into the Bahamas and then back northeastward towards Bermuda. Most operational model forecasts, with the notable exception of the ECMWF, struggled to maintain Joaquin's southwestward motion and turned the storm first westward and then

eventually northwestward toward the U.S. coast. We applied the Galarneau and Davis (2013) TC motion error budget equation to two representative GFS forecasts, initialized at 1200 UTC on 29 and 30 Sep, to determine to the extent to which the GFS failure to maintain Joaquin's early southwestward motion resulted from errors in its representing (i) the large-scale steering environment or (ii) the size and/or depth of the TC vortex. For both forecasts, we found a ~ 1-2 m s^{-1} southerly environmental wind bias over Joaquin's optimal steering layer between t = 12-24 h; this "environmental wind error" accounts for roughly half (most) of the t = 12-24 h motion error in the 29 Sep (30 Sep) initialized GFS forecast. Comparison of the 1200 UTC 30 Sep cycle GFS forecast wind and temperature fields against the NCEP FNL shows that the GFS southerly wind bias is consistent with the model generating inadequately strong mid-to-upper level ridging west of Joaquin. The other significant contributor to the 1200 UTC 29 Sep cycle GFS t = 12-24 h track forecast error is a northerly-directed "vortex depth error" that results from the GFS-predicted Joaquin vortex being too shallow to interact strongly with northeasterly mid-to-upper level environmental winds.

Using the WRF model, we have further explored the sensitivity of Joaquin's southwestward motion to variations in the initial conditions. We generated a baseline CTL analysis for 0600 UTC 29 Sep using a 30-h hybrid data assimilation cycle described in chapter 3; a variety of observations are assimilated, including conventional radiosondes, high-resolution AMVs, AMSU-A radiances, and bogus moisture soundings. A 1-km resolution 114-h WRF forecast from the CTL analysis reproduced Joaquin's intensity and structural changes quite well. However, we found that Joaquin's southwest motion (and eventual hairpin loop) can only be well captured if winds and temperature in the WRF outer

three domains (27, 9, and 3-km resolution) are continuously forced toward the NCEP 1˚-FNL using analysis nudging, which suggests that either (i) large-scale flows in the CTL analysis are biased from the true state or (ii) model physics errors in the outer three domains are degrading the large-scale flow representation. We confirmed (i) by finding lower CTL-analyzed geopotential heights, compared to the NCEP 1˚-FNL, over a region extending west and northwest from Joaquin into the eastern continental U. S. and over the full depth of the troposphere. We then evaluated the sensitivity of Joaquin's early southwestward motion to the initial atmospheric state by perturbing specific features in the CTL analysis via assimilation of synthetic observations, and then by running WRF simulations from these analyses with nudging turned off. These tests showed that two features critical to steering Joaquin southwestward are (i) a sufficiently strong subtropical mid-to-upper level ridge northwest of the storm and (ii) a sufficiently deep TC vortex that can interact with the geostrophic flows on the east side of the subtropical ridge.

How do the above findings contribute to our scientific understanding of unusual TC motion? On one hand, they suggest that model misrepresentation of vortex depth may be an important track error source for some TCs, especially for weaker, developing storms that are embedded in vertically sheared environmental flows. Using their track error diagnostic equation applied to WRF forecast output, Galarneau and Davis (2013) showed similar motion sensitivity to vortex depth for Hurricane Earl (2010) during its early development. For these cases, additional inner-core sampling by means of cloudy radiances and aircraft reconnaissance missions may improve track forecasts by improving the model estimate of vortex depth in the initial conditions. Vortex depth is generally correlated with intensity; therefore, improvements in track forecasting may be partly contingent on more

accurate intensity forecasts for these cases. Improvements in TC track and intensity forecasting have traditionally been viewed as independent problems. Additionally, we use the high-resolution CTL simulation to show how reduction of the northwest-to-southeast vortex tilt accounts for a significant portion of Joaquin's early southwest motion. TC motion sensitivity to internal vortex reorganization processes is a topic that has received relatively little attention in the literature – and another example of how model prediction of TC motion may depend upon model resolution of the vortex structure. Finally, Joaquin's high WRF forecast track sensitivity to relatively small initialized geopotential height perturbations in the nearby mid-to-upper level ridge suggests that climatologically unusual TC motion may be inherently less predictable than typical TC motion.

In chapter 4 we introduced a new algorithm for computing backward trajectories from WRF output winds. Trajectory computations for mesoscale flows typically require a small (~10 s) computational timestep to minimize the rapid accumulation of numerical truncation errors. Disk storage constraints often limit the finest possible model output temporal resolution to ~ 5 min, requiring trajectory models to temporally interpolate gridded forecast model output to their computational timestep; this has been traditionally accomplished using LI. Our major motivation for developing this new trajectory model has been to reduce time interpolation errors by implementing an experimental AC algorithm that interpolates WRF-output variables from a reference frame moving with the advective flow velocity, rather than from a fixed frame as in traditional LI. First, we tested our trajectory model on an analytical flow field to verify that the basic code elements are functioning properly. Then we showed how AC improves mean position accuracy over LI for a sample of 10,201 backward trajectories run from the CTL 5-min output, using

reference LI trajectories computed from CTL 1-min output. Finally, we ran backward trajectories through a CB updraft core in WRF-simulated Hurricane Wilma (2005) to show how AC eliminates spurious LI-trajectory w and θ_e oscillations that result from the CB moving significant distances between model output times, relative to its horizontal scale.

We used our trajectory model to address an open question in the TC research community: how do CB updrafts become thermodynamically distinct from the weaker background eyewall ascent, given the rapidly rotating flows? CBs have been shown to precede and/or accompany RI in TCs, and several hypotheses have been put forward regarding their role in facilitating RI (see section 1.1.2). Therefore, it was important for us to better understand the inner-core processes favoring their development in TCs. Previous studies have mostly examined CB structure and thermodynamics in terms of vertical and horizontal cross-sections through model output or from gridded composites derived from Doppler radar. The work presented in chapter 5 (and currently under review as Miller and Zhang 2019c) is, to the best of our knowledge, the first Lagrangian TC study focusing on CB characteristics. Here, we run a large sample of backward trajectories from the WRF-simulated Hurricane Wilma (2005)'s outflow layer. This analysis combines a detailed structural and thermodynamic comparison between a CB parcel and representative background ascent trajectory with a statistical comparison of thermodynamic, microphysical, and vertical acceleration profiles among different trajectory subsamples binned by w_{MAX}.

One of our significant findings has been that CB updrafts tend to originate from portions of the boundary layer where θ_e and ocean surface heat/moisture fluxes are locally larger than those of nearby areas. In the 1980s the highly influential WISHE hypothesis

(Emanuel 1986; Rotunno and Emanuel 1987) re-focused attention on the fact that TC intensification is fundamentally driven by heat fluxes from the ocean rather than from pre-existing conditional instability in the boundary layer (consistent with the fact that TCs typically weaken over land). Because surface heat fluxes are proportional to surface wind speed, the proposed WISHE mechanism is a type of ocean-atmosphere instability. One of WISHE's central assumptions is that TC intensification occurs *in the absence of any* eyewall conditional instability, with eyewall ascent instead being forced by vortex-scale LHR. Here, we show that Wilma's CB parcels are in fact distinguished from the background ascent by their significant thermal buoyancy, in agreement with other recent studies that have found discrete buoyant updraft elements in TC eyewalls (Braun 2002; Eastin et al. 2005a,b). Our results therefore suggest another mechanism through which wind-induced ocean surface heat exchange drives TC intensification – namely, by facilitating development of inner-core CBs, which may in turn hasten eye warming (and associated surface pressure falls) through their compensating subsidence.

Our trajectory analysis also identified two midlevel processes that may act to further differentiate CB updrafts from the background ascent: environmental air entrainment and hydrometeor loading. Although TCs eyewall updraft cores are generally close to saturation, modeling studies of mature TCs, including Wilma, have shown a midtropospheric θ_e minimum in and around the eyewall (Liu et al. 1999; Braun 2002; Miller and Zhang 2019c), perhaps due to mixing with lower-θ_e air from outer regions (Cram et al. 2007). We have found that less parcel θ_e reduction during ascent from the boundary layer to the midtroposphere is another distinguishing CB characteristic, consistent with Wilma's CB updraft cores on average being (i) wider and more resistant to

entrainment and (ii) located in regions of local radial outflow where environmental θ_e is locally higher. We have also found that CB parcels are, on average, characterized by less hydrometeor loading in the low-to-middle troposphere relative to other eyewall updrafts. In other words, they tend to ascend away from "swaths" of higher rainwater mixing ratios being advected cyclonically downstream of existing updrafts. Both low-θ_e air entrainment and hydrometeor loading reduce parcel buoyancy. These findings are consistent with Wilma's CB parcels having stronger midlevel updrafts compared to the background ascent, which enables them to loft larger quantities of supercooled water above the melting level and ultimately acquire their highest thermal buoyancy (and *w*) in the upper troposphere due to fusion latent heat release.

6.2 Future work

In studying CBs and their relationship to RI, this dissertation has focused on Hurricane Wilma (2005), a TC rapidly intensifying under near-ideal environmental conditions. When environmental VWS[27] becomes more significant (i.e., > 5 m s^{-1}), TC vortices tend to tilt downshear and become more asymmetric. VWS has traditionally been understood to inhibit TC intensification because it increases inner core ventilation by lower-θ_e surrounding air, thereby disrupting development of the warm core and the conversion of eyewall latent heating to the swirling winds' kinetic energy. Although observations and numerical simulations have shown that these inhibiting effects generally

[27] TC forecasters and researchers typically define environmental VWS as the vector difference between the mean environmental wind at 200 hPa and 850 hPa, where the mean environmental wind is defined over a disk extending several hundred km outward from the storm center after removal of the TC vortex.

increase with VWS magnitude (Frank and Ritchie 2001), observations have also shown that some TCs can intensify (and even undergo RI) in the presence of so-called "moderate" VWS of ~ 5-10 m s^{-1}. Forecasting TC intensity in moderate-VWS environments can be particularly difficult, especially if environmental conditions are otherwise favorable and there is disagreement in NWP model guidance. It is still an open research question as to why some developing TCs are more "resistant" to environmental VWS.

Although our Hurricane Joaquin (2015) analysis herein has focused on its unusual motion, this storm is also an example of a TC undergoing RI despite moderate environmental VWS. We showed in section 2.5.3 how Joaquin's vortex becomes vertically aligned over the first 18 CTL forecast hours, as a low-level center develops beneath the upper-level center. Previous studies have shown how vertical tilt reduction is a process common to TCs intensifying under moderate VWS (Molinari et al. 2006; Nguyen and Molinari 2015; Rogers et al. 2015; Rios-Berrios et al. 2016; Fischer et al. 2018; Rios-Berrios et al. 2018), but the role of inner-core deep convection in this process is still not well understood. It may be worthwhile to investigate, in a future study, how Joaquin's eyewall deep convection (simulated in CTL but not shown here) may have facilitated the vortex vertical alignment. Few prior studies have tackled the "RI under moderate VWS" problem from a Lagrangian perspective, and the trajectory model developed for this dissertation could serve as a useful tool toward that end. Vorticity budgets along trajectories could shed some light on the role of deep convection in spinning up the swirling winds by stretching and aggregating low-level cyclonic vorticity (Montgomery and Smith 2014; Nguyen and Molinari 2015). This proposed work would also expand upon the results

presented in chapter 5 by exploring how environmental VWS impacts CB structure and thermodynamics.

Further work is also needed toward developing a more general theory of TC intensification. Our section 1.1.2 discussion of the relationship between CBs and RI focused on how CB compensating subsidence facilitates eye warming and hydrostatically-induced surface pressure falls, as shown in Chen and Zhang (2013) and Miller et al. (2015). Other studies have focused on TC intensification from a purely dynamical perspective – in terms of the swirling winds' spinup. Qin et al. (2018b), for example, investigated how RMW contraction and AAM flux convergence governed the RI of Hurricane Wilma (2005). TC pressure and wind fields are often, to a first order, assumed to be in gradient wind balance above the MBL; this implies a lowering of vortex central pressure in response to a V_T increase at the RMW, and vice versa. Moreover, a synergy likely exists between a TC's warm core development and its swirling wind intensification. For example, the efficiency of eyewall latent heat conversion to adiabatic subsidence warming in the eye increases with higher V_T and cyclonic vorticity (i.e., increased inertial stability: Hack and Schubert 1986; Vigh and Schubert 2009), consistent with Chen and Zhang (2013) finding that Wilma's upper-level warm core development was contingent on the spinup of sufficiently robust upper-level V_T. A more difficult question worth addressing comes in the spirit of the proverbial conundrum "which came first – the chicken or the egg?": *is TC intensification ultimately driven by eye warming or by dynamical processes that spin up* V_T*?* Establishment of dynamical relationships between P_{MIN} and V_{MAX} changes is further complicated by the fact that gradient wind balance is not satisfied in the MBL, where frictional effects become important (Montgomery and Smith 2014). Further trajectory

analysis of the Chen et al. (2011) Hurricane Wilma (2005) WRF simulation could be useful in better understanding (i) the upper-level warm core formation, (ii) CB contribution to the V_T spinup, and (iii) any interdependencies between (i) and (ii).

Observations and high-resolution modeling studies over the past two decades have revealed that TC eyewalls have complex three-dimensional structures, even for mature, relatively axisymmetric cases. Flow disturbances embedded in the swirling winds include CBs and eyewall mesovortices (Braun et al. 2006). Future work is needed toward better understanding how these asymmetric structures contribute to the spinup of the swirling winds. Locally, mesovortex circulations (CBs) modulate V_T the through radial eddy flux convergence of AAM (cyclonic vorticity stretching and vertical advection). Older models of TC intensification in V_T assume axisymmetry and balanced dynamics (i.e. thermal and gradient wind balance being maintained) above the MBL (Charney and Eliassen 1964; Ooyama 1982; Shapiro and Willoughby 1982; Rotunno and Emanuel 1987). Therefore, we must ask: *do our existing theoretical TC intensification models need to be modified to account for asymmetric V_T spinup mechanisms?* Or are the asymmetric processes, when considered in their azimuthal averages, implicitly included in the axisymmetric theories?

In addressing the theoretical questions posed above, future research could benefit from high-resolution satellite and in-situ observations of TC inner core regions, as well as from numerical model output. Observational and numerical modeling approaches are complementary. Observations serve as our best approximation to the "true" atmosphere while numerical model output, provided it is thoroughly validated against observations, provides us with reasonably accurate spatially and temporally continuous data. In recent years, computational power has increased to the point that convection-resolving cycled

ensemble forecast systems, such as the PSU WRF-EnKF, can be developed and used for research purposes (Nystrom et al. 2018). We have saved analyses from the 9-km resolution, 80-member WRF-DART system developed for the CTL vortex spinup as described in chapter 3. A future study could run convection-allowing forecasts from the 0600 UTC 29 Sep ensemble analyses. Assuming that the forecast spread is reasonably representative of the meteorological "errors of the day", environmental and inner-core structural differences between intensifying and non-intensifying members could shed some light on how TCs intensify in moderate VWS. Lagrangian processes could be investigated in selected ensemble forecasts using the trajectory model developed for this dissertation. The ensemble sensitivity approach could also be applied to the re-intensification of Hurricane Joaquin (2015) – a process that was not well captured by CTL and the operational NWP guidance. This proposed project could employ a newly developed SST parameterization scheme for WRF (Liu et al. 2019) to test the sensitivity of Joaquin's re-intensification to the storm's movement away from its self-generated SST cold pool.

Appendix A: Trajectory Model Algorithm for Finding Storm Center

Planar views of the simulated Joaquin (2015) horizontal wind and relative vorticity fields reveal a center that tilts ~25 km southward between the z = 3 km and z = 8 km levels over the trajectory computation period (not shown). The technique described below determines the storm center at every height over a user-selected layer for all model output times. The layer bottom (top) center coordinates are assigned to all heights below (above) the layer on the computational grid; subsequently, model-output winds are interpolated to cylindrical coordinates.

A first-guess storm center location for the lowest height is set to the centroid of the region where the sea-level pressure is within 10 hPa (5 hPa) of P_{MIN} when the latter is less than (greater than) 990 hPa. Following Cavallo et al. (2013), the vortex center is defined as the grid point within a specified search box surrounding the first guess with maximum circulation (or equivalently, area-averaged z-component of relative vorticity) within a user-defined circulation radius. Inner-core vorticity patterns for TCs resolved at high resolution can be quite noisy due to small-scale variability in the tangential winds. To generate a horizontally smooth vorticity field representative of the vortex-scale circulation, our algorithm computes horizontal wind gradients as centered differences across 20-km distances and applies five cycles of a nine-point local smoother to the input storm-relative u and v winds and the output vorticity. Center coordinates for each height become the first-guesses for computing the center position of the level above. Alternatively, the sea-level

pressure centroid can be used for all heights; this was done when computing trajectories from the more axisymmetric and upright Wilma (2005) simulated vortex.

The Joaquin (2015) experiments described in Section 4.4.1 use the circulation-based center determining algorithm with a 50 km-wide center search box and a circulation radius that expands linearly with height from 40 km at z = 3 km to 70 km at z = 8 km to account for vortex broadening. Users may optionally have the program output the automatically-determined vortex center coordinates. If the center cannot be reliably determined by either method, they may supply the program with an auxiliary input file containing the center coordinates obtained by visual inspection.

Appendix B: Trajectory Model Computational Considerations

The trajectory computation software developed for this study is written with OpenMP directives and designed to be run on a high-performance computing cluster using shared memory parallelism across multiple processors on a single node. Although the code can be compiled and run as a serial program, parallel processing yields a significant speedup, especially when implementing AC (Table B1). For experiments that use very high temporal resolution (i.e., 1-min) input data and/or interpolate many non-kinematic variables along trajectories, storing the four-dimensional model data arrays during program execution may necessitate using large amounts of processor memory (RAM), depending on the model domain size (Table B1). Should machine RAM capacity become a limiting constraint, program memory usage could be reduced by running a batch of trajectories as a series of sequential jobs over shorter integration periods, using end points as the seed points for the next integration.

Table B1 Wall-clock time and maximum combined processor memory usage for several configurations of an experiment running 10,201 4-h backward trajectories on a 20-processor compute node. Input data is taken from the Hurricane Joaquin (2015) simulation and the AC_{UVW} experiments apply advection correction below z = 16 km to the subdomain configuration described in section 4.2.3.

Time Interpolation Scheme	Input Data Resolution	Variables Interpolated Along Trajectories	Shared Memory Parallel Processing	Wall-clock Time (hh:mm)	Maximum RSS[28] Memory Usage (GB)
LI	5-min	*x,y,z*	yes	00:25	21
AC_{UVW}	5-min	*x,y,z*	yes	02:27	35
AC_{UVW}	1-min	*x,y,z*	yes	05:28	188
AC_{UVW}	1-min	$x,y,z,p,T,AAM,\theta_e,q_v,q_{frz},q_{liq}$[29]	yes	06:45	459
LI	5-min	*x,y,z*	no	01:55	21
AC_{UVW}	5-min	*x,y,z*	no	31:27	37

[28] Resident Set Size (RSS) memory is the portion of the main memory (RAM) on the compute node used by the executable.

[29] q_v, q_{frz}, and q_{liq} refer to the mixing ratios of water vapor, frozen hydrometeors, and liquid hydrometeors, respectively.

Bibliography

Aberson, S. D., 2010: 10 years of hurricane synoptic surveillance (1997-2006). *Mon. Wea. Rev.,* **138,** 1536-1549.

——, K. J. Sellwood, P. A. Leighton, 2017: Calculating dropwindsonde location and time from TEMP-DROP messages for accurate assimilation and analysis. *J. Atmos. Ocean. Tech.,* **34,** 1673-1678.

Anderson, J. L., 2001: An ensemble adjustment Kalman filter for data assimilation. *Mon. Wea. Rev.,* **129,** 2884-2903.

——, 2009: Spatially and temporally varying adaptive covariance inflation for ensemble filters. *Tellus,* **61A,** 72-83.

Aksoy, A., S. D. Aberson, T. Vukicevic, K. J. Sellwood, S. Lorsolo, and X. Zhang, 2013: Assimilation of high-resolution tropical cyclone observations with an ensemble Kalman filter using NOAA/AOML/HRD's HEDAS: Evaluation of the 2008-11 vortex scale analyses. *Mon. Wea. Rev.,* **141,** 1842-1865.

Baker, J., 2010: Cluster analysis of long range air transport pathways and associated pollutant concentrations within the UK. *Atmos. Environ.,* **44,** 563–571.

Bassill, N. P., 2014: An analysis of the operational GFS simplified Arakawa Schubert parameterization within a WRF framework: A Hurricane Sandy (2012) long-term track forecast perspective. *J. Geophys. Res. Atmos.,* **120,** 378-398.

Blake, E. S., and D. A. Zelinsky, 2018: Tropical cyclone report: Hurricane Harvey (AL092017). National Hurricane Center Tech. Rep., 77 pp. [Available online at https://www.nhc.noaa.gov/data/tcr/AL092017_Harvey.pdf.]

Bentley, A. M., L. F. Bosart, and D. Keyser, 2017: Upper-Tropospheric precursors to the formation of subtropical cyclones that undergo tropical transition in the North Atlantic basin. *Mon. Weather Rev.*, **145**, 503–520.

Berg, R., 2016: Tropical cyclone report: Hurricane Joaquin (AL112015). National Hurricane Center Tech. Rep., 36 pp. [Available online at https://www.nhc.noaa.gov/data/tcr/AL112015_Joaquin.pdf]

Beven, J. L. II, R. Berg, and H. Hagen, 2019: Tropical cyclone report: Hurricane Michael (AL142018). National Hurricane Center Tech. Rep., 86 pp. [Available online at https://www.nhc.noaa.gov/data/tcr/AL142018_Michael.pdf]

Black, M. L., R. W. Burpee, and F. D. Marks, Jr., 1996: Vertical motion characteristics of

tropical cyclones determined with airborne Doppler radial profiles. *J. Atmos. Sci.,* **53,** 1887-1909.

Blake, E. S., T. B. Kimberlain, R. J. Berg, J. P. Cangialosi, and J. L. Beven II, 2013: Tropical cyclone report: Hurricane Sandy (AL182012). National Hurricane Center Tech. Rep., 157 pp. [Available online at https://www.nhc.noaa.gov/data/tcr/AL182012_Sandy.pdf]

Bolton, D., 1980: The computation of equivalent potential temperature. *Mon. Wea. Rev.,* **108,** 1046-1053.

Bowman, K. P., J. C. Lin, A. Stohl, and Coauthors, 2013: Input data requirements for Lagrangian trajectory models. *Bull. Amer. Meteor. Soc.,* **94**, 1051-1058.

Brankov, E., S. T. Rao, and P. S. Porter, 1998: A trajectory-clustering-correlation methodology for examining the long- range transport of air pollutants. *Atmos. Environ.,* **32,** 1525–1534.

Braun, S. A., 2002: A cloud-resolving simulation of Hurricane Bob (1991): Storm structure and eyewall buoyancy. *Mon. Wea. Rev.,* **130,** 1573-1592.

——, M. T. Montgomery, and X. Pu, 2006: High-resolution simulation of Hurricane Bonnie (1998). Part I: The organization of eyewall vertical motion. *J. Atmos. Sci.,* **63,** 19-42.

Brennan, M. J., S. J. Majumdar, 2011: An examination of model track forecast errors for Hurricane Ike (2008) in the Gulf of Mexico. *Wea. Forecasting,* **26,** 848-867.

Cangialosi, J., 2015: Tropical cyclone report: Tropical Storm Ida (AL102015). National Hurricane Center Tech. Rep., 14 pp. [Available online at https://www.nhc.noaa.gov/data/tcr/AL102015_Ida.pdf].

——, and J. Franklin, 2016: National Hurricane Center forecast verification report: 2015 hurricane season. NOAA rep., 69 pp. [Available online at https://www.nhc.noaa.gov/verification/pdfs/Verification_2015.pdf]

Cavallo, S. M., R. D. Torn, C. Snyder, W. Wang, and J. Done, 2013: Evaluation of the Advanced Hurricane WRF data assimilation system for the 2009 Atlantic hurricane season. *Mon. Wea. Rev.,* **141,** 523-541.

Chan, J. C. and W. M. Gray, 1982: Tropical cyclone movement and surrounding flow relationships. *Mon. Wea. Rev.,* **110,** 1354-1374.

Charney, J. G., and A. Eliassen, 1964: On the growth of the hurricane depression. *J. Atmos. Sci.,* **21,** 68-75.

Chen, H., D.-L. Zhang, J. Carton, and R. Atlas, 2011: On the rapid intensification of Hurricane Wilma (2005). Part I: Model prediction and structural changes. *Wea. Forecasting,* **26**, 885-901.

——, and ——, 2013: On the rapid intensification of Hurricane Wilma (2005). Part II: Convective bursts and the upper-level warm core. *J. Atmos. Sci.,* **70**, 146-162.

——, and Gopalakrishnan, 2015: A study on the asymmetric rapid intensification of Hurricane Earl (2010) using the HWRF system. *J. Atmos. Sci.,* **72,** 531-550.

Cione, J. J., and E. W. Uhlhorn, 2003: Sea surface temperature variability in hurricanes: implications with respect to intensity change. *Mon. Wea. Rev.,* **131,** 1783-1796.

Cram, T. A., J. Persing, M T. Montgomery, and S. A. Braun, 2007: A Lagrangian trajectory view on transport and mixing processes between the eye, eyewall, and environment using a high-resolution simulation of Hurricane Bonnie (1998). *J. Atmos. Sci.,* **64,** 1835-1856.

Dahl, J. M. L., M. D. Parker, and L. J. Wicker, 2012: Uncertainties in trajectory calculations within near-surface mesocyclones of simulated supercells. *Mon. Wea. Rev.,* **140,** 2959-2966.

Davis, C. A., and L. F. Bosart, 2004: The TT problem: Forecasting the tropical transition of cyclones. *Bull. Am. Meteorol. Soc.*, **85**, 1657–1662.

——, and Coauthors, 2008: Prediction of landfalling hurricanes with the advanced hurricane WRF model. *Mon. Wea. Rev.,* **136,** 1990-2005.

Donelan, M. A., B. K. Haus, N. Reul, W. J. Plant, M. Stiassnie, H. C. Graber, O. B. Brown, and E. S. Saltzman, 2004: On the limiting aerodynamic roughness of the ocean in very strong winds. *Geophys. Res. Lett.,* **31,** L18306.

Dong, K., and C. J. Neumann, 1986: The relationship between tropical cyclone motion and environmental geostrophic flows. *Mon. Wea. Rev.,* **114,** 115-122.

Dowell, D. C., and H. B. Bluestein, 2002: The 8 June 1995 McLean, Texas, storm. Part I: Observations of cyclic tornadogenesis. *Mon. Wea. Rev.,* **130,** 2626-2648.

Doyle, J., J. Moskaitis, J. Feldmeier, and Coauthors, 2017: A view of tropical cyclones from above: The tropical cyclone intensity experiment. *Bull. Amer. Meteor. Soc.,* **98,** 2113-2134.

Dudhia, J., 1989: Numerical study of convection observed during the Winter Monsoon Experiment using a mesoscale two-dimensional model. *J. Atmos. Sci.,* **46,** 3077-3107.

Eastin, M. D., W. M. Gray, and P. G. Black, 2005a: Buoyancy of convective vertical motions in the inner core of intense hurricanes. Part I: General statistics. *Mon. Wea. Rev.,* **133,** 188-208.

——, ——, and ——, 2005b: Buoyancy of convective vertical motions in the inner core of intense hurricanes. Part II: Case studies. *Mon. Wea. Rev.,* **133,** 209-227.

Eliassen, A., 1952: Slow thermally or frictionally controlled meridional circulation in a circular vortex. *Astrophys. Norv.,* **5,** 60 pp.

Emanuel, K. A., 1986: An air-sea interaction theory for tropical cyclones. Part I: Steady-state maintenance. *J. Atmos. Sci.,* **43,** 585-604.

Emanuel, K. A. 1997: Some aspects of hurricane inner-core dynamics and energetics. *J. Atmos. Sci.*, **54**, 1014-1026.

Fang, J., and F. Zhang, 2010: Evolution of multiscale vortices in the development of Hurricane Dolly (2008). *J. Atmos. Sci.,* **68,** 103-122.

Fierro, A. O., J. Simpson, M. A. LeMone, and Coauthors, 2009: On how hot towers fuel the Hadley Cell: An observational and modeling study of line-organized convection in the equatorial trough from TOGA-COARE. *J. Atmos. Sci.,* **66,** 2730-2746.

——, and J. M. Reisner, 2011: High-resolution simulation of the electrification and lightning of Hurricane Rita during the period of rapid intensification. *J. Atmos. Sci.,* **68,** 477-494.

——, E. J. Zipser, M. A. LeMone, and Coauthors, 2012: Tropical oceanic hot towers: need they be undilute to transport energy from the boundary layer to the upper troposphere effectively? An answer based on trajectory analysis of a simulated TOGA-COARE convective system. *J. Atmos. Sci.,* **69,** 195-213.

Fischer, M.S., B.H. Tang, K.L. Corbosiero, and C.M. Rozoff, 2018: Normalized convective characteristics of tropical cyclone rapid intensification events in the North Atlantic and eastern North Pacific. *Mon. Wea. Rev.,* **146,** 1133-1155.

Frank, W. M., and E. A. Ritchie, 2001: Effects of vertical wind shear on the intensity and structure of numerically simulated hurricanes. *Mon. Wea. Rev.,* **129,** 2249–2269.

Franklin, J. L., 1990: Dropwindsonde observations of the environmental flow of Hurricane Josephine (1984): Relation to vortex motion. *Mon. Wea. Rev.,* **118,** 2732-2744.

——, R. J. Pasch, L. A. Avila, J. L. Beven II, M. B. Lawrence, S. R. Stewart, and E. S. Blake, 2006: Atlantic Hurricane season of 2004. *Mon. Wea. Rev.,* **134,** 981–1025.

Fritsch, J. M., and R. A. Maddox, 1981: Convectively driven mesoscale weather systems aloft. Part I: observations. *J. Appl. Meteor.,* **20,** 9-19.

Galarneau, T. J., and C. A. Davis, 2013: Diagnosing forecast errors in tropical cyclone motion. *Mon. Wea. Rev.,* **141,** 405–430.

Gal-Chen, T., 1982: Errors in fixed and moving frame of references: Applications for conventional and Doppler radar analysis. *J. Atmos. Sci.,* **39,** 2279–2300.

Gaspari, G. and S. E. Cohn, 1999: Construction of correlation functions in two and three dimensions. *Quart. J. Roy. Meteor. Soc.,* **125,** 723-757.

Gentry, R. C., T. T. Fujita, and R. C. Sheets, 1970: Aircraft, spacecraft, satellite, and radar observations of Hurricane Gladys, (1968). *J. Appl. Meteor.,* **9,** 837-850.

George, J. M. and W. M. Gray, 1976: Tropical cyclone motion and surrounding parameter relationships. *J. Appl. Meteor.,* **15,** 1252-1264.

Gradshteyn, I. S., and I. M. Ryzhik, 2007: *Table of Integrals, Series, and Products, 7th ed.* Academic Press, 1171 pp.
[Available online at http://fisica.ciens.ucv.ve/~svincenz/TISPISGIMR.pdf].

Gray, W. M., 1977: Tropical cyclone motion and steering flow relationships in the western Atlantic and in the western Pacific. *Preprints, 11th Tech. Conf. on Hurricanes and Tropical Meteorology,* Miami Beach, Amer. Meteor. Soc., 472-477.

Guimond, S. R., G. H. Heymsfield, and F. J. Turk, 2010: Multiscale observations of Hurricane Dennis (2005): The effects of hot towers on rapid intensification. *J. Atmos. Sci.,* **67,** 633–654.

Hack, J. J., and W. H. Schubert, 1986: Nonlinear response of atmospheric vortices to heating by organized cumulus convection. *J. Atmos. Sci.,* **43,** 1559–1573.

Hamill, T. M., J. S. Whitaker, D. T. Kleist, M. Fiorino, and S. G. Benjamin, 2011: Predictions of 2011's tropical cyclones using the GFS and ensemble-based data assimilation methods. *Mon. Wea. Rev.,* **139,** 3243-3247.

Hanley, D., J. Molinari, and D. Keyser, 2001: A composite study of the interactions between tropical cyclones and upper-tropospheric troughs. *Mon. Wea. Rev.,* **129,** 2570-2584.

Hendricks, E. A., M. S. Peng, B. Fu, and T. Li, 2010: Quantifying environmental control on tropical cyclone intensity change. *Mon. Wea. Rev.,* **138,** 3243–3271.

Heymsfield, G. M., J. B. Halverson, J. Simpson, L. Tian, and T. P. Bui, 2001: ER-2 Doppler

radar investigations of the eyewall of Hurricane Bonnie during the Convection and Moisture Experiment-3. *J. Appl. Meteor.,* **40,** 1310-1330.

Hildebrand, P. H., and Coauthors, 1996: The ELDORA/ ASTRAIA airborne Doppler weather radar: High-resolution observations from TOGA COARE. *Bull. Amer. Meteor. Soc.,* **77,** 213–232.

Hogsett, W., and D.-L. Zhang, 2009: Numerical simulation of Hurricane Bonnie (1998). Part III: Energetics. *J. Atmos. Sci.,* **66,** 2678-2696.

Holland, G. J., 1983: Tropical cyclone motion: Environmental interaction plus a beta effect. *J. Atmos. Sci.,* **40,** 328-342.

——, 1984: Tropical cyclone motion: A comparison of theory and observation. *J. Atmos. Sci.,* **41,** 68-75.

Holliday, C. R., and A. H. Thompson, 1979: Climatological characteristics of rapidly intensifying typhoons. *Mon. Wea. Rev.*, **107**, 1022-1034.

Homeyer, C. R., K. P. Bowman, L. L. Pan, and Coauthors, 2011: Dynamical and chemical characteristics of tropospheric intrusions observed during START08. *J. Geophys. Res.,* **116,** D06111, doi:10.1029/2010JD015098.

Hong, S.-Y., Y. Noh, and J. Dudhia, 2006: A new vertical diffusion package with an explicit treatment of entrainment processes. *Mon. Wea. Rev.,* **134,** 2318-2341.

Houtekamer, P. L., H. L. Mitchell, G. Pellerin, M. Buehner, M. Charron, L. Spacek, and B. Hansen, 2005: Atmospheric data assimilation with an ensemble Kalman filter: Results with real observations. *Mon. Wea. Rev.,* **133,** 604-620.

——, and F. Zhang, 2016: Review of the ensemble Kalman filter for atmospheric data assimilation. *Mon. Wea. Rev.,* **144,** 4489-4532.

Houze, R. A., Jr., 1993: *Cloud Dynamics,* Academic Press, 573 pp.

——, W.-C. Lee, and M. Bell, 2009: Convective contribution to the genesis of Hurricane Ophelia (2005). *Mon. Wea. Rev.,* **137,** 2778-2800.

Hsiao, L.-F., C.-S. Liou, T.-C. Yeh, Y.-R. Guo, D.-S. Chen, K.-N. Huang, C.-T. Terng, and J.-H. Chen, 2010: A vortex relocation scheme for tropical cyclone initialization in Advanced Research WRF. *Mon. Wea. Rev.,* **138,** 3298-3315.

Jones, S. C., 1995: The evolution of vortices in vertical shear. Part I: Initially barotropic vortices. *Quart J. Roy. Meteor. Soc.,* **121,** 821-851.

Jorgensen, D. P., 1984: Mesoscale and convective-scale characteristics of mature hurricanes. Part II: Inner core structure of Hurricane Allen (1980). *J. Atmos. Sci.,*

41, 1287-1311.

——, E. J. Zipser, and M. A. LeMone, 1985: Vertical motions in intense hurricanes. *J. Atmos. Sci.,* **42,** 839-856.

Kain, J. S., and J. M. Fritsch, 1990: A one-dimensional entraining detraining plume model and its application in convective parameterization. *J. Atmos. Sci.,* **47,** 2784-2802.

Kaplan, J., and M. DeMaria, 2003: Lager-scale characteristics of rapidly intensifying tropical cyclones in the north Atlantic basin. *Wea. Forecasting*, **18**, 1093-1108.

——, ——, and A. Knaff, 2010: A revised tropical cyclone rapid intensification index for the Atlantic and eastern North Pacific basins. *Wea. Forecasting*, **25**, 220–241.

Kieu, C. Q., H. Chen, and D.-L. Zhang, 2010: An examination of the pressure–wind relationship in intense tropical cyclones. *Wea. Forecasting,* **25,** 895–907.

Kristiansen, N. I., A. Stohl, A.J. Prata, and Coauthors, 2012: Performance assessment of a volcanic ash transport model mini-ensemble used for inverse modeling of the 2010 Eyjafjallajökull eruption. *J. Geophys. Res.,* **117,** D00U11.

Kuo, Y.-H., M. Skumanich, P. L. Haagenson, and J. S. Chang, 1985: The accuracy of trajectory models as revealed by the observing system simulation experiments. *Mon. Wea. Rev.,* **113,** 1852-1867.

Landsea, C. W., and J. P. Cangialosi, 2018: Have we reached the limits of predictability for tropical cyclone track forecasting? *Bull. Amer. Meteor. Soc.,* doi:10.1175/BAMS-D-17-0136.1.

Liu, Y., D.-L. Zhang, and M. K. Yau, 1999: A multiscale numerical study of Hurricane Andrew (1992). Part II: Kinematics and inner-core structures. *Mon. Wea. Rev.,* **127,** 2597-2616.

Liu, Z., C. S. Schwartz, C. Snyder, and S.-Y. Ha, 2012: Impact of assimilating AMSU-A radiances on forecasts of 2008 Atlantic tropical cyclones initialized with a limited-area ensemble Kalman filter. *Mon. Wea. Rev.,* **140,** 4017-4034.

Liu, X., J. Wei, D.-L. Zhang, and W. Miller**,** 2019: Parameterizing sea surface temperature cooling induced by tropical cyclones. 1: Theory and application to Typhoon Matsa (2005). *Journal of Geophysical Research: Oceans*, **124,** https://doi.org/10.1029/2018JC014117.

Lorenz, E. N., 1969: Atmospheric predictability as revealed by naturally occurring analogues. *J. Atmos. Sci.*, **26**, 636–646.

Lynch, P., 1997: The Dolph-Chebyshev window: A simple optimal filter. *Mon. Wea. Rev.,* **125,** 655-660.

——, and X.-Y. Huang, 1992: Initialization of the HIRLAM model using a digital filter. *Mon. Wea. Rev.,* **120,** 1019-1034.

Majumdar, S. J., S. D. Aberson, C. H. Bishop, R. Buizza, M. S. Peng, and C. A. Reynolds, 2006: A comparison of adaptive observing guidance for Atlantic tropical cyclones. *Mon. Wea. Rev.,* **134,** 2354-2372.

Markowski, P., and Y. Richardson, 2010: *Mesoscale Meteorology in Midlatitudes.* Wiley-Blackwell, 430 pp.

Marks, F. D., Jr., and R. A. Houze, Jr., 1987: Inner core structure of Hurricane Alicia from airborne Doppler radar observations. *J. Atmos. Sci.,* **44,** 1296-1317.

——, ——, and J. F. Gamache, 1992: Dual-aircraft investigation of the inner core of Hurricane Norbert. Part I: Kinematic structure. *J. Atmos. Sci.,* **49,** 919-942.

May, P. T., and D. K. Rajopadhyaya, 1996: Wind profiler observations of vertical motion and precipitation microphysics of a tropical squall line. *Mon. Wea. Rev.,* **124,** 621–633.

McFarquhar, G. M., B. F. Jewett, M. S. Gilmore, S. W. Nesbitt, and T.-L. Hsieh, 2012: Vertical velocity and microphysical distributions related to rapid intensification in a simulation of Hurricane Dennis (2005). *J. Atmos. Sci.,* **69,** 3515–3534.

Miller, W., H. Chen, and D.-L. Zhang, 2015: On the rapid intensification of hurricane Wilma (2005). Part III: Effects of latent heat of fusion. *J. Atmos. Sci.,* **72**, 3829–3849.

——, and D.-L. Zhang, 2019a: Understanding the unusual looping track of Hurricane Joaquin (2015) and its forecast errors. *Mon. Wea. Rev.*, **147,** 2231-2259.

——, and ——, 2019b: A three-dimensional trajectory model with advection correction for tropical cyclones: Algorithm description and tests for accuracy. *Mon. Wea. Rev.*, **147,** 3145-3167.

——, and ——, 2019c: A three-dimensional trajectory model with advection correction for tropical cyclones: Tracing the roots of convective bursts in the eyewall. *Mon. Wea. Rev.,* under review.

Mlawer, E. J., S. J. Taubman, P. D. Brown, M.J. Iacono, and S.A. Clough, 1997: Radiative transfer for inhomogeneous atmospheres: RRTM, a validated correlated-k model for the longwave. *J. of Geophys. Res. Atmos.,* **102,** 16663-16682.

Molinari, J., P. Dodge, D. Vollaro, K. L. Corbosiero, and F. Marks Jr., 2006: Mesoscale aspects of the downshear reformation of a tropical cyclone. *J. Atmos. Sci.,* **63**, 341–354.

Montgomery, M. T., M. E. Nicholls, T. A. Cram, and A. B. Saunders, 2006: A vortical hot tower route to tropical cyclogenesis. *J. Atmos. Sci.,* **63,** 355–386.

——, and R. K. Smith, 2014: Paradigms for tropical cyclone intensification. *Aust. Meteorol. Ocean., Bruce Morton Memorial Volume,* **64,** 37-66.

Morrison, H., 2016: Impacts of updraft size and dimensionality on the perturbation pressure and vertical velocity in cumulus convection. Part I: Simple, generalized analytic solutions. *J. Atmos. Sci.,* **73,** 1441-1454.

——, 2017: An analytic description of the structure and evolution of growing deep cumulus updrafts. *J. Atmos. Sci.,* **74,** 809-834.

Morton, B. R., G. Taylor, and J. S. Turner, 1956: Turbulent gravitational convection from maintained and instantaneous sources. *Proc. Roy. Soc. London,* **234A,** 1–23.

Nguyen, S. V., R. K. Smith, and M. T. Montgomery, 2008: Tropical-cyclone intensification and predictability in three dimensions. *Q. J. R. Meteorol. Soc.,* **134,** 563-582.

Nguyen, L. T., and J. Molinari, 2015: Simulation of the downshear reformation of a tropical cyclone. *J. Atmos. Sci.*, **72**, 4529–4551.

Nolan, D. S., 2007: What is the trigger for tropical cyclogenesis? *Aust. Meteor. Mag.,* **56,** 241–266.

Nystrom, R. G., F. Zhang, E. B. Munsell, S. A. Braun, J. A. Sippel, Y. Weng, and K. Emanuel, 2018: Predictability and dynamics of Hurricane Joaquin (2015) explored through convection-permitting ensemble sensitivity experiments. *J. Atmos. Sci.,* **75,** 401-424.

Onderlinde, M. J., and D. S. Nolan, 2016: Tropical cyclone-relative environmental helicity and the pathways to intensification in shear. *J. Atmos. Sci.,* **73,** 869-890.

Ooyama, K., 1969: Numerical simulation of the lifecycle of tropical cyclones. *J. Atmos. Sci.,* **26,** 3-40.

——, 1982: Conceptual evolution of the theory and modeling of the tropical cyclone. *J. Meteor. Soc. Japan,* **60,** 369-380.

Parrish, D. F., and J. C. Derber, 1992: The National Meteorological Center's spectral statistical interpolation analysis system. *Mon. Wea. Rev.,* **120,** 1747-1763.

Pasch, R. J., E. S. Blake, H. D. Cobb III, and D. P. Roberts, 2006: Tropical cyclone report: Hurricane Wilma, 15–25 October 2005. NOAA/NHC, 27 pp. [Available online at https://www.nhc.noaa.gov/data/tcr/AL252005_Wilma.pdf.]

Persing, J., and M. T. Montgomery, 2003: Hurricane superintensity. *J. Atmos. Sci.,* **60,** 2349–2371.

Press, W. H., S. A. Teukolsky, W. T. Vetterling, and B. P. Flannery, 1992: *Numerical Recipes in Fortran: The Art of Scientific Computing.* Vol 1. 2d ed. Cambridge University Press, 933pp.

Qin, N., D.-L. Zhang, and Y. Li, 2016: A statistical analysis of steady eyewall sizes associated with rapidly intensifying hurricanes. *Wea. Forecasting*, **31**, 737-742.

——, and ——, 2018a: On the extraordinary intensification of Hurricane Patricia (2015). Part I: Numerical experiments. *Wea. Forecasting*, **33**, 1205-1224.

——, ——, W. Miller, and C. Q. Kieu, 2018b: On the rapid intensification of Hurricane Wilma (2005). Part IV: Inner-core dynamics during the steady RMW stage. *Quart. J. Roy. Meteor. Soc.,* **144**, 2508-2523.

Rappaport, E. N., and Coauthors, 2009: Advances and challenges at the National Hurricane Center. *Wea. Forecasting,* **24,** 395–419.

Reasor, P. D., M. T. Montgomery, F. D. Marks, and J. F. Gamache, 2000: Low-wavenumber structure and evolution of the hurricane inner core observed by airborne dual-Doppler radar. *Mon. Wea. Rev.,* **128,** 1653-1680.

——, R. F. Rogers, and S. Lorsolo, 2013: Environmental flow impact on tropical cyclone structure diagnosed from airborne Doppler radar composites. *Mon. Wea. Rev.,* **141,** 2949-2969.

Reynolds, R. W., T. M. Smith, C. Liu, D. B. Chelton, K. S. Casey, and M. G. Schlax, 2007: Daily high-resolution blended analyses for sea surface temperature. *J. Climate,* **20,** 5473-5496.

Rios-Berrios, R., R.D. Torn, and C.A. Davis, 2016: An ensemble approach to investigate tropical cyclone intensification in sheared environments. Part I: Katia (2011). *J. Atmos. Sci.,* **73**, 71– 93.

——, C. Davis, and R. Torn, 2018: A hypothesis for the intensification of tropical cyclones under moderate vertical wind shear. *J. Atmos. Sci.,* doi:10.1175/JAS-D-18-0070.1.

Rodgers, E. B., W. S. Olson, V. M. Karyampudi, and H. F. Pierce, 1998: Satellite-derived latent heating distribution and environmental influences in Hurricane Opal (1995). *Mon. Wea. Rev.,* **126,** 1229-1247.

Rogers, R. F., 2010: Convective-scale structure and evolution during a high-resolution simulation of tropical cyclone rapid intensification. *J. Atmos. Sci.,* **67,** 44-70.

——, P. Reasor, and S. Lorsolo, 2013: Airborne Doppler observations of the inner-core structural differences between intensifying and steady-state tropical cyclones. *Mon. Wea. Rev.,* **141,** 2970–2991.

——, P. D. Reasor, and J. A. Zhang, 2015: Multiscale structure and evolution of Hurricane Earl (2010) during rapid intensification. *Mon. Wea. Rev.,* **143,** 536-562.

Rössler, C. E., T. Paccagnella, and St. Tibaldi, 1992: A three-dimensional atmospheric trajectory model: Application to a case study of Alpine lee cyclogenesis. *Meteor. Atmos. Phys.,* **50,** 211–229.

Rotunno, R., and J. P. Klemp, 1982: The influence of the shear-induced pressure gradient on thunderstorm motion. *Mon. Wea. Rev.,* **110,** 136-151.

——, and K. A. Emanuel, 1987: An air–sea interaction theory for tropical cyclones. Part II: Evolutionary study using a nonhydrostatic axisymmetric numerical model. *J. Atmos. Sci.,* **44,** 542– 561.

Schubert, W. H., M. T. Montgomery, R. K. Taft, and Coauthors, 1999: Polygonal eyewalls, asymmetric eye contraction, and potential vorticity mixing in hurricanes. *J. Atmos. Sci.,* **56,** 1197-1223.

Shapiro, A., K. M. Willingham, and C. K. Potvin, 2010: Spatially variable advection correction of radar data. Part I: Theoretical considerations. *J. Atmos. Sci.,* **67,** 3445–3456.

——, S. Rahimi, C. K. Potvin, and L. Orf, 2015: On the use of advection correction in trajectory calculations. *J. Atmos. Sci.,* **72,** 4261-4280.

Shapiro, L. J., and H. E. Willoughby, 1982: The response of balanced hurricanes to local sources of heat and momentum. *J. Atmos. Sci.,* **39,** 378–394.

Skamarock, W. C., and Coauthors, 2008: A description of the Advanced Research WRF version 3. NCAR Tech Note NCAR/TN-475+STR, 113 pp. [Available online at http://www2.mmm.ucar.edu/wrf/users/docs/arw_v3.pdf.]

Schwartz, C. S., Z. Liu, X.-Y. Huang, Y.-H. Kuo, and C.-T. Fong, 2013: Comparing limited-area 3DVAR and hybrid variational-ensemble data assimilation methods for typhoon track forecasts: sensitivity to outer loops and vortex relocation. *Mon. Wea. Rev.,* **141,** 4350-4372.

——, ——, and ——, 2015: Sensitivity of limited-area hybrid variational-ensemble analyses and forecasts to ensemble perturbation resolution. *Mon. Wea. Rev.,* **143,**

3454-3477.

Stauffer, D. R. and N. L. Seaman, 1990: Use of four-dimensional data assimilation in a limited-area mesoscale model. Part I: experiments with synoptic-scale data. *Mon. Wea. Rev.,* **118,** 1250-1277.

Stern, D. P. and F. Zhang, 2013: How does the eye warm? Part II: Sensitivity to vertical wind shear and a trajectory analysis. *J. Atmos. Sci.,* **70,** 1849-1873.

Stewart, J., 1999: *Multivariable calculus, 4th ed.* Brooks/Cole, 511 pp.

Stoelinga, M. T., 2009: A users' guide to RIP version 4.7: A program for visualizing mesoscale model output. [Available online at http://www2.mmm.ucar.edu/wrf/users/docs/ripug.htm.]

Stohl, A., 1996: Trajectory statistics: A new method to establish source-receptor relationships of air pollutants and its application to the transport of particulate sulfate in Europe. *Atmos. Environ.,* **28,** 1255-1266.

——, and H. Kromp-Kolb, 1994: Origin of ozone in Vienna and surroundings, Austria. *Atmos. Environ.,* **28,** 1255-1266.

——, G. Wotawa, P. Seibert, and H. Kromp-Kolb, 1995: Interpolation errors in wind fields as a function of spatial and temporal resolution and their impact on different types of kinematic trajectories. *J. Appl. Meteor.,* **34,** 2149–2165.

Taylor, G. I. and Green, A. E., 1937: Mechanism of the production of small eddies from large ones, *Proc. Roy. Soc. London* **158A,** 499-521.

——, 1938: The spectrum of turbulence. *Proc. Roy. Soc. London,* **164A**, 476-490.

Thompson, G., R. M. Rasmussen, and K. Manning, 2004: Explicit forecasts of winter precipitation using an improved bulk microphysics scheme. Part I: Description and sensitivity analysis. *Mon. Wea. Rev.,* **132,** 519-542.

——, P. R. Field, R. M. Rasmussen, and W. D. Hall, 2008: Explicit forecasts of winter precipitation using an improved bulk microphysics scheme. Part II: implementation of a new snow parameterization. *Mon. Wea. Rev.,* **136,** 5095-5115.

Torn, R. D., G. J. Hakim, and C. Snyder, 2006: Boundary conditions for limited-area ensemble Kalman filters. *Mon. Wea. Rev.,* **134,** 2490-2502.

——, and ——, 2008: Performance characteristics of a pseudo-operational ensemble Kalman filter. *Mon. Wea. Rev.,* **136,** 3947-3963.

——, 2010: Performance of a mesoscale ensemble Kalman filter (EnKF) during the NOAA high-resolution hurricane test. *Mon. Wea. Rev.,* **138,** 4375-4392.

——, J. S. Whitaker, P. Pegion, T. M. Hamill, and G. J. Hakim, 2015: Diagnosis of the source of GFS medium-range track errors in Hurricane Sandy (2012). *Mon. Wea. Rev.,* **143,** 132-152.

——, T. J. Elless, P. P. Papin, and C. A. Davis, 2018: Tropical cyclone track sensitivity in deformation steering flow. *Mon. Wea. Rev.,* **146**, 3183–3201.

Velden, C., W. E. Lewis, W. Bresky, D. Stettner, J. Daniels, S. Wanzong, 2017: Assimilation of high-resolution satellite-derived atmospheric motion vectors: Impact on HWRF forecasts of tropical cyclone track and intensity. *Mon. Wea. Rev.,* **145,** 1107-1125.

Vigh, J. L., and W. H. Schubert, 2009: Rapid development of the tropical cyclone warm core. *J. Atmos. Sci.,* **66,** 3335-3350.

Wang, X., C. Snyder, and T. M. Hamill, 2007: On the theoretical equivalence of differently proposed ensemble/3D-Var hybrid analysis schemes. *Mon. Wea. Rev.,* **135,** 222-227.

——, D. M. Barker, C. Snyder, and T. M. Hamill, 2008a: A hybrid ETKF-3DVAR data assimilation scheme for the WRF Model. Part I: Observing system simulation experiment. *Mon. Wea. Rev.,* **136,** 1190-1200.

——, ——, ——, and ——, 2008b: A hybrid ETKF-3DVAR data assimilation scheme for the WRF model. Part II: real observation experiments. *Mon. Wea. Rev.,* **136,** 5132-5147.

——, 2011: Application of the WRF hybrid ETKF-3DVAR data assimilation system for hurricane track forecasts. *Wea. Forecasting,* **26,** 868-884.

Wang, Y., and G. J. Holland, 1996: Tropical cyclone motion and evolution in vertical shear. *J. Atmos. Sci.,* **53,** 3313-3332.

Wang, Z., 2014: Characteristics of convective processes and vertical velocity from the tropical wave to tropical cyclone stage in a high-resolution numerical model simulation of Tropical Cyclone Fay (2008*). J. Atmos. Sci.,* **71,** 896–915.

Willoughby, H. E., J. A. Clos, and M. G. Shoreibah, 1982: Concentric eye walls, secondary wind maxima, and the evolution of the hurricane vortex. *J. Atmos. Sci.*, **39**, 395-411.

Wilks, D. S., 2011: *Statistical Methods in the Atmospheric Sciences*. Elsevier Academic Press, 676 pp.

Wu, C.-C., and K. Emanuel, 1995: Potential vorticity diagnostics of hurricane movement. Part I: A case study of Hurricane Bob (1991). *Mon. Wea. Rev.,* **123,** 69-92.

——, T.-S. Huang, and K.-H. Chou, 2004: Potential vorticity diagnosis of the key factors affecting the motion of Typhoon Sinlaku (2002). *Mon. Wea. Rev.,* **132,** 2084-2093.

Wu, T.C., H. Liu, S. Majumdar, C. Velden, and J. Anderson, 2014: Influence of assimilating satellite-derived atmospheric motion vector observations on numerical analyses and forecasts of tropical cyclone track and intensity. *Mon. Wea. Rev.,* **142,** 49-71.

——, C. Velden, S. Majumdar, H. Liu, and J. Anderson, 2015: Understanding the influence of assimilating subsets of enhanced atmospheric motion vectors on numerical analyses and forecasts of tropical cyclone track and intensity with an ensemble Kalman filter. *Mon. Wea. Rev.,* **143,** 2506-2531.

Zagrodnik, J. P., and H. Jiang, 2014: Rainfall, convection, and latent heating distributions in rapidly intensifying tropical cyclones. *J. Atmos. Sci.,* **71,** 2789-2809.

Zhang, D.-L., Y. Liu, and M. K. Yau, 2000: A multiscale numerical study of Hurricane Andrew (1992). Part III: Dynamically induced vertical motion. *Mon. Wea. Rev.*, **128**, 3772-3788.

——, Y. Liu, and M. K. Yau, 2001: A multiscale numerical study of Hurricane Andrew (1992). Part IV: Unbalanced flows. *Mon. Wea. Rev.*, **129**, 92-107.

——, Y. Liu, and M. K. Yau, 2002: A multiscale numerical study of Hurricane Andrew (1992). Part V: Inner-core thermodynamics. *Mon. Wea. Rev.*, **130**, 2745-2763.

——, and H. Chen, 2012: Importance of the upper-level warm core in the rapid intensification of a tropical cyclone. *Geophys. Res. Lett.,* **39,** L02806, doi:10.1029/2011GL050578.

Zhang, X., Y. Li, D.-L. Zhang, and L. Chen, 2018: A 65-year climatology of unusual tracks of tropical cyclones in the vicinity of China's coastal waters. *J. Appl. Meteor. Clim.,* **57,** 155-170.

Zhang, J., and T. Gal-Chen, 1996: Single-Doppler wind retrieval in the moving frame of reference. *J. Atmos. Sci.,* **53,** 2609–2623.

Zhu, T. and D.-L. Zhang, 2006: The impact of the storm-induced SST cooling on hurricane intensity. *Adv. Atmos. Sci.*, **23**, 14-22.